HZG REPORT 2013-3 // ISSN 2191-7833

The Magnetic Spin Structure of $Fe_{50}Pt_{50-x}Rh_x$ Films: A Neutron Diffraction Study

(Vom Promotionsausschuss des Fachbereichs Physik der Universität Hamburg im Jahr 2012 als Dissertation angenommene Arbeit)

J. Fenske

Helmholtz-Zentrum
Geesthacht
Zentrum für Material- und Küstenforschung

HZG REPORT 2013-3

The Magnetic Spin Structure of $Fe_{50}Pt_{50-x}Rh_x$ Films: A Neutron Diffraction Study

(Vom Promotionsausschuss des Fachbereichs Physik der Universität Hamburg im Jahr 2012 als Dissertation angenommene Arbeit)

J. Fenske

Helmholtz-Zentrum Geesthacht
Zentrum für Material- und Küstenforschung GmbH | Geesthacht | 2013

Die HZG Reporte werden kostenlos abgegeben.
HZG Reports are available free of charge.

Anforderungen/Requests:

Helmholtz-Zentrum Geesthacht
Zentrum für Material- und Küstenforschung GmbH
Bibliothek/Library
Max-Planck-Straße 1
21502 Geesthacht
Germany
Tel.: +49 4152 87-1690
Fax.: +49 4152 87-1717
E-Mail: bibliothek@hzg.de

Druck: HZG-Hausdruckerei

ISSN 2191-7833

Helmholtz-Zentrum Geesthacht
Zentrum für Material- und Küstenforschung GmbH
Max-Planck-Straße 1
21502 Geesthacht

www.hzg.de

HZG REPORT 2013-3

The Magnetic Spin Structure of $Fe_{50}Pt_{50-x}Rh_x$ Films: A Neutron Diffraction Study

(Vom Promotionsausschuss des Fachbereichs Physik der Universität Hamburg im Jahr 2012 als Dissertation angenommene Arbeit)

Jochen Fenske

139 pages with 77 figures and 9 tables

Abstract

In the work presented here the structural and magnetic properties of $Fe_{50}Pt_{50-x}Rh_x$ alloys with different Rh concentration (x=5, 10, 17.5 and 25) and thicknesses (100 nm, 200 nm, 300 nm and 500 nm) have been analyzed with macroscopic measurements and magnetically sensitive probes with resolution on the atomic range. Compared to previous studies on bulk $Fe_{50}Pt_{50-x}Rh_x$ alloys with macroscopic measurements the magnetically sensitive investigations on the thin films allow together with structure factor calculations not only the determination of general magnetic properties but for the first time the development of a detailed model of the magnetic configuration.

The structural analysis and macroscopic magnetic measurements were carried out by X-ray diffraction and MOKE measurements, respectively, indicating that the films are well chemically ordered in a bct structure and show different magnetic phases depending on the composition.

A more detailed analysis of the magnetic properties has been carried out by unpolarized and polarized neutron diffraction. The measurements showed that in the 200 nm thick $Fe_{50}Pt_{50-x}Rh_x$ films a transition between a ferromagnetic (FM) order in the in-plane direction and an antiferromagnetic (AF) order in the out-of-plane direction takes place with increasing Rh concentration. Additionally a temperature driven AF-FM transition can be observed in the film with x=10. Measurements with the application of an external magnetic field induce a FM order in the out-of-plane direction in the films with low Rh concentration while the AF ordered films with high Rh content are not affected by the field. The thickness of the $Fe_{50}Pt_{40}Rh_{10}$ films has in a range from 100 nm to 500 nm almost no influence on the fundamental magnetic properties. Only the AF-FM transition of the thicker films is more rapid with increasing temperature.

The applications of detailed structure factor calculations allow to develop a model of the magnetic configuration of the $Fe_{50}Pt_{50-x}Rh_x$ alloys. The magnetic moments in the films with low Rh concentration are FM ordered with a dominant alignment in the out-of-plane direction while in the films with high Rh concentration they are AF ordered and are dominantly orientated in the in-plane direction. The different magnetic configurations can be described by a phenomenological model considering two major contributions: The first term is a bilinear anisotropic Hamiltonian with direction dependent exchange constants and the second term includes the easy axis anisotropy as well as the fourfold tetragonal anisotropy. The phenomenological model indicates that the easy axis anisotropy is dominant for low Rh concentration while the fourfold tetragonal anisotropy becomes prominent for high Rh concentrations.

Die Magnetische Spin Struktur von $Fe_{50}Pt_{50-x}Rh_x$ Filmen: Eine Neutronendiffraktions-Studie

Zusammenfassung

In der hier präsentierten Arbeit wurden die strukturellen und magnetischen Eigenschaften von $Fe_{50}Pt_{50-x}Rh_x$ Legierungen mit unterschiedlicher Rh Konzentration (x=5, 10, 17.5 und 25) und Schichtdicken (100 nm, 200 nm, 300 nm und 500 nm) untersucht. Hierfür wurden makroskopische Messungen und magnetisch sensitive Sonden mit Auflösungen im Bereich atomarer Abstände eingesetzt. Im Gegensatz zu früheren Untersuchungen von Volumen $Fe_{50}Pt_{50-x}Rh_x$ Legierungen mit makroskopischen Untersuchungsmethoden, erlauben die magnetisch sensitiven Messungen nicht nur die Bestimmung der allgemeinen magnetischen Eigenschaften, sondern zum ersten Mal auch die Entwicklung eines detaillierten Modells der magnetischen Anordnungen.

Die strukturellen Untersuchungen und die makroskopisch magnetischen Messungen wurden mit Röntgendiffraktion und MOKE Messungen durchgeführt. Die Ergebnisse dieser Untersuchungen zeigen, dass die Filme eine gute chemische Ordnung mit bct Struktur haben. Des Weiteren wurden Hinweise auf unterschiedliche magnetische Phasen gefunden, die von der Rh Konzentration der Filme abhängen.

Genauere Untersuchungen der magnetischen Eigenschaften wurden mit unpolarisierter und polarisierter Neutronendiffraktion durchgeführt. Diese Messungen zeigen in den 200 nm dicken $Fe_{50}Pt_{50-x}Rh_x$ Filmen mit ansteigender Rh Konzentration einen Übergang von einer ferromagnetischen (FM) Ordnung in der Richtung parallel zur Probenebene zu einer antiferromagnetischen (AF) Ordnung in der Richtung senkrecht zur Probenebene. Ein weiterer AF-FM Übergang kann mit ansteigender Temperatur in dem Film mit $x=10$ beobachtet werden. Messungen mit einem externen angelegten Magnetfeld zeigen eine Induktion einer FM Ordnung in Richtung senkrecht zur Probenebene. Dieser Effekt wurde nur in Filmen mir niedriger Rh Konzentration gefunden, während Filme mit hohem Rh Gehalt nicht beeinflusst werden von einem externen Magnetfeld.

Die Schichtdicke der $Fe_{50}Pt_{40}Rh_{10}$ Filme hat in einem Bereich von 100 nm bis 500 nm nahezu keinen Einfluss auf die grundlegenden magnetischen Eigenschaften der Filme. Es wurde lediglich beobachtet, dass der AF-FM Übergang in den dickeren Filmen mit steigender Temperatur schneller von statten geht.

Die Anwendung von detaillierten Strukturfaktorrechnungen ermöglichte es ein genaues Modell der magnetischen Anordnung zu entwickeln, welches zeigt, dass die Filme mit geringer Rh Konzentration eine FM Ordnung haben, in der die magnetischen Momente in Richtung senkrecht zur Probenebene orientiert sind. Filme mit hohem Rh Gehalt haben wiederum eine AF Ordnung. Hier sind die magnetischen Momente in Richtung parallel zur Probenebene ausgerichtet. Die unterschiedlichen magnetischen Anordnungen können mit Hilfe eines phänomenologischen Modells beschrieben werden. Dieses Modell berücksichtigt zwei Beiträge: Der erste Ausdruck ist ein bilinearer anisotroper Hamilton-Operator mit Richtungsabhängigen Austauschkonstanten und der zweite Ausdruck beinhaltet die easy axis Anisotropie, sowie die fourfold tetragonal Anisotropie. Das phänomenologische Modell deutet für geringere Rh Konzentrationen eine dominante easy axis Anisotropie an, während die fourfold tetragonal Anisotropie für hohe Rh Konzentrationen dominant wird.

Manuscript received / Manuskripteingang in Druckerei: 21. März 2013

Contents

1. Introduction

The improvement of fabrication techniques for artificially structured thin films and layered structures, e.g. templating, lithography etc., provide systems of excellent quality and allow the tailoring of these systems on an almost atomic level [1, 2]. It allows in general to change system parameters, e.g. the film thickness, the composition in alloys or the chemical order, independently with a high degree of precision. Artificially structures are therefore ideally suited to study fundamental physics. For example, magnetic properties of a system can be studied in respect of different crystallographic aspects. Moreover, the magnetic properties of a system can be tuned by the tailoring of the structure which offers new opportunities for technological applications. In the information technology one of the most prominent examples is the use of thin films for hard-disk-drives (HDD) which reduced the production costs and increased the storage density [3]. The improvement of the storage media allowed a doubling of the storage density approximately every two years which is also known as Moore's law.

HDDs with longitudinal recording technology were the dominant data storage devices until recently. Here, the data is stored in grains with the magnetization parallel to the media surface [3]. Problems in the recording media emerge if the grain size reaches a critical value. Below this limit the magnetization of the grains can be thermally excited, becomes unstable and partially flip. The flipping of the magnetization without any external magnetic field is called superparamagnetism and is the threshold of any recording media [3, 4]. Since the grain sizes and, associated with this, the storage density of the longitudinal media are on their limits the recording technology is nowadays more and more replaced by perpendicular recording media [3]. The advantage of these media is that they have in general a higher magnetocrystalline anisotropy compared to the longitudinal media which allow the grain size to be even smaller before the superparamagentic limit is reached and thus they provide higher recording densities. In the perpendicular geometry the magnetization of the grains are perpendicular to the media surface.

Today's recording media use magnetic materials with a high magnetocrystalline anisotropy of larger than 10^7erg/cm^3 like CoPtCr based alloys (0.2×10^7erg/cm^3) that guarantee a high thermal stability, a lifetime above ten years and a storage density of about 600 Gbits/in^2 [3, 5]. The aim, however, is to access even higher storage densities beyond 1 Tbit/in^2. One possible candidate for such a high density recording media is FePt in the equiatomic composition. FePt has a high perpendicular anisotropy of about 7×10^7erg/cm^3 [6, 5] which allows to increase the storage density by a factor of about 10. The problem arising from the high anisotropy is in general a high coercivity which makes high magnetic fields necessary to write the data on the media. In case of FePt magnetic fields of about 7 T are necessary but today's write heads can only reach a write field of about 1.7 T [7]. New technologies have been explored to reduce the write field like the heat assisted magnetic recording (HAMR) which is also known as thermally assisted magnetic recording (TAR) [8, 9]. In this technique the storage medium is heated during the writing process. Close to the Curie point the anisotropy is reduced and thus also the magnetic write field. The heating to high temperatures, however, suffers from certain drawbacks. For the FePt medium thermal stresses are expected if it is heated close to the Curie temperature of about 500°C which causes problems at the head disk interfaces and reduces the signal to noise ratio [10]. One possible solution for this so-called trilemma between media signal to noise, writability and thermal stability is to combine the recording medium with a soft underlayer [11]. The combination of a high anisotropic, ferromagnetic recording media with a low anisotropic, ferromagnetic underlayer reduces the coercivity of the recording media and helps to reverse its magnetization at a reduced write field [10, 12].

A promising candidate for such an underlayer is FeRh [13, 14, 15]. First measurements on the FePt/FeRh bilayer showed that the necessary write field can be significantly reduced [10, 12, 16]. The different structures of both components, i.e. face-centered-tetragonal (fct) for FePt and body-centered-cubic (bcc) for FeRh, however, lead to lattice distortions at their interfaces and therefore reduces the effective recording density.

To overcome the problems of the lattice mismatch it is suggested to introduce a third element into the crystal matrix. If Pt in the FePt alloys is partially replaced by Rh measurements on the bulk $\mathrm{Fe}_{50}\mathrm{Pt}_{50-x}\mathrm{Rh}_x$ system demonstrate that at low Rh concentrations the FM order of FePt is conserved and the Curie temperature is lowered. In certain composition ranges even an AF-FM transition can be found like in FeRh [17, 18]. These magnetic behaviors as well as the better lattice match between the different $\mathrm{Fe}_{50}\mathrm{Pt}_{50-x}\mathrm{Rh}_x$ alloys makes it an interesting candidate for technological applications.

For these applications, in particular, in HDDs the use of thin films is preferred to reduce production costs and device sizes. It is well known that the magnetic properties of such systems with reduced sizes can differ drastically from the one of the bulk system due to dimensionality effects. The information about the magnetic changes is essential for further technological applications. A challenge arising from the introduction of a third element into the crystal matrix is that the process of the magnetic transitions is not fully understood. Here, a good knowledge of the spin configuration is mandatory.

The research on the bulk $\mathrm{Fe}_{50}\mathrm{Pt}_{50-x}\mathrm{Rh}_x$ system carried out so far mainly used macroscopic measurements, e.g. vibrating sample magnetometer measurements [17, 18, 19]. These methods are suited to study the macroscopic magnetic properties of the system but not to examine the magnetic configuration in detail. For these measurements a technique is needed which not only accesses the structure on an atomic scale but also probes the magnetic configuration of the magnetic moments. Here, neutrons are ideal suited since they carry a magnetic moment themselves and therefore interact directly with the magnetic moments of a material (i.e. unpaired electrons). Furthermore with a wavelength in the range of 1Å (thermal neutrons), similar to atomic distances in condensed matter, neutrons are ideal to resolve interatomic distances [20]. The neutron diffraction investigations of the nuclear and magnetic structure on an atomic scale allow in combination with structure factor calculations the development of a detailed model of the magnetic configuration.

The aim of this work is to investigate the magnetic properties and the spin configuration of $\mathrm{Fe}_{50}\mathrm{Pt}_{50-x}\mathrm{Rh}_x$ films. The study does not only shed light on the atomic spin structure of the system but also investigates dimensionality effects. In a first step the spin configuration is analyzed in dependence on the temperature while the influence of an applied magnetic field on the magnetic configuration is investigated in a second step. Finally the influence of the film thickness on the magnetic properties is analyzed in more detail which should give knowledge about the dimensionality effects. For the investigations of the magnetic spin structure both unpolarized and polarized neutron diffraction were performed. Beforehand the samples were characterized by X-ray diffraction and MOKE

measurements.
In the following chapter a detailed motivation for the $Fe_{50}Pt_{50-x}Rh_x$ system is given with a wide overview of past and recent research on related systems like FePt and FeRh. The last part of this chapter deals with the recent investigations on the bulk $Fe_{50}Pt_{50-x}Rh_x$ system. Chapter 3 gives a short overview of the fundamentals of the here applied scattering physics. Chapter 4 deals with the instrumental set-ups used for the investigations. In chapter 5 the results obtained with the different methods are presented and discussed. Additionally structure factor calculations are introduced which are necessary to distinguish between different magnetic configuration models. Chapter 6 summarizes the results and gives a brief outlook for future investigations.

2. $Fe_{50}Pt_{50-x}Rh_x$ related Systems

In this chapter the investigation of the $Fe_{50}Pt_{50-x}Rh_x$ system will be motivated. It will be highlighted why the system is of scientific interest as well as a prominent candidate for future technological spintronics applications. The chapter is divided in three parts. The first and the second part deals with the past and recent investigations on $Fe_{100-x}Pt_x$ and $Fe_{100-x}Rh_x$ systems, respectively. In the last part ternary FePt and FeRh based alloys will be discussed with the main focus on the former investigations on the bulk $Fe_{50}Pt_{50-x}Rh_x$ system.

2.1. $Fe_{100-x}Pt_x$

Since many years $Fe_{100-x}Pt_x$ systems are one of the most heavily investigated systems due to their interesting magnetic properties and the variety of their crystallographic structures. The $Fe_{100-x}Pt_x$ systems near the equiatomic state (x=50) have drawn much attention as materials for high density recording media [21]. The $L1_0$ FePt alloys in the ordered phase are FM ordered with a high coercivity. Here, particularly its high anisotropy ($K_U = 7 \times 10^7 \mathrm{erg/cm^3}$) which is essential for a good thermal stability of storage media, makes FePt to one of the prime candidates for future recording media.

An important prerequisite for such magnetic properties is the good crystallographic and chemical order of the system. In the disordered state the FePt system is still FM ordered but possesses no significant anisotropy and therefore only a low thermal stability. One possibility to achieve the ordered state is to anneal the disordered FePt alloys to about 600°C-1300°C depending on the composition. During the annealing process the FePt system undergoes a phase transition from a disordered face-centered-cubic (fcc) A1-type structure to a face-centered-tetragonal (fct) $L1_0$-type structure [22, 23, 24]. The fraction of the ordered phase increases with the annealing time [25]. Another important feature of the post annealing procedure and the corresponding tetragonal distortion is the transition from a magnetic soft material without significant coercivity to a hard magnet with a high increase of the coercivity of up to 9 kOe [26].

Another important ingredient for high density recording media is the orientation of the magnetic moments and therefore the crystallographic orientation of the FePt alloys to overcome the superparamagnetic limit by the help of materials with perpendicular magnetic geometry. The $L1_0$ FePt alloy grows usually in the [111] preferred orientation with an in-plane magnetic anisotropy [27]. For the desired perpendicular magnetic anisotropy the alloy needs a [001] orientation which can be provided by the growth on different substrates like CrRu, MgO or RuAl [28, 29].

Besides the substrate and the magnetic order also the composition of the alloys plays an important role for its magnetic properties. The ordered fct phase of $Fe_{100-x}Pt_x$ can only be achieved in a composition range of $35 \leq x \leq 55$ (see Fig. 2.1). For lower and higher compositions the alloy grows in a cubic $L1_2$-type structure. Particularly the composition around the $FePt_3$ alloy exhibits interesting properties [30, 31, 32, 33]. The ordered $FePt_3$

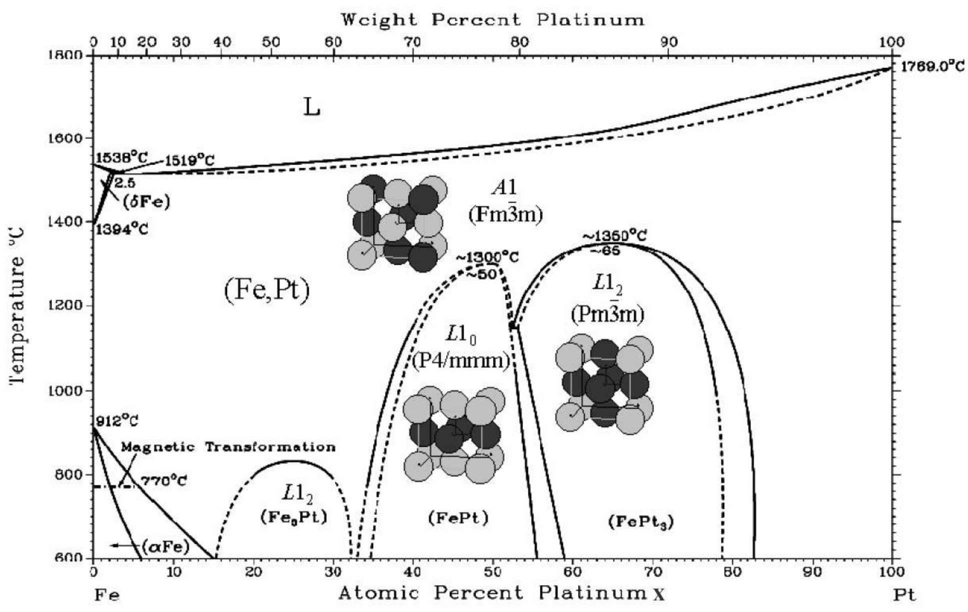

Figure 2.1.: Phase diagram of the $Fe_{100-x}Pt_x$ system with the corresponding crystallographic structures [36] in dependence of the temperature. L, A1, $L1_0$ and $L1_2$ are the strukturbericht symbols for the different crystal structures (adapted from [37]).

alloys have two different AF phases depending on the temperature [34]. At low temperature, T<160 K, it shows the so-called Q_1-phase. In this state, the Fe moments are located in alternating ferromagnetic layers along the (110) plane and the AF unit cell is given by the doubling of the $L1_2$ unit cell along the (001)- and (010)-axis. In this configuration the Fe atoms carry a magnetic moment of about $3.3\mu_B$. In slightly Fe enriched $FePt_3$ the Q_1-phase changes into a second AF-phase below T<100 K which is called the Q_2-phase. The Fe moments are now located in alternating ferromagnetic layers along the (100) plane with a magnetic moment of about $2.0\mu_B$. The unit cell in this phase is here given only by the doubling of the $L1_2$ unit cell along the (001)-axis. It is important to note that only the Fe atoms carry a magnetic moment in both AF phases without inducing any moment on the Pt atoms. In the FM phase of the ordered FePt alloys, however, the Fe atoms as well as the Pt atoms show a magnetic moment of $2.83\mu_B$ and $0.41\mu_B$, respectively [35]. The induction of the magnetic moment on the Pt atoms in the FM phase can be explained by the eight Fe nearest neighbors which surround one Pt atom (see the structure insets in Fig. 2.1). The orientation of the magnetic moments of Fe in the same direction leads to a resulting magnetization at the Pt site and thus induces a magnetic moment on it. In the AF phase, on the other hand, the magnetic moments of the Fe atoms have opposite orientations which results to a zero net magnetic moment at the Pt site.

The previous section gives a short impression about the particular growth conditions which have to be fulfilled to achieve high density recording media. Besides these conditions, however, different tasks are still unresolved to use ordered FePt alloys as recording media.

The high anisotropy of FePt provides a good thermal stability but due to the inherent high coercivity also high write fields are necessary to write the information on the recording system. A solution would be to heat the system close to the Curie point to about 500°C to lower the necessary write field. At such high temperatures, however, problems at the head-disk interfaces are expected, i.e. due to thermal stresses that reduce the signal to noise ratio. A solution for the so-called trilemma, between thermal stability, writability and the media signal to noise ratio, is the combination of the recording system with an underlayer to lower the write field.

It should be noted, that besides the technological application the $\mathrm{Fe}_x\mathrm{Pt}_{100-x}$ system it is also interesting for the investigation of fundamental effects in magnetism. As discussed above the FePt_3 alloys have an AF order in the ordered state as well as a FM order for the FePt alloy or the disordered state. A combination of both states makes the system a good candidate to study exchange mechanism, i.e. exchange bias [38, 39]. By the use of $\mathrm{Fe}_{100-x}\mathrm{Pt}_x$ with almost the same lattice constants (FePt: a=3.863 Å, c=3.710 Å [40] and FePt_3: a=3.866 Å [30]) lattice strain can be avoided. Therefore it offers the possibility to study intrinsic magnetic exchange coupling phenomena between two magnetic phases without the influence of lattice distortions at the interfaces.

2.2. $\mathrm{Fe}_{100-x}\mathrm{Rh}_x$

A good candidate for a magnetic underlayer is a soft magnetic material with an AF-FM phase transition slightly above room temperature. The AF phase of the underlayer provides additional thermal stability to the FePt recording media during the storage of the information while the FM phase lowers the magnetic write field which will be discussed in more detail later. The heating to temperatures of slightly above room temperature reduces thermal stresses that were expected by heating the FePt alloy close to the Curie temperature of about 500°C. A possible candidate for such an underlayer is the $\mathrm{Fe}_x\mathrm{Rh}_{100-x}$ system due to its particular magnetic properties which will be discussed in the following. Similar to $\mathrm{Fe}_{100-x}\mathrm{Pt}_x$ the magnetic and structural properties of the bulk $\mathrm{Fe}_x\mathrm{Rh}_{100-x}$ alloys depend on their composition. In a composition range of about $26 \leq x \leq 45$ the alloy is purely AF with no phase transition [13] while for $x > 64$ the alloy becomes paramagnetic [14]. The composition range near the equiatomic state ($51 \leq x \leq 60$) is again of most interest, because they exhibit an AF-FM phase transition. The changes in the magnetic properties with the composition are also accompanied with structural changes. For $\mathrm{Fe}_{100-x}\mathrm{Rh}_x$ alloys below $x < 56$ only the body-centered-cubic (bcc) structure is observable while in the range of about $56 \leq x \leq 63$ the bcc and the fcc structure coexist [41]. Furthermore, X-ray diffraction measurements demonstrated that for the equiatomic state (x=50) the appearance of the different structures is temperature dependent: at temperatures above the AF-FM transition temperature of T=350 K only the bcc structure is present while below the system partially transforms to the fcc structure [15]. Associated with the AF-FM transition is a volume expansion of about 1%. A second magnetic transition from FM to PM was found at a temperature of about T_c=670 K.

Mössbauer spectroscopy and neutron diffraction measurements furthermore show that in the AF phase only the Fe atoms carry a magnetic moment of $3.3\mu_B$ while the Rh atoms have no magnetic moment at all similar as it was observed in the FePt alloys. In the FM phase, on the other hand, a magnetic moment of $0.9\mu_B$ was found for the Rh atoms while at the same time the moments of the Fe atoms are slightly reduced to $3.2\mu_B$ [42].

Another feature that makes the FeRh alloy very interesting for technological application is that in thin films the transition temperature of the AF-FM transition can be modified by the choice of the substrate. The transition temperature for FeRh grown on a sapphire substrate, for example, is lower than for FeRh grown on a MgO substrate due to tensile in-plane strain which favors the FM over the AF state [43]. Furthermore the transition temperature can be lowered by an external magnetic field [44].

Other important factors for technological applications of magnetic materials are the switching dynamics between the AF and FM state. First time resolved X-ray magnetic circular dichroism measurements on 30 nm polycrystalline thin $Fe_{48.5}Rh_{51.5}$ films by Radu et al. [45] showed that the switching process between the AF-FM state is a rapid nucleation and slow expansion process of FM regions which replace the AF order.

FeRh is an ideal candidate for an underlayer in a FePt recording system due to the AF-FM transition close to room temperature (T=350 K). First experiments by Thiele on FePt/FeRh bilayer systems showed that the magnetic write field can be reduced. The different lattice parameters of FeRh (a=2.986Å [46]) and FePt (a=3.863Å), however, cause large lattice distortions or even canted growth of the FePt media. Since the magnetic properties of the FePt alloys depend strongly on the structure and the growth direction, the distortion would influence the magnetic properties and therefore reduce the storage density of the FePt media. To achieve a smoother lattice match both materials can be doped by a third element as it will be shown in the next section.

The read and write process in these coupled media follow the same principles. The FePt/FeRh system, for example, is heated during the writing process up to a temperature T_0 in the range of about $350\,K<T<670\,K$ where the FeRh system is in the ferromagnetic state. The coupling of the high anisotropic, ferromagnetic FePt with the low anisotropic, ferromagnetic FeRh reduces the coercivity of the FePt alloy by a factor of two to three via an exchange spring mechanism. The exchange spring are strongly nonuniform magnetization distributions located mainly in the FeRh alloy which later penetrate into the FePt alloy and helps to reverse its magnetization at a reduced write field [47, 16]. The data are thereafter stored at a temperature where the FeRh system is in the AF state ($T<350\,K$) and thus the anisotropy of the FM FePt is high providing a good thermal stability. More details of the coupling process can be found in Ref. [12, 47, 48, 49].

2.3. ternary FeRh and FePt based alloys

The previous chapters gave a short overview about the magnetic properties of the FePt and FeRh alloys and their potential in real devices for technological applications. It was also pointed out that their use is hampered by abrasion effects when the FePt system is heated close to the Curie point or by complications of the structural growth due to the large lattice mismatches with the FeRh underlayer. To overcome these limitations the FePt as well as the FeRh alloys can be combined with a third element, e.g. to reduce the Curie temperature of the FePt system and to achieve a smoother lattice match between the FePt and FeRh system. These so-called pseudo-binary or ternary alloys will be discussed in the following.

A good knowledge of the magnetic and structural properties of the ternary alloys is mandatory for further technological developments since it is well known that the magnetic properties of FeRh and FePt alloys can differ drastically if a third element is introduced into the crystal matrix. For example, the addition of Ni or Cu into the FePt alloy replacing the Fe atoms lowers the Curie temperature [10, 50, 51]. Here, Cu proved to be more effective than Ni [52]. The replacement of Fe by Ni, on the other hand, reduces the coercivity [53] and therefore lowers the write field of the system. It is important to note that the fct structure is conserved if the third element is introduced into the FePt crystal matrix and associated with this the perpendicular orientation of the magnetic moments.

Similar to FePt also the magnetic properties of FeRh alloys can be modified by the addition of a third element. If Rh is partly replaced by a small amount of Pd or Ni the AF-FM transition temperature decreases [54, 55, 56, 57] while it increases if Ir or Pt is added to the alloy [18, 58]. The cubic structure of the FeRh based alloy, however, is conserved during the addition of a third element, as long as the amount of substitution is small.

For higher amounts, on the other hand, not only the transition temperature but also the crystal structure as well as the magnetic phase itself are affected as will be shown in the following. Here, we will concentrate mainly on the partial substitution of Rh for Pt in the FePt alloys since these ternary alloys lower the Curie temperature like the FePtNi or FePtCu which is preferable for technological applications, e.g. HAMR. In contrast to the two alloys described above the $\mathrm{Fe}_{50}\mathrm{Pt}_{50-x}\mathrm{Rh}_x$ alloy is a more promising candidate for a recording system with an FeRh underlayer due to the better lattice match which leads to smoother interfaces and the potential for higher recording densities. The effect of the Pt substitution for Rh in the bulk FeRh alloy or Rh for Pt in the bulk FePt alloy, respectively, is presented in the following.

X-ray diffraction studies showed that the bulk $\mathrm{Fe}_{50}\mathrm{Pt}_{50-x}\mathrm{Rh}_x$ system has for concentrations of $x \geq 45$ an ordered bcc structure (B2), while for concentrations of $x \leq 40$ a transition to an ordered body-centered-tetragonal (bct) structure of the CuAuI type ($L1_0$) takes place [17]. This bct phase stabilizes with increasing Pt content. The structural transitions in dependence on the Pt or Rh concentration, respectively, are also accompanied by changes of the magnetic properties.

A detailed study of the magnetic properties of the bulk $\mathrm{Fe}_{50}\mathrm{Pt}_{50-x}\mathrm{Rh}_x$ system were carried out by the group of Yuasa. They used measurements of the linear thermal expansion (LTE) [19], the magnetostriction, the resistivity [18], a pendulum type and a vibrating sample magnetometer as well as Mössbauer spectroscopy [17, 59] to investigate the magnetic properties of the alloys. By the comparison of the magnetization measurements of the magnetometer with, for example, the LTE coefficient it can be shown that the AF-FM phase transition is accompanied by a sharp drop of the LTE coefficient, while the resistivity measurements showed a discontinuous behavior. The different measurements indicate three different temperature driven magnetic transitions in the bulk $\mathrm{Fe}_{50}\mathrm{Pt}_{50-x}\mathrm{Rh}_x$ alloy (see Fig. 2.2): For a Rh content of about $14<x<40$ an AF-PM transition was found while the measurements refer to an AF-FM-PM transition in a composition range of $9.5<x<14$. A FM-PM phase transition was observed in a range of $0<x<9.5$ and for compositions above $x=42$, where the $\mathrm{Fe}_{50}\mathrm{Pt}_{50-x}\mathrm{Rh}_x$ alloys have a bcc structure, an AF-FM-PM phase transition can be observed. It is important to note that the AF-FM transition is of first order while the FM-PM phase transition is of second order. A more detailed study of the triple point has been carried out by the group of Takizawa. By the use of magnetization measurements and Mössbauer spectroscopy together with X-ray diffraction they concluded that the triple point is located at about $x=14.25$ and at a temperature of about $T=388\,\mathrm{K}$ [58].

Further magnetostriction measurements on the $\mathrm{Fe}_{50}\mathrm{Pt}_{50-x}\mathrm{Rh}_x$ system showed that the AF-FM transition can be induced by an external applied magnetic field. Another feature of the magnetic field is a reduction of the transition temperature [19].

X-ray diffraction measurements for the bct structured $\mathrm{Fe}_{50}\mathrm{Pt}_{50-x}\mathrm{Rh}_x$ system with Rh concentrations below $x \leq 40$ showed that no structural changes occur around the observed magnetic transitions. The AF-FM transition, on the other hand, is accompanied by an increase of the lattice parameter c while the lattice parameter a decreases. For the AF-FM transition in the bulk $\mathrm{Fe_{50}Pt_{40}Rh_{10}}$ system, for example, a decreases of about 0.3% can be observed for the lattice parameter a while at the same time the parameter c increases of about 0.75% (see Fig. 2.3). The decrease and increase, respectively, lead consequently to an increase of the c/a-ratio of about 1.05% as well as to an increase of the volume of about 0.15%. A similar behavior can be observed for the AF-PM transition. Here, the volume of the $\mathrm{Fe_{50}Pt_{35}Rh_{15}}$ system increases of about 0.15% and the c/a ratio increases of about 0.36%.

Besides the discontinuity of the c/a-ratio due to the magnetic transitions it was also shown that the c/a-ratio as well as the volume increases with the Pt concentration of the $\mathrm{Fe_{50}Pt_{50-x}Rh_x}$ alloys. The c/a-ratio increases here of about 14.7% from 1.185 for x=50 to 1.359 for x=0. At the same time the volume of the unit cell changes from 26.49Å^3 to 27.53Å^3 which is an increase of about 3.8%. For compositions of x=49, 37.5 and x=10, however, a discontinuous behavior of the volume and the c/a-ratio can be observed. The reason is a change of the dominant magnetic order, only for the $\mathrm{Fe_{50}Pt_{12.5}Rh_{37.5}}$ system the discontinuity is due to a martensitic transformation.

First measurements on thin films were carried out by Lu on 50 nm thin $\mathrm{Fe_{50}Pt_{50-x}Rh_x}$ alloys in the Rh rich regime ($50 \leq x \leq 37.5$) to investigate how the reduced sample dimension changes the magnetic properties [60, 61, 62]. By the use of X-ray diffraction, vibrating sample magnetometer and energy dispersion fluorescence X-ray spectrometry measurements a similar behavior as in the bulk system was observed with an increase of the AF-FM transition temperature with the Pt content. Furthermore they showed that an external magnetic field reduces the transition temperature. It is important to note that in the regime of $x \leq 42.5$ the 50 nm thin $\mathrm{Fe_{50}Pt_{50-x}Rh_x}$ alloys still have the bcc structure of FeRh.

The previous investigations on $\mathrm{Fe_{50}Pt_{50-x}Rh_x}$ alloys have been carried out with macroscopic measurement methods. These methods are able to study the macroscopic magnetic properties of the alloys but they are not sensitive to probe length scales with a resolution on the atomic range. Therefore they are not able to study the magnetic configuration of the alloys in detail which is essential for future applications as already mentioned in the introduction. The measurements on thin $\mathrm{Fe_{50}Pt_{50-x}Rh_x}$ films so far have been only carried out in the Rh rich regime. Data of thin alloy films in the Pt rich regime is still missing. The behavior of the AF-FM transition in the $\mathrm{Fe_{50}Pt_{40}Rh_{10}}$ alloy, for example, is not known in thin films. Furthermore in the previous experiments the alloy thickness and its influence on the magnetic properties has not been investigated in detail. To investigate these aspects of the $\mathrm{Fe_{50}Pt_{50-x}Rh_x}$ alloys the magnetic properties and configuration of $\mathrm{Fe_{50}Pt_{50-x}Rh_x}$ films in the Pt rich regime ($x \leq 25$) will be investigated in the following by the use of a magnetic sensitive probe with a wavelength in the atomic range. Neutron diffraction measurements will be carried out in dependence on temperature (10 K-500 K), magnetic field (up to 12 T) and sample thickness (100 nm-500 nm). The next chapter will give an introduction to the neutron scattering theory followed by a description of the instruments used for the investigations.

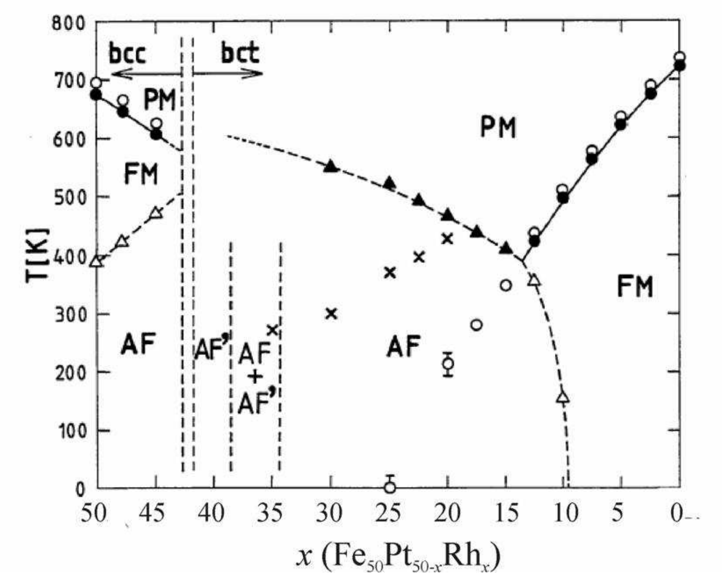

Figure 2.2.: Magnetic phase diagram of the bulk $Fe_{50}Pt_{50-x}Rh_x$ system. Here AF' labels the martensic antiferromagnetic, AF the antiferromagnetic, FM the ferromagnetic and PM the paramagnetic phase (adepted from [17]).

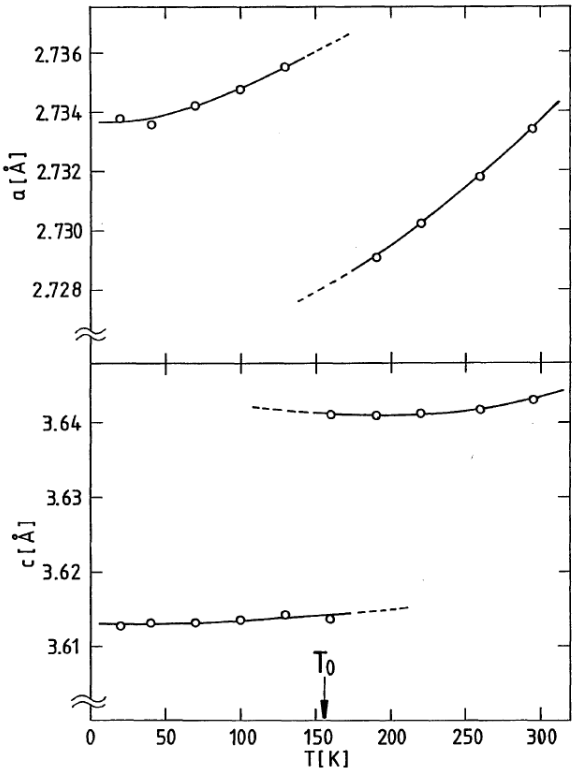

Figure 2.3.: Temperature dependence of the lattice constants a and c for the bulk $Fe_{50}Pt_{40}Rh_{10}$ alloy near the AF-FM transition temperature T_0 (adepted from [17]).

3. Scattering Theory

In this chapter a brief overview of the scattering theory is given. Most of the formula have been taken from reference [63] with additions from references [64, 65, 66, 67, 68]
For the structural analysis of condensed matter different particles are used as probes, as there are protons, neutrons, electrons, photons or atoms. The neutron and photon scattering, the latter in the X-ray regime, have some advantages compared to the scattering with electrons, protons or He-atoms. Both scattering methods are not limited to a small surface region but can penetrate deeper into the material due to their comparatively weak interaction with matter. Therefore they are ideal probes for the non-destructive study of bulk materials as well as thin films or multilayer.
Neutrons interact with the nucleus of an atom. Since they are also spin one-half particles they carry a magnetic moment and interact with the unpaired electrons in matter making them sensitive to detect magnetism. X-rays or photons, on the other hand, are spin one particles and carry no magnetic moment themselves. As an electromagnetic wave they interact with the electron shells of an atom and are also sensitive to the magnetic moments in matter. This interaction occurs between the spins of the electrons in matter and the electromagnetic field as well as an interaction of the orbital momentum of the electrons and the magnetic field of the electromagnetic wave [69]. Compared to neutron scattering these interactions are in general weak, but can be drastically enhanced by tuning the photon energy to the absorption edge of the magnetic site. Here, the magnetic interaction can be even larger as for neutrons but it is limited to a certain energy range which restrains the accessible reciprocal space for most cases. For 3d transition metals, e.g. Fe, a significant enhancement of the magnetic interaction can be only observed in the soft X-ray regime. In this regime the X-rays are strongly absorbed by the matter and as a consequence the penetration depth is reduced which limits the investigation of thicker films and bulk samples to surface regions. Also measurements with the scattering vector $\vec{Q}$ oriented in-plane are difficult due to the absorption. Considering the properties of both probes they can be used complementarilly to study the nuclear and the magnetic structure of matter. The advantages or disadvantages of one of both probes depend strongly on the sample system. For the investigations presented here of the $\mathrm{Fe}_{50}\mathrm{Pt}_{50-x}\mathrm{Rh}_x$ alloys neutrons are the probe of choice due to their higher penetration depths and the larger accessible Q-range.
The properties of neutrons and X-rays are summarized in table 3.1. The scattering theory for elastic neutron scattering and further information on the interaction with matter will be discussed in the following.

3.1. Scattering Geometry

Figure 3.1 shows a typical elastic scattering process in the reflection geometry. The incident beam with the incident angle θ_i in respect to the sample surface and the wave vector $\vec{k}_i = 2\pi/\lambda$ with the wavelength λ is scattered at the surface and reflected under the

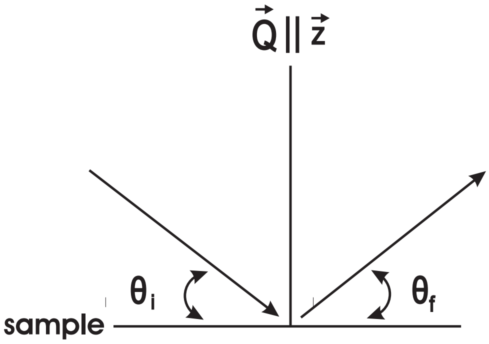

Figure 3.1.: Schematic sketch of a typical elastic scattering process in reflection from a sample.

angle θ_f with the wave vector $\vec{k}_f$. The momentum transfer of the process is the difference of the incident and scattered wave vector and denoted as the scattering vector $\vec{Q}$:

$$\vec{Q} = \vec{k}_f - \vec{k}_i. \tag{3.1}$$

In this work only elastic scattering will be considered, where $\left|\vec{k}_i\right| = \left|\vec{k}_f\right|$, which means that no energy transfer to the sample occurs and the wavelength of the neutrons is unaltered throughout the scattering process. The scattering vector is then defined in the following way:

$$\mid \vec{Q} \mid = \mid \vec{k}_f - \vec{k}_i \mid = 4\pi/\lambda \cdot \sin\theta. \tag{3.2}$$

For the specular case it is $\theta_i = \theta_f = \theta$ and $\vec{Q}$ perpendicular to the plane of incidence.

3.2. Kinematical Scattering Theory

A typical scattering process of photons in the X-ray regime or neutrons is visualized in Fig. 3.2. An incident plane wave $\psi_0 = e^{ikx}$ propagates along the x-direction and interacts with a scatterer. The scatterer in this process can be described by a potential V. If this potential is considered as localized, i.e. the sphere of interaction of V is small compared to the space dimension of the wave package, the potential can be described as point-like. Additionally it can be assumed that for X-ray photons and neutrons the interaction of

	Neutrons	**X-rays** (photons)
elementary particles	Quarks:udd	exchange particle of the electromagnetic interaction
Charge	0	0
Mass	$m_n = 1,675 \times 10^{-27} kg$	0
Spin	1/2	1
magnetic dipole Moment	$\mu_n = -1,913\mu_k$	0
Wave equation	Schrödinger equation	Maxwell equations
Momentum	$\vec{p} = m\vec{v} = \hbar\vec{k}$; $p = h/\lambda$	$\vec{p} = \hbar\vec{k}$; $p = h/\lambda$
Energy	$E = \frac{mv^2}{2} = \frac{\hbar^2 k^2}{2m} = k_B T$	$E = h\nu = \frac{hc}{\lambda}$

Table 3.1.: Properties of neutrons and X-rays

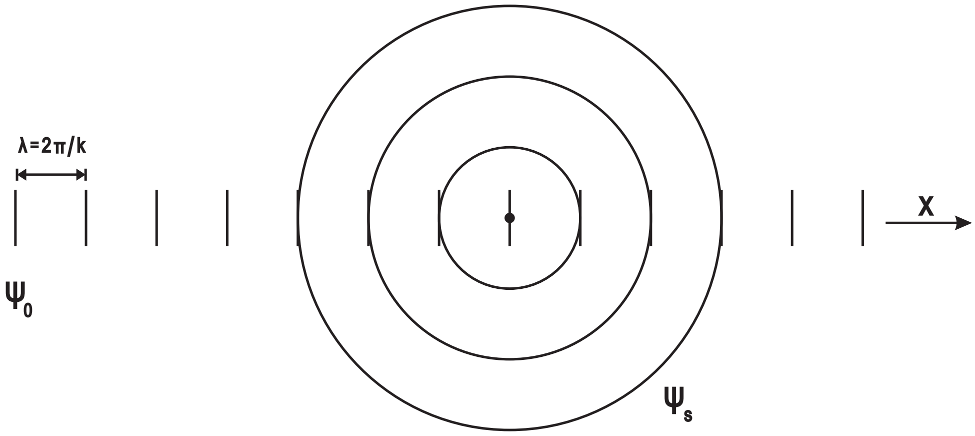

Figure 3.2.: Schematic sketch of the scattering process of a neutron or X-ray beam represented by a plane wave ψ_0 with a wavelength λ and a point like scatterer resulting in a spherical wave ψ_s (adapted from [70]).

the wave package with the potential is in general weak and multiple scattering can be excluded. These assumptions are taken into account in the Born approximation which is used to describe the scattering process under these conditions. Here, the interaction of the incident beam with the point like scatterer can then be described as a perturbation of the incident plane wave ψ_0 by the potential V and thus the scattered wave in far distance ($r \to \infty$) by a spherical wave. The entire scattering process is then given by a superposition of a transmitted plane wave which continues to propagate along the x-direction and a scattered spherical wave [63]:

$$\psi_s(\vec{r}) = e^{ikx} + f(\theta)\frac{e^{ikr}}{r}, \tag{3.3}$$

with the scattering amplitude $f(\theta)$ which is the Fourier transform of the scattering potential:

$$f(\theta) = A(\vec{Q}) \propto b \int d^3 r e^{i\vec{Q}\vec{r}} \delta(\vec{r} - \vec{R}_n) = b e^{i\vec{Q}\vec{R}_n}, \tag{3.4}$$

with the scattering vector $\vec{Q}$ as defined in equation 3.1, $\vec{R}_n$ the positions of the scatterer and with b as the scattering length. The scattering intensity is then given by:

$$I(\vec{Q}) = \mid A(\vec{Q}) \mid^2 = \mid A(\vec{Q}) A^*(\vec{Q}) \mid \propto \mid b e^{i\vec{Q}\vec{r}} \mid^2 . \tag{3.5}$$

This term describes the interaction between the incident beam and the scatterer. Further details to the scattering length in neutron and X-ray diffraction will be given in the next section. It is important to note that in a typical scattering experiment only the intensity or the square of the amplitude, respectively, is measured and therefore the phase information is lost. In this case the only way to gain information about the structure of a sample is by comparison of the measured and calculated scattering intensity.

3.2.1. Scattering length of Neutrons and X-rays

The scattering length describes the interaction of the beam with the scatterer. Since neutrons and X-rays interact physically in a different way with matter one has to distinguish between both probes.

Neutrons

Neutrons interact with the nucleus and the unpaired electrons of an atom. Therefore a nuclear (b^n) and a magnetic (p) part for the neutron scattering length have to be considered.
For the nuclear scattering process with neutrons the scatterer can be described by the Fermi pseudo potential [63]:

$$V(\vec{r}) = \frac{2\pi\hbar^2}{m_n} b\delta(\vec{r} - \vec{R}_n). \tag{3.6}$$

In the Fermi potential it is considered that the wavelength of neutrons ($\approx 10^{-10}$m) is large compared to the small size of the nucleus and the short range of the strong interaction (both in the range of $\approx 10^{-15}$m). Therefore the scatterer can be assumed to be point-like and the nuclear scattering process can be described by a scalar scattering length b^n which is independent of $\vec{Q}$. Another feature of the nuclear scattering length is an unsystematical variation throughout the periodic table which gives often a large scattering contrast between elements with similar order number Z or isotopes. Some elements have even negative b^n, e.g. H or Mn.
Since neutrons are spin one-half particles they interact with the magnetic moment in the sample (i.e. unpaired electrons). This interaction can be described by the magnetic scattering length p [71]:

$$p = \frac{e^2\gamma}{2mc^2} gJf(\theta) = \left(2.7 \times 10^{-5}\text{Å}\right) \cdot gJf(\theta), \tag{3.7}$$

where $\gamma = \frac{\mu_n}{\mu_k} = -1.913$ is the gyromagnetic moment of neutrons, μ_k the nuclear magneton and g the Landé-factor which includes contribution from the spin and angular orbital moment: $g = 1 + \frac{J(J+1)+S(S+1)-L(L+1)}{2J(J+1)}$ where S is the spin and L the orbital angular moment, J is the Spin-Orbit quantum number. The magnetic form factor $f(\theta)$ is given by the Fourier transform of the dispersion of the unpaired electron spins. Since the diameter of the orbitals is of the same size as the neutron wavelength the magnetic scattering length is $\vec{Q}$-dependent in contrast to the nuclear part (see section 4.5).
The contribution of the magnetic part to the scattering length is also very sensitive to the polarization state of the incident neutrons and its orientation to the magnetic moments of the scatterer. This will be discussed in section 3.2.3 in more detail.

X-rays

In contrast to neutrons X-rays interact with the electronic shells of the atoms. The scattering of X-rays from electrons is called Thomson scattering, e.g. the scattering from a free electron is described by the scattering length [70]:

$$r_e = \frac{e^2}{m_e c^2}, \tag{3.8}$$

where e is the charge of electron, m_e the electron mass and c the velocity of light. For the scattering process on a condensed matter sample all electrons in the atomic shells contribute to the scattering process. Since the shells have a dimension in the same range as the wavelength of the incident X-rays they can not be treated as point scatterer. As a consequence one has to integrate over all contributing electrons by considering their phase relations leading to the scattering factor f_e:

$$f_e = \int \rho_e(r) e^{i\vec{Q}r} dV, \tag{3.9}$$

with ρ_e denoting the electron density. This integral over the shell of an atom is called the atomic form factor. The total scattering length of an atom can be written as [65]:

$$b^x = r_e(f_e + \Delta f_e^{'} + \Delta f_e^{''}), \tag{3.10}$$

where the terms $\Delta f_e^{'}$ and $\Delta f_e^{''}$ are correction terms, which become important if the photon energy is near a resonance, denoting the real and imaginary parts of the dispersion and absorption correction, respectively. Since the scattering process of X-rays can not be considered as point-like the scattering length show a $\vec{Q}$-dependence similar to the magnetic scattering length of neutrons with a slower decay along $\left|\vec{Q}\right|$. Another important consequence is the quasi linear like behavior of the scattering length b^x with the atomic number of the elements throughout the periodic table since the strength of the scattering process for X-rays is directly dependent on the number of electron participating to the scattering process.

3.2.2. Bragg Scattering from a Crystal

A three dimensional perfect crystal can be described by three independent basic vectors $\vec{a}_1$, $\vec{a}_2$, $\vec{a}_3$. These vectors form the unit cell with the volume $V = \vec{a}_1 \cdot (\vec{a}_2 \times \vec{a}_3)$. The translation vector that leads from one point in the unit cell to an equivalent point in an other cell is called lattice vector $\vec{T} = u\vec{a}_1 + v\vec{a}_2 + w\vec{a}_3$, where u, v, w are integers. A so-called Bravais lattice consists of all points that are described by the lattice vector $\vec{T}$ [72].

For every crystal lattice in the real space exists an equivalent reciprocal lattice in the reciprocal space that can be described by the reciprocal lattice vector $\vec{G}$:

$$\vec{G} = h\vec{a}_1^* + k\vec{a}_2^* + l\vec{a}_3^*. \tag{3.11}$$

The reciprocal lattice vector with the Miller indices h, k and l is perpendicular to the (h,k,l)-lattice planes and is defined in such a way that the following relation is satisfied:

$$exp(i\vec{G}\vec{T}) = 1. \tag{3.12}$$

The vectors of the reciprocal lattice and that of the real space are linked to each other by [65]:

$$\vec{a}_1^* = \frac{2\pi}{V}\vec{a}_2 \times \vec{a}_3, \qquad \vec{a}_2^* = \frac{2\pi}{V}\vec{a}_3 \times \vec{a}_1, \qquad \vec{a}_3^* = \frac{2\pi}{V}\vec{a}_1 \times \vec{a}_2. \tag{3.13}$$

The distance between the (hkl)-planes in the perpendicular direction is called the lattice plane distance d_{hkl} and the planes parallel to the (hkl)-plane are called lattice plane bands. The reciprocal lattice vector and the lattice distance are linked by the following equation:

$$\mid \vec{G}_{hkl} \mid = \frac{2\pi}{d_{hkl}}. \tag{3.14}$$

where the reciprocal lattice vector is perpendicular to the lattice planes.
The equation 3.5 can now be written for one atom per unit cell as:

$$I(\vec{Q}) \propto \mid b \mid^2 \mid \sum_{u,v,w} e^{i\vec{Q}\vec{T}} \mid . \tag{3.15}$$

For a three dimensional crystal with the basic vectors $\vec{a_1}$, $\vec{a_2}$, $\vec{a_3}$ the scattering amplitude is given by [63]:

$$A(\vec{Q}) = b \sum_{uvw}^{UVW} e^{iu\vec{Q}\vec{a}_1} e^{iv\vec{Q}\vec{a}_2} e^{iw\vec{Q}\vec{a}_3}, \tag{3.16}$$

leading to an expression for the scattered intensity of:

$$\begin{aligned} I(\vec{Q}) \propto \mid A(\vec{Q}) \mid^2 &= \mid b^2 \mid \frac{\sin^2(U\vec{Q}\vec{a}_1)\sin^2(V\vec{Q}\vec{a}_2)\sin^2(W\vec{Q}\vec{a}_3)}{\sin^2(\frac{1}{2}\vec{Q}\vec{a}_1)\sin^2(\frac{1}{2}\vec{Q}\vec{a}_2)\sin^2(\frac{1}{2}\vec{Q}\vec{a}_3)} \\ &= \mid b^2 \mid L_1^2(\vec{Q}\vec{a}_1)L_2^2(\vec{Q}\vec{a}_2)L_3^2(\vec{Q}\vec{a}_3), \end{aligned} \tag{3.17}$$

with the Laue functions $L_i(\vec{Q}\vec{a}_i) = \frac{\sin^2(N\vec{Q}\vec{a}_i)}{\sin^2(\frac{1}{2}\vec{Q}\vec{a}_i)}$. The main maxima appear at positions where the scattering vector satisfies the relation $\vec{Q} = \frac{n \cdot 2\pi}{a_i}$ $(n = u, v, w; \quad i = 1, 2, 3)$. The more lattice planes or scatterer, respectively, contribute the sharper and more intense are the main maxima. Between the main maxima appear $n-2$ subsidiary maxima due to higher order scattering. The solution for the main maxima is exactly given if the Laue condition is fulfilled, which can be written by equation 3.14 as:

$$\vec{Q} = \vec{G}. \tag{3.18}$$

The scattering process where equation 3.18 is fulfilled is called Bragg scattering except in the case of $\vec{Q} = 0$, where no scattering takes place. The Laue conditions are equivalent to the Bragg-law which can be written as [65]:

$$\lambda = 2d_{hkl}\sin\theta, \tag{3.19}$$

with θ denoting the incident angle relative to the lattice planes. By the use of equation 3.14, 3.18 and the Bragg law one can obtain the well known formula for the momentum transfer at the scattering process:

$$\left|\vec{Q}\right| = \frac{4\pi}{\lambda}\sin\theta. \tag{3.20}$$

The scattering from a Bravais lattice as described above takes only one atom per unit cell into account. For n atoms per unit cell the position of the n-th scatterer is given by $\vec{R_n} = \vec{T} + \vec{\rho}$. Here it is $\vec{\rho} = \sum_i m_i \vec{a}_i$ (where m_i are rational numbers and i=1,2,3) the positions of the scatterer. From equation 3.15 the scattered intensity can be calculated with:

$$I(\vec{Q}) \propto \left|F(\vec{Q})\right|^2 = \left|\sum_n e^{i\vec{Q}\vec{R}_n} b_n\right|^2 . \tag{3.21}$$

$F(\vec{Q})$ denotes here the structure factor which contains information about the configuration of the atoms in the unit cell and is one important factor for the relative peak intensity. In the case of pure Bragg scattering the structure factor can be written as:

$$F(\vec{G}) = \sum_n b_n e^{i\vec{G}\vec{\rho}} = \sum_n b_n e^{2\pi i(hm_1+km_2+lm_3)}. \tag{3.22}$$

In this equation the following relations were used:

$$\begin{aligned} \vec{a}_1 \cdot \vec{a}_1^* &= \vec{a}_2 \cdot \vec{a}_2^* = \vec{a}_3 \cdot \vec{a}_3^* = 2\pi \\ \vec{a}_1 \cdot \vec{a}_2^* &= \vec{a}_1 \cdot \vec{a}_3^* = \vec{a}_2 \cdot \vec{a}_3^* = 0. \end{aligned} \tag{3.23}$$

At certain conditions the structure factor can become zero ($F = 0$) due to destructive interference effects. In a bcc structure for example with only one kind of atoms all reflections are forbidden for which the sum of the Miller indices $h + k + l$ results in an odd number.

It is important to note that the above description is only valid for perfect crystals. Real crystals can be described as a conglomeration of many perfect crystallites that are slightly shifted and canted to each other. The so-called mosaic crystals have different sizes and similar orientations. Information about the mosaic spread of the crystals can be gained by the evaluation of rocking scans, since the larger the mosaic spread the broader is the angular distribution of the peaks. The average size of the crystals, on the other hand, can be determined by the Debye-Scherrer approximation [73]:

$$B(2\theta) = \frac{0.89\lambda}{L\cos\theta}, \tag{3.24}$$

with $B(2\theta)$ the Full Width at Half Maximum (FWHM) of the radial measured peak, λ the wavelength of the used radiation and L the coherence length.

3.2.3. Magnetic Scattering

In the following the magnetic scattering process will be described. Here, two cases have to be distinguished. In the unpolarized case the neutron beam consists ideally of equal amounts of spin up and down neutrons, while in the polarized case only one spin state of the neutrons, spin up or spin down, is present.

unpolarized case

As mentioned above neutrons interact with the core of an atom as well as with its magnetic moments. Therefore two independent contributions have to be considered for the scattering intensity of unpolarized neutrons [65]:

$$\begin{aligned} \mid F(\vec{Q}) \mid^2 &= \mid F_n(\vec{Q}) \mid^2 + \mid F_{mag}(\vec{Q}) \mid^2, && (3.25) \\ \text{with} \mid F_n(\vec{Q}) \mid^2 &= \mid \sum_i b_i e^{i\vec{Q}\vec{r}_i} \mid^2 && (3.26) \\ \mid F_{mag}(\vec{Q}) \mid^2 &= \sum_i \sum_j p_i \vec{q}_i p_j \vec{q}_j e^{i\vec{Q}(\vec{r}_i - \vec{r}_j)}, && (3.27) \end{aligned}$$

where F_n denotes the nuclear term, F_{mag} the magnetic term, b_i the nuclear scattering length and p_i, p_j the magnetic scattering lengths (see the section above). The vector $\vec{q}$ is the so-called Halpern vector, describing the magnetic interaction [65]:

$$\vec{q} = \vec{\epsilon}(\vec{\epsilon}\vec{K} - \vec{K}), \tag{3.28}$$

with $\vec{\epsilon}$ indicating the unit vector perpendicular to the scattering plane and the vector $\vec{K}$ pointing in the direction of the magnetic moments. If $\vec{\epsilon}$ is parallel to $\vec{K}$ then $\vec{q} = 0$

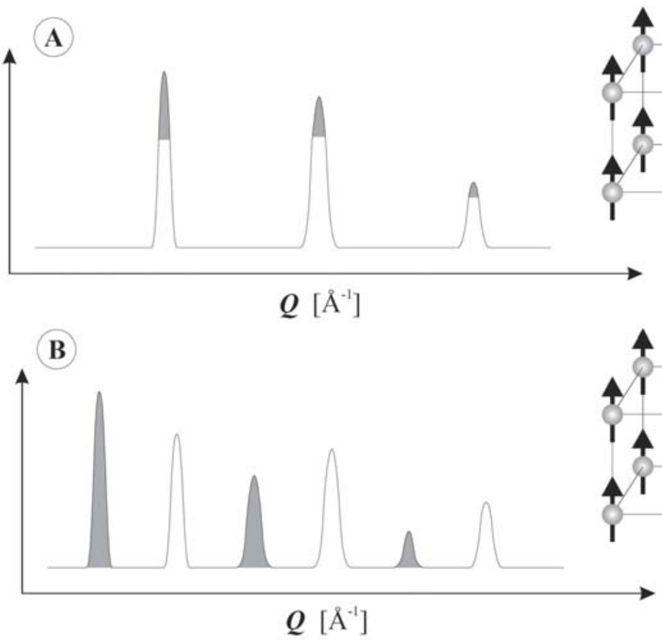

Figure 3.3.: Diffraction spectra of unpolarized neutrons scattered from a simple cubic structure. Picture **A** shows the spectra of a ferromagnetic cubic structure. Picture **B** refers the antiferromagnetic case. The gray labeled intensity regions are the magnetic contributions to the intensity (adapted from [74]).

while $\vec{q}$ reaches its maximum in the case of $\vec{\epsilon}$ being perpendicular to $\vec{K}$. In a saturated ferromagnetic material all spins are aligned parallel as shown in Fig. 3.3. In this case it is:

$$\vec{q}_i \vec{q}_j = q^2 = \sin^2 \alpha, \tag{3.29}$$

where α is the angle between the unit vectors $\vec{\epsilon}$ and $\vec{K}$. In the ferromagnetic case it can be easily seen that the magnetic contributions appear at the same Q-positions as for the nuclear reflections. Therefore, only the peak intensity is changing due to the additional contributions of the magnetic scattering.

In the simplest antiferromagnetic case, where the spins of two ferromagnetic sublattices point in different directions, atom pairs exist with $\vec{K}_i = -\vec{K}_j$. In this case it can be written $\vec{q}_i \vec{q}_j = q^2 = -\sin^2 \alpha$ and equation 3.27 is modified to [65]:

$$\mid F_{mag}(\vec{Q}) \mid^2 = \sin^2 \alpha \sum_i \sum_j (\pm) p_i p_j e^{i\vec{Q}(\vec{r}_i - \vec{r}_j)} \tag{3.30}$$

The plus and minus represent the spins of atom pairs being parallel or antiparallel. Due to the doubling of the unit cell in the magnetic case in comparison to the nuclear one additional magnetic peaks appear at the half order positions between the nuclear peaks (see Fig. 3.3).

polarized case

For the description of the polarized neutron scattering a different ansatz will be used. As discussed before neutrons are spin one-half particles and carry a magnetic moment and interact with the magnetic field of the unpaired electrons. This interaction can be described by the potential V_m [63]:

$$V_m = -\vec{\mu_n} \cdot \vec{B}, \tag{3.31}$$

where $\vec{\mu_n}$ denoting the neutron spin given by:

$$\vec{\mu_n} = -\gamma\mu\vec{\sigma}. \tag{3.32}$$

In this equation μ denotes the nuclear magneton and $\gamma = -1.913$ the gyromagnetic factor of the neutrons. $\vec{\sigma}$ indicates the spin operator. The magnetic field of the unpaired electrons results from two parts: the dipole field of the spin moment $\vec{B_s}$ defined as:

$$\vec{B_s} = \vec{\nabla} \times (\frac{\vec{\mu_e} \times \vec{R}}{R^3}), \tag{3.33}$$

where μ_e is defined as $\mu_e = -2\mu_B\vec{S}$, and on the magnetic field from the orbital moment B_L following from Biot Savart law:

$$\vec{B_L} = -\frac{e}{c}\frac{\vec{v_e} \times \vec{R}}{R^3}. \tag{3.34}$$

To explain this scattering process the introduction of the differential cross section $(\frac{d\sigma}{d\Omega})$ is useful. The cross section is defined by [75]:

$$(\frac{d\sigma}{d\Omega}) = \frac{\text{number of interacting particles/unit time} \times \text{unit cone } d\Omega}{\text{number of incident particles/unit time} \times \text{unit area} \times \text{unit cone } d\Omega}. \tag{3.35}$$

For elastic scattering processes the differential cross section is proportional to the scattering intensity and thus to the square of the scattering amplitude: $(\frac{d\sigma}{d\Omega}) \propto I(\vec{Q}) \propto \left|A(\vec{Q})\right|^2$. For the magnetic scattering process the differential cross section can be expressed as follows [63]:

$$(\frac{d\sigma}{d\Omega}) = (\frac{m}{2\pi\hbar^2}) \left|\left\langle \vec{k_f}\vec{\sigma}_z^f \left|V_m\right| \vec{\sigma}_z^i\vec{k_i} \right\rangle\right|^2, \tag{3.36}$$

and by using 3.31 as the expression for the potential V_m, the scattering amplitude can be written as:

$$(\frac{d\sigma}{d\Omega}) = (\gamma r_0)^2 \left|\frac{1}{2\mu_B}\left\langle S_z^f \left|\vec{\sigma} \cdot \vec{M}_\perp(\vec{Q})\right| S_z^i \right\rangle\right|^2. \tag{3.37}$$

$\vec{M}(\vec{Q})$ is the Fourier transformed of the magnetization density:

$$\vec{M}(\vec{Q}) = \int e^{i\vec{Q}\vec{r}}\vec{M}(\vec{r})dr^3 \tag{3.38}$$

with

$$\vec{M}_\perp = \hat{\vec{Q}} \times \vec{M}(\vec{Q}) \times \hat{\vec{Q}} = \vec{M}(\vec{Q}) - \hat{\vec{Q}}(\vec{M}(\vec{Q}) \cdot \hat{\vec{Q}}). \tag{3.39}$$

$\vec{M}(\vec{r})$ denotes here the magnetization on an atomic scale. The corresponding geometry of the scattering process is shown in Fig. 3.4. It should again be noted that only magnetic moments perpendicular to $\vec{Q}$ contribute to the scattering amplitude.
Considering the equation 3.37 the scattering amplitude $\left|A(\vec{Q})\right|$ can be written as:

$$A(\vec{Q}) = -\frac{\gamma_n r_0}{2\mu_B}\left\langle S_z^f \left|\vec{\sigma} \cdot \vec{M}_\perp\right| S_z^i \right\rangle = -\frac{\gamma_n r_0}{2\mu_B}\left\langle S_z^f \left|\vec{\sigma}_a\right| S_z^i \right\rangle \vec{M}_\perp(\vec{Q})_a, \tag{3.40}$$

where $\vec{\sigma}_a$ are the Pauli spin matrices:

$$\vec{\sigma}_x = \begin{pmatrix} 0 & 1 \\ 1 & 0 \end{pmatrix}; \qquad \vec{\sigma}_y = \begin{pmatrix} 0 & -i \\ i & 0 \end{pmatrix}; \qquad \vec{\sigma}_z = \begin{pmatrix} 1 & 0 \\ 0 & 1 \end{pmatrix}. \tag{3.41}$$

The spin up and down states can be written as $\begin{pmatrix} 1 \\ 0 \end{pmatrix} = |+\rangle$ and $\begin{pmatrix} 0 \\ 1 \end{pmatrix} = |-\rangle$, respectively. The spin matrices can now be expressed as:

$$\begin{aligned} \vec{\sigma}_x \,|+\rangle &= |-\rangle \;; & \vec{\sigma}_x \,|-\rangle = |+\rangle \\ \vec{\sigma}_y \,|+\rangle &= i\,|-\rangle \,; & \vec{\sigma}_y \,|-\rangle = -i\,|+\rangle \\ \vec{\sigma}_z \,|+\rangle &= |+\rangle \;; & \vec{\sigma}_z \,|-\rangle = |-\rangle \,. \end{aligned} \tag{3.42}$$

Considering the equations for the spin matrices the magnetic scattering amplitude is given by:

$$A(\vec{Q}) = -\frac{\gamma_n r_0}{2\mu_B} \begin{cases} \vec{M}_{\perp z}(\vec{Q}) \\ -\vec{M}_{\perp z}(\vec{Q}) \\ \vec{M}_{\perp x}(\vec{Q}) - i\vec{M}_{\perp y}(\vec{Q}) \\ \vec{M}_{\perp x}(\vec{Q}) + i\vec{M}_{\perp y}(\vec{Q}) \end{cases} \quad \text{for} \begin{cases} + \rightarrow + \;\; (NSF) \\ - \rightarrow - \;\; (NSF) \\ + \rightarrow - \;\; (SF) \\ - \rightarrow + \;\; (SF) \end{cases}. \tag{3.43}$$

In the first two cases, denoted as Non-Spin-Flip (NSF) scattering, the spin state of the neutron is unaltered by the scattering process. Here, the scattering amplitude represents the part of $\vec{M}_{\perp}(\vec{Q})$ being parallel to the polarization of the neutrons. In the two (++) and (- -) NSF states the spins of the sample are oriented parallel to the guide field and perpendicular to $\vec{Q}$. The guide field H serves as the quantization axis that aligns the neutron spins parallel to the field.

In the last two cases the spins are flipped during the scattering process and is consequently called Spin-Flip scattering (SF). In this process the scattering amplitude expresses the part of $\vec{M}_{\perp}(\vec{Q})$ being perpendicular to the polarization of the neutrons. In other words, the scattering of the neutrons at the spins of the sample which are oriented perpendicular to the guide field as well as to the scattering vector $\vec{Q}$ contribute to these terms. A sketch of the orientation of the SF and NSF components in the case of the guide field being perpendicular to the scattering vector $\vec{Q}$ is shown in Fig. 3.5.

By the choice of the scattering vector $\vec{Q}$ in respect to the guide field, i.e. parallel or perpendicular to each other, different magnetic components can be observed. In the case of a perpendicular orientation, the NSF and SF scattering channels describe magnetic moments along and perpendicular to the guide field, respectively. For the NSF scattering two cases have to be distinguished: If both NSF channels have identical intensity the material can be in an antiferromagnetic or paramagnetic phase as well as have no magnetic contribution at all, i.e. the intensities are of pure nuclear origin. A difference of both NSF channels, on the other hand, can be attributed to a nonzero net magnetic moment along the guide field direction. Such a resulting magnetic moment can be due to a FM order or a non-collinear structure with a non-zero net moment. Intensity in the SF channels, on the other hand, can be only of magnetic origin. It should be noted that in case of a perpendicular orientation of the scattering vector $\vec{Q}$ in respect to the guide field or the quantization axis z, respectively, the vector is parallel to the x- or y-axis. Considering equation 3.43 and taking into account that only contributions of the magnetic moments perpendicular to the scattering vector can be observed, it can be concluded that only one

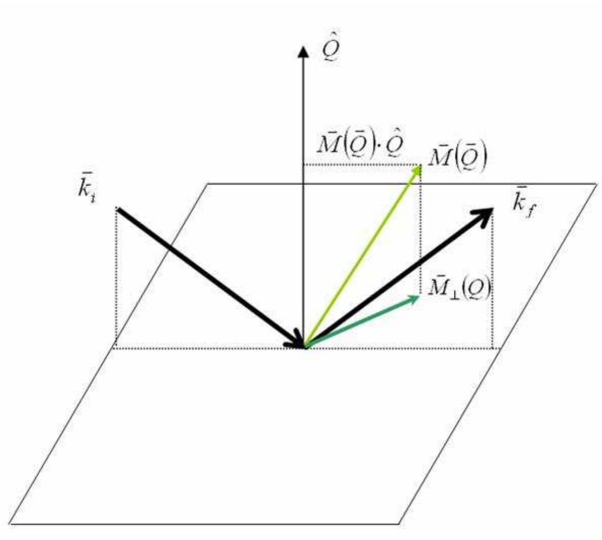

Figure 3.4.: Magnetic scattering process from a sample. For more details see the text.

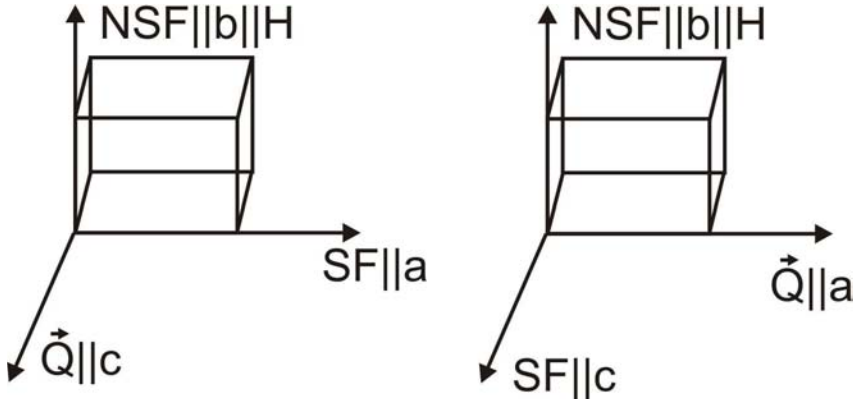

Figure 3.5.: Orientation of the SF and NSF components for the polarized neutron diffraction. On the left side the orientation for the scattering vector $\vec{Q}$ being along the out-of-plane direction and on the right side the geometry for $\vec{Q}$ oriented in the in-plane direction.

component $\vec{M}_{\perp x}$ or $\vec{M}_{\perp y}$ contributes to the scattering amplitude $A(\vec{Q})$. Consequently the intensity $I(\vec{Q})$ of both SF (+-) and (-+) channel is always the same.

In the case of a parallel orientation of the guide field and the scattering vector the SF channel describe again magnetic moments perpendicular to the guide field. The NSF channels, on the other hand, would be sensitive to magnetic moments along the guide field but since the scattering vector is parallel to the guide field and magnetic moments along $\vec{Q}$ are not observable their intensities are only of pure nuclear origin. It should be noted that in the case of the parallel orientation of the guide field (quantization axis z) and the scattering vector magnetic moments along the x- and y-axis can be observed in the SF scattering. Taking both components $\vec{M}_{\perp x}$ and $\vec{M}_{\perp y}$ into account that contribute to the scattering amplitude it can be concluded that in contrast to the previous case an intensity difference between both SF channels is possible. Such an effect is observable in helical materials with different number of left and right turning spirals.

4. Experimental Methods and Instrumentation

In this chapter the experimental set-ups and instruments are described that have been used to grow, characterize and analyze the $\mathrm{Fe}_{50}\mathrm{Pt}_{50-x}\mathrm{Rh}_x$ films. Additionally a summary of the data treatment is presented that was used for the data analysis.

4.1. Sample Preparation

All the samples of this work were grown by the group of Gary J. Mankey in the sputtering chamber ADAM at the MINT center at the University of Alabama. In this work a brief description of the sputtering chamber ADAM is given. A detailed description can be found in the PhD-thesis of P. Mani [76].

A sketch of a typical sputtering chamber is shown in Fig. 4.1. A voltage of about 500 V is applied between the target and the sample yielding a potential difference. Here, the target acts as the cathode while the substrate is the anode. The potential difference ionizes the Ar gas which works as the working gas. The Ar^+ ions and the electrons form together a plasma. An additional applied external magnetic field bunches the Ar^+ ions near the target surface which increases the plasma density and enables a high sputtering rate. The Ar^+ ions lose their energy by collisions with the target which lead to ejections of target atoms. These target atoms form finally the film on the substrate. Depending on several parameters, e.g. sample temperature, applied voltage, etc., two principle growth modes are possible. There is, on the one hand, the layer by layer growth, where the next layer begins to grow when the previous layer is completed. On the other hand, the atoms can conglomerate at certain positions at the sample and form island like structures which is called island growth. Often not optimized growth conditions lead to intermixtures of both growth processes.

An important factor in neutron scattering is the signal to noise ratio since only a sufficient high ratio allows an appropriate investigation of the condensed matter. For an increase of this ratio one can try to optimize the amount of scatterer available in the sample which leads to a higher scattered intensity. The amount of scatterer in thin films is strongly reduced compared to bulk systems. In order to compensate the reduction of the scatterers one can increase the sample size. To achieve large sample sizes of good quality the layer by layer growth was used in this work which provides large sample sizes of up to $2.5\,\mathrm{cm}\times 2.5\,\mathrm{cm}$ with homogeneously distributed films.

4.2. X-ray Instruments

The X-ray measurements were performed at the X-ray diffractometer RöDi at Helmholtz-Zentrum Geesthacht (HZG) the former GKSS using a Cu target. To produce X-rays electrons are accelerated by a high voltage onto the Cu target. Then these electrons are

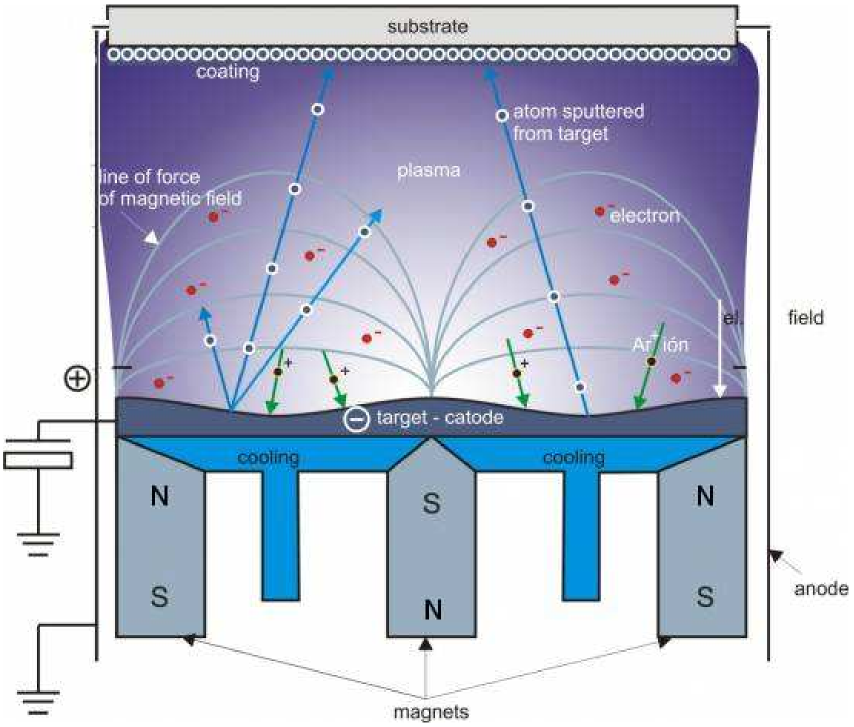

Figure 4.1.: Sputtering process (adapted from [77])

slowed down by collision with the Cu target. The radiation generated by this deceleration is called Bremsstrahlung and gives a continuous X-ray spectrum. If the electrons hit the Cu target with a sufficient energy, they can knock out an electron out of an inner shell of the Cu target and the vacancy is filled again by electrons from higher energy states of the atom. By this recombination X-rays characteristic of the target material are generated which in general are more intense by several order of magnitudes as the continuous Bremsstrahlung. For the Cu target used at RöDi the main contribution of the characteristic spectra are the CuKα_1, CuKα_2 and CuKβ radiation. A Ni-filter with a K-absorption-edge at about $\lambda = 1.488\,\text{Å}$ is used to absorb higher X-ray energies, particular the CuKβ ($\lambda = 1.392\,\text{Å}$) radiation. The CuK$\alpha_1$ ($\lambda = 1.54059\,\text{Å}$) and CuK$\alpha_2$ ($\lambda = 1.54441\,\text{Å}$), on the other hand, are almost unhindered emitted. A splitting in the spectrum of diffraction scans for in Q sharp defined peaks is due to the slightly different wavelengths of the CuKα_1 and CuKα_2 radiation. The X-ray beam is then parallelized by a Göbel mirror [78] which leads to a significant gain of intensity at the sample position. Another feature of the Göbel mirror is an additional suppression of the CuKβ radiation as well as the Bremsstrahlung while the reflectivity of the CuKα_1, CuKα_2 radiation is still about 70%-90%.

The size of the emitted X-ray beam used in the experiment is defined by slits in front and behind the sample. The beam and sample size is important for geometrical corrections of the experimental data. The data treatment of the X-ray and neutron data will be described in more detail in section 4.5.

4.3. MOKE Instruments and Technique

The magneto optic Kerr effect (MOKE) measurements were carried out at the University of Hamburg. The MOKE instrument is a static ellipsometer using a helium-neon-laser which has a wavelength of 632.8 nm by a power of 5 mW and provides linear polarized light in a ratio of 500:1. For a higher polarization rate a Glan-Thompson prism is installed into the beam which has a cancellation factor of smaller than 10^{-7}. The polarized beam is reflected from the sample at an angle of 45° with the sample itself mounted between the pole shoes of an electromagnet (see Fig. 4.2). The pole shoes have a distance of 3 cm which allow one to apply magnetic fields of up to 1T at the sample position. The actual value of the magnetic field is measured by a Hall-sensor that is mounted on one of the pole shoes. For the detection of the reflected light a combination of a second Glan-Thompson prism and a phototransistor with an amplifier is used. For a high intensity a focusing lens is installed in front of the phototransistor. An additional optical filter helps to minimize the influence of the environmental light.

The set-up of the MOKE instrument allows measurements of the polar and the longitudinal Kerr effect. In the polar mode the sample surface is mounted perpendicular to the applied magnetic field and a $\lambda/4$-plate is used to measure the ellipticity. The $\lambda/4$-plate transforms longitudinal polarized light into circular or elliptical polarized light and vice versa. This effect is, here, used to measure the ellipticity of the light: the larger the ellipticity the higher the transmission and consequently the measured intensity. In the longitudinal set-up the sample surface is orientated parallel to the magnetic field and the measurements are carried out without the $\lambda/4$-plate.

The MOKE measurements make use of the effect that the polarization vector of linear polarized light rotates about the so-called Kerr rotation angle θ when it is reflected from a magnetized material. Additionally the polarization state changes from linear to elliptic. The degree of the ellipticity is given by the Kerr ellipticity ϵ. These two effects can be explained in the following way: Linear polarized light is a superposition of left and right circular polarized light in-phase with identical amplitudes. In case of a magnetic material the refraction indices of left and right circular light are different which leads during a scattering process to a phase shift between them and a rotation of the resulting polarization vector of about θ. Additionally they have different absorption coefficients and consequently the amplitudes of both reflected waves are different. This so-called magnetic circular dichroism leads to an elliptic polarization of the light [79]. Since the Kerr rotation as well as the Kerr ellipticity are proportional to the magnetization of the sample it is possible to measure hysteresis loops by determining the rotation and ellipticity, respectively, as a function of the applied magnetic field. By the use of the longitudinal and the polar Kerr effect, the resulting in-plane and perpendicular magnetization can be measured, respectively. The geometry for both cases is shown in Fig. 4.3.

It is important to note that in the signal of the longitudinal Kerr effect still a contribution of the polar Kerr effect can be embedded. To correct the data from this contribution it is necessary to measure additionally the longitudinal Kerr effect with the inverse light path. If both data sets are added up the polar Kerr effect should cancel out since it possesses the opposite sign in both configurations. More detailed information about the Kerr effect and the experimental set-up can be found in the PhD-thesis of H. Stillrich [80].

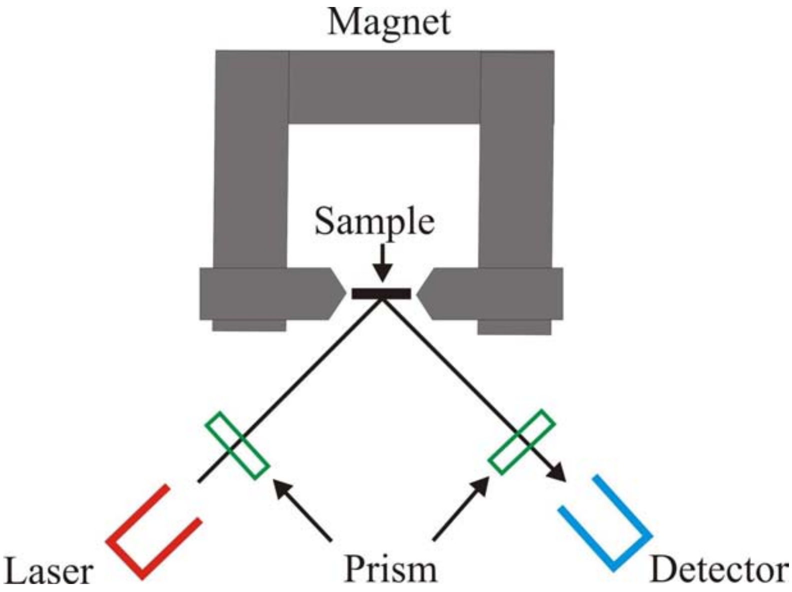

Figure 4.2.: MOKE set-up in the longitudinal mode. For more details see the text.

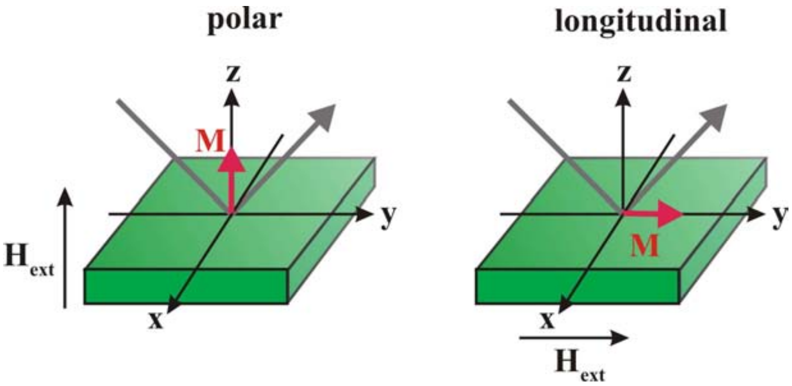

Figure 4.3.: Geometries of the polar and longitudinal Kerr effect.

4.4. Neutron Instruments

The neutron diffraction measurements were performed at four different instruments. The unpolarized measurements were carried out at POLDI at the HZG and D23 at the ILL. The cold triple axis machine IN12 at ILL was used for both unpolarized and polarized measurements with polarization analysis. At the thermal three axis spectrometer IN3 at the ILL additional polarized measurements with polarization analysis were performed. The main parameters of these instruments are listed in table 4.1 at the end of this section.

POLDI

The two axis diffractometer POLDI sketched in Fig. 4.4 was located at the end of the curved neutron guide 7 at the 5 MW research reactor in Geesthacht (FRG-1). The instrument was operated in general in two different modes: The time-of-flight (TOF) mode by taking advantage of the white beam provided from the thermal neutron guide and selecting the wavelength by a chopper and the diffraction mode. The latter mode was exclusively used in this work and will be explained here in more detail.
In the diffraction mode the instrument was operated monochromatically, i.e. only a certain neutron wavelength is used for the experiments. Therefore the neutrons produced by the reactor with a broad wavelength spectrum have to be monochromatized. A first filtering is provided by the curved Ni coated neutron guide 7. The Ni coated guide permit under certain conditions the total reflection of the neutrons. A simplified rule for the total reflection is: wavelength[Å] × 0.1°. These conditions are easily fulfilled by thermal and cold neutrons which are reflected by the guide of an angle of about 1°, while for neutrons in the hot or epithermal regime the angles of total reflection are much smaller 0.01° and 0.05°, respectively, and thus the probability of total reflection is much smaller. Therefore the guides act as a kind of low pass filter for the wavelength distribution. The filtering effect becomes more effective in the case of a curved neutron guide. More details to the curved guide can be found in reference [81].
The final wavelength in the diffraction mode is selected by a pyrolytic graphite PG (002) monochromator with a lattice spacing of $d_{hkl} = 3.55\,\text{Å}$, making use of Bragg's law: $\lambda = 2d_{hkl}\sin\theta$. The wavelength can be chosen by the angle θ of the monochromator to the incident neutron beam. At POLDI the wavelength can be set between 1 Å and 3.6 Å. In the work presented here the wavelength was fixed at $\lambda = 1.8\,\text{Å}$. It is important to note that a crystal monochromator not only allows the primary wavelength λ to be reflected but also higher orders in energy (e.g. $\lambda/2$). These higher orders contribute to the background or result in unwanted reflections. For a wavelength of 1.8 Å the $\lambda/2$ contamination is about 8%.
For the suppression of these higher orders a velocity selector was used which allows only a certain wavelength spectrum to pass. The wavelength can be chosen by the rotation velocity of its curved lamellas. Too slow or too fast neutrons hit the lamellas which are coated with neutron absorbing material ^{10}B. More details to the higher order suppression via velocity selectors can be found in the article of Wagner [82]. In the experiments presented here the velocity was set to 20833 rpm which is equivalent to a wavelength of 1.9 Å. The selector has a resolution of $\frac{\lambda}{\Delta\lambda} \approx 10\%$ which means that also other wavelength are transmitted through the selector. The wavelength offset of the selector reduces the flux intensity of the desired wavelength of 1.8 Å but the advantage is that at the same time the flux ratio of λ to $\lambda/2$ is significant increased compared to the set-up without the wavelength offset (see Fig. 4.5). In this set-up the suppression of the $\lambda/2$-contamination

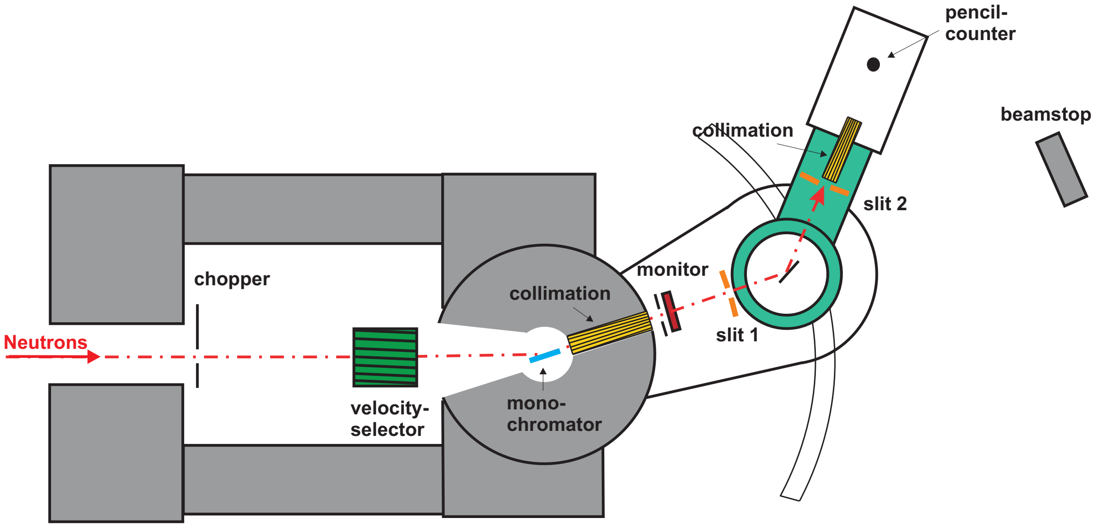

Figure 4.4.: Schematic top view of the diffractometer POLDI at HZG. The grey marked section represents the shielding of the instrument. For more details see text.

is larger than 10^4.

Furthermore the beam can be collimated by different collimators. The collimators consists of several absorber foils coated with neutron absorbing material Be or Gd with a length l mounted parallelly in a distance of d allowing only neutrons to pass through with a divergence smaller than $2 \arctan \frac{d}{l}$. In this work a collimator with a value of 30' and 60' were used in front and behind the sample (see sketch Fig. 4.4). Additionally Cd-slits can be used to define the neutron beam on the sample position and on the detector, respectively, and to reduce the background noise. ^{3}He filled pencil counters were used for the monitoring and detection of the beam. Since the task of the monitor is only to monitor the incident beam intensity without cutting too much off, its probability of detection is highly reduced (efficiency 1%) compared to the ^{3}He counter of the detector (efficiency close to 100%).

For the neutron diffraction experiments at POLDI a closed cycle refrigerator with a temperature range from 10 K up to 325 K and a cryofurnace with a temperature range between 4 K up to 475 K was used.

D23

The instrument D23 is like POLDI a two axis diffractometer. It is installed at the thermal neutron guide H25 at the 58 MW reactor at the ILL. A curved neutron guide prevents the contamination of the fast neutrons. The diffractometer has the capability to be set-up with two monochromators a vertical focusing PG (002) and a Heusler (111) for polarized measurements as it is shown in Fig 4.6. In this work only unpolarized neutrons were used for the measurements and therefore the second monochromator was not installed. The wavelength for the experiments was generally set to about 2.38 Å. In contrast to POLDI the $\lambda/2$-contamination was suppressed here by a graphite-filter which is orientated in such a way that only the wavelengths of higher order satisfy the conditions of the Bragg law. These higher order wavelengths are then scattered out of the beam while the designated wavelength is transmitted through the filter. The efficiency of the filter depends here strongly on the wavelength, i.e. for a wavelength of $\lambda = 2.384$ Å the $\lambda/2$-contamination is less than 0.1%.

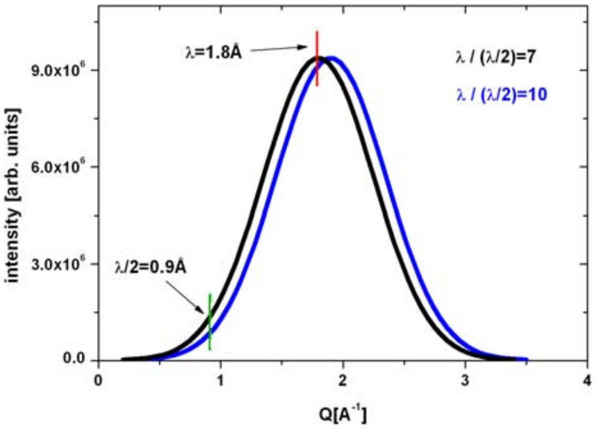

Figure 4.5.: Schematic sketch of the effect of the wavelength offset for the velocity selector. The black and blue lines are the intensity distributions behind the selector without and with the wavelength offset.

Another difference to the set-up of POLDI is that the goniometer at the sample position has no cradle. To compensate for it, the gas filled ^{3}He detector can be lifted in a range between -28°$<\nu<$29°. For the measurements presented in this work different sample environments were used like orange cryostats (1.5 K - 300 K), cryofurnaces (1.5 K - 500 K) and cryomagnets (1.5 K - 300 K, up to 12 T). Details to the sample environment can be found at reference [83].
D23 was used in addition to POLDI to perform the temperature dependent measurements with and without field. The advantages of D23 compared to POLDI are a higher neutron flux and the various sample environments which were available at the ILL, in particular the high magnetic field cryomagnets.

IN12

In contrast to the other two instruments IN12 is a three-axis spectrometer. It is located at the cold double curved neutron guide H142 at the ILL. By the use of a double curved guide the suppression of fast neutrons is higher compared to a single curved guide. The vertical focusing PG (002) monochromator allows to select wavelengths between 2.3 Å and 6 Å. For wavelength larger than 4 Å, the $\lambda/2$-contamination becomes significant and needs to be suppressed by a Beryllium-filter. The suppression by the Be-filter bases again on the Bragg law taking advantage of the effect that the filter becomes transparent for neutrons above a certain wavelength. The higher order wavelength (e.g. $\lambda/2$) are now scattered by the polycrystalline Beryllium while the designated wavelength are transmitted almost unopposed. The monochromatized neutron beam can be defined by different collimations in front and behind the sample.
An obvious difference to the two axis machines is the additional axis of the three axis spectrometer with the analyzer (see Fig 4.7). The additional axis allows in particular energy dispersive measurements. In this work, however, we focus only on elastic measurements. The advantage of the analyzer allows one to select only elastic scattered neutrons which fulfill the Bragg conditions of the analyzer. Neutrons that are scattered inelastic from the sample change their energy and associated with this their wavelength and are not scattered from the analyzer to the detector. It should be noted that for the two axis

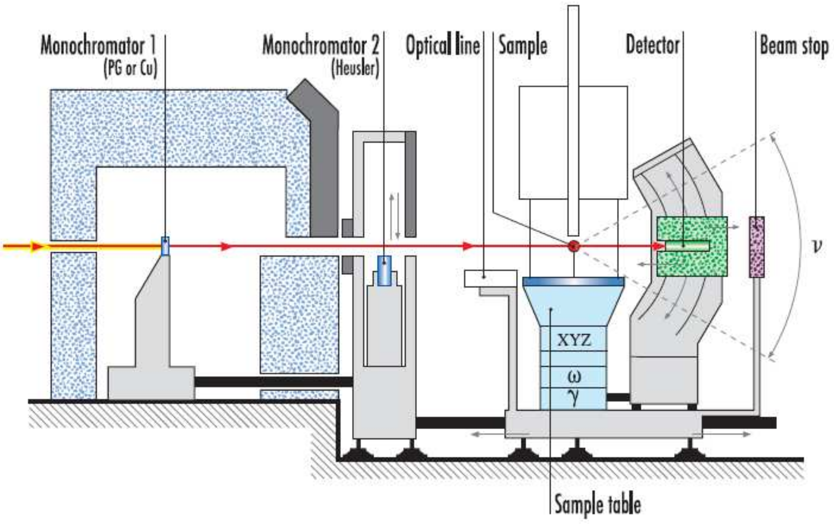

Figure 4.6.: Side view of the diffractometer D23 at ILL (adapted from [84]). The monochromator 2 is only used for polarized measurements.

instruments the inelastic scattering appears as an additional background [71] which can be suppressed here. A horizontal focusing PG (002) monochromator at the analyzer position is used for the unpolarized measurements providing a low background and a good signal to noise ratio. For the polarization analysis of a polarized measurement a Heusler (111) analyzer is installed. The Heusler analyzer reflects only one spin state of the neutrons (up or down) and allows in combination of a spin flipper the analysis of the polarization state of the scattered neutrons. In the polarized measurements a supermirror bender provides the polarization of the incident neutron beam with a degree of polarization of 95% and higher. The guide field at the sample position that conserves the neutron polarization is provided by a Helmholtz-coil or by the cryomagnets used for the experiments. To define the spin states of the incoming and scattered neutrons two flippers are placed at the positions of the diaphragms. In both the polarized and unpolarized measurements the scattered neutrons are detected by a gas filled ^{3}He finger detector. The same sample environment was used at IN12 as at D23 with cryomagnets up to 5 T.
At IN12 mainly polarized neutron diffraction measurements with polarization analysis were carried out, however, it also has advantages for the unpolarized measurements as, for example, a lower background compared to D23. A disadvantage of IN12 is the use of neutrons in the cold wavelength range which shifts the accessible Q-range to lower values compared to the thermal instruments D23 and POLDI. As a consequence not the whole Q-range of interest was accessible for the $Fe_{50}Pt_{50-x}Rh_x$ films.

IN3

IN3 is like IN12 a three axis spectrometer, using thermal neutrons instead of cold neutrons. It is located at the thermal guide H24 at the ILL. In this work IN3 was used as a diffractometer which provides polarized neutrons with polarization analysis. The polarization of the neutrons is provided by a supermirror bender while for the analysis of the neutrons a Heusler (111) analyzer was installed (see Fig. 4.8). The guide field at the sample position is set by permanent magnets in front and behind the sample. These

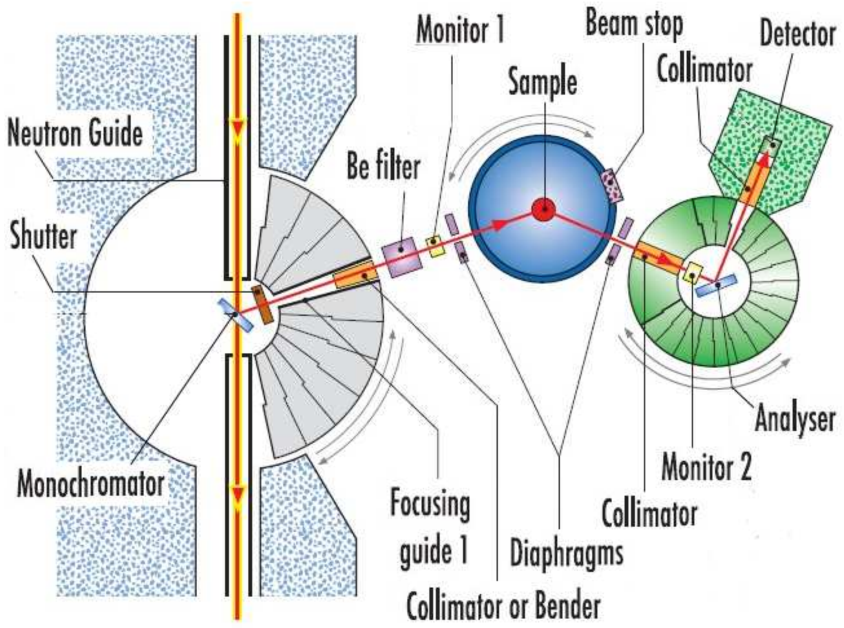

Figure 4.7.: Schematic sketch of the top view of the three axis instrument IN12 at ILL (adapted from [84]). The Be-filter can be used optional and the bender is only used for the polarized neutron measurements. For the polarized measurements the flippers were placed at the positions of the diaphragms.

	POLDI	D23	IN12	IN3
Monochromator	PG(002) (non focusing)	PG(002) (vertical focusing)	PG(002) (vertical focusing)	PG(002) (double faced)
Take-off-angle	$10° < 2\theta_M < 65°$	$16° < 2\theta < 50°$	$15° < 2\theta_M < 90°$	
Wavelength	λ=1 - 3.6Å	λ=1 - 3Å	λ=0.23 - 6Å	λ=1.9 - 4.8Å
Flux	$0.8 \times 10^5 \mathrm{cm}^{-2}\mathrm{s}^{-1}$ (polarized)	$2 \times 10^6 \mathrm{cm}^{-2}\mathrm{s}^{-1}$ (polarized)	$1.0 \times 10^7 \mathrm{cm}^{-2}\mathrm{s}^{-1}$ (polarized)	$2 \times 10^6 \mathrm{cm}^{-2}\mathrm{s}^{-1}$ (polarized)
Detector	^{3}He-Detector	^{3}He-Detector	^{3}He-Detector	^{3}He-Detector

Table 4.1.: Details of the neutron instruments POLDI, D23, IN12 and IN3.

magnets provide a vertical guide field at the sample position of about 30 Gauss which was sufficient to keep the polarization state of the neutrons for the subsequent polarization analysis.
Polarized neutron diffraction measurements with polarization analysis were carried out at IN3 in addition to IN12 for the $Fe_{50}Pt_{45}Rh_5$ film.

4.5. Data Treatment

For the analysis of the experimental data some important corrections have to be applied to the measured raw data. First of all the background signal must be determined and then subtracted from the raw data. The source of this background can be γ-rays, neutrons that are scattered inelastic from the sample or neutrons that are scattered from the environment and arrive in the detector. Electronic noise of the counting electronics can be also a contributing factor to the background signal.

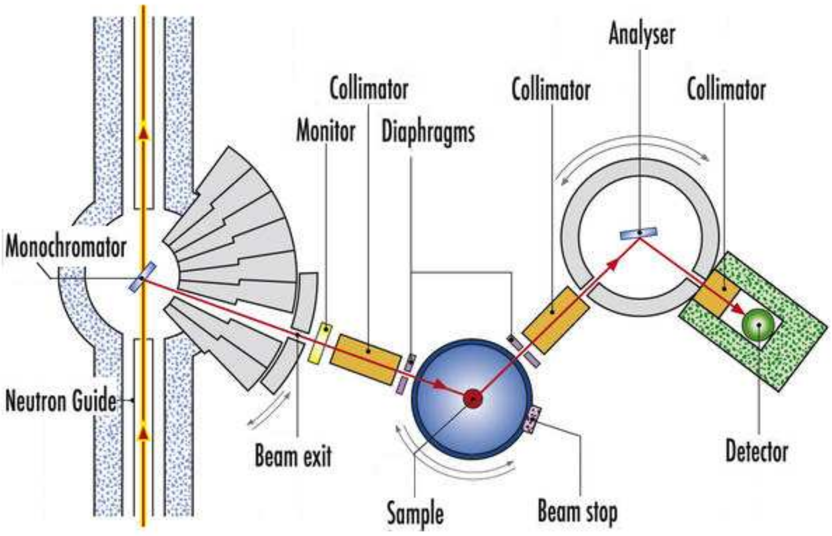

Figure 4.8.: Top view on the thermal three axis instrument IN3 at ILL (adapted from [84]). For the polarized measurements the collimations are replaced by guide fields. The flippers are placed at the positions of the diaphragms.

illumination effects

The measured intensity of the scattered beam needs to be corrected for the geometry of the experiment. The corrections mainly depend on the size of the sample and the width of the incident beam. One of these is the so-called foot print correction. At small angles of the incoming beam in respect to the sample surface only a part of the full beam contributes to the scattering process. Here, the detected intensity has to be accordingly corrected. In the simple case of a cubic or rectangular shaped sample illuminated by a parallel beam which is defined by a slit of the width W a footprint of the length L can be expected:

$$\sin\theta = \frac{W}{L} \tag{4.1}$$

The critical angle θ_c, where the footprint of the beam is the same as the sample width W, is defined by:

$$\sin\theta_c = \frac{W}{l}, \tag{4.2}$$

where l is the width of the sample. The fraction of the beam that illuminates the sample below θ_c is then given as follows:

$$\frac{l}{L} = \frac{\sin\theta}{\sin\theta_c}. \tag{4.3}$$

In order to correct the measurements, the data below θ_c have to be divided by equation 4.3. The second effect takes the material into account that contributes as a scatterer. The more scatterers are involved in the scattering process the higher the intensity of the measured peaks. Above the critical angle θ_c only a part of the scatterers are illuminated by the neutron beam and thus contribute to the scattering process depending on the sample rotation. Therefore the data above θ_c has to be multiplied by the equation 4.3. Here, it should be noted that for the simplest case of a rectangular sample and a 90°

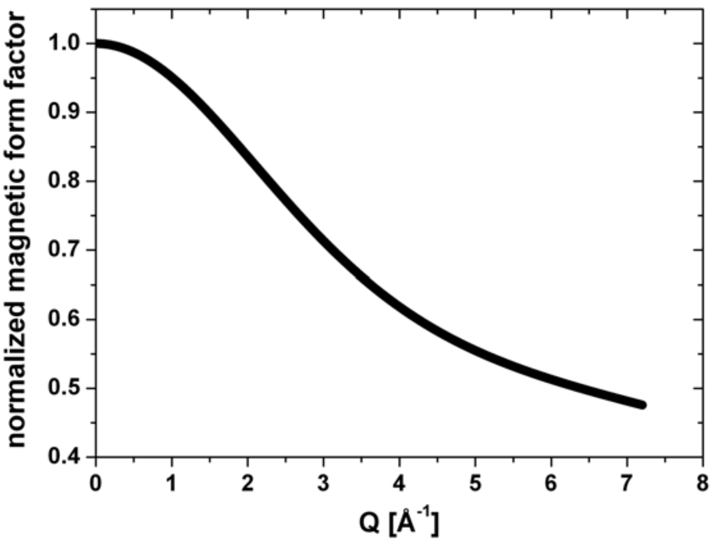

Figure 4.9.: Normalized Q-dependence of the magnetic form factor of Fe.

orientation to the sample holder only one correction is necessary, since the one is already included in the other one. Only for complicated sample shapes and orientations both corrections need to be considered at the same time.

magnetic form factor

As already discussed in the previous chapter the magnetic scattering length p is Q-dependent. This dependence is taken into account by the magnetic form factor $f(\vec{Q})$ (see Fig. 4.9). An approximation for small Q is given by:

$$f(\vec{Q}) = (L + 2S)\,\langle j_0(q)\rangle + L\,\langle j_2(q)\rangle\,, \tag{4.4}$$

where $\langle j_0(s)\rangle$ is given by $\langle j_0(s)\rangle = Ae^{-as^2} + Be^{-bs^2} + Ce^{-cs^2} + D$ and $\langle j_2(s)\rangle$ is defined as $\langle j_2(s)\rangle = (Ae^{-as^2} + Be^{-bs^2} + Ce^{-cs^2} + D)s^2$ with $s = \sin\theta/\lambda$. Since the orbital and the spin magnetic moment L and S as well as the prefactors (A to D) and the exponents (a to c) are unknown at the present stage for the different $\mathrm{Fe_{50}Pt_{50-x}Rh_x}$ films, the values are approximated by assuming that they differ not significantly from the values of α-Fe. A detailed explanation of the calculation and values for the prefactors can be found in reference [85]. For the magnetic moment the values $S = 2.23$ and $L = 0.043$ were used [86].

polarization state

In the case of measurements with polarized neutrons the data have to be corrected for the polarization of the incident neutrons. The polarization of the neutrons is in general less than 100% due to imperfection of the polarizer and the flippers. In particular, in a polarized neutron beam with predominant spin up neutrons also some neutrons with spin down are present. In the case of pure NSF scattering the neutrons with the opposite spin will be detected in the SF channel instead of the NSF channel and vice versa. A figure of merit is the NSF to SF scattering ratio, which is called flipping ratio. In general this ratio is determined from a non magnetic reflection:

$$R = \frac{I_{NSF}}{I_{SF}} \tag{4.5}$$

I_{NSF} and I_{SF} denote the Intensity of the NSF and SF channels, respectively. To correct the neutron data the Intensity of the NSF channel has to be divided by the flipping ratio R and the result has to be subtracted or added to the intensity of the SF or NSF channel, respectively.

5. Measurements and Results

The $Fe_{50}Pt_{50-x}Rh_x$ films were grown by magnetron co-sputtering in an UHV chamber as described in the previous chapter. The chamber had a base pressure of less than 1×10^{-8} mbar and was back filled with ultra pure Ar to a pressure of 4.5×10^{-5} mbar. As substrate a single crystal MgO (001) was used which was degassed at 700°C for a few hours before the deposition of the layers. To provide a good epitaxial growth a combination of Cr followed by Pt was reported to be ideal to grow FePt layer with $L1_0$ structure [87]. Here, the thicknesses of the seed layers were chosen to be 3 nm and 12 nm for the Cr and Pt layer, respectively. It proved to be a good choice for the growth of $L1_0$ structured $Fe_{50}Pt_{50-x}Rh_x$ films. To prevent oxidation the films were capped by a 2 nm Pt layer. In a first step four films of $Fe_{50}Pt_{50-x}Rh_x$ were grown with different Rh concentrations of x=5, 10, 17.5 and 25. The sputter rates of the individual Fe, Pt and Rh targets were calibrated by quartz crystal microbalance for each composition in such a way that the nominal thicknesses of the films have a value of 200 nm. In a second step three $Fe_{50}Pt_{40}Rh_{10}$ films with different thicknesses of 100 nm, 300 nm and 500 nm were grown.

The following sections are divided in two parts, investigating the influence of the Rh concentration and of the thickness of the $Fe_{50}Pt_{50-x}Rh_x$ layer on the structural and magnetic properties, respectively.

5.1. X-ray characterization

For the characterization of the structural properties of the samples X-ray diffraction measurements were carried out at the X-ray diffractometer RöDi at HZG (see chapter 4). The measurements provide information about the quality of the crystal structure and the chemical order. The latter one is a measure for the distribution of the Fe and Pt/Rh atoms in the crystal, e.g. the atoms can be distributed uniformly or occupy only certain sites in the crystal.

5.1.1. Composition

Figure 5.1 shows the X-ray diffraction scans for the 200 nm thick $Fe_{50}Pt_{50-x}Rh_x$ films with different Rh concentrations probing the sample along the growth direction (out-of-plane). Three peaks can be detected in the four films. In general the strongest peak corresponds to the (002) reflection of the MgO substrate at $2\theta = 42.998°$. Since the films were aligned on the (002) reflection of the $Fe_{50}Pt_{50-x}Rh_x$ films and thus slightly detuned in respect to the optimum alignment on the MgO substrate the intensity of the sharp MgO reflections is decreased as it can be seen in particular for the $Fe_{50}Pt_{25}Rh_{25}$ film. The two remaining peaks are due to the (001) and (002) Bragg reflections of the deposited $Fe_{50}Pt_{50-x}Rh_x$ film. The position of these peaks shifts with lower Rh concentration to higher 2θ values, e.g. for x=5 the (002) reflection can be found at $2\theta = 48.938°$ while for x=25 the peak shifts to an angle of $2\theta = 51.444°$. The shifts indicate a lattice expansion perpendicular to the sample plane (c-direction) with decreasing Rh content as expected considering the

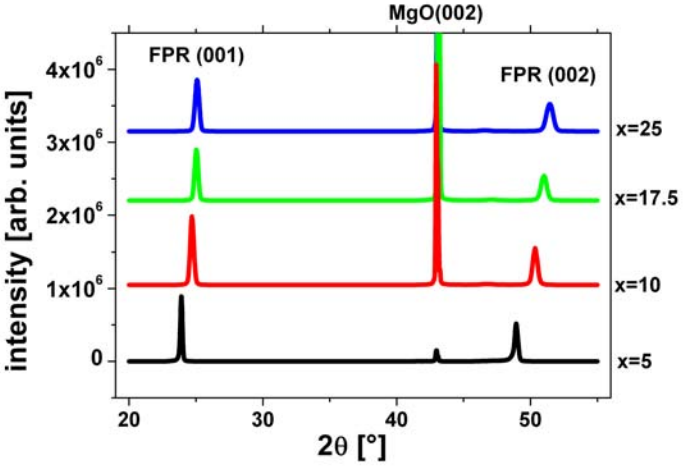

Figure 5.1.: Comparison of the out-of-plane X-ray diffraction scans of the $Fe_{50}Pt_{50-x}Rh_x$ (FPR) films for different Rh compositions x. (Note: for x=5 the sample was slightly detuned in respect for the MgO reflection).

lattice constant c of the FeRh and FePt alloys of 2.986Å and 3.710Å, respectively.

The appearance of the first order reflection (001) is a signature of chemical order in the $L1_0$ structure of the $Fe_{50}Pt_{50-x}Rh_x$ films. If the films were chemically disordered the first order reflection would be forbidden due to destructive interference.

The degree of order of the films is defined by the order parameter S [88, 76] and can be calculated from the X-ray diffraction measurements by:

$$S = \sqrt{\frac{I_{001}|F_{002}|^2 L_p^{002}}{I_{002}|F_{001}|^2 L_p^{001}}}, \tag{5.1}$$

with I_{hkl} the integrated peak intensity of the corresponding peak, $L_p = \frac{1+\cos^2 2\theta}{\sin^2\theta\cos\theta}$ the Lorentz polarization correction [89] and F_{hkl} the structure factor. The (002) peak is a fundamental reflection which is also present in the case of a disordered film. The intensity of this peak is given by constructive interference of the scattered X-rays from the Fe, Pt and Rh atoms. Since in a disordered film the atoms can occupy every site in the lattice the structure factor F_{hkl} for the second order reflection is given by [76]:

$$F_{002} = 2f_{av}, \tag{5.2}$$

where f_{av} is the average structure factor for all atoms in the unit cell. By considering the different contributions of the atoms to the structure factor the average structure factor of the (002) reflection can be calculated as follows [76]:

$$f_{av} = \frac{50f_{Fe} + (50-x)f_{Pt} + xf_{Rh}}{100}. \tag{5.3}$$

The (001) peak is in contrast to the (002) peak a superstructure reflection which is only present in chemically ordered films. Its peak intensity is the result of the destructive interference of the Fe and Pt/Rh atoms and the structure factor given by [76]:

$$F_{001} = f_{Pt/Rh} - f_{Fe}, \tag{5.4}$$

	x=5	x=10	x=17.5	x=25
FWHM[°]	0.66	0.65	0.7	0.52
S	0.79	0.91	0.93	0.92
L[Å]	390	266	249	219

Table 5.1.: Parameters of the X-ray diffraction scans for the composition dependence. The FWHM of the rocking scan of the (001) reflections, the order parameter S and the coherence length L. The coherence length was obtained from the FWHM of the radial diffraction scans as an average of the first and second order reflections of the films (see equation 3.24).

where $f_{Pt/Rh}$ is the weighted average structure factor for the Pt and Rh atoms. It is important to note that in the chemically ordered films the Fe and Pt/Rh atoms occupy only certain sites in the lattice (see Fig. 5.7) but the distribution of the Pt and Rh atoms on the Pt/Rh sites is unknown. Similar to equation 5.3 an average structure factor has to be calculated taking the different contributions of the Pt and Rh atoms into account [76]:

$$f_{Pt/Rh} = \frac{(50-x)f_{Pt} + x f_{Rh}}{50} \tag{5.5}$$

With these equations the order parameters for the different films can be determined. Besides the order parameter also the Full Width at Half Maximum (FWHM) of the rocking scans can give information on the crystalline structure of the samples. As already discussed in the chapter 3 real crystals consist often of small crystallites which are tilted to each other (mosaic spread) and the relative tilt of those crystallites can be determined by the FWHM of the rocking scan. In the rocking scans 2θ is fixed to a certain value and the sample is rotated in such a way that the angle of the incident beam is varied in respect to the sample surface. Another indication of the quality of the structure is the coherence length L which can be calculated from the FWHM of the radial measured Bragg reflections and the Debye-Scherrer approximation (see equation 3.24). Here, the FWHM is used to determine the average crystallite size. These parameters are summarized in table 5.1.

All films have an order parameter above $S>0.79$ which is relatively close to the perfect order of $S=1$. The films with $x \geq 10$ even have an order parameter above $S>0.9$. The small values of the FWHM ($\leq 0.7°$) of the rocking scans around the (001) reflections (see exemplarily the rocking scan for the $Fe_{50}Pt_{32.5}Rh_{17.5}$ film in Fig. 5.2) and the coherence lengths of $L>200$ Å (see table 5.2) indicate that the films possess a good crystallinity, even though they are not single crystals. In fact the FWHM of the rocking scans show the presence of small crystallites in the sample which are slightly tilted to each other.

Additional scans have been performed in the sample plane to investigate the orientation of the film in respect to the MgO-substrate as well as the structure of the film itself. Therefore so-called phi-scans have been carried out around the (101) reflection of the films and the (202) peaks of the MgO substrates. In the phi-scans the detector is fixed to a certain 2θ value and the sample is rotated around the angle ϕ (see Fig. 5.3). To access the different peaks the samples have to be rotated about 52° for the film peaks and for the MgO reflections at about 45° in ψ-direction (see Fig. 5.3). In case of the tetragonal

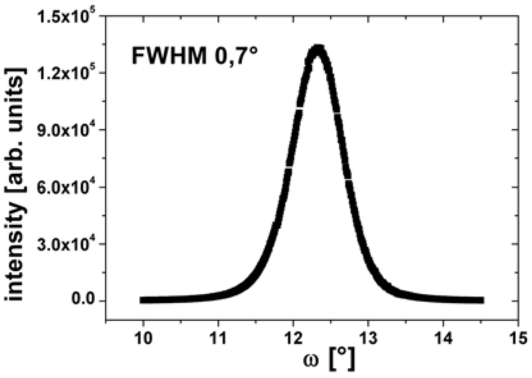

Figure 5.2.: Rocking scan of the (001) reflection of the $Fe_{50}Pt_{32.5}Rh_{17.5}$ film.

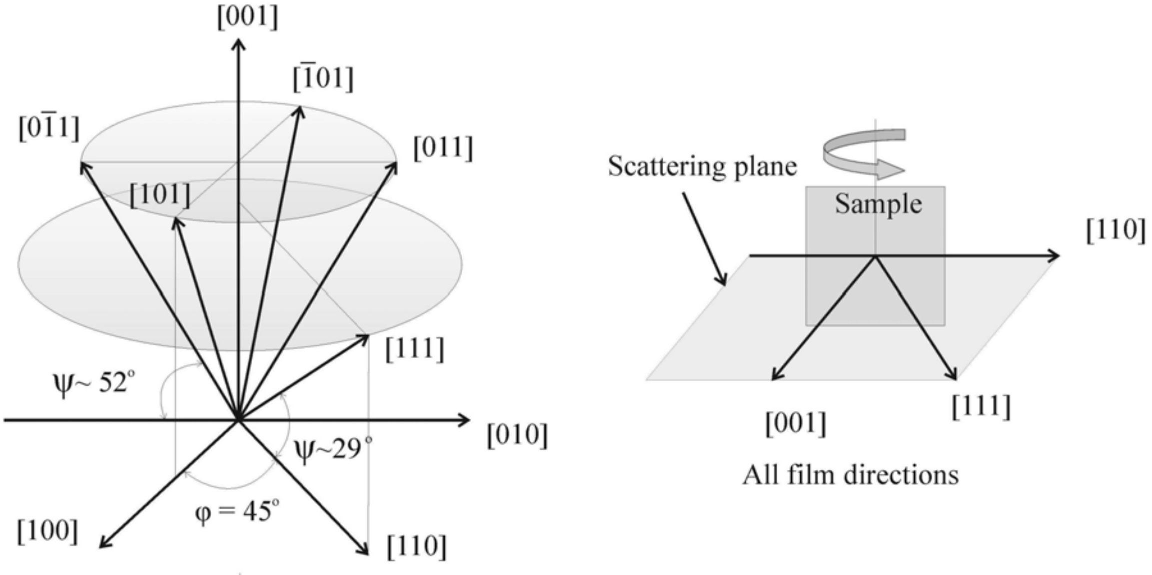

Figure 5.3.: Orientation of the different sample directions and the orientation of the scattering plane (adapted from [76]).

lattice the angles ψ can be calculated by [64]:

$$\cos\psi = \frac{\frac{h_1h_2+k_1k_2}{a^2} + \frac{l_1l_2}{c^2}}{\left(\frac{h_1^2+k_1^2}{a^2} + \frac{l_1^2}{c^2}\right)^{\frac{1}{2}}\left(\frac{h_2^2+k_2^2}{a^2} + \frac{l_2^2}{c^2}\right)^{\frac{1}{2}}}, \tag{5.6}$$

the indices 1, 2 denote two scattering planes which include the angle ψ. Figure 5.4 shows exemplarily the phi-scan of the $Fe_{50}Pt_{25}Rh_{25}$ film. Further phi-scans of the other Rh concentrations show nearly identical pattern and are therefore not illustrated here. Four peaks of the film can be easily observed: the (101), (011), $(\bar{1}01)$ and the $(0\bar{1}1)$ shifted from the corresponding MgO reflections by $\Delta\phi$ =45°. Considering the crystallographic relations between the film and the substrate this reveals a 45° shift of the (100)-vector of the film in respect to the (100)-vector of the substrate. Furthermore the appearance of the four in-plane film peaks is a clear evidence for the bct structure of the film. In a $L1_0$ structure of the fct phase the (101), (011), $(\bar{1}01)$ and the $(0\bar{1}1)$ reflection are forbidden due to destructive interference. Additional in-plane phi-scans were measured around the

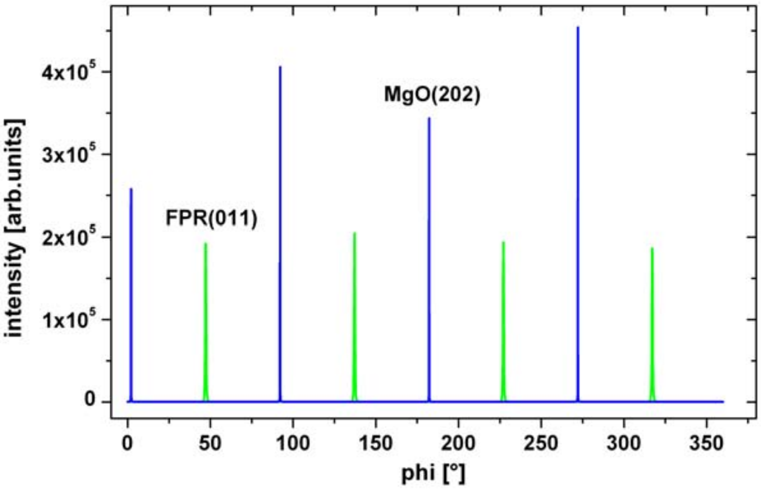

Figure 5.4.: Phi-scan at the (011) reflection of the $Fe_{50}Pt_{25}Rh_{25}$ film (green color) and the (202) reflection of the MgO substrate (blue color). The peaks of the film are 45° shifted in respect to the reflections of the MgO substrate.

(111)-reflection of the film with ψ=29° confirming the good crystalline structure of the film (see Fig. 5.5).

Besides the chemical order and crystallinity, the lattice constants can be determined from the X-ray diffraction scans. The out-of-plane lattice parameter c can be calculated from the Q-positions of the (002) or (001) reflections of the films, respectively, by using equation 3.14. The determination of the in-plane lattice parameter a is slightly more complex since its calculation depends also on the lattice parameter c [90]:

$$\frac{1}{d_{hkl}^2} = \frac{h^2+k^2}{a^2} + \frac{l^2}{c^2}. \tag{5.7}$$

This relation in combination with equation 3.14 can be used to determine the in-plane lattice parameter from the Q-position of the (101) or (111) reflection of the film. Figure 5.6 shows the lattice parameters a and c for the different Rh concentrations. It can be seen that c decreases with higher Rh content from 3.728 Å for x=5 to 3.556 Å for x=25. Contrary to that the in-plane lattice parameter a increases with higher Rh content from 2.741 Å for x=5 to 2.779 Å for x=25. As a consequence of the increase and decrease of the lattice constants a and c, respectively, the c/a- ratio decreases with increasing Rh concentration from 1.358 to 1.278. The decreasing and increasing of the lattice constant c and a with the Rh content indicates a lattice contraction in the out-of-plane direction and an expansion in the in-plane direction. The c/a-ratio of $1 < c/a < \sqrt{2}$, on the other hand, shows that the bct structure is an intermediate structure between the bcc structure of FeRh ($c/a = 1$) and the disordered fcc structure of FePt ($c/a = \sqrt{2}$). The ordered fct structure of FePt, however, has a similar c/a^*-ratio of 1.363. It is important to note that most materials with $L1_0$ structure have a fct phase [91] like the ordered FePt system. To compare the c/a-ratio with a bct structure the relation $a^* = \frac{\sqrt{2a_{fct}^2}}{2}$ was used. The corresponding lattice constants a and a^* are shown in Fig. 5.7.

The results from the X-ray diffraction measurements of the 200 nm thick films are similar

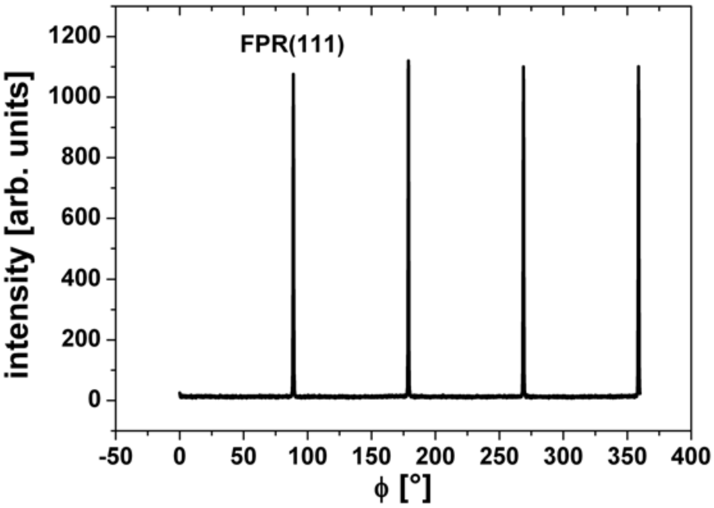

Figure 5.5.: Phi-scan of the (111) reflection from the $Fe_{50}Pt_{45}Rh_5$ film. The sample is rotated of about 29° in ψ.

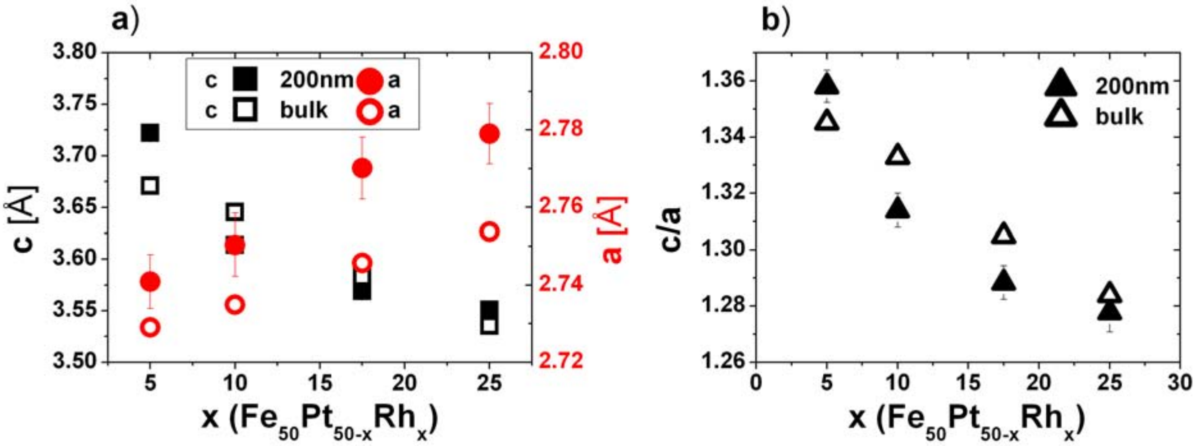

Figure 5.6.: **a)** Lattice parameter a and c as function of the Rh content x: The lattice constants c were obtained as an average of the first and second order peak positions while the lattice parameters a were determined from the average of the (011) and (111) peak positions in the X-ray diffraction scans. **b)** c/a-ratio as a function of the Rh composition. The solid symbols are the values for the 200 nm film and the open symbols represent the values of the bulk system [17].

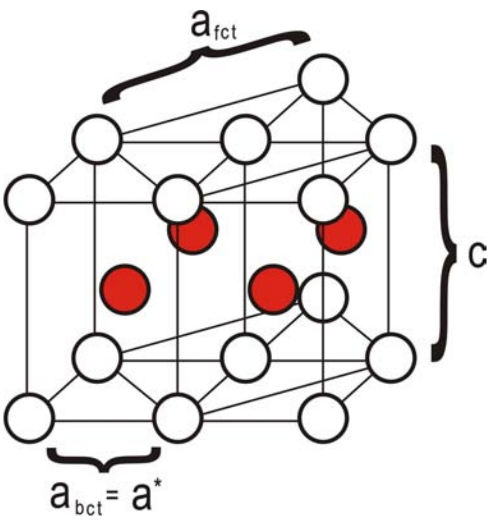

Figure 5.7.: Sketch of the $L1_0$ structure with the lattice constants a_{bct} for the bct lattice and a_{fct} for the fct lattice. Details to the lattice constant a^* can be found in the text.

to the one for the bulk $Fe_{50}Pt_{50-x}Rh_x$ system [17]. Both systems have a bct structure and also the lattice constants show a similar behavior. The only difference is that the values of the lattice constants a in the thin films are larger.

5.1.2. Film Thickness

The X-ray diffraction scans of the $Fe_{50}Pt_{40}Rh_{10}$ films with different thicknesses are plotted in Fig. 5.8 showing the first (001) and the second (002) order reflections. Here the (002) reflections from the MgO substrates are absent which can be explained by the sharpness of these peaks and the slightly more detuned alignment in respect to the MgO substrate as it was measured for the films in the previous section.

The appearance of the first order reflections of the films indicate the well chemically ordered $L1_0$ structure of the films as already discussed in the previous section.

Table 5.2 summarizes the values of the order parameter, the coherence length and the FWHM of the rocking scans. The order parameter S increases with decreasing sample thickness. While the 500 nm thick film has an order parameter of about S=0.79, it increases to S=0.91 for the thinnest film of 100 nm. It shows that the chemical order of these films is of the same quality as it was observed for the 200 nm thick films before. The crystalline quality is also reflected by the small FWHM of the rocking scans of the (001) reflections (FWHM$\leq$ 1.3) as well as in the relative large coherence length of L>190 Å which are again similar to the previous results on the concentration dependent films.

As described above additional scans have been carried out along the in-plane direction around the (011) and (111) reflections of the $Fe_{50}Pt_{40}Rh_{10}$ films as well as around the (202) peak position of the MgO substrate. Similar to Fig. 5.4 and Fig. 5.5 for the 200 nm films all in-plane reflections of the films are shifted by 45° in respect to the reflections of the substrate. As pointed out before it is an evidence for the bct structure of the $Fe_{50}Pt_{40}Rh_{10}$ films.

The X-ray diffraction measurements of the $Fe_{50}Pt_{40}Rh_{10}$ films of the second series showed that no structural changes occur if the sample thickness is varied in a range from 100 nm to 500 nm. Moreover, there is no indication of any significant changes of the lattice con-

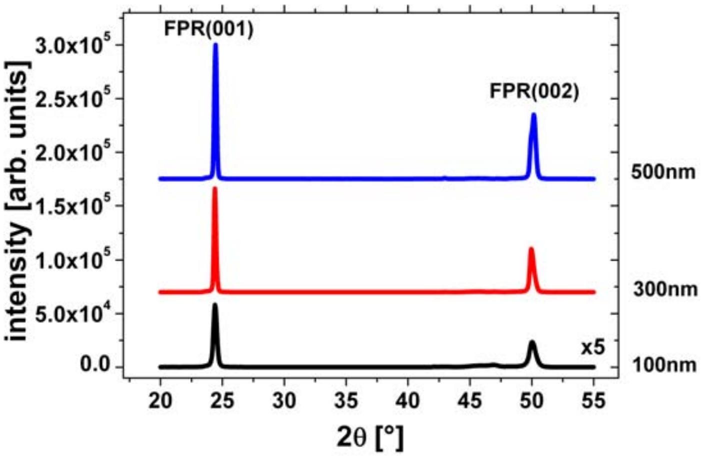

Figure 5.8.: Comparison of the out-of-plane X-ray diffraction scans of the $Fe_{50}Pt_{40}Rh_{10}$ (FPR) films for different sample thicknesses. The intensity of the 100nm film was multiplied by a factor of 5.

	100 nm	300 nm	500 nm
FWHM[°]	1.33	0.69	0.66
S	0.91	0.85	0.79
L[Å]	190	307	277

Table 5.2.: Parameters of the X-ray diffraction scans for the $Fe_{50}Pt_{40}Rh_{10}$ samples with different thickness. The Full Width at Half Maximum (FWHM) of the rocking scan of the (001) reflections, the order parameter S and the coherence length L. The coherence length was obtained from the FWHM of the radial diffraction scans as an average of the first and second order reflections of the films.

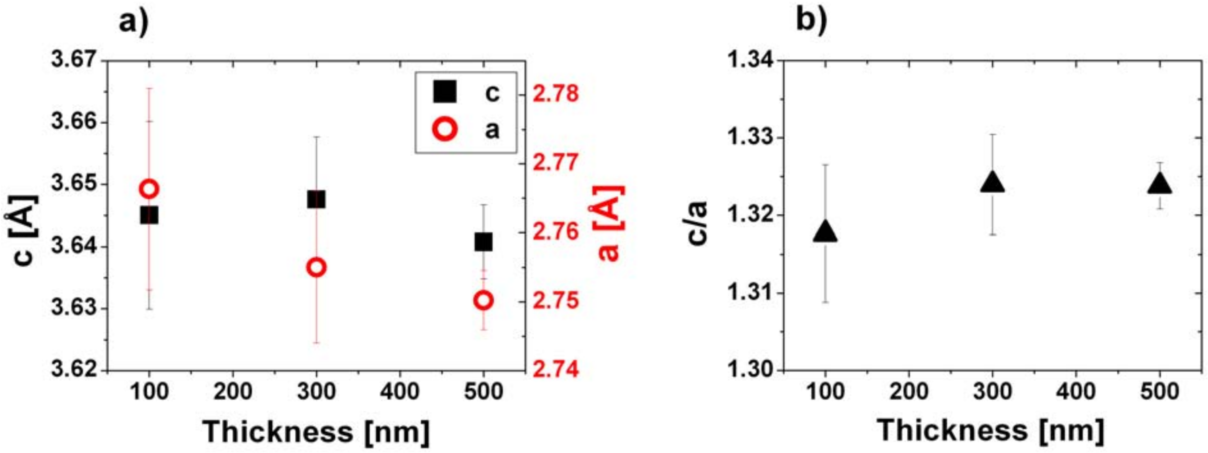

Figure 5.9.: **a)** Lattice parameter a and c as function of the sample thickness. The lattice parameters c were obtained as an average of the first and second order peak positions while the lattice parameters a were determined from the average of the (011) and (111) peak positions in the X-ray diffraction scans. **b)** c/a-ratio as a function of the sample thickness.

stants. The decreases of both lattice parameters a and c are in the range of the error bars and can therefore be considered as quasi constant. As a consequence also the c/a-ratio (see Fig. 5.9 b) remains constant. These results show that the bct structure is still conserved if the sample thickness is varied in a range of at least up to 500 nm.

The X-ray diffraction measurements of both sample series with composition and thickness dependence confirm that the $Fe_{50}Pt_{50-x}Rh_x$ samples have a $L1_0$ (bct) structure with [001]-orientation similar to the bulk alloys studied by Yuasa [17]. Furthermore the measurements show that the films are oriented in such a way that the (001), (111) and (110) reflections lie in a scattering plane. Figure 5.3 summarizes the orientation and the relations between the different scattering planes.

5.2. Structure Factor Calculation

The presence or absence of certain reflections in the X-ray diffraction measurements allow to draw conclusions about the atomic structure of the $Fe_{50}Pt_{50-x}Rh_x$ films by comparison of the observed reflection intensities with structure factor calculations. In the previous chapter 3 it was shown that the structure factor is proportional to the measured scattering intensity: $I \propto |F|^2$ (see equation 3.21). By using this relation information about intensity ratios of different reflections can be obtained which can be used for example to determine the degree of the chemical order (see equation 5.1). Besides the determination of the nuclear structure the structure factor calculations allow to distinguish between magnetic and nuclear contributions to different reflections. Moreover, by comparing the structure factor calculations, i.e. the calculated peak intensities, with the measured peak intensities of neutron diffraction experiments the order and orientation of the magnetic moments can be determined in detail. In the following the calculation of the nuclear and magnetic structure factor used here will be outlined in more detail.

The structure factor of the bct structure can be calculated by the use of the equations

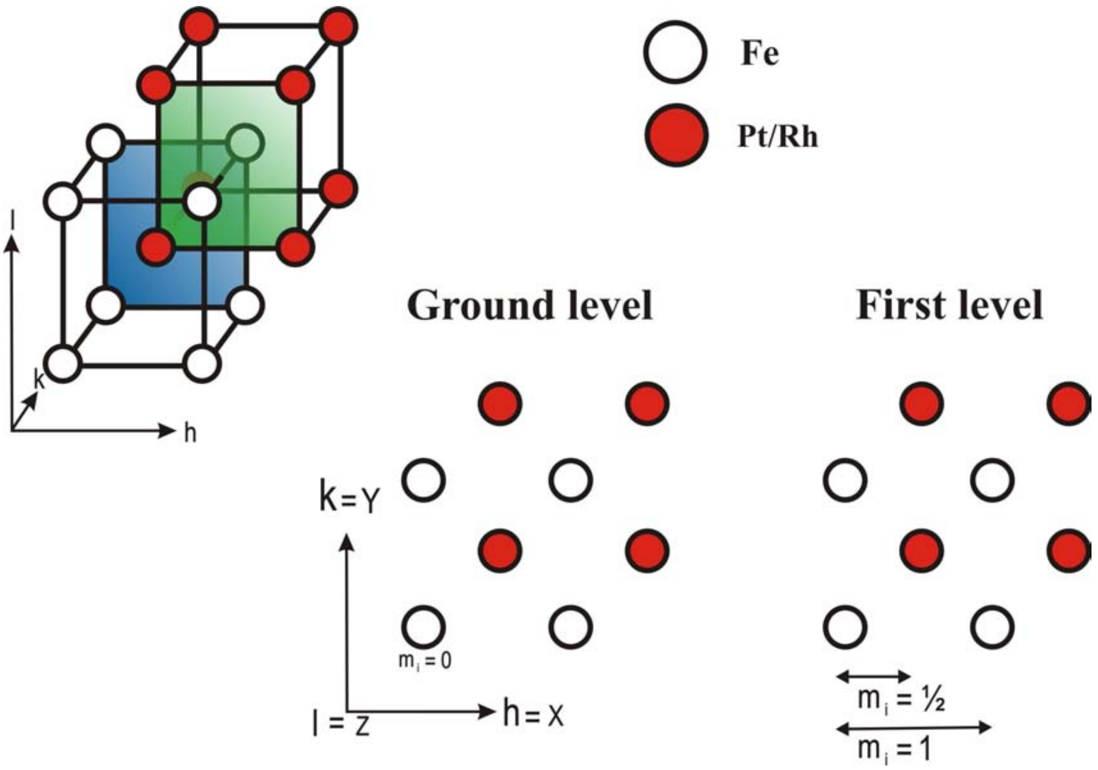

Figure 5.10.: Magnetic unit cell of the bct structure. The right side shows the top view on the bct structure. The Fe and Pt/Rh atoms in the ground and first level have different positions in z-direction as can be seen in the sketch on the left side. For more details see the text.

3.22-3.30. The calculation based on the configuration of the magnetic unit cell which is shown in fig. 5.10. Compared to the nuclear unit cell of the $\mathrm{Fe_{50}Pt_{50-\mathit{x}}Rh_{\mathit{x}}}$ alloy consisting of 1 Fe and 1 Pt atom the magnetic unit cell has to be extended to 8 Fe and 8 Pt/Rh atoms to describe the different possible magnetic orders, in particular AF order. The right hand side of the figure shows a top view of the magnetic unit cell. The positions of the atoms is expressed by m_i with $i = x, y, z$ indicating the corresponding direction. The distance between two Fe atoms or two Pt/Rh atoms is $m_i = 1$ while the distance between a Fe and a Pt/Rh atom is defined as $m_i = 1/2$. It is important to note that the definition of the distance is valid for all h, k, l-directions. Furthermore the distance between the ground level and the first level is also $m_i = 1$. The origin of this coordinate system is set to the Fe atom on the ground level which is marked with $m_i = 0$, i.e. $m_x = m_y = m_z = 0$. The structure factor for the magnetic unit cell can be now written as:

$$\begin{aligned} F(\vec{Q}) &= F_n(\vec{Q}) + F_{mag}(\vec{Q}), && (5.8)\\ \text{with } F_n(\vec{Q}) &= \sum_i b_i e^{2\pi i(hm_x+km_y+lm_z)} && (5.9)\\ F_{mag}(\vec{Q}) &= \sum_i (\pm) p_i e^{2\pi i(hm_x+km_y+lm_z)}. && (5.10) \end{aligned}$$

For the discussion the structure factor will be separated in the magnetic and the nuclear part. The nuclear structure factor can be further separated in a structure factor part for the Fe atoms and the Pt/Rh atoms, respectively:

$$F_n(\vec{Q}) = F_{Fe}(\vec{Q}) + F_{Pt/Rh}(\vec{Q}) = \sum_{xyz} b_{Fe} e^{2\pi i(hm_x+km_y+lm_z)} + \sum_{xyz} b_{Pt/Rh} e^{2\pi i(hm_x+km_y+lm_z)}, \tag{5.11}$$

where b_{Fe} and $b_{Pt/Rh}$ are the scattering lengths of the Fe and the Pt/Rh atoms, respectively. From the X-ray data it is known that the $\mathrm{Fe_{50}Pt_{50-\mathit{x}}Rh_{\mathit{x}}}$ films are well ordered, i.e. the Fe and Pt/Rh atoms only occupy certain sites in the crystal. Since the distribution of the Pt/Rh atoms is assumed to be random, an average scattering length will be considered (see section 5.1):

$$b_{Pt/Rh} = \frac{(50-x)b_{Pt} + x b_{Rh}}{50}, \tag{5.12}$$

with x denoting the amount of Rh and b_{Pt} and b_{Rh} are the scattering length of Rh and Pt, respectively. By considering all atoms in the unit cell three cases can be distinguished for the nuclear structure factor:

$$F^{nuc}_{hkl} = \begin{cases} 8(b_{Fe} + b_{Pt-Rh}) & \text{for } h+k+l = even \\ 8(b_{Fe} - b_{Pt-Rh}) & \text{for } h+k+l = odd \\ 0 & \text{for } h+k+l = \frac{n}{2} \end{cases}, \tag{5.13}$$

where n denotes odd numbers.

In the case of neutron scattering the values for the scattering length of Fe is 9.45 fm, for Pt 9.6 fm and for Rh 5.88 fm, resulting in the structure factors given in table 5.3. As already mentioned the measured scattering intensity is proportional to the square of the structure factor $I \propto |F|^2$. Considering the given unit cell the following conclusions can be derived from the structure factor calculations for a neutron diffraction experiment: The second order reflections (002) and (200) have a strong nuclear contribution while it will

	x=5	x=10	x=17.5	x=25
h+k+l=even	18.678	18.306	17.748	17.19
h+k+l=odd	0.222	0.594	1.125	1.71

Table 5.3.: Nuclear structure factors F_{hkl} for different $Fe_{50}Pt_{50-x}Rh_x$ compositions in fm units.

be reduced for the first order reflections (001), (100) and (111) due to the different sign for the Fe and Pt/Rh atoms in the structure factor terms, respectively. Furthermore it can be expected that with higher Rh concentration the scattering intensity or the nuclear contribution to the scattering intensity, respectively, of the second order peaks decreases while it increases for the first order reflections.

In the next step the magnetic structure factor will be calculated. The structure factor can be again separated in the contributions of the Fe and the Pt/Rh atoms, respectively:

$$\begin{aligned} F_{mag}(\vec{Q}) &= F_{Fe}^{mag}(\vec{Q}) + F_{Pt/Rh}^{mag}(\vec{Q}) \\ &= \sum_{xyz}(\pm)p_{Fe}e^{2\pi i(hm_x+km_y+lm_z)} + \sum_{xyz}(\pm)p_{Pt/Rh}e^{2\pi i(hm_x+km_y+lm_z)}, \end{aligned} \quad (5.14)$$

where p_{Fe} and $p_{Pt/Rh}$ denote the magnetic scattering length of Fe and Pt/Rh, respectively. The sign ($\pm$) taking into account neighboring magnetic moments being antiferromagnetically or ferromagnetically ordered.

For the magnetic structure factor two principle cases will be considered, an AF and a FM ordered $Fe_{50}Pt_{50-x}Rh_x$ film. In the AF case three solutions for the magnetic scattering length are possible:

$$F_{hkl}^{mag} = \begin{cases} 0 & \text{for } h+k+l = even \\ 0 & \text{for } h+k+l = odd \\ 8(p_{Fe}+p_{Pt-Rh}) & \text{for } h+k+l = \frac{n}{2} \end{cases} \quad (5.15)$$

In case of a FM order the relative spin direction of the neutrons to the magnetic moments of the sample has to be considered: In the case of the parallel orientation of the neutron spin to the magnetic moments of the sample the structure factors are given by:

$$F_{hkl_p}^{mag} = \begin{cases} 8(p_{Fe}+p_{Pt-Rh}) & \text{for } h+k+l = even \\ 8(p_{Fe}-p_{Pt-Rh}) & \text{for } h+k+l = odd \\ 0 & \text{for } h+k+l = \frac{n}{2} \end{cases} \quad (5.16)$$

In the case of an antiparallel orientation of the neutron to the magnetic moments of the system the structure factors are given by:

$$F_{hkl_a}^{mag} = \begin{cases} -8(p_{Fe}+p_{Pt-Rh}) & \text{for } h+k+l = even \\ -8(p_{Fe}-p_{Pt-Rh}) & \text{for } h+k+l = odd \\ 0 & \text{for } h+k+l = \frac{n}{2} \end{cases} \quad (5.17)$$

The measured peak intensity for the unpolarized neutrons is then given by the sum of both contributions: $\frac{1}{2}F_{hkl_p}^2 + \frac{1}{2}F_{hkl_a}^2$. It is important to note that in the FM as well as in the AF case an order of the magnetic moments perpendicular to the scattering vector $\vec{Q}$ is assumed. If the magnetic moments are not completely aligned perpendicular to $\vec{Q}$, the intensity from the magnetic scattering decreases and the angle of the magnetic moments with respect to $\vec{Q}$ has to be considered (see section 5.5). Furthermore, the presence or absence of the different reflections depends on the exact alignment of the magnetic moments, e.g. in the bct structure AF configurations are possible with the magnetic moments oriented perpendicular to the scattering vector $\vec{Q}$ of the $(\frac{1}{2}00)$ reflection which do not contribute to its intensity due to destructive interference.

Since the intensity in the neutron diffraction measurements is proportional to the square of the structure factor and by considering both contributions, the nuclear and magnetic structure factor, the following conclusion can be drawn: The first and second order reflections contain besides the nuclear contribution also a magnetic contribution from a FM order if present. Moreover, the equations 5.13, 5.16 and 5.17 show clearly, that in the case of FM order the ratio between the magnetic and the nuclear contribution is much larger for the first order than for the second order peak intensity and easier to be observed. Therefore the first order Bragg reflections will be the prime candidates to study the FM order in the samples. Half order reflections, on the other hand, are only present if an AF order exists.

5.3. MOKE

The MOKE measurements in this section were carried out at the University of Hamburg (see chapter 4). These measurements provide information about macroscopic magnetic properties, e.g. the magnetic anisotropy of the films. From the shape of the hysteresis loops also first indications of the microscopic magnetic spin structure can be obtained since the microscopic spin structure influences the magnetization reversal process.
However, it should be noted that the penetration depths of the laser light (λ=632.8 nm) is only about 20 nm [92, 93]. Therefore the observed behaviors are limited to the surface region of the 200 nm thick films where surface effects can play an important role which can differ significantly from the behavior of the rest of the film.
The measurements of the polar and longitudinal Kerr effect for the films with different Rh concentrations are plotted in Fig. 5.11. For the $Fe_{50}Pt_{50-x}Rh_x$ films with x=17.5 and x=25 the Kerr rotation and ellipticity are around zero for the entire range of the applied magnetic field. Such a behavior can be explained in three ways. One possible explanation is that both films have no magnetic moments that can be oriented in the applied magnetic field. Another possibility for the absence of the signal is that both films are in the paramagnetic state and the applied field is not high enough to orient the moments in the field direction. The third interpretation is that the films are AF ordered and therefore have no resulting magnetic moment and the magnetic field of 1 T is not high enough to align the AF coupled spins and induce a non-zero magnetic net moment along the field direction. It should be noted that the distinction of the three cases is not possible with the MOKE measurements if only measured at room temperature.
The $Fe_{50}Pt_{45}Rh_5$ film shows a linear hysteresis for the longitudinal geometry which is typical for hard axis hysteresis curves. A similar behavior can be observed for the polar geometry for small fields, but it shows an open hysteresis if the magnetic field is in the range of the saturation magnetization ($\mu_0 H = 600\,\mathrm{mT}$) which indicates an alignment of the magnetic moments along an easy axis. Therefore the film with x=5 has an out-of-plane anisotropy. Taking the linear part into account the shape of the hysteresis loop can be explained in the following way: In the linear region ($\mu_0 H = 0 - 300\,\mathrm{mT}$) the magnetic moments align parallel to the applied magnetic field but are uniformly distributed in different domains of spin up or down. Such a spin configuration gives a zero magnetization

perpendicular to the sample plane (parallel to the applied magnetic field). Similar behaviors were observed in Co/Pt [94], [80] or Co/Pd multilayers [95]. There it was shown with magnetic force microscopy (MFM) that the linear region of the MOKE hysteresis loops corresponds to up and down domains with labyrinth structures which are called maze pattern or labyrinth domain pattern. With increasing magnetic field the part of the uniformly distributed maze patterns decreases while the domains with orientation in field direction increase. Close to the saturation magnetization almost all spins are aligned along the applied magnetic field and only isolated domains remain with opposite magnetization direction, the so-called bubble domains. Furthermore MFM measurements of Co/Pt showed that if a saturating magnetic field is applied in-plane the magnetic moments form for low magnetic fields stripe domains with the magnetic moments oriented parallel or antiparallel to the applied magnetic field [94]. It is important to note that the observed effects could be only limited to the surface region and not be representative for the entire 200 nm $Fe_{50}Pt_{45}Rh_5$ film.

The measurements of the longitudinal and polar Kerr effect for the $Fe_{50}Pt_{40}Rh_{10}$ film show no saturation effects of the hysteresis curves but the high magnetic signal in the measurements with polar geometry is a strong indication of a FM order in the film. Since no saturation effects can be observed for both Kerr geometries no clear information about the anisotropy can be achieved. Considering the strong magnetic signal for the polar geometry, similar to the $Fe_{50}Pt_{45}Rh_5$ film, an out-of-plane anisotropy can be expected.

It should be noted that the hysteresis curves of the polar rotation of the film with x=5 and x=10 should be symmetric around zero. The observed shift can be explained as follows: A Glan-Thompson prism is used to minimize the signal in the alignment of the experiment, in the actual measurements the prism is tilted from the minimum to achieve a low signal from the sample. The signal is in general expected to be linear and the linearity is considered in the data treatment. In the measurements presented here a non linearity occurs due to the high magnetic signal which was not considered in the data treatment and leads to the observed shift of the hysteresis curves but has no influence on the fundamental magnetic properties, e.g. the anisotropy.

In summary the MOKE measurements on the four 200 nm thick films reveal no FM order for the $Fe_{50}Pt_{32.5}Rh_{17.5}$ and the $Fe_{50}Pt_{25}Rh_{25}$ films while the $Fe_{50}Pt_{40}Rh_{10}$ and the $Fe_{50}Pt_{45}Rh_5$ film show FM behavior. Furthermore the MOKE measurements on the film with x=5 indicate an out-of-plane anisotropy while the film with x=10 can not be saturated in fields of 1 T and no clear conclusion about the anisotropy can be drawn. Since the magnetic signal is similar to the one for the film with x=5 an out-of-plane anisotropy can be expected. The MOKE measurements in this work have exclusively been performed at room temperature and thus the observed magnetic properties can be only stated for this temperature.

5.4. Neutron Diffraction

The MOKE measurements have given first indications about the magnetic properties and the magnetic configurations of the different $Fe_{50}Pt_{50-x}Rh_x$ films but as already pointed out, the technique only probes the surface region which may differ from the bulk regime. To investigate the magnetic structure in more detail a method is needed which is able to probe the magnetic configuration on a microscopic or even atomic level and to be able to access the whole sample volume. For this task polarized and unpolarized neutron diffrac-

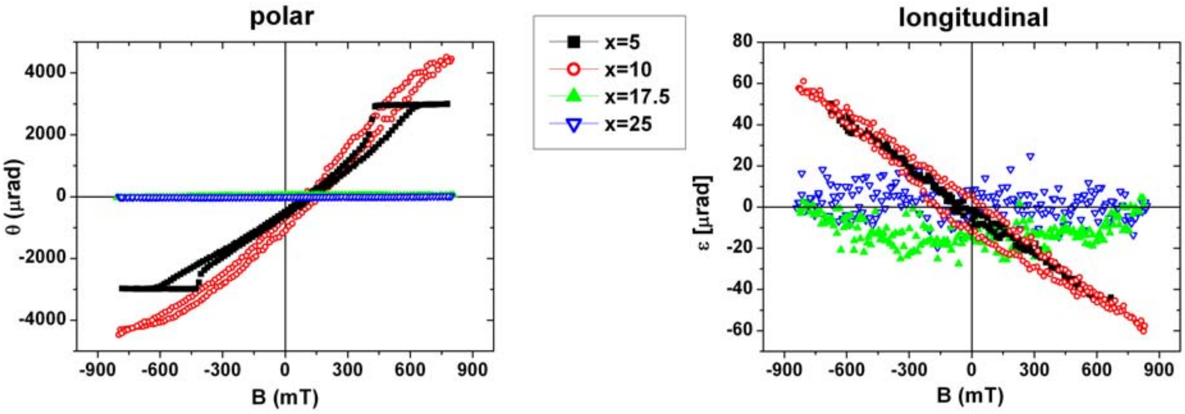

Figure 5.11.: Hysteresis curves of the $Fe_{50}Pt_{50-x}Rh_x$ films with x=5 (black squares), x=10 (red circles), x=17.5 (green solid triangles) and x=25 (blue open triangles) for the polar Kerr rotation and longitudinal Kerr ellipticity.

tion is an ideally suited technique. As already mentioned in the introduction, cold and thermal neutrons possess a wavelength in the range of atomic distances (in the Å-regime) and interact with the core of an atom as well as with the unpaired electrons hence enabling one to study the nuclear and the magnetic structures on an atomic level. Furthermore, the neutrons possess a much higher penetration depth than photons, particularly for the laser light in the visible range used in the MOKE measurements. The high penetration depth allows measurements of the entire sample material, i.e. of the film of interest and is not restricted to the surface.

In the following the data of the polarized and unpolarized neutron diffraction measurements will be presented. As discussed in section 3.2.3 the unpolarized neutron diffraction measurements are sensitive to the magnetic moments which are perpendicular to the scattering vector $\vec{Q}$. It is important to note, however, that no distinction between magnetic moments in the plane is possible by using unpolarized neutrons. In particular, it can not be distinguished between the orientation of magnetic moments along the in-plane axes a or b, respectively. By comparison of the integrated intensities of different Bragg reflections by means of structure factor calculations information about the magnetic order, e.g. AF or FM order, and their orientation can be gained, in particular if the magnetic order is along the in-plane or out-of-plane direction. The determination of the different components of the magnetic moments along the different symmetry axes, however, requires the analysis of polarization states of the neutrons during the scattering process provided by polarized neutron diffraction with polarization analysis (see section 3.2.3).

In the following sections the neutron diffraction data is presented in detail. All the unpolarized neutron diffraction measurements were carried out at POLDI, D23 and IN12 (see chapter 4). Latter instrument was also used for the polarized measurements with polarization analysis. Some additional measurements for the $Fe_{50}Pt_{45}Rh_5$ film were performed at IN3. The guide field in these measurements was oriented in such away that it was set parallel to one of the in-plane axes which is here denoted without loss of generality as the b-axis of the $Fe_{50}Pt_{50-x}Rh_x$ films.

The neutron diffraction measurements in this chapter are divided in two parts showing the dependence of the data on the composition and on the thickness, respectively. All data presented in the following are corrected for sample illumination, the Q-dependence of the magnetic form factors and normalized by the beam monitor as described in section

4.5.

5.4.1. Composition

Before the neutron diffraction data is presented for the individual $Fe_{50}Pt_{50-x}Rh_x$ compositions some general remarks will be given first: Most of the diffraction investigations were carried out with unpolarized neutrons to identify the nuclear and magnetic order in the samples. Due to the symmetry of the bct structure of the samples the first, second and half order reflections along two orthogonal directions [001] and [100] were examined. The other in-plane direction along [010] is crystallographically identical to [100] and therefore no differences to the reflections along the [100] direction are expected. Since it is possible that the magnetic moments are not aligned along the symmetry axes additional reflections ((111) and $(\frac{1}{2}\frac{1}{2}\frac{1}{2})$) along diagonal symmetry directions have been measured additionally. In section 5.2 the structure factor calculations were discussed in detail for the bct structure of the $Fe_{50}Pt_{50-x}Rh_x$ samples. From this discussion the following conclusions can be drawn:

1. Any observed half order reflections are exclusively due to an AF order.
2. First and second order reflections possess always a nuclear contribution with a possible FM part.

For the AF order of the half order reflections the doubling of the unit cell should be kept in mind. For the first and second order reflections it is important to note that the nuclear part for the first order reflections is significant less compared to the second order reflections. Therefore the magnetic contribution due to the FM order will be more visible for the first order reflections as already pointed out before. Therefore the discussion of FM contributions to the scattering intensity will be focused on the first order while changes in the structural properties, e.g. lattice constants, are more prominent at the second order Bragg reflections due to the larger shift in Q.

Further diffraction measurements were carried out with polarized neutrons for selected reflections to identify the orientation of the magnetic moments in the plane perpendicular to the scattering vector $\vec{Q}$.

$Fe_{50}Pt_{45}Rh_5$

Figure 5.12 presents the neutron diffraction results for the $Fe_{50}Pt_{50-x}Rh_x$ film with the lowest Rh doping for the here investigated films of x=5. Here, only intensity of the first and second order Bragg reflections along the [100]- and [001]-direction as well as of the (111) Bragg reflection can be observed. The (222) reflection was not accessible in the experimental set-up. Intensity of the half order peaks in any of the proposed directions was not detected indicating that for the low concentration of 5% Rh no AF order is present for the whole temperature range.

The out-of-plane reflection (002) shows constant values of the integrated intensities over the whole temperature range within the error bars. Such a behavior indicates an absence of a magnetic contribution to the peak intensity. A similar behavior is present for the (001) reflection. Here, the neutron diffraction measurements indicate only a very slight decrease of the integrated intensity with increasing temperature. This slight decrease of intensity is not of magnetic origin but can be explained by thermal fluctuations and associated with it a decrease of the signal to noise ratio (for more details see the appendix A). The two in-plane Bragg reflections, (100) and (200), on the other hand show a significant temperature dependence. Their integrated intensities decrease with increasing temperature, whereas the effect is much stronger observable at the first order peak as discussed before. As pointed out in the section 3.2.3 the changes in the intensity can be attributed to a FM contribution. A nearly identical behavior can be observed for the (111) Bragg reflection. The decrease of the integrated peak intensities can be fitted by a power law which is shown in the following. The temperature dependence of a spontaneous magnetization [96, 97] can be described by the equation:

$$M(T) = M_0 D(1 - \frac{T}{T_c})^{\beta}, \tag{5.18}$$

where D is a factor near unity which represents the misfit between the above expression and the behavior of real substances at T=0 K. It is sensitive to such factors as the details of the spin-wave spectrum, e.g. the spin-wave gap at k=0 and the spin-wave dispersion [98]. T_c and β denote the critical temperature and the critical exponent, respectively. Since the integrated intensity I of a magnetic peak is proportional to the magnetization M and the magnetic moment, respectively: $I \propto p^2 \propto m^2$ and $M \propto m$, where m denotes the magnetic moment and p is the magnetic scattering length, (see section 5.5 and 3) the above equation can be written as:

$$\sqrt{\frac{I(T)}{I_0}} \propto \frac{M(T)}{M_0} = D\left(1 - \frac{T}{T^*}\right)^{\beta^*}, \tag{5.19}$$

with $I(T)$ denoting the integrated intensity, β^* the transition exponent, T^* the transition temperature and T the temperature parameter. It is important to note that the power law 5.18 is used to calculate phase transitions in ferromagnets [97] and antiferromagnets [98]. Therefore T_c is equivalent to the Curie or the Néel temperature of a system and β indicates whether the transition is of first ($\beta \to 0$) or second order ($\beta > 0$). In the work presented here the power law 5.19 is used to fit the intensity decreases of the magnetic reflections.

Fitting the decay of the integrated intensities of the (100) and (111) reflections by the power law leads to a transition temperature of about $T^*_{100} = 521\,\mathrm{K} \pm 2\,\mathrm{K}$ and $T^*_{111} = 510\,\mathrm{K} \pm 4\,\mathrm{K}$, respectively.

Considering the results from the unpolarized neutron diffraction measurements which indicate magnetic contributions to the in-plane but not to the out-of-plane first and second order reflections, respectively, one can conclude that the $Fe_{50}Pt_{45}Rh_5$ film shows pure FM behavior with the main distribution of the magnetic moments in the out-of-plane direction. A transition to the PM state can be observed slightly above T=500 K. The decrease of the integrated intensities of the (100) and (111) reflections indicate a continuous FM-PM transition which is also indicated by the values of the transition exponents of about β^*=0.31.

From the bulk $Fe_{50}Pt_{50-x}Rh_x$ systems it is known that the magnetic and structural transitions are accompanied by discontinuous or abrupt changes of the lattice parameters as well as the c/a-ratio [17]. Such effects are also often observed in materials with first order transitions to the FM or from the FM state due to magnetostriction. In the $Fe_{50}Pt_{50-x}Rh_x$ film with x=5 no transition of such a kind can be found up to temperatures of T=500 K. However, the knowledge of the temperature behavior of the lattice constants in thin films

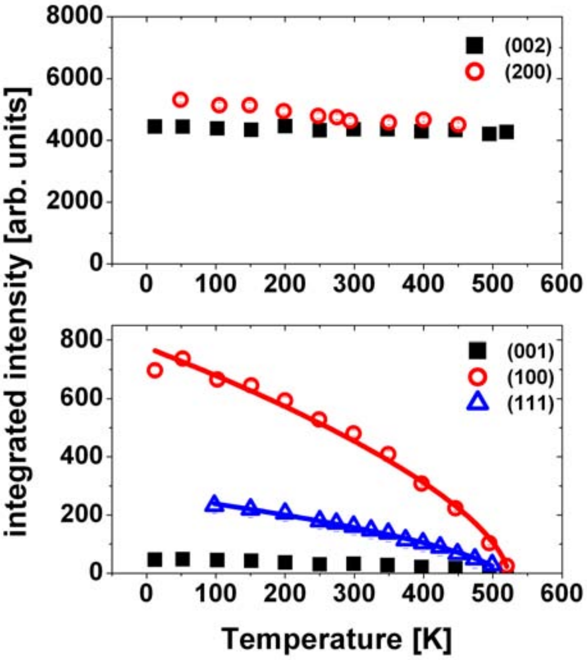

Figure 5.12.: Temperature dependence of the integrated neutron diffraction intensity of the $Fe_{50}Pt_{45}Rh_5$ film at two in-plane (200), (100) (open symbols) and two out-of-plane (002), (001) reflections (solid symbols) as well as the (111) reflection. The red and blue line for the (100) and (111) peaks are fits with the power law 5.19. The $(00\frac{1}{2})$, $(\frac{1}{2}00)$ and $(\frac{1}{2}\frac{1}{2}\frac{1}{2})$ reflections can not be observed.

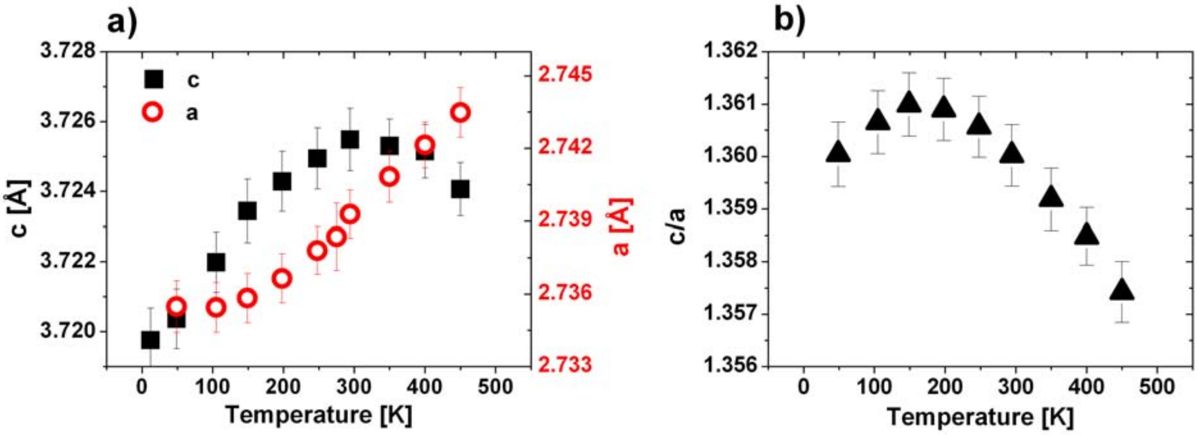

Figure 5.13.: **a)** The variation of the lattice parameter a and c of the $Fe_{50}Pt_{45}Rh_5$ film with temperature. **b)** The temperature dependence of the c/a-ratio.

without magnetic transitions helps to assign changes of the lattice constants, e.g. abrupt changes, to magnetic transitions.

The lattice parameter a and c can be calculated from the peak positions of the second order reflections (002) and (200), respectively, using the equations $d_{hkl} = \frac{2\pi}{Q}$ and 5.7. The corresponding results are plotted in Fig. 5.13. The lattice parameter c increases with increasing temperature up to a maximum at about T=300 K before it decreases slightly again. The lattice parameter a, on the other hand, shows a continuous increase with temperature. No abrupt changes can be observed for both lattice parameter a and c, as well as for the c/a-ratio confirming the absence of magnetic transitions in the observed temperature range.

In order to extract more detailed information about the magnetization in the sample, e.g. about the orientation of the magnetic moments, measurements with polarized neutrons with polarization analysis of the diffracted beam were carried out. As pointed out in detail in section 3.2.3 the polarization analysis enables one to distinguish between the different contributions of the magnetization in the sample perpendicular to the scattering vector $\vec{Q}$ and in respect to the applied guide field (e.g. NSF or SF scattering, see section 3.2.3). It should be noted that the guide field for the film with x=5 was oriented in contrast to the other films along the a-axis which corresponds to the [100]-direction in the reciprocal space.

Figure 5.14 shows two reflections (002) and (100) of the $Fe_{50}Pt_{45}Rh_5$ film analyzed by polarized neutron diffraction at IN12. It is important to note that for the in-plane reflection (100) the magnetic field was parallel to the scattering vector $\vec{Q}$. Since the unpolarized neutron diffraction measurements reveal no magnetic transitions the polarization analysis was limited to two distinct temperatures, T=100 K and T=305 K, respectively. The (002) reflection exhibit identical intensity in both NSF channels (++ and - -) but no significant intensity in the SF channel. This behavior also does not change with increasing temperature as it was already observed in the unpolarized neutron diffraction measurements indicating once more the absence of a magnetic contribution for this reflection. The polarization analysis of the first order in-plane (100) reflection reveals, on the other hand, the dominant intensity in the SF channel while only a small constant component is observed in the NSF channels. It should be noted that the data presented here is corrected for polarization efficiency as described in section 4.5. The small component of the NSF

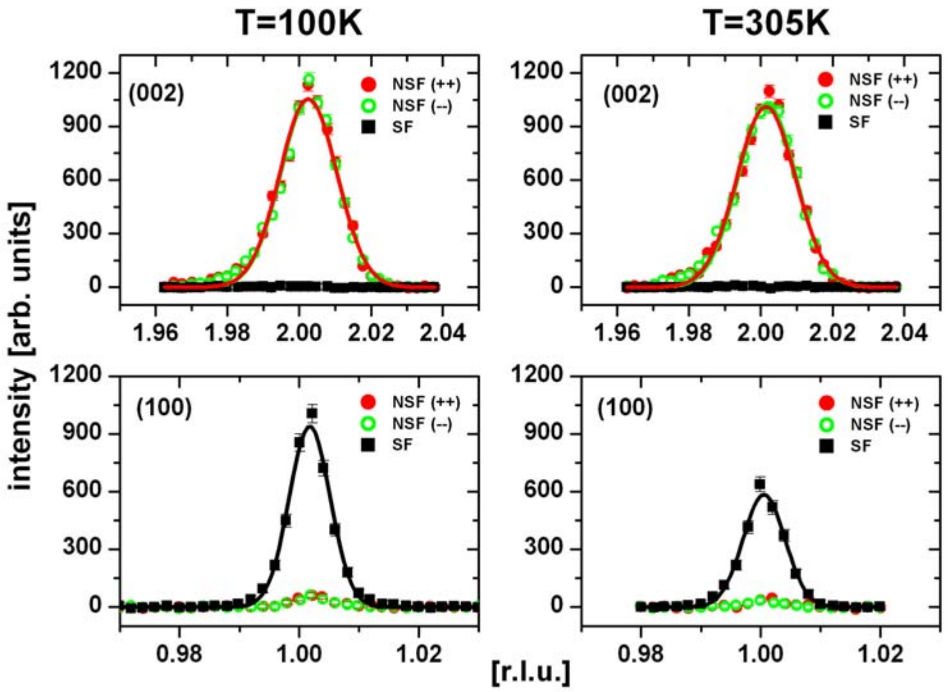

Figure 5.14.: Polarized neutron diffraction scans of the $Fe_{50}Pt_{45}Rh_5$ film for the (002) and the FM (100) reflection at T=100 K and T=305 K plotted against the individual reciprocal lattice units (r.l.u.). The guide field was oriented along the [100]-direction (a-axis) of the film.

channels is therefore real and not due to polarization inefficiency. Since the magnetic field is parallel to the scattering vector for the (100) reflection a magnetic signal can not be observed in the NSF channels and the origin of the small NSF component is purely nuclear while the observation of the SF intensity can only be caused by magnetic moments which have perpendicular components to the guide field and the scattering vector $\vec{Q}$ along the in-plane or the out-of-plane direction. Considering the absence of SF intensity of the (002) reflection and the identical intensity of the NSF channels it follows that the magnetic moments have no in-plane components and are directed in the out-of-plane direction. It should be pointed out that unlike a FM contribution with moments along the guide field which would cause a splitting of both NSF channels, no splitting can be detected in the SF channels therefore only one SF channel is shown here (for more details see section 3.2.3).

In an additional step the decrease of the second order (200) reflection was examined by polarized neutron diffraction with polarization analysis in order to verify if the decrease is of magnetic or has a structural origin (e.g. lattice vibration). The measurements were carried out at the thermal three axis instrument IN3 since the cold three axis instrument IN12 was unable to access the high Q-values of the (200) reflection. The guide field was set again along the a-axis parallel to the in-plane scattering vector. To study the magnetic effect the ratio of the NSF to the SF intensity was analyzed. For comparison, this flipping ratio was also measured for the second order reflection (002) of the film which is a pure nuclear Bragg reflection. For reflections of pure nuclear origin the ratio should be constant with temperature while in the case of a magnetic contribution to the (200) peak, with respect to the results of the (100) reflection, the ratio should increase due

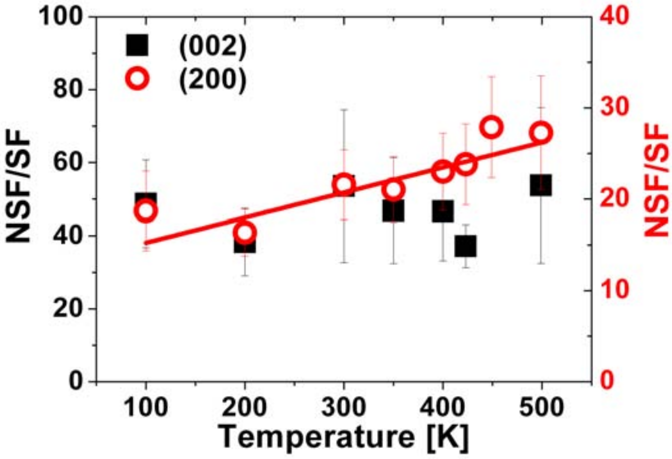

Figure 5.15.: Flipping ratio (NSF/SF) of the $Fe_{50}Pt_{45}Rh_5$ film for the nuclear Bragg peak (002) and the (200) reflection as function of the temperature. The red line is a guide to the eyes.

to the decrease of the SF intensity. The corresponding results for both reflections are shown in Fig. 5.15. The flipping ratio of the (002) reflection is constant within the error bars with a mean value of the flipping ratio of about 45±7. This value is in good agreement with the flipping ratio of the (002) reflection of the MgO substrate which was measured to determine the intrinsic flipping ratio. This confirms the pure nuclear origin of the (002) reflection. The flipping ratio of the in-plane (200) reflection, on the other hand, increases from a value of 18±4 for T=100 K to a value of 27±6 for T=500 K. The increase is a strong indication for a magnetic contribution to the (200) peak intensity and confirms the magnetic origin of the observed decrease in intensity of the unpolarized data.

In summary the unpolarized and polarized neutron diffraction measurements of the $Fe_{50}Pt_{45}Rh_5$ film reveal a FM out-of-plane alignment of the magnetic moments without any temperature driven reorientation of the magnetic moments.

$Fe_{50}Pt_{40}Rh_{10}$

In Fig. 5.16 the results of the unpolarized neutron diffraction analysis of the $Fe_{50}Pt_{40}Rh_{10}$ film are plotted. The half, first and second order reflections along the [001]- and [100]-direction as well as the (111) and $(\frac{1}{2}\frac{1}{2}\frac{1}{2})$ reflection were observed. At low temperature the half order reflections exhibit significant intensity, in particular the $(00\frac{1}{2})$ reflection which is the most dominant reflection. The integrated intensities of these peaks decrease with increasing temperature. The decay of the intensities can again be fitted by the power law (equation 5.19). For the out-of-plane half order reflection a transition temperature of about $T^*_{00\frac{1}{2}}$=330 K±4 K can be determined while the $(\frac{1}{2}00)$ and $(\frac{1}{2}\frac{1}{2}\frac{1}{2})$ reflections are already vanished at about $T^*_{\frac{1}{2}00}$=252 K±3 K and $T^*_{\frac{1}{2}\frac{1}{2}\frac{1}{2}}$=230 K±30 K, respectively. The integrated intensity of the (100) reflection, on the other hand, increases with increasing temperature with a maximum at about T=300 K where the half order reflections are almost vanished. For higher temperature T>300 K the peak intensity decreases again. Fitting the decay by the power law leads to a transition temperature of about T^*_{100}=414 K±20 K.

A similar behavior can be observed for the (111) reflection but the error bars are much larger due to the lower intensity. From the structure factor calculation it is obvious that both peak intensities (100) and (111), respectively, have contributions from a FM order. Such a FM order should also lead to a magnetic contribution in the (200) reflection but the integrated intensity of the peak shows no visual increase with temperature (see Fig. 5.16). The circumstance that the magnetic contribution to the (200) reflection can be observed in the film with x=5 but not in the film with x=10 can be explained by the different instruments used for the neutron diffraction measurements with different signal to noise ratios. The much lower ratio for the measurements of the $Fe_{50}Pt_{40}Rh_{10}$ film leads to larger error bars for the (200) intensities, e.g. it is only about 2% for the films with x=5 but 14% for the film with x=10. Considering the magnetic contribution of the (100) reflection and the Q-dependence of the magnetic form factor this value is in the same range as the expected magnetic contribution to the (200) reflection. In the raw data the contribution is even lower than the error and therefore no clear signal of a magnetic contribution can be observed in the measurements. Since the fraction of the magnetic contribution to the (200) peak intensity can not be determined the integrated intensity was not corrected for the Q-dependence of the magnetic form factor.

The first and second order reflections along the [001]-direction, on the other hand, show both constant intensities over the whole temperature range indicating to be only of nuclear origin.

Considering the results from the unpolarized neutron diffraction measurements obtained for the $Fe_{50}Pt_{40}Rh_{10}$ film a transition from a dominant AF order out-of-plane to a dominant FM order in-plane takes place in a temperature range from about T=100 K to T=330 K. A second magnetic transition from the FM to the PM phase can be observed above T=400 K. The decays of the half order reflections as well as the first order reflections (100) and (111) indicate continuous magnetic transitions which is also reflected in the transition exponents $\beta^* > 0.2$ (see table 5.4).

In contrast to the film with x=5 a temperature driven AF-FM transition can be determined in the film with x=10. In the following, the changes in the lattice constants a and c will be discussed to examine if these behaviors can be also observed for the lattice constants. The temperature dependent lattice constants determined by the position of the second order reflections (002) and (200) are presented in Fig. 5.17. Similar to the sample with x=5, the lattice constant c increases with temperature up to a maximum at about T=300 K before it slightly decreases again. The lattice parameter a exhibits again a continuous increase over the whole temperature range in respect to the error bars. A behavior similar to the lattice constant c can also be observed for the c/a-ratio it increases up to temperatures of about T=300 K and then decreases again. Both lattice constants as well as the c/a-ratio show no abrupt changes indicating that the observed magnetic transitions are not accompanied by sudden structural changes.

The unpolarized neutron diffraction measurements reveal an AF order with the magnetic moments dominantly oriented in-plane for low temperature and a dominant FM order with the moments oriented out-of-plane for high temperatures. To examine the different contributions of the magnetic moments to the symmetry axes polarized neutron diffraction with polarization analysis have been carried out at low temperature T=150 K where the film has a dominant AF order and at T=300 K where the dominant order is FM. It should be noted that for the polarized measurements with polarization analysis shown in Fig. 5.18 the scattered intensity is significant lower (less than 50%) than for the unpolarized neutron diffraction due to the restriction of the incident neutron beam to

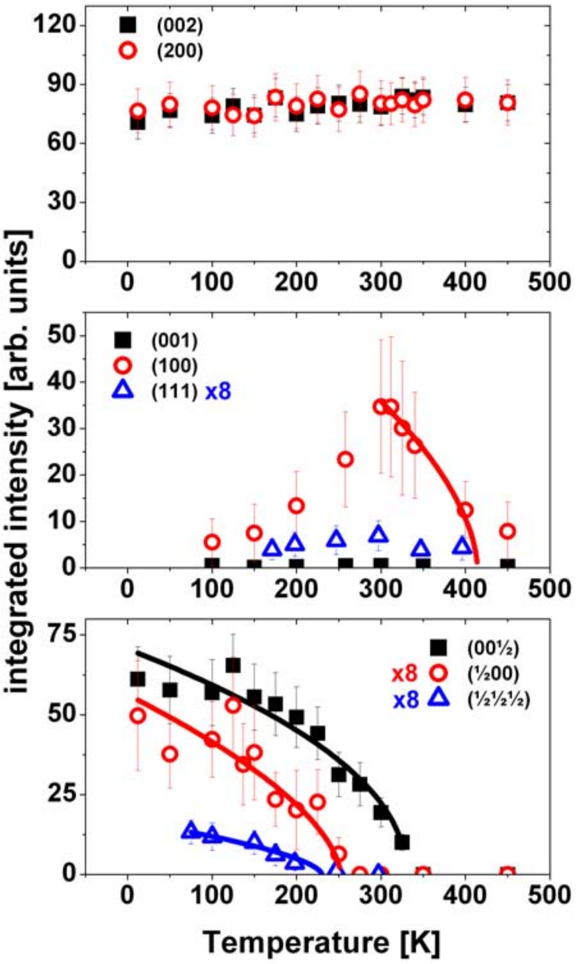

Figure 5.16.: Temperature dependence of the integrated peak intensities of the $Fe_{50}Pt_{40}Rh_{10}$ film at three in-plane (200), (100) and ($\frac{1}{2}00$) reflections (open symbols) and three out-of-plane (002), (001) and ($00\frac{1}{2}$) reflections (solid symbols) as well as the (111) and ($\frac{1}{2}\frac{1}{2}\frac{1}{2}$) peak. The intensities of the (111), ($\frac{1}{2}00$) and ($\frac{1}{2}\frac{1}{2}\frac{1}{2}$) reflection have been multiplied by a factor 8.

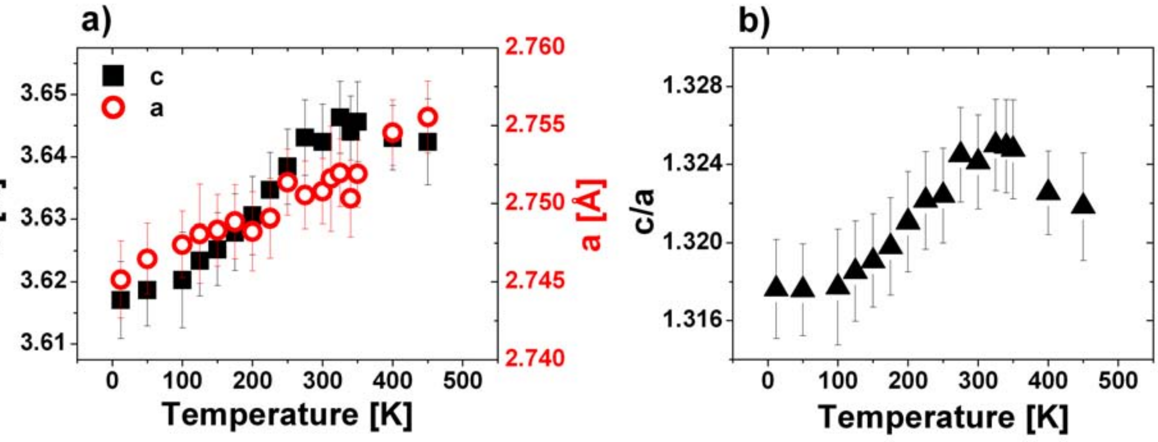

Figure 5.17.: **a)**Temperature dependence of the lattice parameter a and c. **b)** The variation of the c/a-ratio of the $Fe_{50}Pt_{40}Rh_{10}$ film with temperature.

only one spin state and loss of intensity due to flippers and mirrors used for the flipping of the neutron spin and the polarization analysis of the scattered neutrons, respectively. Therefore only the reflections with the highest intensity could be investigated while other peaks, i.e. $(\frac{1}{2}\frac{1}{2}\frac{1}{2})$ and (111) were already too weak to be analyzed. The magnetic guide field for the polarized measurements was oriented here in-plane along the b-axis.
The most dominant AF reflection is the $(00\frac{1}{2})$ peak which shows intensity in the polarization analysis in the SF as well as in the NSF channel. For low temperatures the intensity in the SF channel is slightly higher than for the SF channel while for high temperatures both intensities are almost identical. Since both scattering channels show intensity it can be concluded that magnetic components along the b-axis as well as along the a-axis contribute to the AF out-of-plane half order reflection. The in-plane $(\frac{1}{2}00)$ reflection exhibit intensity only in the NSF channel indicating that the contributions to the reflection are only due to magnetic moments oriented in-plane. The FM (100) reflection has in contrast to the AF reflections intensity only in the SF channel. Considering the results from the unpolarized neutron diffraction measurements this shows that only magnetic moments along the c-axis contribute to the peak intensity. The same behavior is found for higher temperatures. The increase of the intensity was already observed in the unpolarized neutron diffraction data.

In summary the unpolarized and polarized neutron diffraction measurements of the $\mathrm{Fe_{50}Pt_{40}Rh_{10}}$ film showed a dominant AF order in the out-of-plane direction for low temperature with an orientation of the magnetic moments in-plane. For high temperature a dominant FM order in the in-plane direction can be observed with the magnetic moments aligned along the out-of-plane axis c. In a temperature range between T=100 K and T=300 K a transition from the AF to the FM order takes place. A second magnetic transition to the PM phase can be observed above T=400 K.

$\mathbf{Fe_{50}Pt_{32.5}Rh_{17.5}}$

The MOKE measurements of the $\mathrm{Fe_{50}Pt_{32.5}Rh_{17.5}}$ film did not show an indication of a FM order in the sample. Unpolarized neutron diffraction measurements now allow one to investigate the presence of any other magnetic order. The integrated intensities and their temperature dependencies are shown in Fig. 5.19. The half, first and second order reflections can be observed along the [001]-direction while for the [100]-direction only the second and half order peaks appear. Additionally intensity at the $(\frac{1}{2}\frac{1}{2}\frac{1}{2})$ peak can be measured. Intensity around the (111) reflection was not observed.
The first and second order reflections in both [001]- and [100]-direction have constant intensities over the whole temperature range within the error bars indicating that these reflections are of pure nuclear origin. The out-of-plane half order reflection $(00\frac{1}{2})$, on the other hand, shows a significant temperature dependence, i.e. its integrated intensity decreases with increasing temperature. Applying the power law 5.19 a transition temperature of about $T^*_{00\frac{1}{2}}$=408 K±10 K can be determined with a transition exponent of about $\beta^* = 0.15 \pm 0.05$. The integrated intensities of the $(\frac{1}{2}00)$ and $(\frac{1}{2}\frac{1}{2}\frac{1}{2})$ reflections are much weaker compared to the $(00\frac{1}{2})$ reflection, but also indicate a decrease of the integrated intensity with similar parameters.
Considering the results from the unpolarized neutron diffraction and the structure factor calculations one can summarize that the $\mathrm{Fe_{50}Pt_{50-\mathit{x}}Rh_{\mathit{x}}}$ film has an AF order with the magnetic moments dominantly oriented in-plane. The fit of the out-of-plane half order

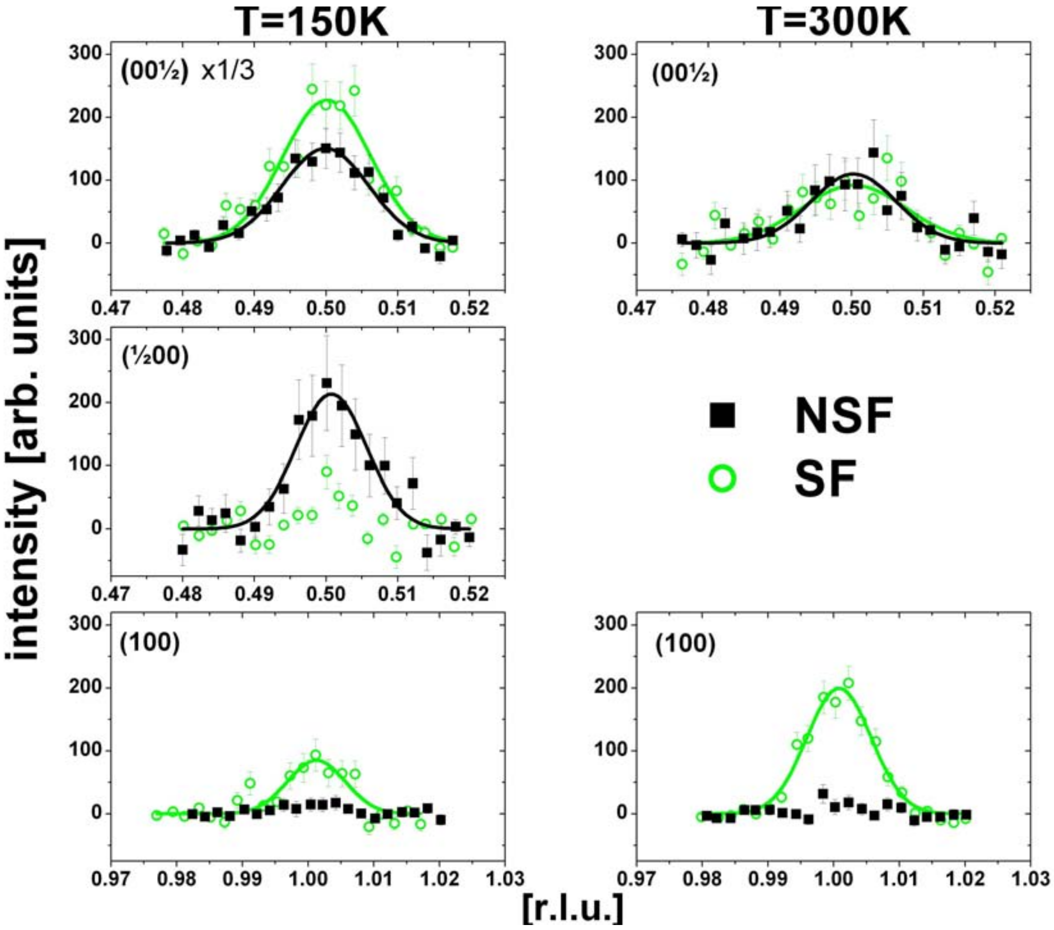

Figure 5.18.: Polarized neutron diffraction scans of the $Fe_{50}Pt_{40}Rh_{10}$ film for the AF $(00\frac{1}{2})$, $(\frac{1}{2}00)$ and the FM (100) reflection at T=150 K and T=300 K. The data of the $(\frac{1}{2}00)$ reflection have been multiplied by a factor of 1/3. The guide field for the measurements was oriented along the [010]-direction (b-axis) of the film.

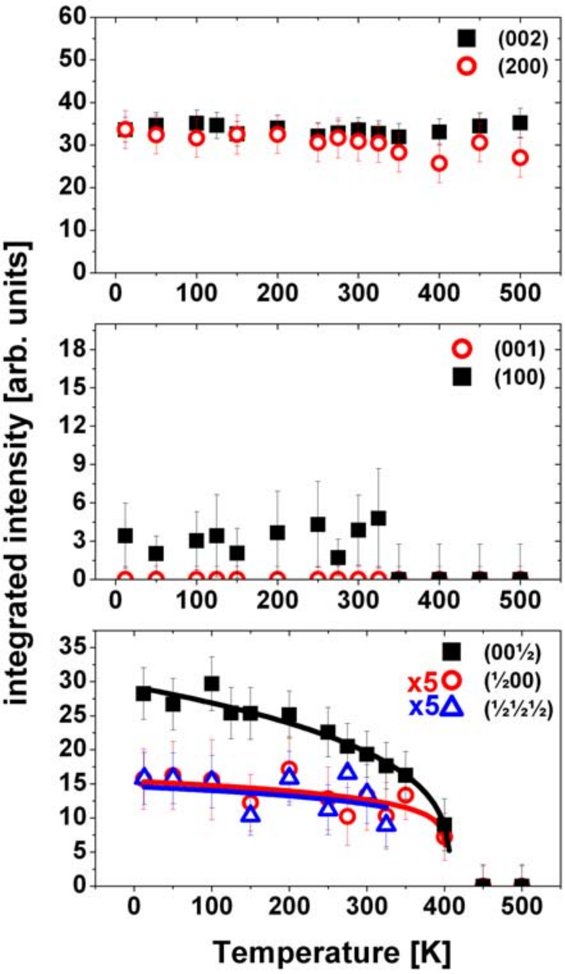

Figure 5.19.: Temperature dependence of the integrated peak intensities of the $Fe_{50}Pt_{32.5}Rh_{17.5}$ film at three in-plane (200), (100), ($\frac{1}{2}$00) reflections (open symbols) and three out-of-plane (002), (001) and (00$\frac{1}{2}$) reflections (solid symbols) as well as the ($\frac{1}{2}\frac{1}{2}\frac{1}{2}$) peak. The intensities of the half order reflections ($\frac{1}{2}$00) and ($\frac{1}{2}\frac{1}{2}\frac{1}{2}$) have been multiplied by a factor 5.

integrated peak intensity indicates a transition to the PM phase above T=400 K.

The lattice constant a and c presented in Fig. 5.20 are almost constant for low temperatures T<100 K and increase continuously for higher temperatures. A similar behavior can be found for the c/a-ratio. No abrupt changes can be observed in the lattice constants a, c and in the c/a-ratio which is an indication for the absence of crystallographical changes up to temperatures of about T=500 K.

Polarized neutron diffraction measurements with polarization analysis were carried out for the $Fe_{50}Pt_{32.5}Rh_{17.5}$ film to examine the different contributions of the magnetic moments to the symmetry axes and their temperature dependencies. Since the unpolarized neutron diffraction data indicate that the first and second order reflections have a nuclear origin and the intensity of the ($\frac{1}{2}\frac{1}{2}\frac{1}{2}$) peak is too low to be measured in the polarization analysis the measurements were restricted to the in-plane and out-of-plane half order reflections. Furthermore, no magnetic transitions can be found in the sample therefore the polarization analysis was only carried out at two distinct temperatures, T=200 K and T=330 K, respectively. For an AF order no differences in the intensity are expected be-

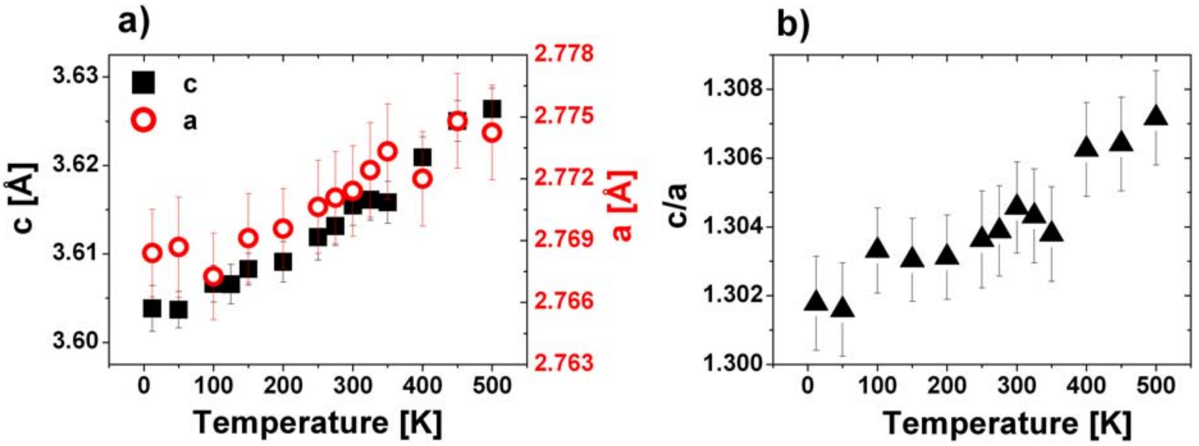

Figure 5.20.: **a)** Temperature dependence of the lattice parameter a and c of the $Fe_{50}Pt_{32.5}Rh_{17.5}$ film. **b)** The variation of the c/a-ratio with temperature.

tween both NSF and both SF channels, respectively, which was experimentally confirmed for the $Fe_{50}Pt_{32.5}Rh_{17.5}$ film. Therefore only one combined component is shown in Fig. 5.21. The guide field in the polarization measurements was oriented along the b-axis of the film.
For both temperatures the $(00\frac{1}{2})$ reflection exhibits identical intensity in the SF and NSF channel within the error bars and both channels show a decrease of the intensity with increasing temperature as it was already observed in the unpolarized neutron diffraction. The presence of both scattering channels indicates that components of the magnetic moments pointing along the in-plane direction contribute to the AF-order. The half order reflection $(\frac{1}{2}00)$ exhibits intensity only in the NSF channel excluding any out-of-plane orientation of the magnetic moments for this reflection.

In summary of the $Fe_{50}Pt_{32.5}Rh_{17.5}$ film one can conclude that the film has a dominant AF order in the out-of-plane direction with the magnetic moments predominantly oriented in-plane. The transition to the paramagnetic phase can be expected above T=400 K.

$Fe_{50}Pt_{25}Rh_{25}$

Figure 5.22 shows the results from the unpolarized neutron diffraction measurements for the $Fe_{50}Pt_{25}Rh_{25}$ film. The half, first and second order reflections along the [001]- and [100]-direction as well as the $(\frac{1}{2}\frac{1}{2}\frac{1}{2})$ reflection can be observed, while the (111) peak was not present at any temperature.
At low temperature (T<200 K) only the $(\frac{1}{2}\frac{1}{2}\frac{1}{2})$ reflection can be measured which remains the strongest reflection up to T=225 K. Then it strongly decays and vanishes at around $T^*_{\frac{1}{2}\frac{1}{2}\frac{1}{2}}$=276 K±4 K (see table 5.4). At T=200 K the $(00\frac{1}{2})$ reflection appears and becomes most dominant with a maximum at around 290 K. For higher temperatures it rapidly decays again. The fit with the power law leads to a transition temperature of about $T^*_{00\frac{1}{2}}$=354 K±6 K. Around the same temperature as the $(00\frac{1}{2})$ reflection, the in-plane $(\frac{1}{2}00)$ peak appears which becomes most prominent at around T=350 K which correspond to its intensity maximum. A decay of the intensity can be observed for higher temperatures until it vanishes at about $T^*_{\frac{1}{2}00}$=469 K±13 K. The first and second order reflections along the [001]- and [100]-direction are, on the other hand, constant within the error bars indi-

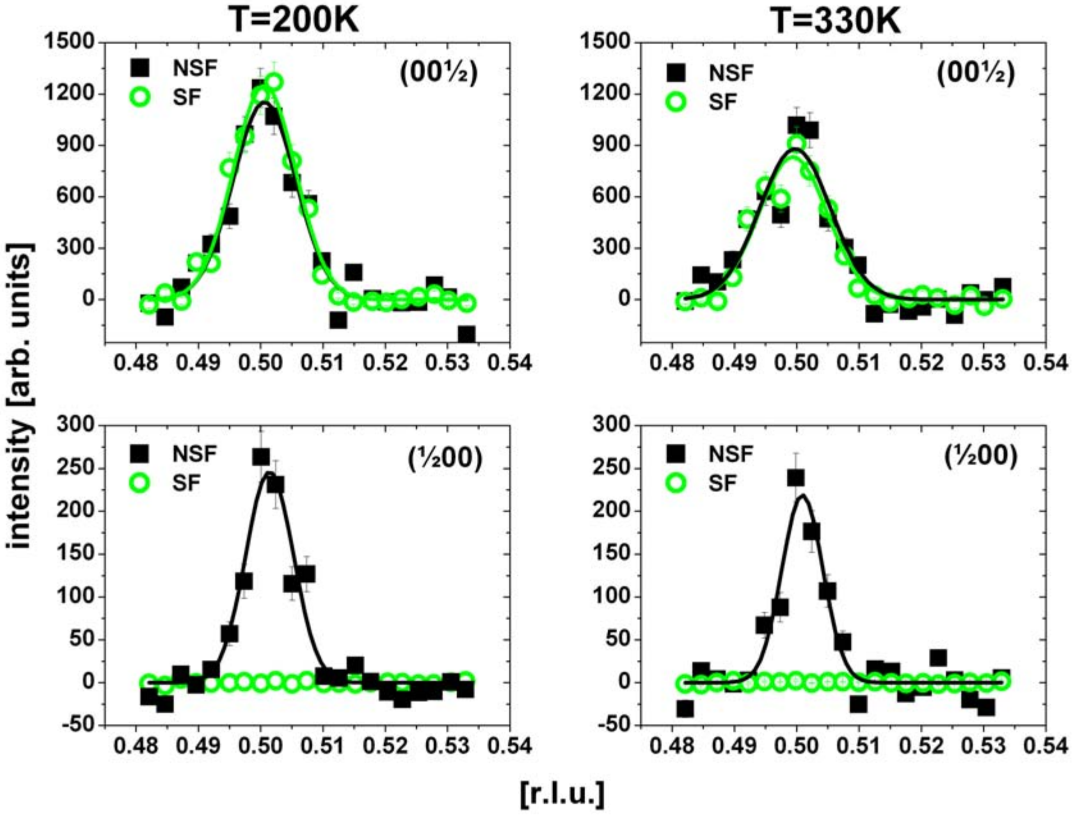

Figure 5.21.: Polarization analysis of the $Fe_{50}Pt_{32.5}Rh_{17.5}$ film for the half order $(00\frac{1}{2})$ and $(\frac{1}{2}00)$ reflection at T=200 K and T=330 K. The guide field was directed along the [010]-direction (b-axis) of the film.

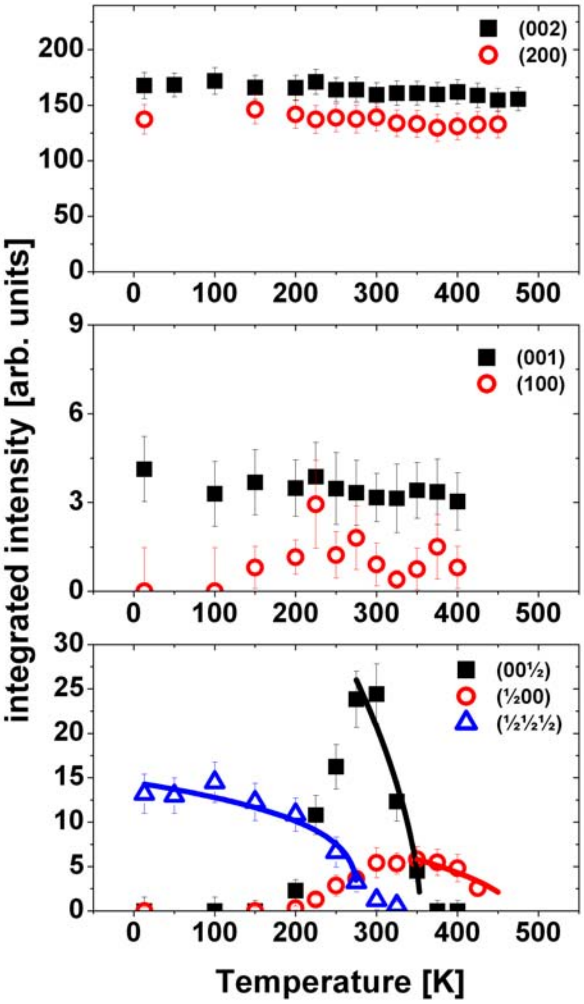

Figure 5.22.: Temperature dependence of the integrated neutron diffraction intensities of the $Fe_{50}Pt_{25}Rh_{25}$ film at the half, first and second order reflections along the [001]- (solid symbols) and [100]-direction (open symbols) as well as the $(\frac{1}{2}\frac{1}{2}\frac{1}{2})$ peak. The lines are fits to equation 5.19.

cating that no magnetic components contribute to their intensity.

From the unpolarized neutron diffraction measurements one can conclude that at low temperature an AF order is present along the [111]-direction while in a temperature range between $200\,\mathrm{K}<\mathrm{T}<350\,\mathrm{K}$ an AF order in the out-of-plane direction becomes dominant. For temperature $\mathrm{T}>350\,\mathrm{K}$ another AF order in the in-plane direction is dominant before the film becomes paramagnetic above $\mathrm{T}=470\,\mathrm{K}$. The slow decays of the half order reflections indicate continuous transitions between the different AF orders and to the PM phase, respectively, which is also expressed in the fitted values of the transition exponents listed in table 5.4.

Fig. 5.23 describes the behavior of the lattice constants a and c and the c/a-ratio with temperature. Both lattice constants a and c increase continuously while the c/a-ratio show only a slight indication of an increase. As already observed in the other films no abrupt changes can be found indicating that the transitions of the dominant reflection are not accompanied by drastic changes of the crystal structure.

The polarized neutron diffraction analysis of the $Fe_{50}Pt_{25}Rh_{25}$ film was carried out at

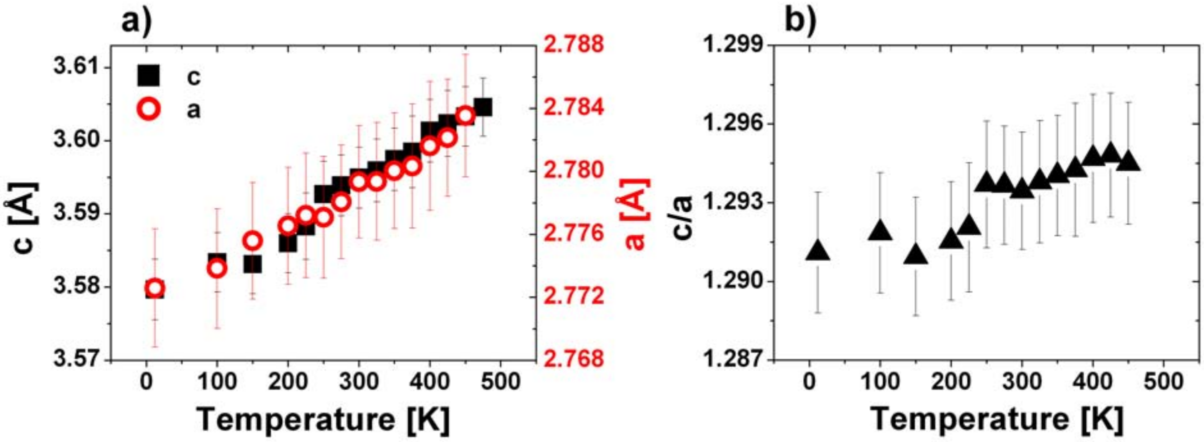

Figure 5.23.: **a)** The variation of the lattice parameter a and c of the $Fe_{50}Pt_{25}Rh_{25}$ film with temperature. **b)** Temperature dependence of the c/a-ratio.

various temperature with the magnetic guide field directed along the b-axis. Figure 5.24 shows the analysis in more detail for two distinct temperatures: At T=250 K where the $(00\frac{1}{2})$ reflection is dominant and at T=330 K where both $(00\frac{1}{2})$ and $(\frac{1}{2}00)$ peaks have quasi identical intensities. Besides the half order reflections also the first order peaks (001) and (100) were analyzed. Here, both NSF channels and one SF channel was measured. The first order reflections show almost identical intensity in both NSF channels for both temperatures while no intensity can be found in the SF channel indicating that the measured intensity is of pure nuclear origin without any FM contribution. The $(00\frac{1}{2})$ reflection, on the other hand, shows for both temperatures identical intensities in the SF and NSF channel, only the intensity drops for higher temperatures as already seen in the unpolarized neutron diffraction measurements. The identical intensities of both scattering channels indicate magnetic moments with components along the a- and b-axis. The $(\frac{1}{2}00)$ reflection also exhibits intensity in both the SF and the NSF channel, but with different intensities. While the NSF channel is strong at T=250 K, the SF channel becomes slightly dominant at T=330 K indicating that magnetic moments along as well as perpendicular to the guide field contribute to the AF order but with a temperature driven slight reorientation of the magnetic moments from the in-plane to the out-of-plane direction. A more detailed temperature analysis of the polarized neutron diffraction is presented in Fig. 5.25. Here, it can be seen that the dominant intensity of the $(\frac{1}{2}00)$ reflection changes from the NSF to the SF channel at about T=315 K. Furthermore, the SF channel becomes more dominant with higher temperature.

The neutron diffraction measurements reveal an AF order along the [111]-direction for low temperature that changes to an AF order in the out-of-plane direction for higher temperature and for even higher temperature an AF order in the in-plane direction can be found before the film becomes PM above T=470 K. The polarization analysis of the $Fe_{50}Pt_{25}Rh_{25}$ film indicates components of the magnetic moments along the three symmetry axes. Here, the contribution of the components in the out-of-plane direction becomes dominant for higher temperature.

The data from the neutron diffraction measurements are summarized in table 5.4. The measurements reveal a FM order for the $Fe_{50}Pt_{50-x}Rh_x$ film with x=5 while the film

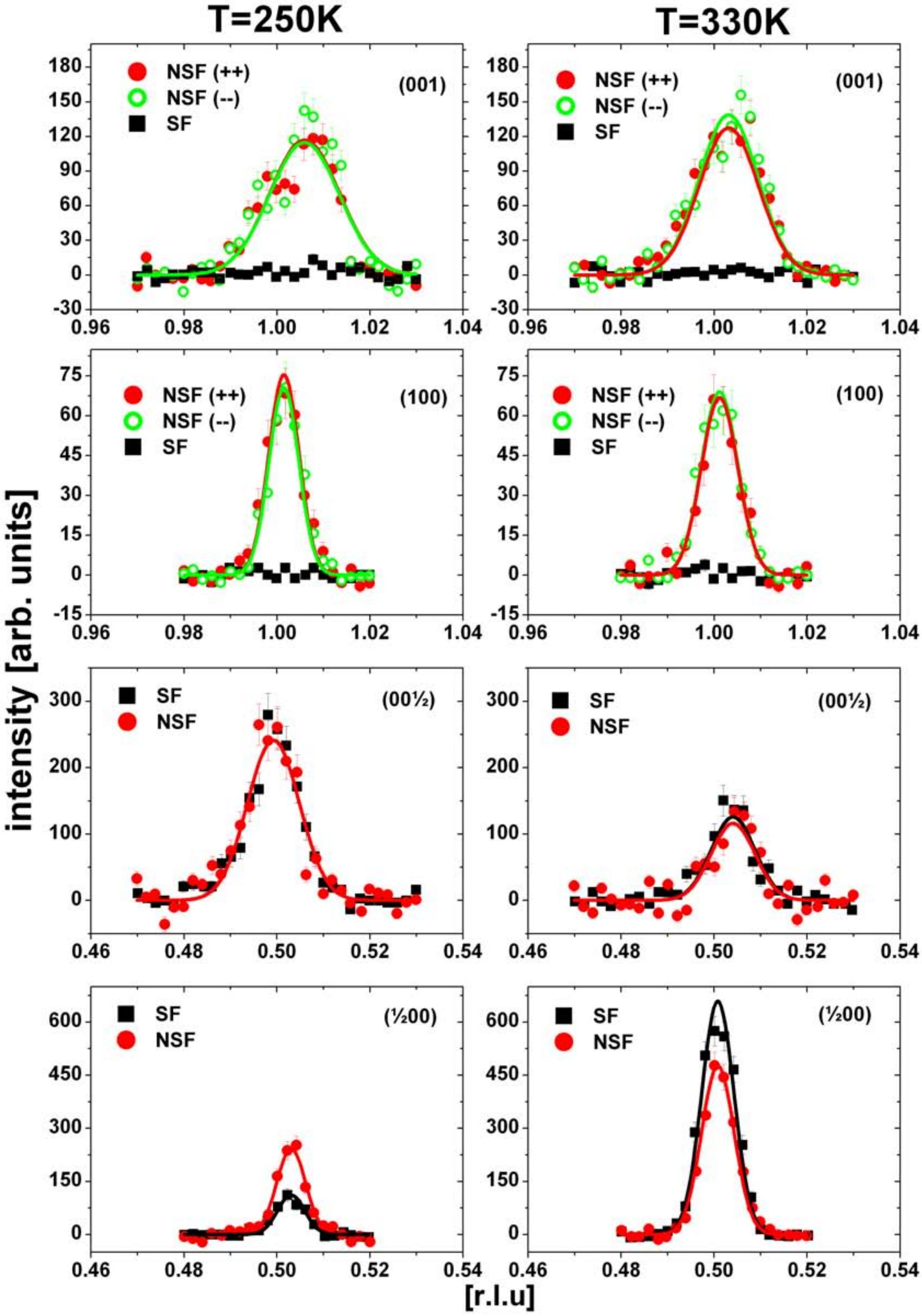

Figure 5.24.: Polarization analysis of the half and first order reflections along the [100]- and [001]-direction of the $Fe_{50}Pt_{25}Rh_{25}$ film at T=250 K and T=330 K. Shown is the raw data with background subtraction. The guide field in the measurements was directed along the [010]-direction (b-axis) of the film.

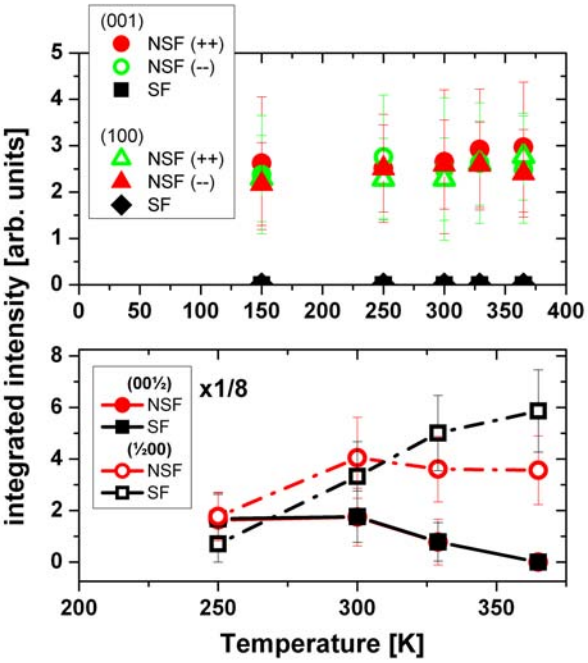

Figure 5.25.: Polarization analysis of the $Fe_{50}Pt_{25}Rh_{25}$ film for the nuclear Bragg reflections (001), (100) and the AF $(00\frac{1}{2})$, $(\frac{1}{2}00)$ peaks. Plotted are the integrated intensities (including the data treatment) against the temperature. The integrated intensity of the $(00\frac{1}{2})$ reflection has been multiplied by a factor 1/8.

with x=17.5 has a pure AF order. The magnetic behavior of the film with x=10 can be considered as an intermixture of the $Fe_{50}Pt_{45}Rh_{5}$ film and the $Fe_{50}Pt_{32.5}Rh_{17.5}$ film showing the transition from an AF behavior at low temperature to a FM order at high temperature. The $Fe_{50}Pt_{25}Rh_{25}$ film exhibits similar to the film with x=17.5 a pure AF behavior, but in contrast the AF order changes with temperature. The results of the polarization analysis show that the magnetic moments in the films with AF order are dominantly oriented along the in-plane direction while in FM ordered films the magnetic moments are aligned along the out-of-plane direction. An exception is the $Fe_{50}Pt_{25}Rh_{25}$ film since in this film the dominant orientation of the AF aligned magnetic moments changes with the temperature.

The decay of the different reflections can be fitted by the power law 5.19 leading to the transition temperatures in the table 5.4. The examined Néel and Curie temperatures of the samples highlighted in the table are about T=100 K lower compared to the bulk system [17]. Additionally the decrease of the integrated intensities show no abrupt or rapid behavior which is also reflected in the values of the transition exponents β^* in the range between 0.2 and 0.3 (see table 5.4).

Considering the in-plane and out-of-plane lattice constants a and c of the different films one can see that the magnetic configuration is also reflected in these parameters. Both lattice constants increase in the four films with the temperature due to thermal expansions of the lattice as expected, but the c/a-ratios show different behaviors depending on the magnetic configuration in the films. For the AF ordered films with x=25 and x=17.5 a continuous increase of the ratio can be observed with temperature while for the FM ordered film with x=5 a decrease of the c/a-ratio can be found. In the film with x=10

	(001)	(100)	$(00\frac{1}{2})$	$(\frac{1}{2}00)$	$(\frac{1}{2}\frac{1}{2}\frac{1}{2})$
x=5	const.	**521K±2K** **0.31±0.02**	no peak	no peak	no peak
x=10	const.	**414K±20K** **0.29±0.06**	330K±4K 0.24±0.03	252K±3K 0.3±0.1	230K±30K 0.3±0.1
x=17.5	const.	const.	**408K±10K** **0.15±0.05**	slight decrease	slight decrease
x=25	const.	const.	354K±6K 0.3±0.1	**469K±13K** **0.2±0.09**	276K±4K 0.14±0.05

Table 5.4.: Transition temperatures and exponents for the different 200 nm $Fe_{50}Pt_{50-x}Rh_x$ films. The highlighted values are the Néel and Curie temperatures, respectively, of the corresponding films.

again a transition between these behaviors is present. The change from a continuous growth to a decrease of the c/a-ratio indicates magnetostriction effects during the AF-FM transition. In the bulk $Fe_{50}Pt_{40}Rh_{10}$ alloy the AF-FM transition is associated by discontinuities of the lattice constants and the c/a-ratio. In the 200 nm thick film only a continuous behavior of the parameters can be observed which can be explained by the fact that the parameters are determined from the average over all contributing domains (AF and FM domains).

5.4.2. Magnetic Field

The temperature and magnetic field dependent data were obtained at the instruments IN12 and D23 at the ILL. The measurements were carried out to examine the magnetic field dependence of the different compositions, e.g. to investigate if it is possible to manipulate the magnetic transitions or even introduce them into the system if they are not present before. Four $Fe_{50}Pt_{50-x}Rh_x$ films with x=5, 10, 17.5 and 25 have been analyzed with the magnetic field directed in the in-plane and out-of-plane direction. The magnetic fields up to 12 T were provided by different superconducting magnets with horizontal (up to 5 T) and vertical magnetic field (up to 12 T). The temperature in these measurements was limited to T=315 K due to technical restrictions of the cryomagnets.

The focus of the magnetic field measurements is on the $Fe_{50}Pt_{40}Rh_{10}$ film since this is the most promising candidate for a manipulation of the magnetic transition temperature by the application of a magnetic field due to the observed AF-FM transition (see previous section).

$Fe_{50}Pt_{40}Rh_{10}$

The measurements for the $Fe_{50}Pt_{40}Rh_{10}$ film were carried out by using two distinct superconducting magnets covering the magnetic field ranges from 0 T to 5 T and from 5 T to 12 T, respectively. A temperature range from T=100 K to the maximum temperature of about T=312 K available by the superconducting magnet was selected which includes the observed AF-FM transition at zero field.

Figure 5.26 presents the magnetic field dependence of the $(00\frac{1}{2})$ and $(\frac{1}{2}00)$ reflections for different temperatures and clearly shows that the integrated intensities of both half order reflections can be suppressed by the application of an in-plane magnetic field. The in-

	$(00\frac{1}{2})$	$(\frac{1}{2}00)$
0T	T=317K±15K β=0.3±0.1	T=260K±8K β=0.2±0.1
12 T/5 T	T=280K±17K β=0.4±0.2	T=230K±20K β=0.33±0.08

Table 5.5.: Transition temperatures and exponents for the $Fe_{50}Pt_{40}Rh_{10}$ film with and without the application of a magnetic field. The $(00\frac{1}{2})$ reflection was measured at 12 T and the $(\frac{1}{2}00)$ peak at 5 T.

tensity of the out-of-plane half order reflection $(00\frac{1}{2})$ decreases only slightly by magnetic fields of up to 5 T before a more significant decrease can be observed for fields up to 12 T. The suppression of intensity, however, is more pronounced for higher temperatures. The integrated intensity, for example, is reduced only by about 22% from 0 T to 12 T for T=150 K while for T=258 K a decrease of about 68% can be observed. An even more significant intensity decrease can be found for the $(\frac{1}{2}00)$ reflection with a similar temperature behavior. For a temperature of about T=100 K the integrated intensity can be suppressed about 62% by a field of 5 T while for T=200 K the suppression is about 81% at the same magnetic field. It should be noted that the intensity drop to zero from 5 T to 7 T at T=300 K for the $(00\frac{1}{2})$ reflection indicated in Fig. 5.26 can be explained by the two different magnets and instruments used for the measurements. The signal to noise ratio of the instrument and magnet used for the high magnetic field measurements was below the one used for the low magnetic field measurements. The low scattering signal makes it challenging to observe the $(00\frac{1}{2})$ reflection at high field and temperature. The low signal to noise ratio also restricted the study of the magnetic field behavior for the weak $(\frac{1}{2}00)$ reflection for magnetic fields up to 5 T. The influence of the magnetic field on the temperature behavior of the integrated intensity is shown in Fig. 5.27. On the left and right side the temperature curves of the $(00\frac{1}{2})$ reflection at 0 T and 12 T and of the $(\frac{1}{2}00)$ reflection at 0 T and 5 T are plotted, respectively. Fitting the decay of the integrated intensities lead to a transition temperature of about $T^*_{00\frac{1}{2}}$=317 K±15 K for the out-of-plane half order reflection $(00\frac{1}{2})$ without magnetic field. This result is in good agreement with the earlier determined transition temperature of about $T^*_{00\frac{1}{2}}$=330 K±4 K with respect to the error bars. In a field of 12 T the transition temperature is suppressed of about 40 K to $T^*_{00\frac{1}{2}}$=280 K±17 K. A similar decrease of about T=30 K can be also observed for the $(\frac{1}{2}00)$ reflection at 5 T. Without a magnetic field the transition temperature has a value of about $T^*_{\frac{1}{2}00}$=260 K±8 K which is again in good agreement with earlier results ($T^*_{\frac{1}{2}00}$=252 K±3 K) while at a field of 5 T the transition temperature is reduced to $T^*_{\frac{1}{2}00}$=230 K±20 K. It should be noted that the intensity decay is slower in the measurements with the application of a magnetic field. This behavior is reflected in the higher values of the transition exponents (see table 5.5) indicating a more continuous magnetic transition.

Not only the half order but also the first order reflections are influenced by the application of an external magnetic field which indicates changes in the FM configuration (see Fig. 5.28). The integrated intensity of the (001) reflection increases significantly with the magnetic field while for the (100) reflection only a slight increase of its intensity can be detected. Without a magnetic field the integrated intensity of the (001) reflection is very low and constant over the whole temperature range as already observed before in the neutron diffraction measurements indicating its pure nuclear origin. By the application

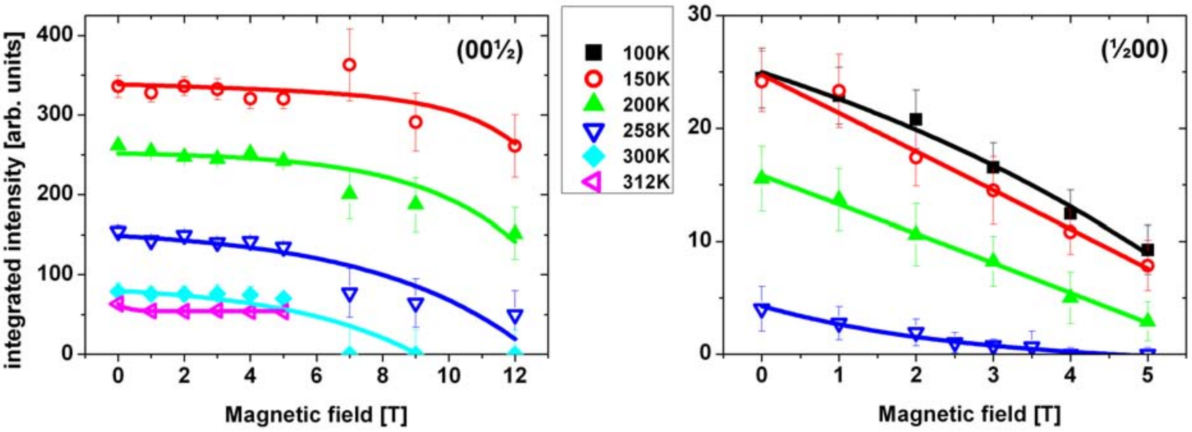

Figure 5.26.: Magnetic field dependence of the integrated peak intensities of the $(00\frac{1}{2})$ and $(\frac{1}{2}00)$ reflection of the $Fe_{50}Pt_{40}Rh_{10}$ film at different temperatures. The lines are guides to the eyes.

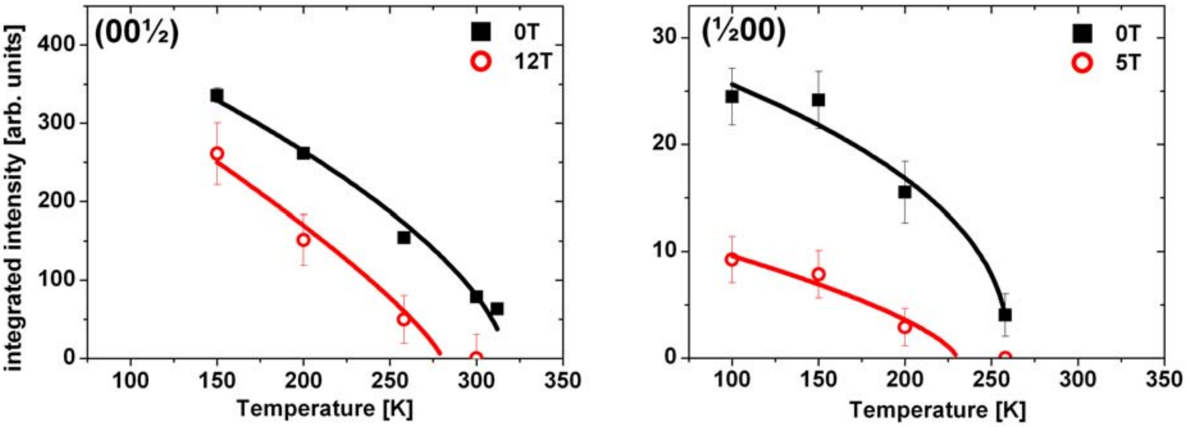

Figure 5.27.: Temperature dependence of the integrated intensities of the $(00\frac{1}{2})$ and $(\frac{1}{2}00)$ reflection of the $Fe_{50}Pt_{40}Rh_{10}$ film for 0 T (black squares) as well as 12 T and 5 T, respectively (open red circles). The black and red lines are fits to the power law 5.19.

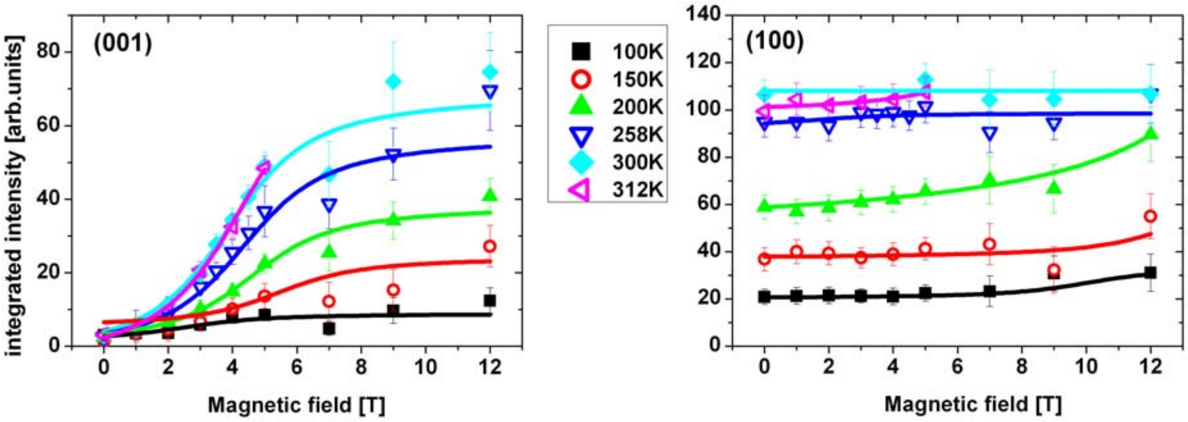

Figure 5.28.: Magnetic field dependence of the integrated intensities of the first order reflections (001) and (100) of the $Fe_{50}Pt_{40}Rh_{10}$ film for different temperatures. The lines are guides to the eyes.

of an external magnetic field the intensity increases. This increase is the stronger the higher the temperature is at the sample position. At T=100 K the integrated intensity grows from 0 T to 12 T about 4 times while at T=300 K it is already a factor of about 27. The (100) reflection, on the other hand, shows only a slight increase with the magnetic field. For temperatures up to T=200 K an increase of about 50% can be determined while for higher temperatures the increase is nearly zero and the integrated intensity can be considered as constant over the whole magnetic field range. The almost constant intensity observed at T=258 K and T=300 K correspond to the temperature region where the (100) reflection reached its intensity maximum without magnetic field.

Figure 5.29 presents the temperature behavior of the integrated intensity of the (001) and (100) reflection at different magnetic fields. For both reflections a similar temperature behavior can be observed by the application of a magnetic field, i.e. both intensities increase with the temperature. The graphs show once more that the effect of the magnetic field is much stronger for the (001) than for the (100) reflection.

Considering the results from the magnetic field dependence of the $Fe_{50}Pt_{40}Rh_{10}$ film one can conclude that the integrated intensity of the half order reflection can be suppressed by the application of a magnetic field directed in-plane along the b-axis. Here, the $(\frac{1}{2}00)$ reflection is more affected and faster suppressed. The integrated intensities of the first order reflections, on the other hand, can be increased by the application of a magnetic field with a much stronger effect on the out-of-plane reflection (001).

The scattering vector of the (001) reflection is oriented along the [001]-axis and as a consequence the measurements are only sensitive to components of the magnetic moments oriented in-plane. Considering the in-plane orientation of the magnetic field and the observed behavior of the different integrated intensities the observations indicate the induction of a FM order in the out-of-plane direction with a reorientation of the magnetic moments in the direction of the applied magnetic field. Furthermore the measurements showed that the transition temperature can be clearly reduced by the application of an external magnetic field.

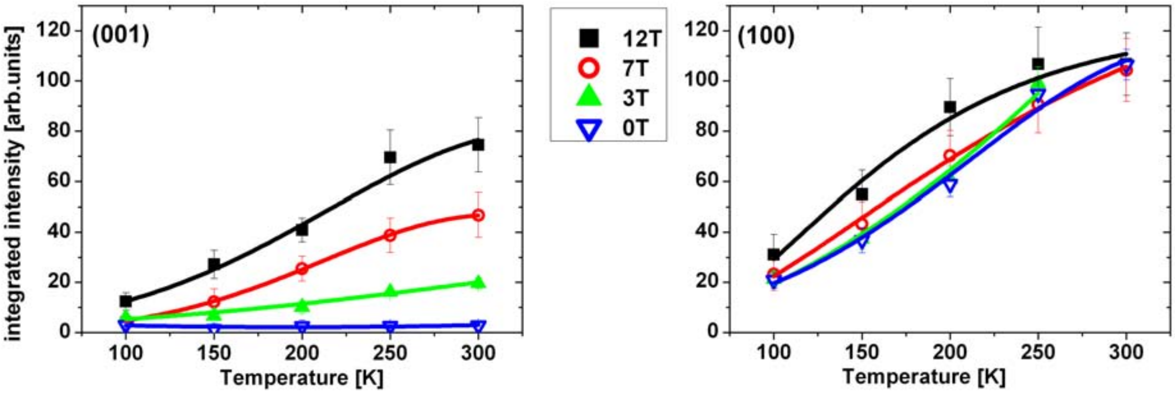

Figure 5.29.: Temperature behavior of the integrated intensities of the (001) and (100) reflection of the $Fe_{50}Pt_{40}Rh_{10}$ film at four distinct magnetic fields 12 T (black squares), 7 T,(open red circles) 3 T (green triangles) and 0 T (blue open triangles). The lines are guides to the eyes.

$Fe_{50}Pt_{45}Rh_5$

The magnetic field dependent neutron diffraction measurements of the $Fe_{50}Pt_{45}Rh_5$ film were carried out with a horizontal superconducting magnet with fields up to 3.5 T applied in-plane along the a-axis of the film which is parallel to the scattering vector $\vec{Q}$ of the (100) reflection. It should be noted that in this set-up the measurements in the in-plane direction are sensitive to magnetic moments directed in the out-of-plane direction and not additionally to in-plane magnetic moments along the magnetic field as in the measurements of the $Fe_{50}Pt_{40}Rh_{10}$ film. The measurements were restricted to the first order reflections (001) and (100) since any intensity from the half order reflections can be already excluded according to the unpolarized neutron diffraction measurements (see section 5.4.1).

The results of the magnetic field investigations are presented in Fig. 5.30. It should be reminded that without a magnetic field the integrated intensity of the (001) reflection is constant with a very low count rate. By the application of an external magnetic field the intensity increases strongly and enhances the signal of about a factor of 10 for 3.5 T without reaching the saturation. The (100) reflection shows in contrast to the (001) reflection a decrease of the integrated intensity with the application of a magnetic field.

Figure 5.31 shows the temperature behavior of the integrated intensities of the (001) and (100) reflection at different magnetic fields. For the (100) reflection an intensity decrease can be observed which is qualitatively nearly identical as for zero magnetic field. The integrated intensity of the (001) reflection shows, on the other hand, only a slight decrease of intensity with temperature by the application of a magnetic field while it is almost zero without field. These results show that the influence of the temperature on the magnetic field dependence is obviously less significant as it is for the $Fe_{50}Pt_{40}Rh_{10}$ film.

The unpolarized neutron diffraction measurements of the $Fe_{50}Pt_{45}Rh_5$ film show an induction of a FM order in the out-of-plane direction with a reorientation of the magnetic moments along the in-plane direction. This is supported by the decrease of the integrated intensity of the (100) reflection indicating that the magnetic moments align in the direction of the applied magnetic field along the a-axis.

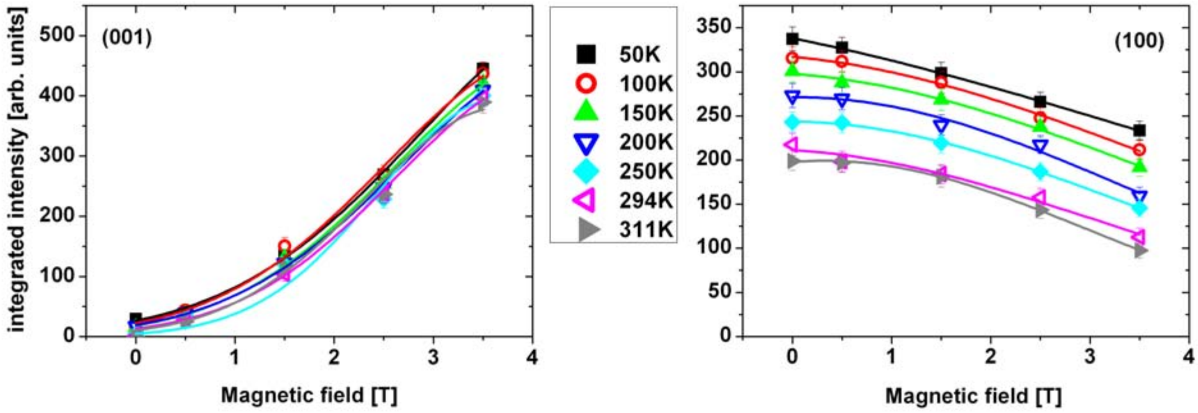

Figure 5.30.: Magnetic field dependence of the integrated intensities of the first order reflections (001) and (100) of the $Fe_{50}Pt_{45}Rh_5$ film for different temperatures. The lines are guides to the eyes.

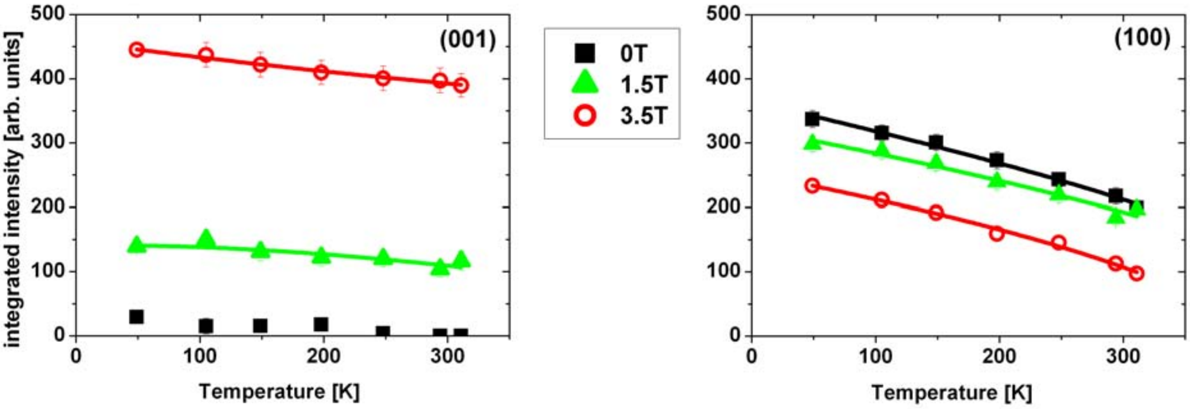

Figure 5.31.: Comparison of the temperature curves of the integrated intensities of the (001) and (100) reflection of the $Fe_{50}Pt_{45}Rh_5$ film for 0 T (black solid squares), 1.5 T (green triangles) and 3.5 T (red open circles). The lines are guides to the eye.

Figure 5.32 shows the results of the polarization analysis of the second order reflection (002) and the first order reflection (100) at 1 T for two distinct temperatures. It is important to note that the integrated intensity of the (001) reflection was too low in intensity to be analyzed at 1 T and the application of higher magnetic fields was not possible in the set-up without loosing the degree of polarization of the neutron beam to large parts. A problem arising in the set-up for higher magnetic fields is that the stray magnetic fields are perpendicular to the guide field and therefore influences the quantization axis of the neutrons. For the in-plane measurements it should be noted that the magnetic field is parallel to the scattering vector $\vec{Q}$. As a consequence any signal in this channel is of pure nuclear origin and no magnetic signal can be detected in the NSF channel (see section 3.2.3).

In contrast to the polarized measurements without a magnetic field, a splitting of both NSF channels (++) and (- -) of the second order reflection (002) can be observed at an external magnetic field of 1 T (compare with Fig. 5.14). A measure for the splitting is the asymmetry ratio:

$$\frac{I^{++} - I^{--}}{I^{++} + I^{--}}, \tag{5.20}$$

with I^{++} and I^{--} denoting the integrated intensities of both NSF channels. The asymmetry ratio at 1 T has a value of about 9% which does not change with temperature as it is exemplarily shown for T=100 K and T=300 K. The splitting of the NSF channels is the fingerprint of a FM contribution which should be also observed in the (001) reflection indicating that the components of the magnetic moments are oriented along the applied magnetic field. The polarization analysis of the (100) reflection, on the other hand, is qualitatively identical to the analysis without a magnetic field. The strong magnetic signal in the SF channel indicates that components of the magnetic moments along the out-of-plane direction contribute to the peak intensity. This contribution decreases with temperature. The NSF intensity is as discussed of pure nuclear origin.

The results from the polarized and unpolarized neutron diffraction measurements for the $Fe_{50}Pt_{45}Rh_5$ film show that with the application of a magnetic field along the a-axis FM aligned magnetic moments pointing in the out-of-plane direction can be tilted along the direction of the magnetic field which induces a FM order in the out-of-plane direction. The FM in-plane order, however, still remains indicating that a magnetic field of 3.5 T was not sufficient to saturate the sample and tilt all magnetic moments along the field direction.

$Fe_{50}Pt_{32.5}Rh_{17.5}$ and $Fe_{50}Pt_{25}Rh_{25}$

The neutron diffraction measurements of the $Fe_{50}Pt_{40}Rh_{10}$ film shows an effect of the magnetic field even at low field values of about 2 T (see Fig. 5.33). A similar behavior can be observed for the $Fe_{50}Pt_{45}Rh_5$ film (see Fig. 5.34). In both cases the magnetic field was directed in-plane. Measurements with even higher magnetic fields of 3.5 T and the highest possible temperature near the magnetic transition show no effect when the field is applied out-of-plane. The AF ordered $Fe_{50}Pt_{32.5}Rh_{17.5}$ and the $Fe_{50}Pt_{25}Rh_{25}$ film, on the other hand, show no effect under the same conditions whether the magnetic field is applied in the in-plane nor in the out-of-plane direction (see Fig. 5.35 and 5.36). The AF structure of the film with x=17.5 could not be modified even by the application of magnetic fields up to 10 T.

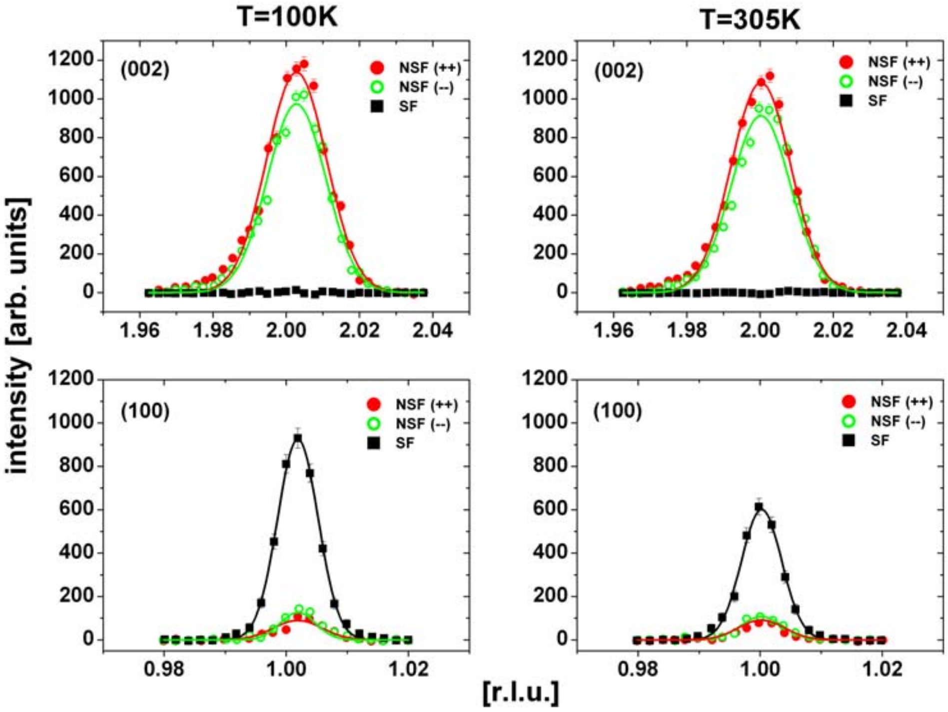

Figure 5.32.: Polarization analysis of the $Fe_{50}Pt_{45}Rh_5$ film for the (002) and (100) reflection at 1 T for T=100 K and T=305 K. Plotted are the integrated intensities against the reciprocal lattice units (r.l.u.). The magnetic field was set along the [100]-direction (a-axis) of the film.

The measurements with the external magnetic field applied along the in-plane directions demonstrated that the field has an effect on the samples with low Rh concentration and those samples which already showed FM behavior at zero magnetic field, i.e. $Fe_{50}Pt_{45}Rh_5$ and $Fe_{50}Pt_{40}Rh_{10}$. For the other samples which have a larger Rh concentration and are AF ordered, $Fe_{50}Pt_{32.5}Rh_{17.5}$ and $Fe_{50}Pt_{25}Rh_{25}$, no effect can be observed for fields up to 3.5 T. For the film with x=10 an induction of a FM order out-of-plane can be observed by the application of a magnetic field. Here, the measurements show a reorientation of the magnetic moments from the out-of-plane to the in-plane direction. The reorientation is accompanied with a lowering of the AF-FM transition temperature. The observed magnetic field effect becomes stronger for higher temperatures. The neutron diffraction measurements with an external field on the film with x=5 also reveal an induction of a FM order out-of-plane with a reorientation of the magnetic moments along the applied field. The influence of the temperature on the effects of the magnetic field is here in contrast to the $Fe_{50}Pt_{40}Rh_{10}$ film significantly lower, i.e. the effect of the magnetic field becomes not significantly stronger for higher temperatures.

5.4.3. Film Thickness

In the following section the influence of the film thickness on the magnetic properties and the magnetic configuration will be investigated. In particular the $Fe_{50}Pt_{40}Rh_{10}$ film is interesting for this study since here the influence of the film thickness on the observed AF-FM transition can be investigated.

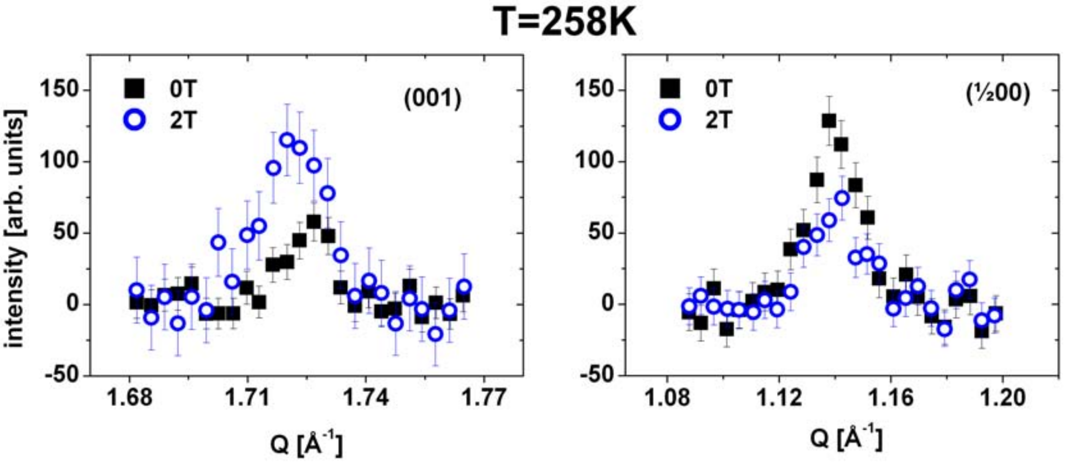

Figure 5.33.: Magnetic field dependence of the (001) and ($\frac{1}{2}$00) reflection of the $Fe_{50}Pt_{40}Rh_{10}$ film at T=258 K for 0 T (black squares) and 1.5 T (open circles). The magnetic field was directed along the b-axis.

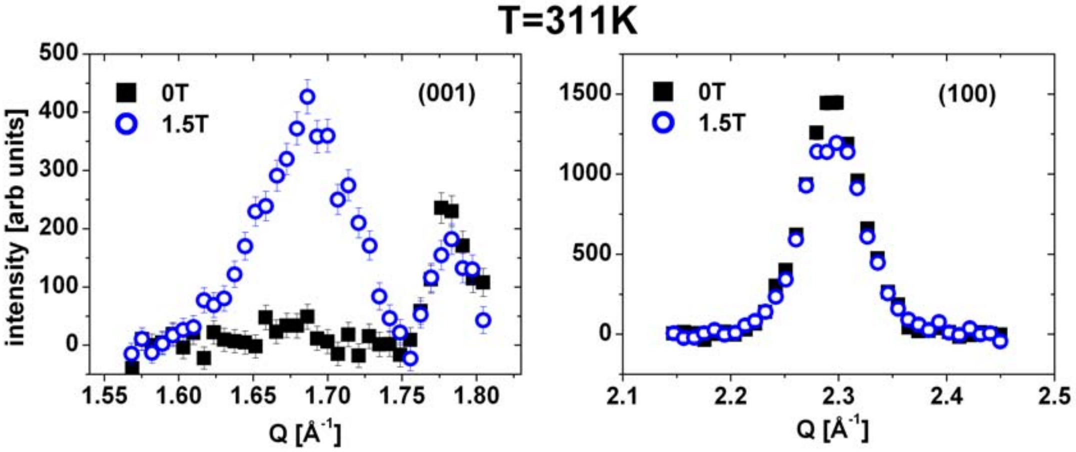

Figure 5.34.: Magnetic field dependence of the (001) and (100) reflection of the $Fe_{50}Pt_{45}Rh_5$ film at T=311 K for 0 T (black squares) and 1.5 T (open circles). The magnetic field was directed along the a-axis.

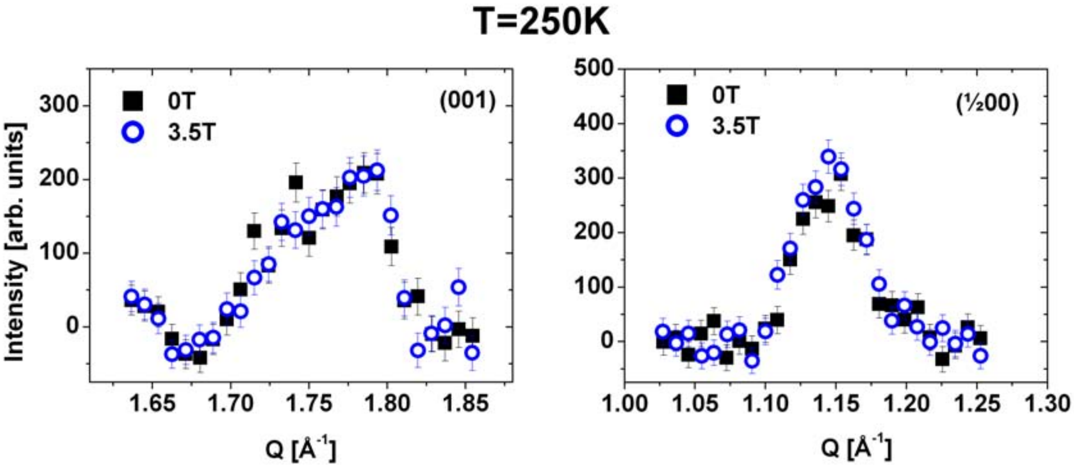

Figure 5.35.: Magnetic field dependence of the (001) and ($\frac{1}{2}$00) reflection of the Fe$_{50}$Pt$_{32.5}$Rh$_{17.5}$ film at T=250 K for 0 T (black squares) and 3.5 T (open circles). The magnetic field was directed in-plane along the b-axis.

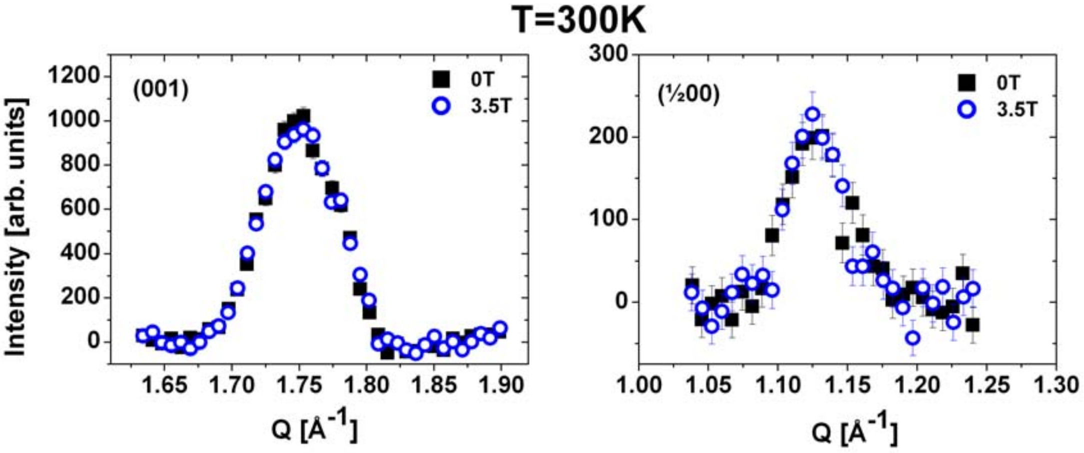

Figure 5.36.: Magnetic field dependence of the (001) and ($\frac{1}{2}$00) reflection of the Fe$_{50}$Pt$_{32.5}$Rh$_{17.5}$ film at T=250 K for 0 T (black squares) and 3.5 T (open circles). The external magnetic field was applied in-plane along the b-axis.

unpolarized neutron diffraction

Figure 5.37 shows the unpolarized neutron diffraction measurements of three $Fe_{50}Pt_{40}Rh_{10}$ films with different thicknesses of 100 nm, 300 nm and 500 nm. The half, first and second order reflections along the [001]- and [100]-direction were investigated. The behavior of the integrated intensities of the observed reflections resembles very much the previous measurements on the 200 nm thick $Fe_{50}Pt_{40}Rh_{10}$ film. The integrated intensities of the half order reflections $(00\frac{1}{2})$ and $(\frac{1}{2}00)$ decrease with increasing temperature. Fitting the decay of the half order reflections with the power law 5.19 a transition temperature of about $T^*_{00\frac{1}{2}} = 377\,\mathrm{K}$ and $T^*_{\frac{1}{2}00}$=282 K can be determined for the in-plane and out-of-plane reflections respectively, for all three films (see table 5.6). The integrated intensities of the (100) reflections, on the other hand, increase abruptly at T=250 K and reach their maxima at about T=325 K before they decrease again. The fitting of the decay of the integrated intensities lead to a transition temperature of about T^*_{100}=400 K for the different (100) reflections with respect to the error bars. The integrated intensities of the out-of-plane (001) reflections, on the other hand, are constant in all three films over the whole temperature range indicating that they are of pure nuclear origin. The temperature behavior of the first order reflections should also be observed in the second order reflections (002) and (200) as already discussed in section 5.2 but the fraction of the magnetic contribution to the peak intensity is once more to low to be determined. It should be noted that the raw data of the second order reflections indicate a temperature behavior of the integrated intensity whose origin is non-magnetic. The data shown here have been corrected for this behavior by the Debye-Waller (DW) factor. More information to the DW-factor can be found in the appendix.

The only clear differences of the various film thicknesses which can be observed are the higher integrated intensities of the thicker films due to larger amount of scatterer in the beam and a faster decay of the integrated intensities of the half order reflections in the thicker films which can also be seen in the lower values of the transition exponents β^* (see table 5.6) indicating an AF-FM transition in a smaller temperature range.

Compared to the 200 nm thick $Fe_{50}Pt_{40}Rh_{10}$ film, the transition temperatures of the $(00\frac{1}{2})$ and the $(\frac{1}{2}00)$ reflections are about T=50 K and T=30 K higher, respectively, while the transition temperature of the (100) reflection is in good agreement with the one determined for the 200 nm film (T^*=414 K±14 K). Another difference is the appearance of the integrated intensity of the (100) peak in a smaller temperature range.

The observed differences to the 200 nm thick film can be attributed to the growth of two different sample series: one series of the 200 nm thick composition dependent $Fe_{50}Pt_{50-x}Rh_x$ films and another for the thickness dependent films. Slight variations in the sample preparation, e.g. slight variations of the growth temperatures, or random growth effects, can lead to slight differences in the film composition, i.e. in the Rh concentration and therefore to a different magnetic behavior. The magnetic phase diagram of the bulk $Fe_{50}Pt_{50-x}Rh_x$ system in Fig. 2.2 showed that slight differences in the Rh concentration lead to drastic changes of the magnetic behavior, in particular for Rh concentrations around x=10. The appearance of the (100) reflection at higher temperature indicates a Rh concentration slightly higher than x=10.

polarized neutron diffraction and magnetic field

The diffraction measurements with unpolarized neutrons have shown that the $Fe_{50}Pt_{40}Rh_{10}$ films with different thicknesses have similar magnetic properties as the previously studied

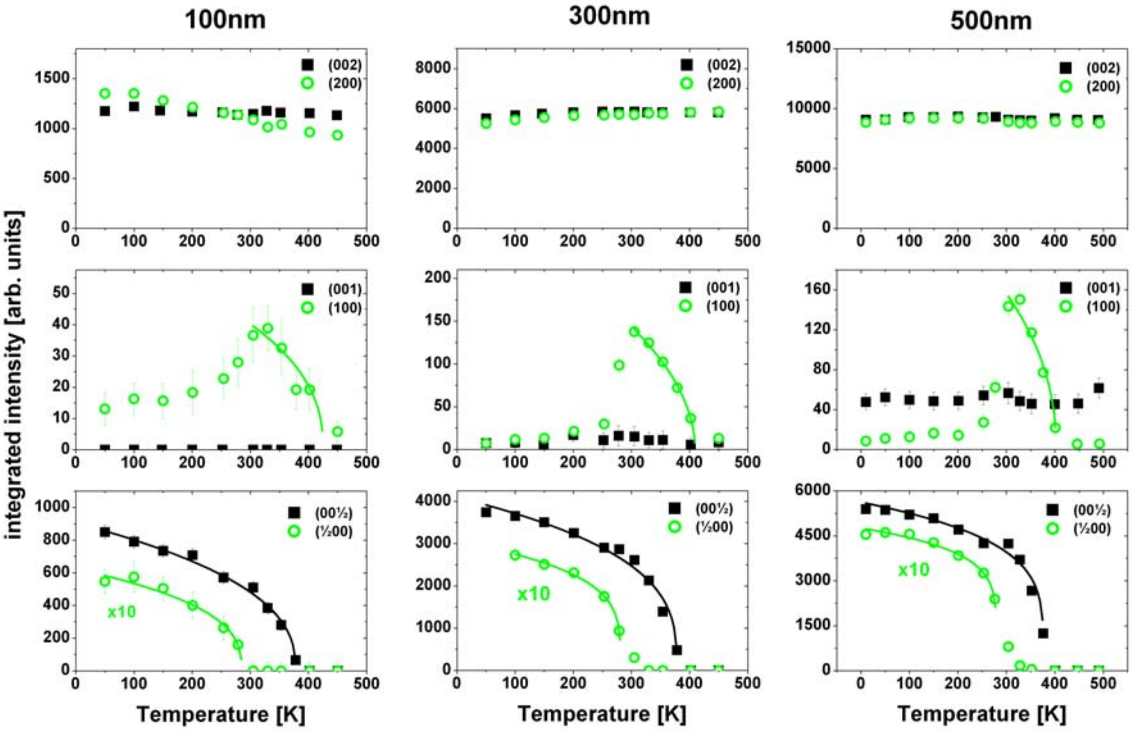

Figure 5.37.: Temperature dependence of the integrated peak intensities for the 100 nm, 300 nm and 500 nm $Fe_{50}Pt_{40}Rh_{10}$ films at the half, first and second order reflections along the [001]- (solid symbols) and the [100]-direction (open symbols). The lines are fits to the power law 5.19.

	(100)	$(00\frac{1}{2})$	$(\frac{1}{2}00)$
100nm	425K±30K	378K±0.8K	285K±5K
	0.21±0.09	0.2±0.01	0.18±0.03
(200nm)	414K±14K	330K±4K	252K±3K
	0.29±0.06	0.24±0.03	0.21±0.06
300nm	409K±12K	378K±0.9K	281K±2K
	0.3±0.1	0.16±0.01	0.12±0.02
500nm	402K±3K	376K±0.8K	279K±6K
	0.23±0.06	0.11±0.01	0.08±0.02

Table 5.6.: Transition temperatures and exponents for the $Fe_{50}Pt_{40}Rh_{10}$ films with different thicknesses from 100 nm to 500 nm. The values of the 200 nm thick film were taken from the previous section.

200 nm thick film. To verify that the magnetic configurations are also similar polarized neutron diffraction with polarization analysis has been performed exemplarily on the 500 nm thick film. Since the unpolarized scans show nearly identical behavior for the 100 nm, 300 nm and 500 nm thick films it can be assumed that also the magnetic configuration is nearly identical for all films.

Four reflections (002), (001), (100) and ($00\frac{1}{2}$) have been analyzed at two distinct temperatures at T=50 K and T=305 K where the film is purely AF and exhibits both magnetic phases (AF/FM), respectively. The (200) and ($\frac{1}{2}00$) reflection can not be observed here due to limitations in the experimental set up (Q-range of the experiment and blind spots of the superconducting magnet used for the experiment). Additionally the influence of a magnetic field applied along the b-axis was investigated by measuring the film at 0 T and 1 T (see Fig. 5.38 and Fig. 5.39).

In the polarized neutron diffraction measurements without magnetic field the out-of-plane reflections (002) and (001) exhibit identical intensities in the NSF channels with no intensities in the SF channel. Moreover, no changes of these behaviors can be observed with temperature indicating a pure nuclear contribution to their intensities.

The in-plane (100) reflection also shows identical intensity in both NSF channels for both temperatures indicating once more a nuclear contribution to the (100) peak intensity. In the SF channel, on the other hand, intensity can be only observed at high temperatures which shows that a FM order is formed with components of the magnetic moments oriented in the out-of-plane direction.

For the ($00\frac{1}{2}$) reflection the intensities in the SF and NSF channel are identical. This behavior does not change with temperature. Only an overall decrease in the intensities for higher temperatures can be observed. The identical intensities of both SF and NSF channels show that components of the magnetic moments along the a- and b-axis contribute to the scattering intensity of the ($00\frac{1}{2}$) reflection.

The same series of polarized measurements were carried out with an applied field of 1 T along the b-axis and is shown in Fig. 5.39. At T=50 K no differences to the polarization analysis without magnetic field can be observed. The polarized measurements at T=305 K, on the other hand, show significant differences when a magnetic field is applied. The (002) reflection has still intensity in both NSF channels but at a field of 1 T a slight splitting between both channels is now present. A more significant splitting of the NSF channels can be seen for the (001) reflection. Here, the intensity of one channel increases drastically while the intensity of the other NSF channel disappears in the background signal. The splitting in the NSF channels indicates a FM order with components of the magnetic moments oriented along the in-plane direction.

For the (100) reflection again the strong SF channel can be observed. The NSF channels, on the other hand, split under the application of a magnetic field. The intensity observed in the SF channel as well as the splitting of the NSF channels is a strong indication that the FM order possess now components of the magnetic moments which are oriented along the in-plane as well as the out-of-plane direction.

For the ($00\frac{1}{2}$) reflection the application of the magnetic field leads at T=305 K to an increase of the SF intensity while the NSF intensity decreases. Still both components of the magnetic moments along the a- and b-axis contribute to the AF order but now the contribution of the components perpendicular to the applied field is much stronger.

In summary of the polarized and unpolarized neutron diffraction investigations on the influence of the film thickness on the magnetic behavior of the $Fe_{50}Pt_{40}Rh_{10}$ film one can

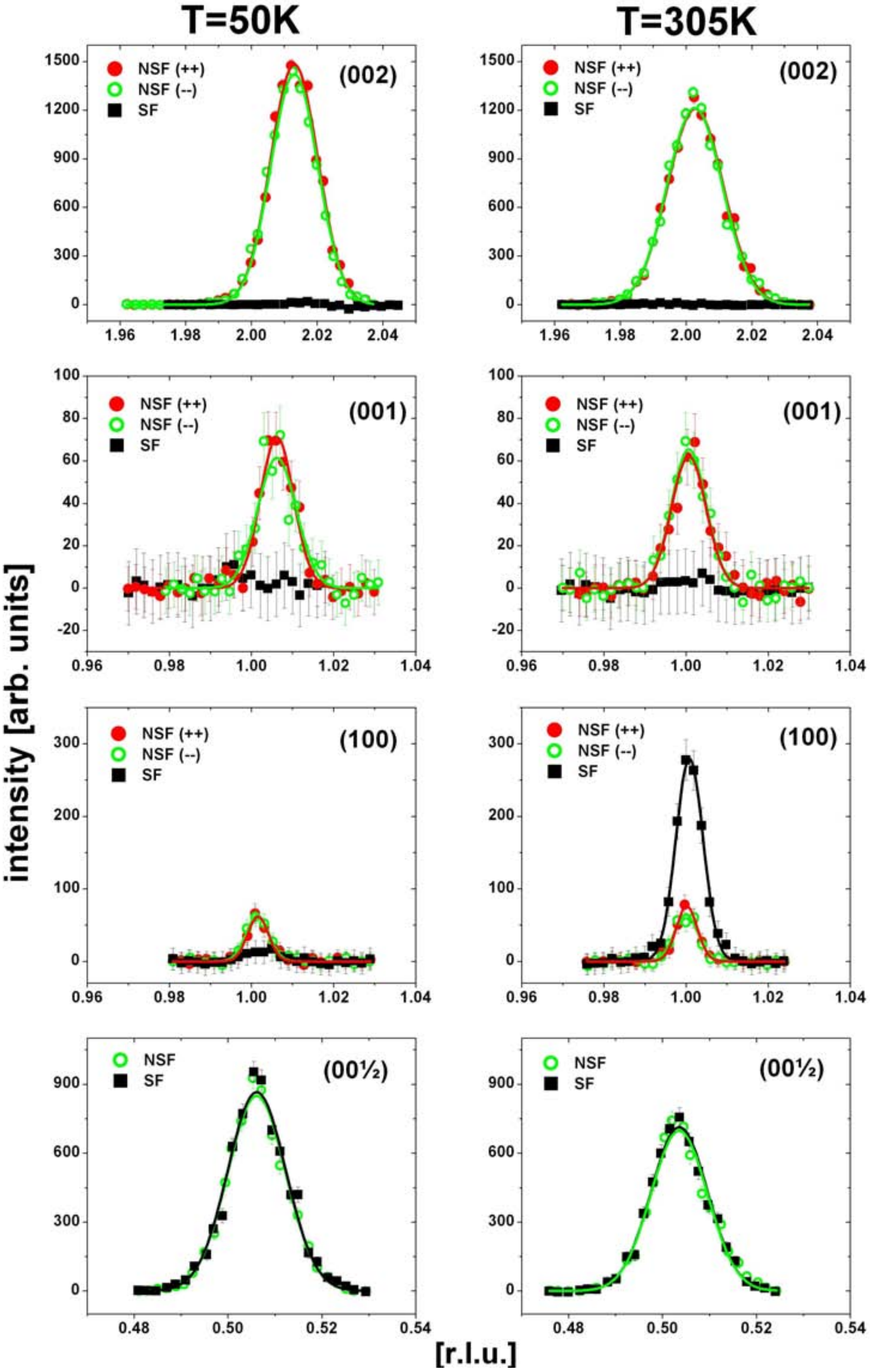

Figure 5.38.: Polarization analysis of the 500 nm $Fe_{50}Pt_{40}Rh_{10}$ film for the (002), (001), (100) and $(00\frac{1}{2})$ reflection at T=50 K and T=305 K.

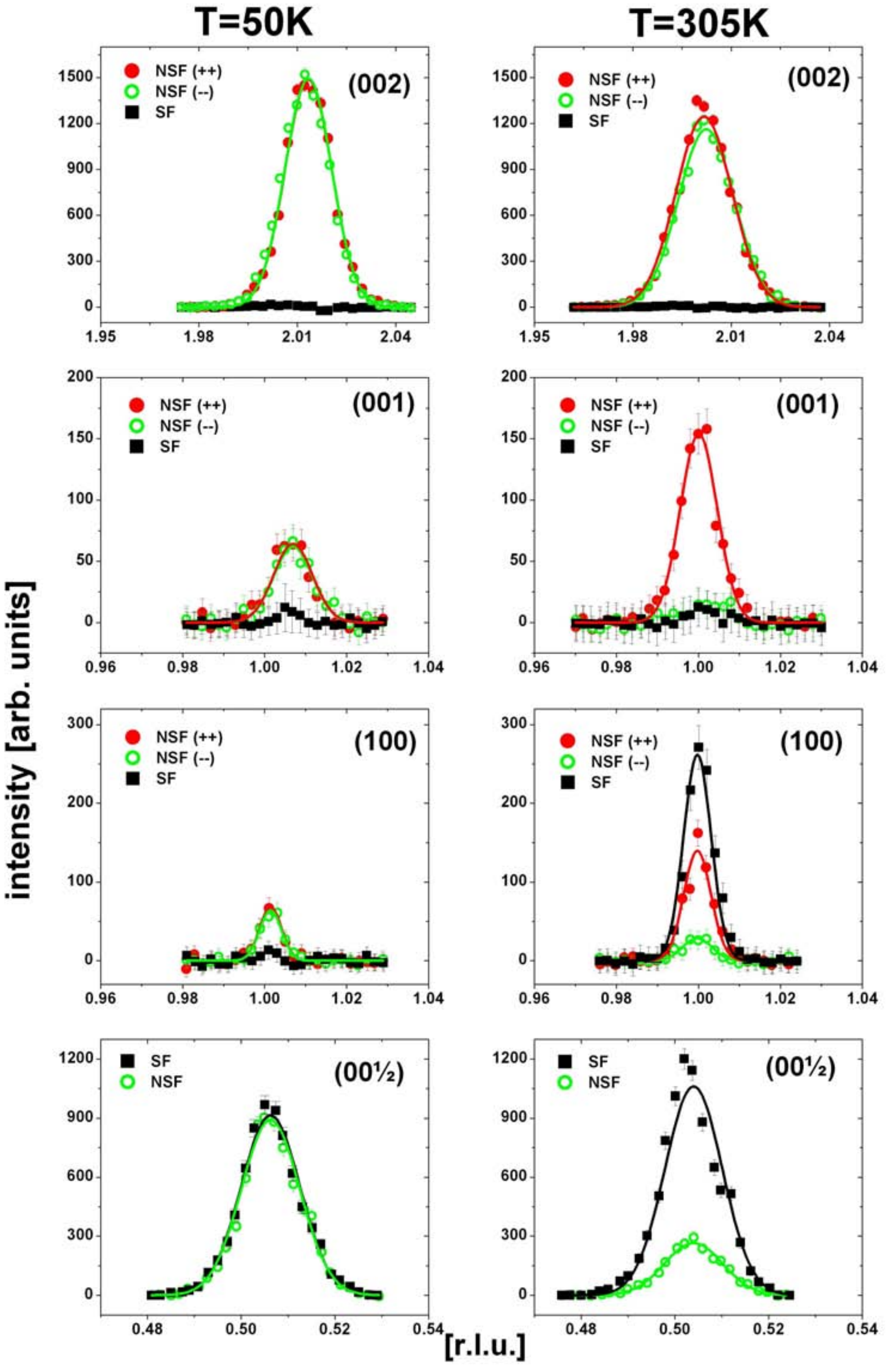

Figure 5.39.: Polarization analysis of the 500 nm $Fe_{50}Pt_{40}Rh_{10}$ film for the (002), (001), (100) and $(00\frac{1}{2})$ reflection at T=50 K and T=305 K within an applied field of 1 T.

conclude that the film thickness in the range from 100 nm to 500 nm has no significant influence on the magnetic order or the transition temperature. At low temperature an AF order with magnetic moments oriented in the in-plane direction can be observed in all three films while at high temperature a transition to a FM order with the magnetic moments dominantly oriented in the out-of-plane direction can be found. The only difference which can be attributed to the thickness is a faster decay of the integrated intensities of the half order reflections for the thicker films indicating an AF-FM transition in a smaller temperature range. Another effect of the film thickness is a higher scattering intensity of the thicker films due to the increased amount of scatterer in the beam.

The measurements with an applied magnetic field of 1 T showed that the field has no effect at low temperature when the films are in the AF state while at high temperature a FM order out-of-plane can be induced with the magnetic moments tilted in the in-plane direction.

The results are very similar to the one for the 200 nm thick $Fe_{50}Pt_{40}Rh_{10}$ film differing in higher transition temperatures for the half order reflections and the appearance of the (100) reflection in a smaller temperature interval. As already pointed out these differences can be explained by slight variations of the compositions. The measurements indicates slightly higher Rh concentrations for the films with different thicknesses.

5.5. Discussion

The neutron diffraction data together with structure factor calculations presented in the previous sections will be used in the following to develop models of the magnetic configurations of the different $Fe_{50}Pt_{50-x}Rh_x$ films. The neutron diffraction measurements give detailed information about the magnetic origin and the orientation of the magnetic moments in different crystallographic planes in the $Fe_{50}Pt_{50-x}Rh_x$ films, i.e. orientation of the magnetic moments in the in-plane (a-b-plane) or the out-of-plane (b-c-plane) direction (for more details see section 5.4). It allows in general to support models with different magnetic configurations if only the qualitative information retrieved from the measurements is considered. Therefore structure factor calculations are necessary to distinguish between these different configurations providing a quantitative measure of the observed intensities which can be compared to the experimental data. By the qualitative as well as quantitative comparison of the measured peak intensities with the structure factor calculations the magnetic configuration can be determined which supports the observed features of the neutron diffraction measurements. The calculations base on the magnetic unit cell of the bct $L1_0$ structure which is shown in Fig. 5.10 and consists of 8 Fe and 8 Pt/Rh atoms. For simplification it will be assumed that only the Fe atoms carry a magnetic moment. As already discussed in section 2 the Pt/Rh-atoms of FePt and FeRh alloys carry no magnetic moment in the AF phase. In the FM phase, however, an induction of magnetic moments on the Pt and Rh atoms, respectively, was proposed [35, 42] and can be therefore also expected for the $Fe_{50}Pt_{50-x}Rh_x$ films. As already pointed out in section 2.1 for the FePt film the induction can be explained by the 8 Fe nearest neighbors which surround one Pt/Rh atom. In the FM phase the magnetic moments of Fe have the same orientation which leads to a resulting magnetization at the Pt site and induces a magnetic moment on it. In the AF phase, on the other hand, the magnetic moments of the Fe atoms have opposite orientations which give a zero magnetization at the Pt site. For the development of a consistent model of the magnetic configuration it is here not mandatory to consider the induction at the Pt/Rh sites since it can be assumed that the

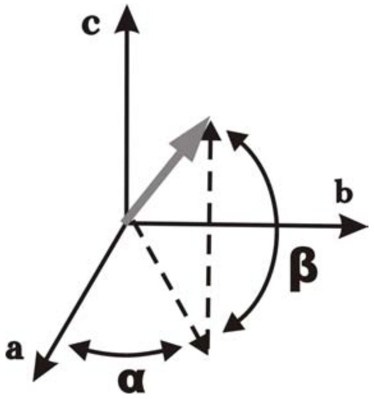

Figure 5.40.: In-plane and out-of-plane angles of the magnetic moment (gray arrow) to the a- and c-axis.

induced magnetic moments of the Pt/Rh atoms orient in the same direction of the Fe magnetic moments. As equations 5.16 and 5.17 show the additional magnetic moment will only reduce or increase the magnetic contribution to the scattering intensity in case of a first or second order reflection, respectively, but does not change the principle magnetic configuration. Taking these assumptions into account the following can be concluded using the equations 5.15 to 5.17:

1. Half order reflections are due to an AF order with a structure factor F given by:

$$F = 8p_{Fe} \tag{5.21}$$

2. First order reflections have a nuclear origin with a possible FM contribution:

$$\begin{aligned} F_+ &= 8(b_{Fe} - b_{Pt/Rh}) + 8p_{Fe} && (5.22)\\ F_- &= 8(b_{Fe} - b_{Pt/Rh}) - 8p_{Fe}. && (5.23)\end{aligned}$$

3. Second order reflections have the same magnetic origin as the first order reflections but in general a stronger nuclear contribution:

$$\begin{aligned} F_+ &= 8(b_{Fe} + b_{Pt/Rh}) + 8p_{Fe} && (5.24)\\ F_- &= 8(b_{Fe} + b_{Pt/Rh}) - 8p_{Fe}. && (5.25)\end{aligned}$$

The structure factors F_+ and F_- for the first and second order reflections consider the magnetic moments of the neutrons being parallel or antiparallel to the FM ordered magnetic moments of the sample. In case of unpolarized neutrons it can not be distinguished between both neutron states and the integrated intensity is given by: $\frac{1}{2}F_+^2 + \frac{1}{2}F_-^2$ while in the case of polarized neutrons a distinction is possible and the integrated intensity is given by: F_+^2 or F_-^2. For the structure factor calculations of the proposed magnetic configurations also the angles of the magnetic moments in respect to the a- and c-axis are taken into account (see Fig. 5.40). It is assumed that all magnetic moments have in general the same angles α and β due to the fourfold symmetry of the bct structure.

For the determination of the magnetic configuration also the tetragonal elongation of the crystallographic structure along the c-axis has to be considered, i.e. one has to distinguish between the in-plane and out-of-plane direction of the sample. The in-plane directions along the a- and b-axis, on the other hand, are in principle interchangeable due to the fourfold symmetry of the crystallographic structure as long as no external force, e.g. a magnetic field in the in-plane direction, is applied which removes this symmetry. One consequence is that the in-plane symmetry supports the presence of four different domains of equal probability. For simplicity the discussion will be here restricted to only one domain. In the other three domains the prospective proposed magnetic configuration is turned in-plane by 90°, 180° and 270°. In the following the 90° and 270° turned domains will be called perpendicular domains and the one in detail discussed here and the 180° turned domains will be named parallel domains. For the calculations it is assumed that all four domains contribute equally to the scattering signal and the integrated intensity can be calculated from the sum over all four domains. As a consequence of the different domains an in-plane reflection, e.g. $(\frac{1}{2}00)$, whose intensity is due to components of the magnetic moments in the in-plane direction has only contributions to two of the four domains, i.e. contributions of the parallel or the perpendicular domains. The magnetic moments in the other two domains have the same configuration but are turned 90° or 270°, respectively, and contribute to the intensity of the reflections in the other in-plane direction, e.g. $(0\frac{1}{2}0)$. Out-of-plane reflections and in-plane reflections with contributions of out-of-plane oriented magnetic moments have, on the other hand, contributions of all four domains to their scattering intensity.

Taking all these assumptions into account a model of the magnetic configuration can be developed which can be used together with the structure factor calculations and the neutron diffraction measurements to determine the in-plane and out-of-plane angles α and β of the magnetic moments as well as the strength of the magnetic order as will be shown in the following.

As already discussed before the integrated intensity is proportional to the structure factor: $I \propto F^2$. The structure factor of a magnetic reflection, on the other hand, includes a magnetic scattering length which is here expressed by $\widetilde{p}(T)$. This term is proportional to the magnetic scattering length p and a temperature dependent term which takes the strength of the magnetic order into account. For the description of the temperature dependence often a power law similar to equation 5.18 is used. Since the integrated intensity is proportional to $\widetilde{p}(T)$ it is a measure for the strength of a magnetic order and can be used to determine this strength as will be shown later.

The following discussion will be divided in two parts. In the first part a model of the magnetic configuration of the $\mathrm{Fe_{50}Pt_{50-x}Rh_x}$ films will be developed. Here, the temperature and magnetic field results will be discussed as well as the influence of the different $\mathrm{Fe_{50}Pt_{40}Rh_{10}}$ film thicknesses on the magnetic configuration and its evolution. The second part includes an explanation of the different magnetic configurations and transitions using a phenomenological model.

5.5.1. Discussion and Model (Temperature)

In this part the influence of the temperature on the magnetic properties and the magnetic configurations of the 200 nm thick $\mathrm{Fe_{50}Pt_{50-x}Rh_x}$ films will be discussed.

The neutron diffraction measurements showed for the films with x=5 and x=17.5 only a single magnetic state, i.e. a FM and an AF phase, respectively, until they become PM. The two films will be discussed first followed by the film with x=10 which showed a temperature driven transition between these two magnetic phases. The measurements of the film with x=25 reveal only AF order until the film becomes PM but indicate temperature

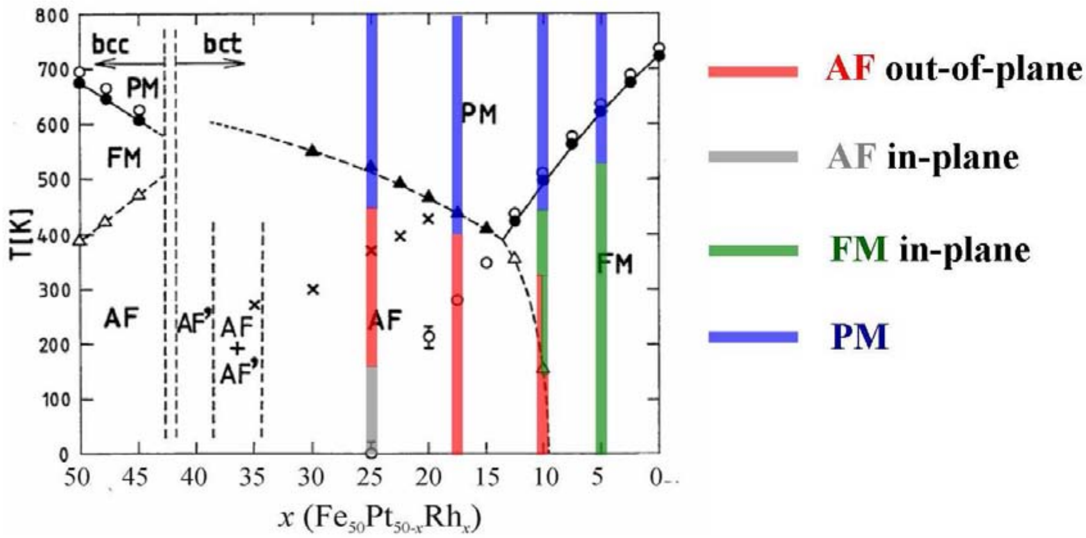

Figure 5.41.: Magnetic phase diagram of the $Fe_{50}Pt_{50-x}Rh_x$ system. The black plotted data are the values for the bulk system while the colored bars are the results of the 200 nm thick films.

driven transitions between different AF configurations. The results are summarized in the magnetic phase diagram in Fig. 5.41.

$Fe_{50}Pt_{45}Rh_5$

The neutron diffraction measurements of the $Fe_{50}Pt_{45}Rh_5$ film reveal only a FM order in the in-plane direction with the magnetic moments oriented along the c-axis. These results allow only one possible magnetic configuration which can be verified by structure factor calculations and is presented in Fig. 5.42.

It should be noted that the structure will be the same for all four domains and therefore only one domain is expected to contribute to the observed intensities. The magnetic configuration proposed here leads to the following structure factors:

$$F_{002} = 8(b_{Fe} + b_{Pt/Rh}) \tag{5.26}$$

$$F_{001} = 8(b_{Fe} - b_{Pt/Rh}) \tag{5.27}$$

$$F_{200} = F_{020} = 8(b_{Fe} + b_{Pt/Rh} \pm p_{Fe} \sin\beta) \tag{5.28}$$

$$F_{100} = F_{010} = 8(b_{Fe} - b_{Pt/Rh} \pm p_{Fe} \sin\beta) \tag{5.29}$$

$$F_{111} = \frac{2}{\sqrt{6}} \cdot 8(b_{Fe} - b_{Pt/Rh} \pm p_{Fe} \sin\beta) \tag{5.30}$$

$$F_{00\frac{1}{2}} = F_{\frac{1}{2}00} = F_{\frac{1}{2}\frac{1}{2}\frac{1}{2}} = 0. \tag{5.31}$$

The prefactor $\frac{2}{\sqrt{6}}$ considers the projection of the magnetic moments along the c-axis ([001]-direction in the reciprocal space) onto a plane perpendicular to the [111]-direction. The ± sign denotes the neutron spins being parallel or antiparallel to the magnetic moments of the film.

The FM order of the magnetic moments pointing along the c-axis reflects the fact that the in-plane first and second order reflections, (100) and (200), respectively, possess a magnetic contribution to the scattering intensity while the out-of-plane reflections (001) and (002) are purely nuclear. Only if the magnetic moments would have a non-zero angle

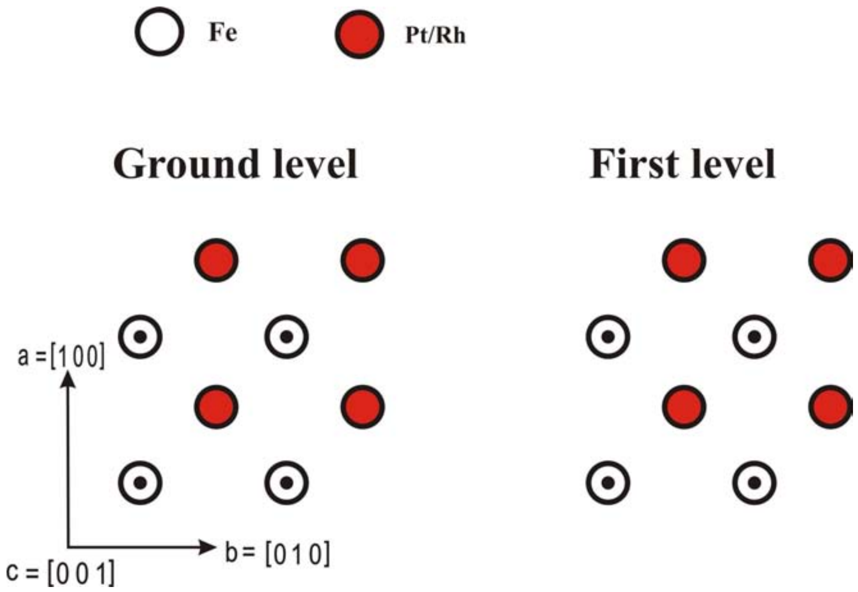

Figure 5.42.: Magnetic spin configuration of the $Fe_{50}Pt_{45}Rh_5$ film.

to the c-axis ($\beta \neq 90°$) the out-of-plane first and second order reflection would also have a magnetic contribution and a temperature behavior of the integrated intensities similar to the in-plane reflections. The structure factor calculations show that the proposed magnetic configuration is not only responsible for the magnetic contributions to the (200), (111) and (100) peak intensities, but also that magnetic contributions to the (020) and (010) peak intensity can be expected. The principle magnetic configuration outlined in Fig. 5.42 remains stable over the whole temperature range until the film becomes PM above T=500 K. In the FM regime the strength of the magnetic order decreases as expected with increasing temperature due to thermal fluctuations of the magnetic moments which is associated with the decay of the integrated intensity of the first and second order reflections along the [100]-direction.

In case of the FM ordered $Fe_{50}Pt_{45}Rh_5$ film the strength of the magnetic order can be expressed by the magnetic scattering length $\widetilde{p}(T)$ which can be determined by comparison of the integrated intensities of the pure nuclear Bragg reflection (002) and the (100) reflection whose intensity has a magnetic contribution from a FM order:

$$\frac{I_{002}}{I_{100}} = \frac{F_{002}^2}{F_{100}^2} = \frac{\left[8(b_{Fe} + b_{Pt/Rh})\right]^2}{8\left[(b_{Fe} - b_{Pt/Rh})^2 + \widetilde{p}_{Fe}^2(T))\right]}, \tag{5.32}$$

and subsequently:

$$\widetilde{p}_{Fe}(T) = \sqrt{\frac{I_{100}(b_{Fe} + b_{Pt/Rh})^2}{I_{002}} - (b_{Fe} - b_{Pt/Rh})}. \tag{5.33}$$

The results of this calculation are shown in Fig. 5.43.

The out-of-plane orientation of the magnetic moments also explains that in the measurements with polarization analysis of the $Fe_{50}Pt_{45}Rh_5$ film significant intensity was only found in the SF channel for the (100) reflection as well as identical intensity in both NSF channels for the (002) reflection. The increasing flipping ratio of the (200) reflection in Fig. 5.15, on the other hand, can be attributed to the decreasing FM order.

It should be noted that the model developed for the $\mathrm{Fe_{50}Pt_{45}Rh_5}$ film bases on the calculations of the magnetic scattering length $\widetilde{p}(T)$. The values of the magnetic scattering length have been calculated from the integrated intensity ratio of the (002) and (100) reflection. To show that the calculated model is not only valid for the (100) reflection the integrated intensity ratios of the (002) reflection and the (200) and (111) reflection, respectively, whose intensities include a magnetic contribution have been calculated (see Fig. 5.44). The data of the (002)/(100) ratio in Fig. 5.44 is shown only for the sake of completeness since here the calculated and the measured data match perfectly because the model bases on this ratio. For the (200) and (111) reflection the calculated ratio differs from the measured one but still shows the same temperature behavior. The slight difference which is almost within the error bars can be explained by different signal to noise ratios for each reflection. This can lead to an overrated or underrated intensity compared to the calculated one. The data, however, show that the model developed for the $\mathrm{Fe_{50}Pt_{45}Rh_5}$ film is not only valid for the (100) but also for the other magnetic reflections.

From the interpretation of the neutron diffraction data accordingly to the model presented here one can conclude that only one domain exists with the magnetic moments directed in the out-of-plane direction. The MOKE measurements indicate, on the other hand, that FM domains with opposite spin direction are present in the sample at zero magnetic field as it was observed in Co/Pt [94, 80] or Co/Pd multilayer [95]. This contradiction can be resolved by taking the penetration depths of the neutrons and photons into account. Since the laser light in the visible regime penetrates only a few nanometers (20 nm - 30 nm) into the sample [92, 93] it can be concluded that the different striped domains observed in the MOKE measurements are only surface effects and do not reflect the magnetic configuration inside the film.

$\mathbf{Fe_{50}Pt_{32.5}Rh_{17.5}}$

In contrast to the $\mathrm{Fe_{50}Pt_{40}Rh_{10}}$ the $\mathrm{Fe_{50}Pt_{32.5}Rh_{17.5}}$ film exhibits only a strong temperature dependent behavior for the half order reflections which are associated with an AF order while the first and second order reflections are quasi constant. The different half order reflections $(00\frac{1}{2})$, $(\frac{1}{2}00)$ and $(\frac{1}{2}\frac{1}{2}\frac{1}{2})$ indicate that the AF order is also present along both the in-plane and the out-of-plane direction. The application of structure factor calculations, as pointed out at the beginning of the section, leads to the model of the magnetic configuration shown in Fig. 5.45. In the proposed magnetic configuration components of the magnetic moments have an out-of-plane orientation along the c-axis at which the nearest neighbors have always opposite spin directions. This configuration gives an AF order in both in-plane directions, i.e. along the a- and b-axis, respectively. The in-plane components of the magnetic moments along the a-axis, on the other hand, are oriented in such a way that the resulting magnetic moments of the ground and first level have opposite sign which also leads to an AF order along the c-axis. Moreover, the components of the magnetic moments along the b-axis form an AF order along the a-axis. The

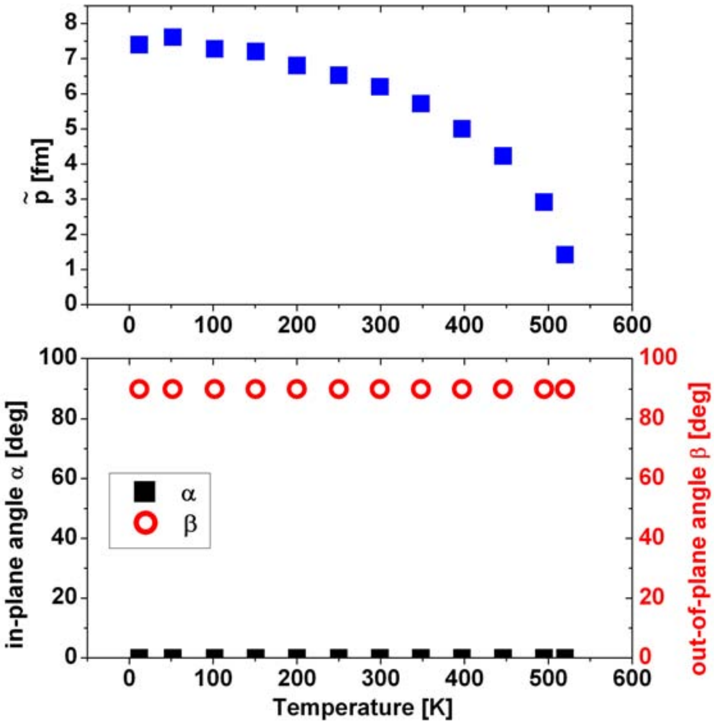

Figure 5.43.: Temperature dependence of the magnetic scattering length $\widetilde{p}(T)$ [upper panel] as well as the in-plane and out-of-plane angles α and β [lower panel] of the $Fe_{50}Pt_{45}Rh_5$ film.

corresponding structure factors for this magnetic configuration are thus given by:

$$F_{002} = F_{020} = F_{200} = 8(b_{Fe} + b_{Pt/Rh}) \tag{5.34}$$

$$F_{001} = F_{010} = F_{100} = 8(b_{Fe} - b_{Pt/Rh}) \tag{5.35}$$

$$F_{00\frac{1}{2}} = 8(p_{Fe}\cos\beta\sin\alpha) \tag{5.36}$$

$$F_{\frac{1}{2}00} = 8(p_{Fe}\cos\beta\cos\alpha) \tag{5.37}$$

$$F_{\frac{1}{2}\frac{1}{2}\frac{1}{2}} = \frac{2}{\sqrt{6}}\cdot 8(p_{Fe}\sin\beta) \tag{5.38}$$

$$F_{0\frac{1}{2}0} = 0 \tag{5.39}$$

Here, magnetic contributions can only be found in the half order reflections due to the AF orientation of the magnetic moments. The in-plane components of the magnetic moments which form the AF order along the a-axis are responsible for the intensity of the $(\frac{1}{2}00)$ reflection while the $(00\frac{1}{2})$ reflection is due to the AF order of the magnetic moments along the c-axis. The appearance of the $(\frac{1}{2}\frac{1}{2}\frac{1}{2})$ reflection indicates that a third AF order with the magnetic moments along the out-of-plane c-axis is necessary to explain the neutron diffraction data. It should be noted that the three half order reflections have contributions from different components of the magnetic moments. But since their integrated intensities show a similar temperature behavior it can be assumed that the different AF orders originate from the same domains which will be discussed in more detail later.

The in-plane angle α in the structure factors of the $Fe_{50}Pt_{32.5}Rh_{17.5}$ film can be determined by comparison of the half order reflections along the [001]- and [100]-direction since both reflections have the same dependencies on the out-of-plane components of the

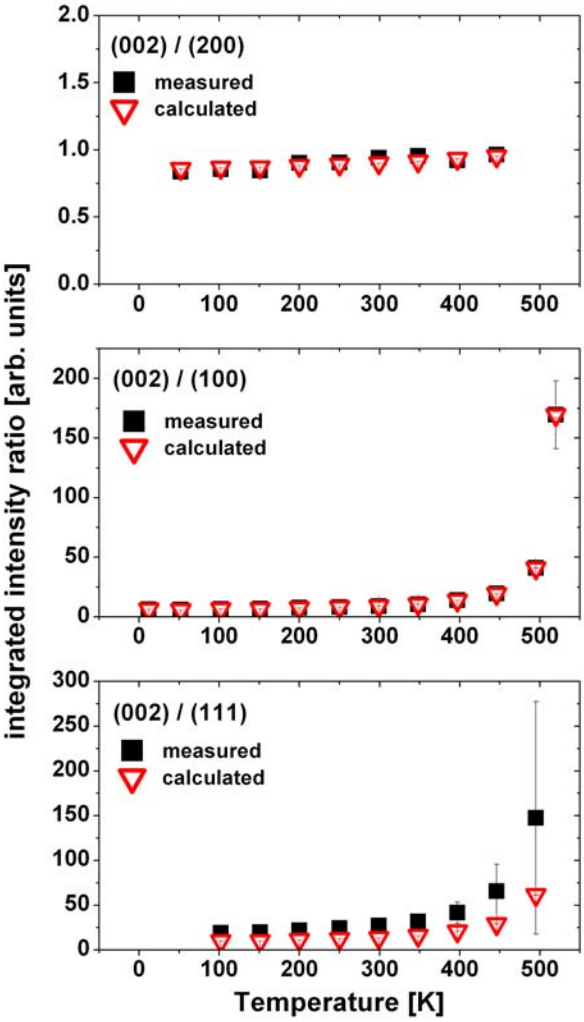

Figure 5.44.: Integrated intensity ratios of the (002) reflection and the (200), (100) and (111) reflection for the measured data (black squares) and the ratios calculated for the model of the $Fe_{50}Pt_{45}Rh_5$ film (red open triangles).

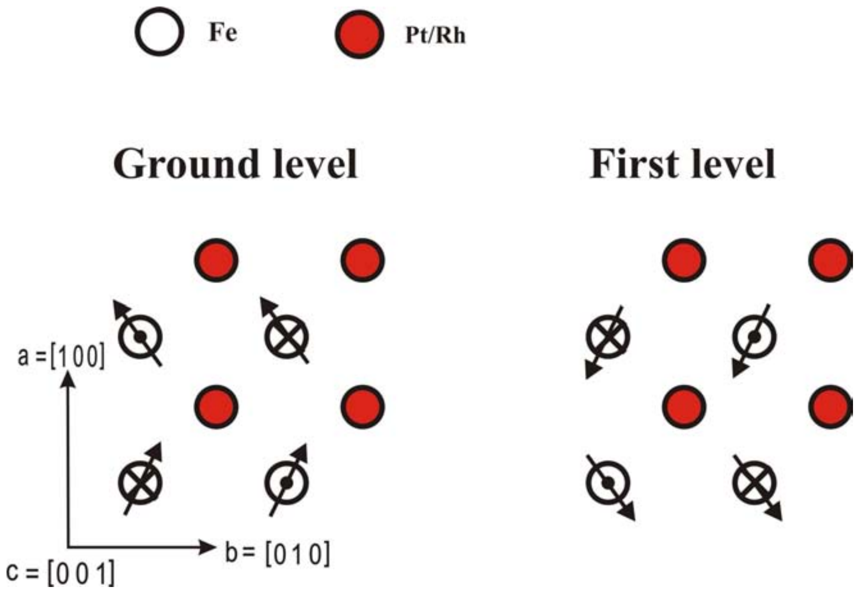

Figure 5.45.: Magnetic spin configuration of the $Fe_{50}Pt_{32.5}Rh_{17.5}$ film.

magnetic moments:

$$\frac{I_{00\frac{1}{2}}}{I_{\frac{1}{2}00}} = \frac{4F^2_{00\frac{1}{2}}}{2F^2_{\frac{1}{2}00}} = \frac{4(8\widetilde{p}_{Fe}(T)\cos\beta\sin\alpha)^2}{2(8\widetilde{p}_{Fe}(T)\cos\beta\cos\alpha)^2} = 2\tan^2\alpha \tag{5.40}$$

and solved for the in-plane angle α:

$$\alpha = \arctan\sqrt{\frac{I_{00\frac{1}{2}}}{2I_{\frac{1}{2}00}}}. \tag{5.41}$$

The factors 2 and 4 in the equation consider the different contributions from the parallel and perpendicular domains to the in-plane and out-of-plane reflections as already discussed before. Only the parallel domains contribute to the scattering intensity of the $(\frac{1}{2}00)$ reflection while all four domains contribute to the intensity of the $(00\frac{1}{2})$ reflection. The out-of-plane angle β, on the other hand, can be determined from the $(\frac{1}{2}\frac{1}{2}\frac{1}{2})$ reflection since its integrated intensity is due to components of the magnetic moments in the out-of-plane direction:

$$\frac{I_{\frac{1}{2}\frac{1}{2}\frac{1}{2}}}{I_{00\frac{1}{2}}} = \frac{F^2_{\frac{1}{2}\frac{1}{2}\frac{1}{2}}}{F^2_{00\frac{1}{2}}} = \frac{(\frac{2}{\sqrt{6}}\cdot 8\widetilde{p}_{Fe}(T)\sin\beta)^2}{(8\widetilde{p}_{Fe}(T)\cos\beta\sin\alpha)^2} = \frac{2}{3}\cdot\frac{\tan^2\beta}{\sin^2\alpha} \tag{5.42}$$

and consequently:

$$\beta = \arctan\sqrt{\frac{64I_{\frac{1}{2}\frac{1}{2}\frac{1}{2}}\sin^2\alpha}{\frac{256}{6}I_{00\frac{1}{2}}}}. \tag{5.43}$$

It should be noted that also the $(\frac{1}{2}\frac{1}{2}\frac{1}{2})$ reflections has contributions from all four domains. The calculated in-plane and out-of-plane angles are presented in Fig. 5.46 and show constant values for both angles over the whole temperature range ($\alpha \approx 64°$, $\beta \approx 20°$). The lower integrated intensities of the $(\frac{1}{2}00)$ and $(\frac{1}{2}\frac{1}{2}\frac{1}{2})$ reflections compared to the one of the $(00\frac{1}{2})$ reflections can not be only explained by the angles. For the comparison also the four domains and their different contributions to the reflections has to be considered as discussed before. For the $(\frac{1}{2}\frac{1}{2}\frac{1}{2})$ reflection additionally the projection of the magnetic moments on a plane perpendicular to the [111]-direction has to be taken in to account. Since the angles of the magnetic moments are constant the observed decays of the intensities must be due to the decreasing strength of the AF order. As already discussed before it is assumed that the different AF orders of the $Fe_{50}Pt_{32.5}Rh_{17.5}$ film are described by the same domains. With this assumption the strength of the magnetic order can be determined by the comparison of the nuclear Bragg peak (002) and the $(00\frac{1}{2})$ reflection which is due to an AF order:

$$\frac{I_{002}}{I_{00\frac{1}{2}}} = \frac{F_{002}^2}{F_{00\frac{1}{2}}^2} = \frac{\left[8(b_{Fe} + b_{Pt/Rh})\right]^2}{(8\widetilde{p}_{Fe}(T)\cos\beta\sin\alpha)^2}, \tag{5.44}$$

and solved for $\widetilde{p}_{Fe}(T)$:

$$\widetilde{p}_{Fe}(T) = \sqrt{\frac{I_{00\frac{1}{2}}(b_{Fe} + b_{Pt/Rh})^2}{I_{002}(\cos\beta\sin\alpha)^2}}. \tag{5.45}$$

The results of the calculations are presented in Fig. 5.46 and show the decrease of the AF order.

The AF orientation of the magnetic moments along the a-axis confirm that only intensity in the NSF channel can be detected in the polarization analysis of the $(\frac{1}{2}00)$ reflection. The observation of equal intensity in both NSF and SF channel for the $(00\frac{1}{2})$ reflection can be explained by the presence of four domains that contribute equally to the scattering intensity of the out-of-plane half order reflection. In the parallel domains only components of the magnetic moments along the a-axis can be observed which are responsible for the intensity in the SF channel. In the perpendicular domains, on the other hand, the magnetic structure is turned 90° and 270°, respectively, and the components of the magnetic moments are now aligned along the b-axis which leads to contributions in the NSF channel.

It should be noted once more that the model presented here consists of four domains, i.e. two parallel and two perpendicular domains, which contribute equally to the scattering intensity of the reflections. Since all three half order reflections show a similar temperature behavior of the integrated intensity it can be assumed that the different AF configurations can be described by the same domain as shown in fig. 5.45. Assuming a model with three different domains which are responsible for one of the AF reflections as it is shown in fig. 5.47 the integrated intensities of the half order reflections can be only explained by different domain sizes or by different strength of the individual AF order in the case of identical domain sizes which is very unlikely.

The model developed for the $Fe_{50}Pt_{32.5}Rh_{17.5}$ film bases on the calculations of the angles α, β and the magnetic scattering length $\widetilde{p}(T)$. In contrast to the $Fe_{50}Pt_{45}Rh_5$ film these parameters have been determined by the use of all measured magnetic reflections. The calculated and measured integrated intensity ratios of the (002) and $(00\frac{1}{2})$, $(\frac{1}{2}00)$ and $(\frac{1}{2}\frac{1}{2}\frac{1}{2})$ reflection, respectively, match therefore perfectly and the data in Fig. 5.48 is only shown for the sake of completeness.

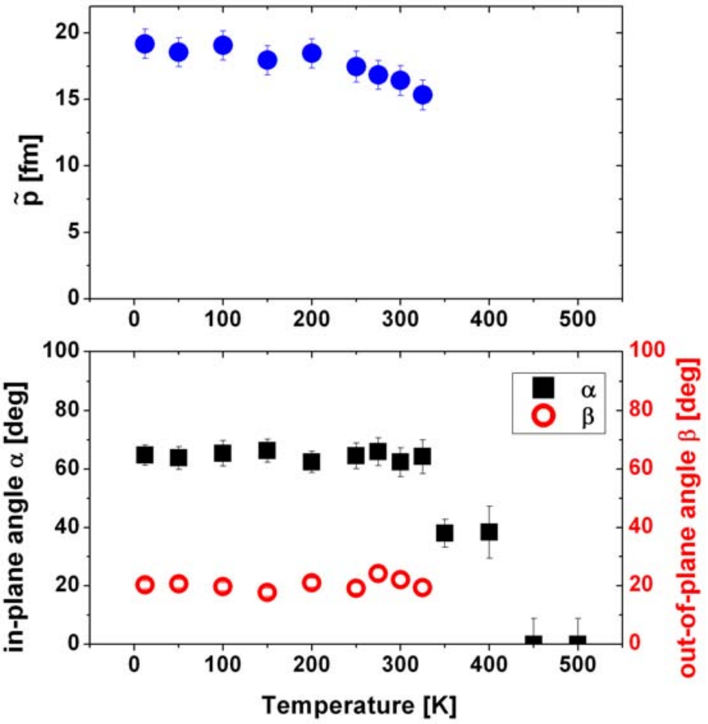

Figure 5.46.: Temperature dependence of the magnetic scattering length $\widetilde{p}(T)$ [upper panel] as well as the in-plane and out-of-plane angles α and β [lower panel] of the $Fe_{50}Pt_{32.5}Rh_{17.5}$ film.

$Fe_{50}Pt_{40}Rh_{10}$

The discussion of the $Fe_{50}Pt_{50-x}Rh_x$ films with x=5 and x=17.5 indicate that these films are in a single magnetic state and have therefore only one magnetic configuration until they become PM. The neutron diffraction measurements of the $Fe_{50}Pt_{40}Rh_{10}$ film, on the other hand, reveal a temperature driven AF-FM transition indicating that at least around the transition region two different magnetic configurations may coexist. The different magnetic configurations will be discussed in the following for selected temperature ranges. Below T<150 K, the neutron diffraction data show the same features as observed for the $Fe_{50}Pt_{32.5}Rh_{17.5}$ film. All three half order reflections can be observed which show a decay of the integrated intensity. The first and second order reflections exhibit again no significant intensity changes indicating the absence of any FM order. Therefore the magnetic configuration will resemble the one for the film with x=17.5 (see Fig. 5.49). The only differences are slightly higher and lower values of the in-plane and out-of-plane angles α and β, respectively (see Fig. 5.50).
At about T=150 K the integrated intensities of the (100) and (111) reflection rise and associated with that a FM order. The integrated intensities of the first and second order reflection along the [001]-direction, on the other hand, are constant. Taking the structure factor calculations and the results of the polarization analysis of the (100) reflection into account which showed a SF signal, the FM order can be attributed to be a FM order in the in-plane direction with components of the magnetic moments aligned along the c-axis. The AF configuration observed at low temperature is still present at T=150 K and the polarization analysis of the half order reflections shows similar results as for the film with x=17.5. The intensity in the NSF channel for the $(\frac{1}{2}00)$ reflection can

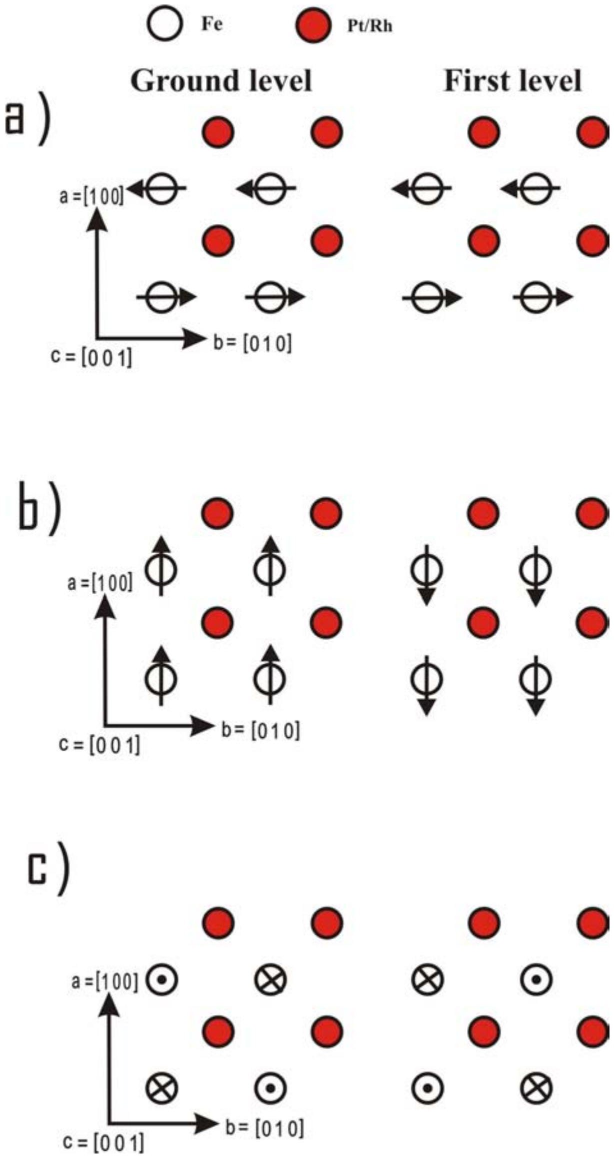

Figure 5.47.: Magnetic configuration of the $Fe_{50}Pt_{32.5}Rh_{17.5}$ film separated in different domains a), b) and c). Domain a) is responsible for the AF $(\frac{1}{2}00)$ reflection. Domain b) is responsible for the $(00\frac{1}{2})$ reflection and the intensity of the $(\frac{1}{2}\frac{1}{2}\frac{1}{2})$ reflection is caused by domain c).

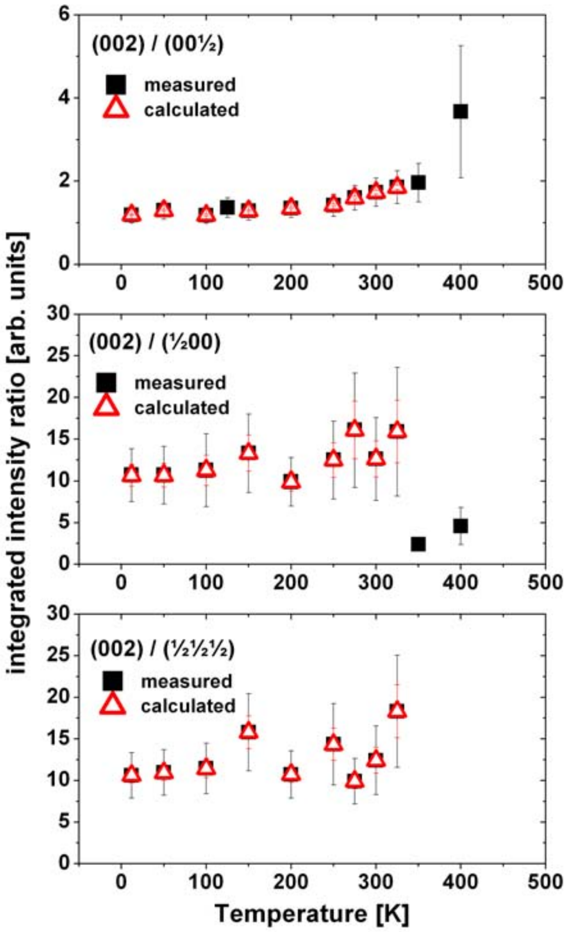

Figure 5.48.: Integrated intensity ratios of the (002) reflection and the $(00\frac{1}{2})$, $(\frac{1}{2}00)$ and $(\frac{1}{2}\frac{1}{2}\frac{1}{2})$ reflection for the measured data (black squares) and the ratios calculated for the model of the $Fe_{50}Pt_{32.5}Rh_{17.5}$ film (red open triangles).

be again explained by the alignment of components of the magnetic moments along the b-axis while the intensity of the NSF and SF channel for the $(00\frac{1}{2})$ reflection is due to the parallel and perpendicular domains. In contrast to the polarization analysis of the $Fe_{50}Pt_{32.5}Rh_{17.5}$ film an intensity difference between both the NSF and the SF channel can be observed which may indicate slightly different sizes of the parallel and perpendicular domains. The occurrence of the FM order in the in-plane direction can be explained by the nucleation of FM domains that replaces the AF domains. The AF and FM domains in this model have the same magnetic configuration as for the $Fe_{50}Pt_{32.5}Rh_{17.5}$ and the $Fe_{50}Pt_{45}Rh_{5}$ film, respectively (see Fig. 5.49). In the film with x=17.5 the parallel and perpendicular AF domains were homogeneous distributed. In the film with x=10 the polarized neutron diffraction measurements indicate that the homogeneous distribution is disturbed. A possible explanation for this observation is that the nucleation process of the FM domains takes place in a localized region of the film, i.e. the FM domains replace AF domains in the perpendicular or the parallel domains, resulting in different AF domain sizes.

The AF reflections $(00\frac{1}{2})$, $(\frac{1}{2}00)$ and $(\frac{1}{2}\frac{1}{2}\frac{1}{2})$ have a similar temperature behavior as it was observed in the $Fe_{50}Pt_{32.5}Rh_{17.5}$ film therefore it can be again assumed that the different AF configurations can be described by the same domains. A coexistence of the FM order and the AF order in one domain can be excluded due to the conflict of the AF order and the FM order in the in-plane direction which contribute to the integrated intensities of the $(\frac{1}{2}\frac{1}{2}\frac{1}{2})$ and the (100) reflection, respectively. A coexistence of both reflections as it is observed in the neutron diffraction measurements would not be possible. Due to these considerations the further discussion of the $Fe_{50}Pt_{40}Rh_{10}$ film will be restricted to the model with different domains being either in the AF or FM state.

In a temperature range between $150\,K<T<300\,K$ the integrated intensity of the (100) and (111) reflection increases to their maxima while the intensity of the half order reflections decreases until they vanish at different temperatures. The increase and decrease of the integrated intensities, respectively, can be attributed to the decay and growth of the AF and FM domains, respectively. The different transition temperatures of the half order reflections, on the other hand, can be explained by changes in the angles α and β. Considering the integrated intensities of the half order reflections and the equations 5.41 and 5.43 the results of the angels α and β shown in Fig. 5.50 can be derived. It can be seen that the magnetic moments turn in-plane with increasing temperature up to T=230 K when β becomes finally zero and the $(\frac{1}{2}\frac{1}{2}\frac{1}{2})$ reflection disappears. Starting at T=230 K, a further reorientation of the magnetic moments can be observed in the direction of the a-axis. At about T=252 K this process leads to an in-plane angle α of 90° and the disappearance of the $(\frac{1}{2}00)$ reflection. Now only the AF order in the out-of-plane direction remains with the magnetic moments aligned along the a-axis in the parallel domains and along the b-axis in the perpendicular domains.

Furthermore, at the temperature of T=300 K both NSF and SF channel of the $(00\frac{1}{2})$ reflection now show nearly identical intensity which indicates that the contributions of the parallel and perpendicular domains are quasi equal. A very likely explanation is that the FM domains are now homogeneously distributed and have replaced the same sizes of perpendicular and parallel AF domains.

At about T=330 K the $(00\frac{1}{2})$ reflection disappears and only the (100) reflection remains which is attributed to the complete replacement of the AF by the FM domains. The $Fe_{50}Pt_{40}Rh_{10}$ film is now in a single domain state until it becomes PM above T=400 K.

The observed intensity decays of the FM reflections, in particular the (100) reflection,

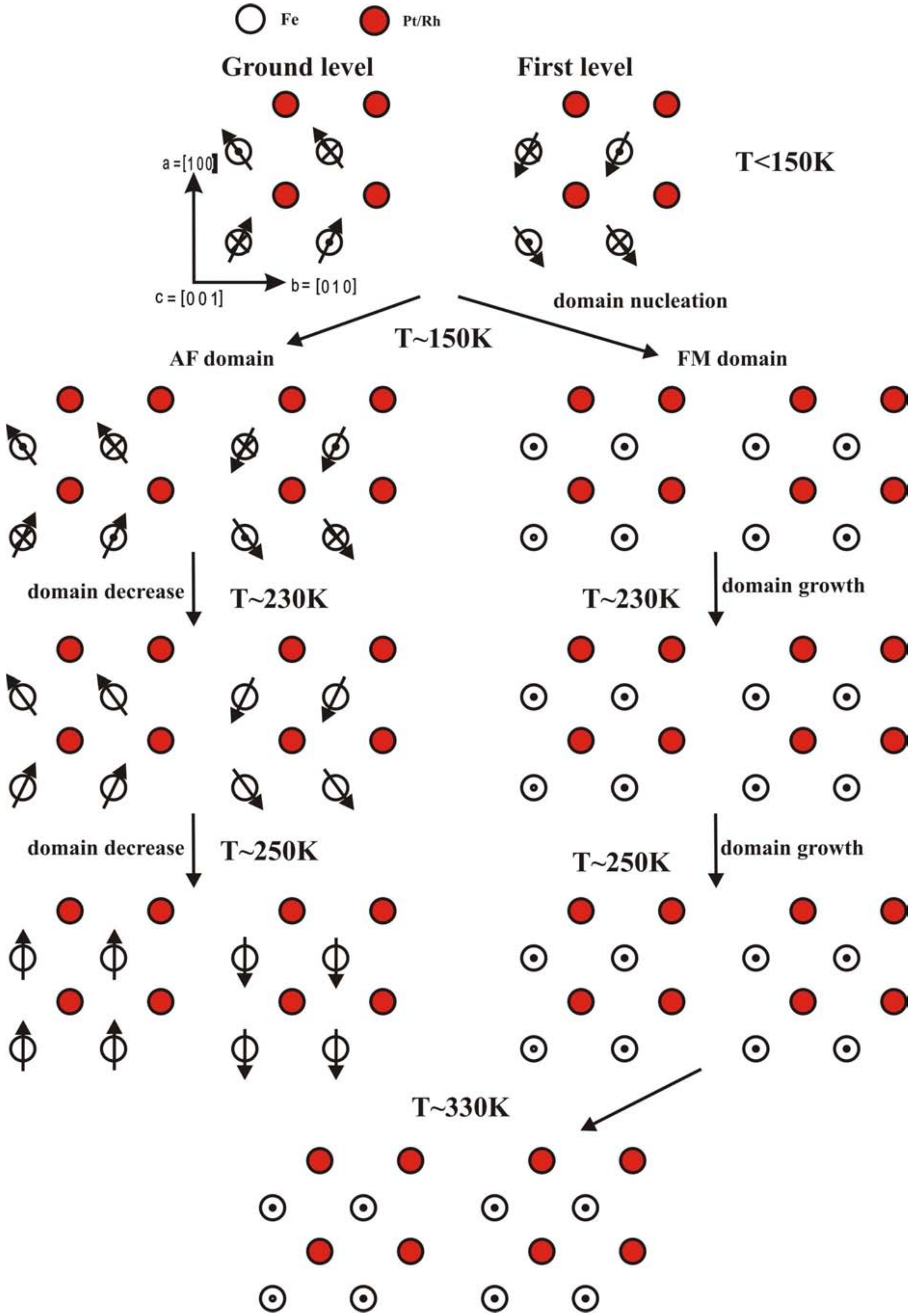

Figure 5.49.: Magnetic spin configuration of the $Fe_{50}Pt_{40}Rh_{10}$ film and its temperature evolution.

can not be explained by the domain replacement but by the decrease of the strength of the magnetic order. For the calculation of the magnetic scattering length $\widetilde{p}(T)$ which is a measure of the strength of the magnetic order in the system, here, both the AF and the FM domains have to be taken into account. The results are shown in Fig. 5.50 using the equations 5.45 and 5.33. The increase and decrease of the magnetic scattering length $\widetilde{p}(T)$ for the FM and AF domains, respectively, can again be attributed to the growth and decrease of the domain sizes. Taking the sum of the observed magnetizations of both domains the magnetic strength of the whole $\mathrm{Fe_{50}Pt_{40}Rh_{10}}$ film remains quasi constant up to T=300 K. For higher temperatures a decrease of the overall magnetic order can be found which is responsible for the observed intensity decays of the different reflections, in particular of the (100) reflection.

The model presented here of the $\mathrm{Fe_{50}Pt_{40}Rh_{10}}$ film bases on the angles α, β and the magnetic scattering length $\widetilde{p}(T)$ which have been calculated by the use of the integrated intensities of the AF $(00\frac{1}{2})$, $(\frac{1}{2}00)$, $(\frac{1}{2}\frac{1}{2}\frac{1}{2})$ and the FM (100) reflection. The calculated and measured ratios of the (002) reflection and these reflection match therefore perfectly as can be seen in Fig. 5.51. The calculated ratio of the (002) and (111) reflection, on the other hand, differs from the measured one. This can again be attributed to the different signal to noise ratios of the individual reflections and an overrated or underrated measured intensity compared to the calculated one. The measured and calculated data, however, show both the same temperature dependence. Both ratios decrease with increasing temperature up to about T=300 K before the ratio increases again. This behavior shows that the model developed here is not only valid for the reflections $(00\frac{1}{2})$, $(\frac{1}{2}00)$, $(\frac{1}{2}\frac{1}{2}\frac{1}{2})$ and (100) which are the basis of the model but also for other magnetic reflections.

$\mathbf{Fe_{50}Pt_{25}Rh_{25}}$

The neutron diffraction data of the $\mathrm{Fe_{50}Pt_{25}Rh_{25}}$ film reveal similar to the film with x=10 temperature driven magnetic transitions. In contrast to the $\mathrm{Fe_{50}Pt_{40}Rh_{10}}$ film these transitions occur here between different AF orders. The different AF configurations will be discussed in the following for selected temperature ranges.

Below T=150 K only the half order reflection along the [111]-direction is present and shows an intensity decay with increasing temperature. The first and second order reflections, on the other hand, are constant indicating the absence of FM order. The models of the $\mathrm{Fe_{50}Pt_{32.5}Rh_{17.5}}$ and the $\mathrm{Fe_{50}Pt_{40}Rh_{10}}$ film showed that the $(\frac{1}{2}\frac{1}{2}\frac{1}{2})$ reflection is due to out-of-plane components of the magnetic moments taking this into account the same can be assumed for the $(\frac{1}{2}\frac{1}{2}\frac{1}{2})$ reflection of the $\mathrm{Fe_{50}Pt_{25}Rh_{25}}$ film as it is shown in Fig. 5.52.

From about T=150 K intensity at the $(00\frac{1}{2})$ and $(\frac{1}{2}00)$ reflection can be observed and associated with this is the appearance of a different AF order. The integrated intensities of both reflections increase up to maxima at about T=300 K and T=350 K, respectively. The polarization analysis showed not only intensity in both the NSF and the SF channel for the $(00\frac{1}{2})$ reflection as it was found in the film with x=17.5 but also in the $(\frac{1}{2}00)$ reflection. It indicates that the magnetic moments aligned along the b- and c-axis form an AF order in the in-plane direction along the a-axis and contribute to the intensity of the $(\frac{1}{2}00)$ reflection. The intensity of the $(00\frac{1}{2})$ reflection, on the other hand, is due to components of the magnetic moments along the a-axis which form an AF order in the out-of-plane direction. Considering the increase and decrease of the integrated intensities of the $(00\frac{1}{2})$, $(\frac{1}{2}00)$ and $(\frac{1}{2}\frac{1}{2}\frac{1}{2})$ reflections, respectively, and the coexistence of these peaks

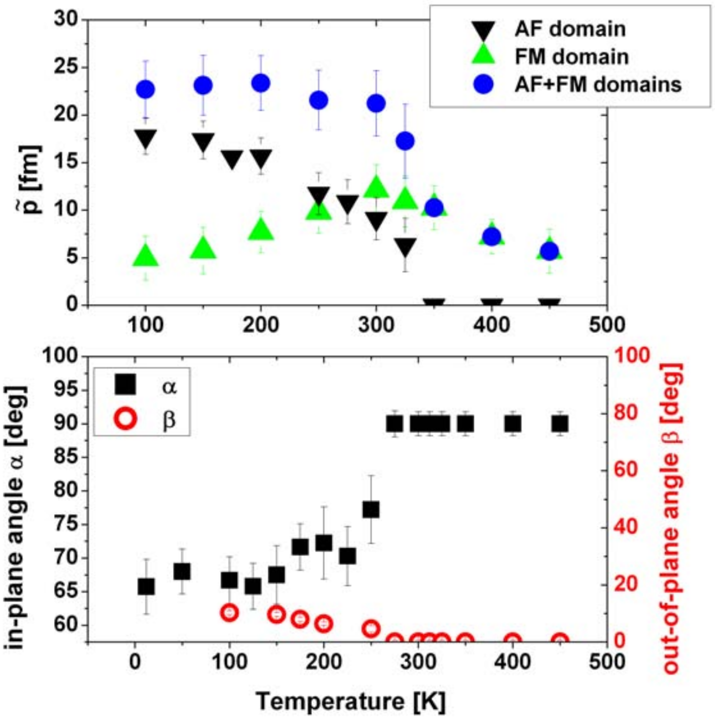

Figure 5.50.: Temperature dependence of the magnetic scattering length $\widetilde{p}(T)$ [upper panel] and the in-plane and out-of-plane angles α and β [lower panel] of the $Fe_{50}Pt_{40}Rh_{10}$ film. Note: only the angles of the AF domain are shown since in the FM domain all magnetic moments are oriented in the out-of-plane direction ($\beta = 90°$).

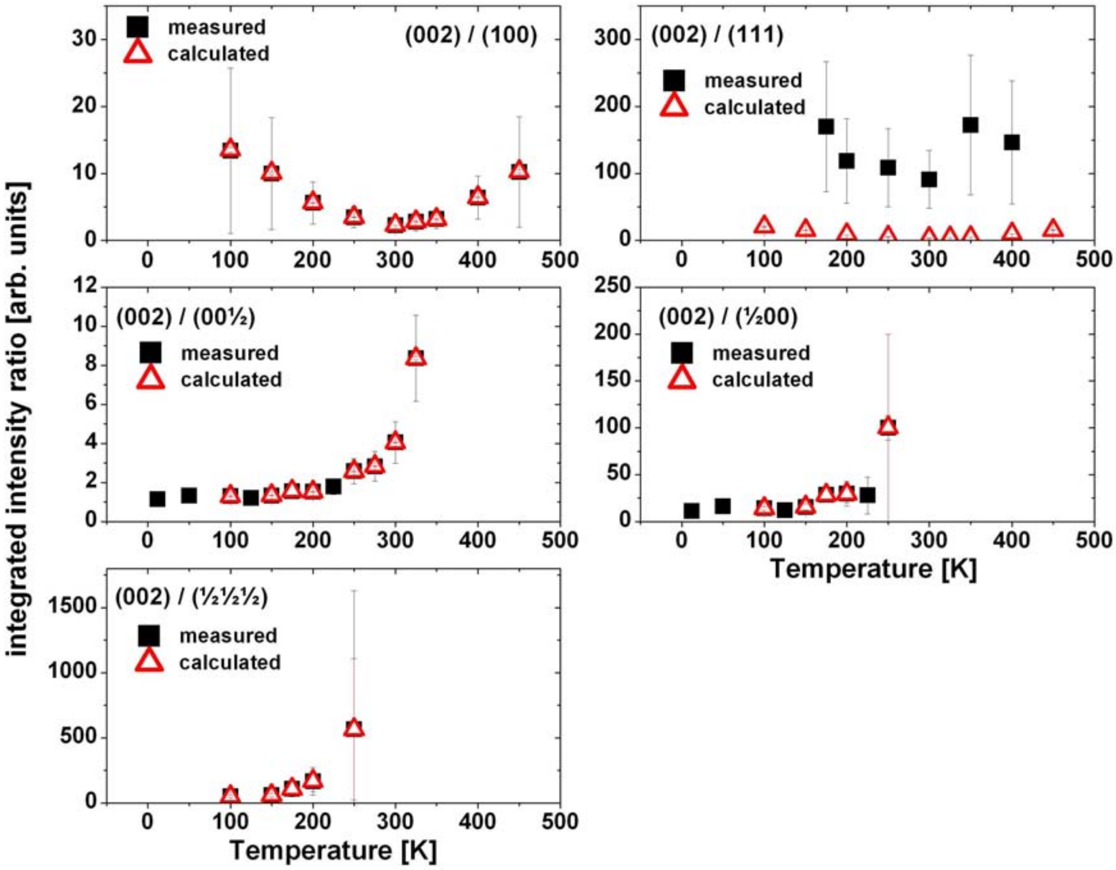

Figure 5.51.: Integrated intensity ratios of the (002) reflection and the FM (100) and (111) reflection as well as the AF $(00\frac{1}{2})$, $(\frac{1}{2}00)$ and $(\frac{1}{2}\frac{1}{2}\frac{1}{2})$ reflections for the measured data (black squares) and the ratios calculated for the model of the $Fe_{50}Pt_{40}Rh_{10}$ film (red open triangles).

over a temperature range between T=150 K and T=300 K, the presence of two different domains can be expected. The AF order responsible for the $(\frac{1}{2}\frac{1}{2}\frac{1}{2})$ peak intensity can be associated with one domain which will be called in the following domain *I* and the AF order responsible for the other half order reflections $(00\frac{1}{2})$ and $(\frac{1}{2}00)$, respectively, is present in a different domain named in the following domain *II*. The decay and increase of the integrated intensities of the half order reflections can be thus explained by the nucleation and growth of domain *II* which substitutes domain *I*. This process is completed at about T=275 K where only domain *II* remains in the film. It should be noted that domain *I* is a single domain while domain *II* represent four equivalent domains, i.e. two parallel and two perpendicular domains, as it was already discussed before. These domains are again responsible for the identical intensity of the SF and NSF channel of the $(00\frac{1}{2})$ reflection.

Another strong indication of the presence of two different domains is the out-of-plane component of the magnetic moments observed for the $(\frac{1}{2}00)$ reflection. These components form alternating FM layers along the a-axis which contribute to the peak intensity of the $(\frac{1}{2}00)$ reflection but not to the $(\frac{1}{2}\frac{1}{2}\frac{1}{2})$ reflection due to destructive interference. Since this AF order of the $(\frac{1}{2}00)$ reflection is in conflict with the AF order that is responsible for the peak intensity of the $(\frac{1}{2}\frac{1}{2}\frac{1}{2})$ reflection both AF orders can not coexist in the same domain. The integrated intensities of the $(00\frac{1}{2})$ and $(\frac{1}{2}00)$ reflection, on the other hand, show a similar temperature behavior and it can be assumed that their AF configuration originates from the same domains. Therefore the model of two different domains will be used for the further discussion of the magnetic configuration. Considering both domains the following structure factors can be derived:

$$\begin{aligned}
F_{002} = F_{020} = F_{200} &= 8(b_{Fe} + b_{Pt/Rh}) && (5.46)\\
F_{001} = F_{010} = F_{100} &= 8(b_{Fe} - b_{Pt/Rh}) && (5.47)\\
F_{00\frac{1}{2}} &= 8(p_{Fe}\cos\beta\sin\alpha) && (5.48)\\
F_{\frac{1}{2}00} &= 8(p_{Fe}\cos\beta\cos\alpha + p_{Fe}\sin\beta) && (5.49)\\
F_{\frac{1}{2}\frac{1}{2}\frac{1}{2}} &= \frac{2}{\sqrt{6}}\cdot 8(p_{Fe}\sin\beta) && (5.50)\\
F_{0\frac{1}{2}0} &= 0. && (5.51)
\end{aligned}$$

The decrease and growth of the different domains is not sufficient to explain all observed temperature features of the integrated intensities. In particular it can not explain the different maxima of the half order reflections in domain *II* nor the change in the NSF to SF ratio of the $(\frac{1}{2}00)$ reflection with temperature. Therefore also a reorientation of the magnetic moments in domain *II* must take place. This is reflected in the in-plane and out-of-plane angles α and β. It is important to note that the calculation of the angles differs from the other films due to the out-of-plane components of the magnetic moments that contribute to the $(\frac{1}{2}00)$ peak intensity. This fraction can be determined from the polarization analysis of the half order in-plane reflection by comparison of the NSF and the SF intensity leading to the expression:

$$\frac{I_{00\frac{1}{2}}}{xI_{\frac{1}{2}00}} = \frac{4F^2_{00\frac{1}{2}}}{2F^2_{\frac{1}{2}00}} = \frac{4(8\widetilde{p}_{Fe}(T)\cos\beta\sin\alpha)^2}{2(8\widetilde{p}_{Fe}(T)\cos\beta\cos\alpha)^2} = 2\tan^2\alpha, \qquad (5.52)$$

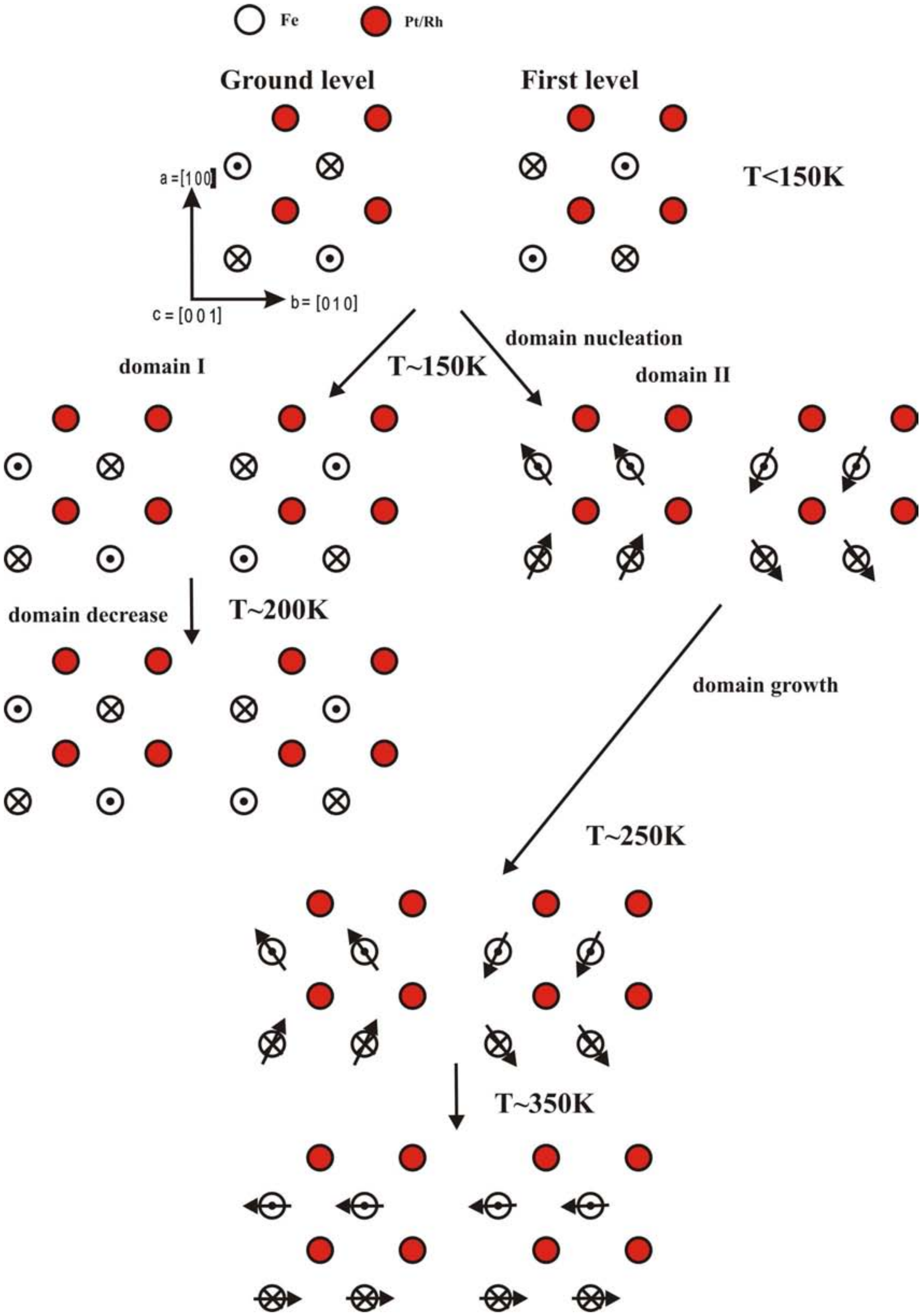

Figure 5.52.: Magnetic spin configuration of the $Fe_{50}Pt_{25}Rh_{25}$ film and its temperature evolution.

and can be solved for the in-plane angle α:

$$\alpha = \arctan\sqrt{\frac{I_{00\frac{1}{2}}}{2xI_{\frac{1}{2}00}}} \tag{5.53}$$

Here x denotes the fraction of the intensity which is due to in-plane components of the magnetic moments. The out-of-plane angle β is then given by:

$$\frac{xI_{\frac{1}{2}00}}{(1-x)I_{\frac{1}{2}00}} = \frac{F^2_{\frac{1}{2}00_{in}}}{F^2_{\frac{1}{2}00_{out}}} = \frac{(8\widetilde{p}_{Fe}(T)\cos\beta\cos\alpha)^2}{(8\widetilde{p}_{Fe}(T)\sin\beta)^2} = \frac{\cos^2\alpha}{\tan^2\beta}, \tag{5.54}$$

and solved for β:

$$\beta = \arctan\sqrt{\frac{(1-x)\cos^2\alpha}{x}} \tag{5.55}$$

$F^2_{\frac{1}{2}00_{out}}$ and $F^2_{\frac{1}{2}00_{in}}$ denote the structure factors of the out-of-plane and in-plane components of the magnetic moments. The results of the angle calculation presented in Fig. 5.53 show that the out-of-plane angle β increases with the temperature and associated with it the contribution of the in-plane AF order with the magnetic moments aligned in the out-of-plane direction. It is responsible for the increase of the SF intensity of the polarization analysis of the $(\frac{1}{2}00)$ reflection relative to the NSF channel. The in-plane angle α, on the other hand, decreases with the temperature until at about T=354 K the magnetic moments have no components anymore along the a-axis. The observed overall decreases of the intensity of the half order reflections $(00\frac{1}{2})$ and $(\frac{1}{2}00)$ at higher temperatures can be explained by the decreasing strength of the magnetic order. The values of the magnetic scattering length $\widetilde{p}(T)$ in the case of the $Fe_{50}Pt_{25}Rh_{25}$ film can be determined from the sum of the scattering length of domain *I* and *II*. The magnetic scattering length $\widetilde{p}(T)$ of domain *I* is given by:

$$\frac{I_{\frac{1}{2}\frac{1}{2}\frac{1}{2}}}{I_{002}} = \frac{F^2_{\frac{1}{2}\frac{1}{2}\frac{1}{2}}}{F^2_{002}} = \frac{(\frac{2}{\sqrt{6}}\cdot 8\widetilde{p}_{Fe}(T))^2}{\left[8(b_{Fe}+b_{Pt/Rh})\right]^2} \tag{5.56}$$

and consequently:

$$\widetilde{p}_I(T) = \sqrt{\frac{I_{\frac{1}{2}\frac{1}{2}\frac{1}{2}}\left[8(b_{Fe}+b_{Pt/Rh})\right]^2}{\frac{256}{6}I_{002}}}. \tag{5.57}$$

The magnetic scattering length of domain *II* can be determined by:

$$\frac{I_{\frac{1}{2}00}}{I_{002}} = \frac{2F^2_{\frac{1}{2}00}}{4F^2_{002}} = \frac{2\left[8(\widetilde{p}_{Fe}\cos\beta\cos\alpha + \widetilde{p}_{Fe}(T)\sin\beta)\right]^2}{4\left[8(b_{Fe}+b_{Pt/Rh})\right]^2}, \tag{5.58}$$

and solved for $\widetilde{p}_{Fe}(T)$:

$$\widetilde{p}_{II}(T) = \sqrt{\frac{2I_{\frac{1}{2}00}(b_{Fe}+b_{Pt/Rh})^2}{I_{002}(\cos\beta\cos\alpha+\sin\beta)^2}}. \tag{5.59}$$

The results are shown in Fig 5.53. The decrease and increase of $\widetilde{p}(T)$ for domain *I* and *II*, respectively, can be explained by the decrease and growth of the different AF domains. Taking the sum of both domains an unexpected increase of $\widetilde{p}(T)$ can be observed in a temperature range from T=150 K up to T=250 K. Associated with it is an increase of the

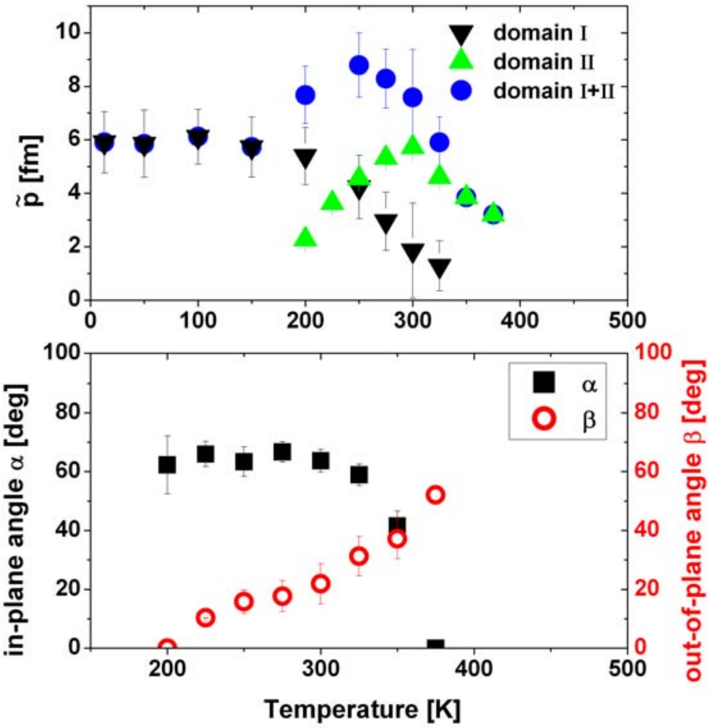

Figure 5.53.: Temperature dependence of the magnetic scattering length $\widetilde{p}(T)$ [upper panel] as well as the in-plane and out-of-plane angles α and β [lower panel] of the $Fe_{50}Pt_{25}Rh_{25}$ film. Note: only the angles of domain *II* are shown since in domain *I* all magnetic moments are oriented in the out-of-plane direction ($\beta = 90°$).

magnetic strength. The reason for this behavior is not known at the present stage. A possible explanation would be a different value of the magnetic moment for the different AF configurations of domain *I* and *II*. Similar to the different magnetic moment observed in the Q_1- and Q_2-phase of $FePt_3$ [34] (see section 2.1). Above T=250 K the strength of the magnetic order decreases again which is responsible for the decay of $\widetilde{p}(T)$.
The model of the magnetic configuration for the $Fe_{50}Pt_{25}Rh_{25}$ film bases on the integrated intensities of the AF reflections $(00\frac{1}{2})$, $(\frac{1}{2}00)$ and $(\frac{1}{2}\frac{1}{2}\frac{1}{2})$. These intensities have been used to calculate the angles α, β and the magnetic scattering length $\widetilde{p}(T)$. It is important to note that in contrast to the other films the angle β has been calculated only by the use of the intensity of the $(\frac{1}{2}00)$ reflection (see equation 5.54). As a consequence the calculated and measured $(002)/(\frac{1}{2}00)$ ratio matches perfectly (see Fig. 5.54). The same is true for the integrated intensity ratio of the (002) and $(\frac{1}{2}\frac{1}{2}\frac{1}{2})$ reflection since all values of domain *I* base on this ratio. The $(002)/(00\frac{1}{2})$ ratio is calculated considering both angles α, β and the magnetic scattering length $\widetilde{p}(T)$. The calculated ratio differs only slightly from the measured one and shows that all parameters, in particular the angle β, are well defined and are able to describe the temperature behavior of the $(002)/(00\frac{1}{2})$ ratio. The almost perfect match of the data indicates here again that the magnetic configuration of the $Fe_{50}Pt_{25}Rh_{25}$ film is not only valid for the magnetic reflections used to develop the model but also for all other magnetic reflections.

In summary of this section one can conclude that the 200 nm thick $Fe_{50}Pt_{45}Rh_5$ and the $Fe_{50}Pt_{32.5}Rh_{17.5}$ film are in a single magnetic state with only one magnetic configuration

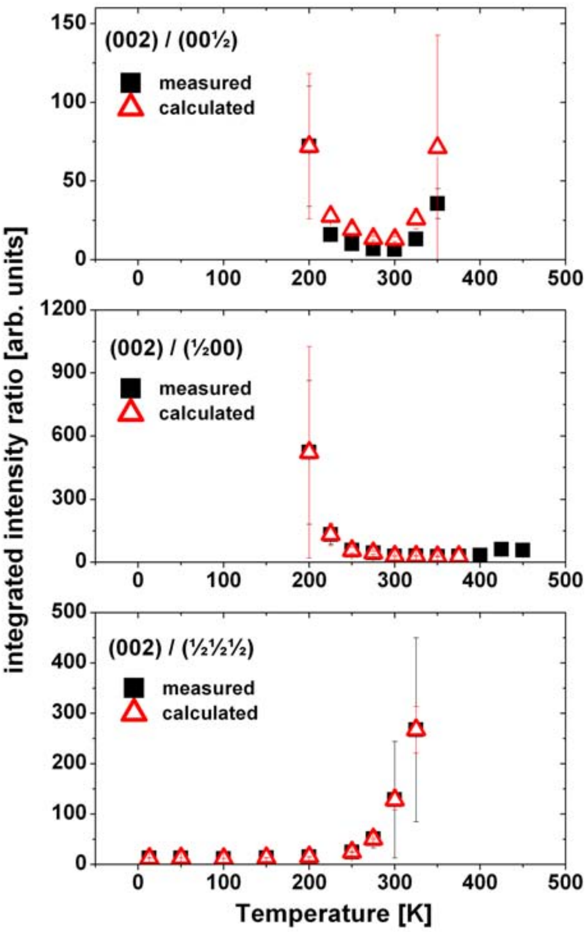

Figure 5.54.: Integrated intensity ratios of the (002) reflection and the $(00\frac{1}{2})$, $(\frac{1}{2}00)$ and $(\frac{1}{2}\frac{1}{2}\frac{1}{2})$ reflection for the measured data (black squares) and the ratios calculated for the model of the $Fe_{50}Pt_{25}Rh_{25}$ film (red open triangles).

	x=5	x=10	x=17.5	x=25
$F_{00\frac{1}{2}}$	0	$8p_{Fe}\sin\alpha\cos\beta$	$8p_{Fe}\sin\alpha\cos\beta$	$8p_{Fe}\sin\alpha\cos\beta$
$F_{0\frac{1}{2}0}$	0	0	0	0
$F_{\frac{1}{2}00}$	0	$8p_{Fe}\cos\alpha\cos\beta$	$8p_{Fe}\cos\alpha\cos\beta$	$8p_{Fe}\cos\alpha\cos\beta+$ $8p_{Fe}\sin\beta$
$F_{\frac{1}{2}\frac{1}{2}\frac{1}{2}}$	0	$\frac{16}{\sqrt{6}}p_{Fe}\sin\beta$	$\frac{16}{\sqrt{6}}p_{Fe}\sin\beta$	$\frac{16}{\sqrt{6}}p_{Fe}\sin\beta$
$F_{\frac{1}{2}\frac{1}{2}0}=$ $F_{\frac{1}{2}0\frac{1}{2}}=$ $F_{0\frac{1}{2}\frac{1}{2}}$	0	0	0	0
F_{001}	$8(b_{Fe}-b_{Pt/Rh})$	$8(b_{Fe}-b_{Pt/Rh})$	$8(b_{Fe}-b_{Pt/Rh})$	$8(b_{Fe}-b_{Pt/Rh})$
$F_{010}=$ F_{100}	$8(b_{Fe}-b_{Pt/Rh}+$ $p_{Fe}\sin\beta)$	$8(b_{Fe}-b_{Pt/Rh}+$ $p_{Fe}\sin\beta)$	$8(b_{Fe}-b_{Pt/Rh})$	$8(b_{Fe}-b_{Pt/Rh})$
F_{111}	$\frac{2}{\sqrt{6}}\cdot 8(b_{Fe}-$ $b_{Pt/Rh})+p_{Fe}\sin\beta)$	$\frac{2}{\sqrt{6}}\cdot 8(b_{Fe}-$ $b_{Pt/Rh})+p_{Fe}\sin\beta)$	$\frac{2}{\sqrt{6}}\cdot 8(b_{Fe}-$ $b_{Pt/Rh})$	$\frac{2}{\sqrt{6}}\cdot 8(b_{Fe}-$ $b_{Pt/Rh})$

Table 5.7.: Structure factors for the parallel domains of the proposed magnetic configurations of the different $Fe_{50}Pt_{50-x}Rh_x$ films.

(FM for x=5 and AF for x=17.5) until they become PM. The $Fe_{50}Pt_{40}Rh_{10}$ film shows a temperature driven transition between these two magnetic configurations. The neutron diffraction measurements of the $Fe_{50}Pt_{25}Rh_{25}$ film reveal also magnetic transitions but here between different AF order. The magnetic transitions in both films can be explained by the nucleation and growth of FM and AF domains, respectively, with temperature.

The decreases of the integrated intensity of the magnetic reflections in the four films can be explained by temperature effects. Thermal fluctuations of the magnetic moments reduce their correlation and associated with this the strength of the magnetic order.

It should be kept in mind that the calculations of the angles α and β as well as the magnetic scattering length $\widetilde{p}(T)$ base on the relative integrated intensities of the different reflections. For the correction of the Q-dependence of the magnetic moment the values of Fe was used. Therefore the actual magnetic form factor of the different $Fe_{50}Pt_{50-x}Rh_x$ alloys can differ from the used one and associated with that the relative integrated intensities. The proposed magnetic configurations, however, will change only slightly as long as the values differ not too drastic from the one of Fe.

The FM configuration proposed here with the magnetic moments directed out-of-plane along the c-axis that leads to the (100), (200) and (111) reflections was also theoretically proposed for the FePt alloy [99]. For the FeRh alloy three different AF configurations were theoretically proposed [100]: An AF configuration where the magnetic moments of the nearest neighbors point in different directions (see fig. 5.47 domain c)), a configuration where the magnetic moments of the first and ground level have opposite spin directions (see fig. 5.47 domain b)) and an AF configuration of the magnetic moments along the a-axis, where the magnetic moments of the first and the ground level have the same orientation (see fig. 5.47 domain a)). The first AF configuration is responsible for the $(\frac{1}{2}\frac{1}{2}\frac{1}{2})$ reflection in the model presented here for the $Fe_{50}Pt_{50-x}Rh_x$ alloys while the latter give intensity for the $(00\frac{1}{2})$ and $(\frac{1}{2}00)$ reflections, respectively. It should be noted that for the FeRh alloys these different configurations do not coexist in one alloy. They have different energy minima and therefore different probabilities depending on the lattice constants [100].

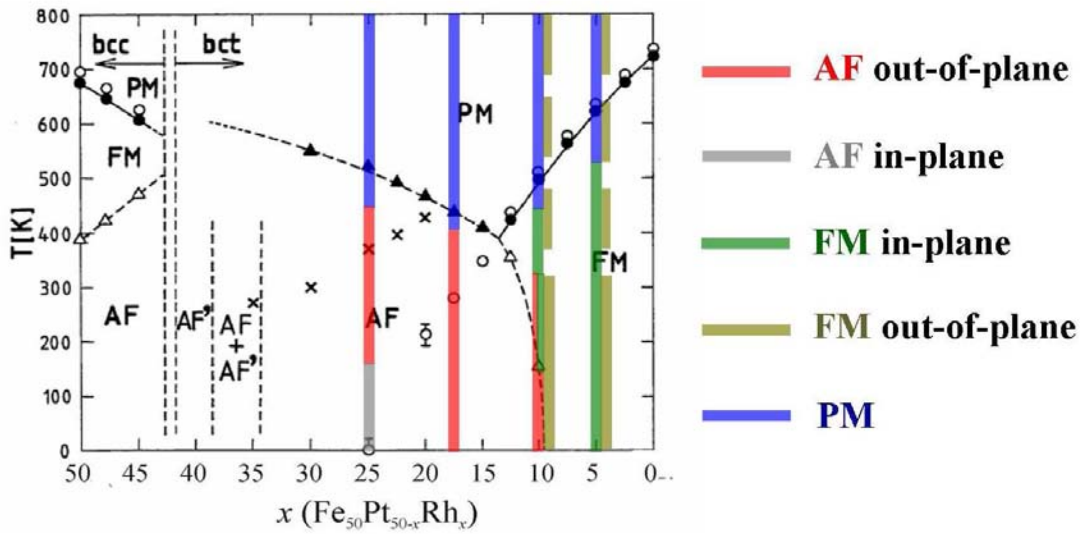

Figure 5.55.: Magnetic phase diagram of the different $Fe_{50}Pt_{50-x}Rh_x$ films. The grey plotted data are the values for the bulk system while the colored bars are the results of the 200 nm thick films with the application of an external magnetic field.

5.5.2. Discussion and Model (Magnetic Field)

The neutron diffraction measurements of the $Fe_{50}Pt_{32.5}Rh_{17.5}$ and the $Fe_{50}Pt_{25}Rh_{25}$ sample showed that both AF ordered films are not affected by the application of magnetic fields up to 10 T and 3.5 T, respectively. The neutron data of the $Fe_{50}Pt_{45}Rh_{10}$ and the $Fe_{50}Pt_{45}Rh_5$ film, on the other hand, reveal an induction of a FM out-of-plane order when the field is applied in-plane. The results of the magnetic field application are summarized in Fig. 5.55. In the following the change of the magnetic configuration will be discussed in more detail, taking into account the results of the structure factor calculations.

$Fe_{50}Pt_{45}Rh_5$

The neutron diffraction measurements of the $Fe_{50}Pt_{45}Rh_5$ film revealed that without a magnetic field the magnetic moments point along the c-axis associated with a FM contribution to the intensity of the (100) reflection. When a magnetic field is applied in-plane along the a-axis the integrated intensities of the (001) and (100) reflection increases and decreases, respectively, which can be attributed to a reorientation of the magnetic moments in the field direction as already discussed before (see Fig. 5.56). Since the field is directed parallel to the scattering vector $\vec{Q}$ for the (100) reflection only components of the magnetic moments perpendicular to it can be detected and consequently the reorientation in field direction leads to a decay of its intensity. The reorientation of the magnetic moments is also confirmed by the polarization analysis. Without an external magnetic field both NSF channels of the (002) reflection have identical intensity while under the application of a magnetic field a splitting of both NSF channels can be observed which is caused by the in-plane components of the magnetic moments. The intensity in the SF channel of the (100) reflection, on the other hand, is due to the still present out-of-plane components of the magnetic moments.

From the neutron diffraction data it can not be distinguished between the scenario of a continuous turning of the moments or a nucleation and growth of domains with magnetic

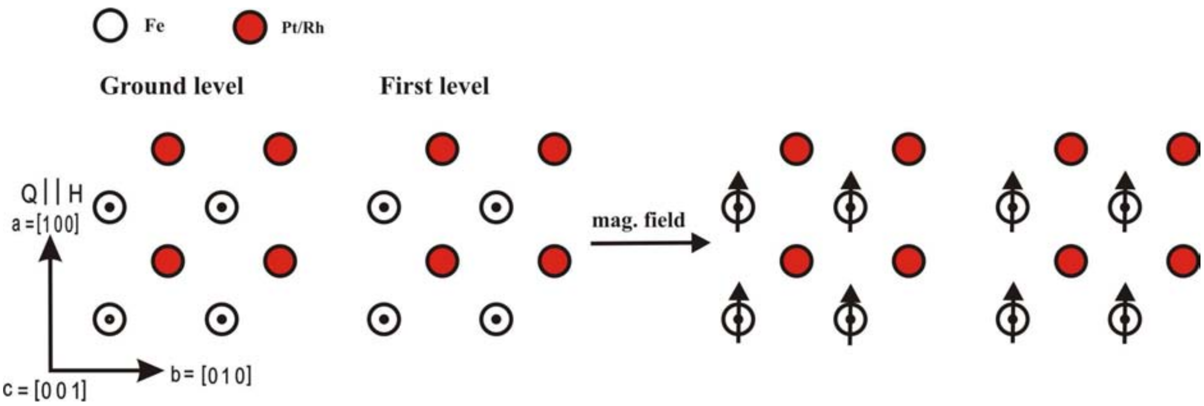

Figure 5.56.: Magnetic configuration of the $Fe_{50}Pt_{45}Rh_5$ film when a magnetic field is applied parallel to the a-axis.

moments oriented along the field.
No saturation of the $Fe_{50}Pt_{45}Rh_5$ film is reached for fields up to 3.5 T. For a temperature of T=250 K a saturation field of about 6 T can be extrapolated from the decay of the integrated intensity of the (100) reflection.

$Fe_{50}Pt_{40}Rh_{10}$

The $Fe_{50}Pt_{40}Rh_{10}$ film showed without the application of a magnetic field intensity changes of the (100) reflection and the half order reflections which were attributed to the presence of different domains, i.e. domains with FM order and domains with an AF order. The other peak intensities were quasi constant. The neutron diffraction measurements with an external magnetic field applied in the in-plane direction along the b-axis, show similar to the film with x=5 an intensity increase of the (001) reflection but also a slight increase of the (100) peak intensity. This behavior can be explained by the reorientation of the magnetic moments in the in-plane direction along the applied field. In the FM domain the reorientation is similar to the $Fe_{50}Pt_{45}Rh_5$ film. The magnetic moments turn from the out-of-plane to the in-plane direction (see Fig. 5.57). In contrast to the $Fe_{50}Pt_{45}Rh_5$ film the scattering vector $\vec{Q}$ for the (100) reflection is here perpendicular to the external field and both components of the magnetic moments can be detected. As a consequence the integrated intensity of the peak would not be influenced by the reorientation. Therefore the observed increase of the intensity must be associated with a change of the magnetic moments in the AF domain forming a FM order. This assumption can be confirmed by the intensity decreases of the half order reflections $(00\frac{1}{2})$ and $(\frac{1}{2}00)$ with the magnetic field. The neutron diffraction measurements of the half order reflection at a certain temperature showed that the integrated intensities of both reflections vanish at different values of the magnetic field. It indicates that the reorientation of the magnetic moments is a continuous process and not a nucleation of FM domains which replaces the AF order. Otherwise the integrated intensities should disappear at the same values of the magnetic field. By the continuous reorientation of the magnetic moments in field direction the components along the b-axis form a FM order along the a- and c-axis while components of the magnetic moments along the a-axis are still AF ordered along the c-axis (see Fig. 5.58). The FM order along the a- and c-axis leads to an additional magnetic contribution to the intensities of the (001) and (100) reflections and explains the observed intensity increase of the (100) peak.

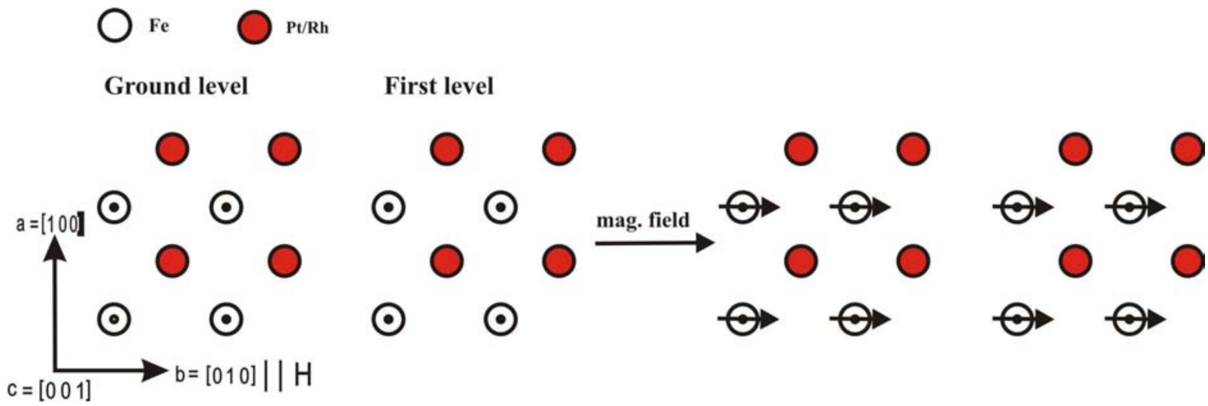

Figure 5.57.: Magnetic configuration of the $Fe_{50}Pt_{40}Rh_{10}$ film in the FM domains when a magnetic field is applied parallel to the b-axis.

The comparison of the $Fe_{50}Pt_{40}Rh_{10}$ and the $Fe_{50}Pt_{45}Rh_5$ film showed that the film with x=5 is in a single domain state and that by the application of an external magnetic field the magnetic moments orient in its direction. The film with x=10 exhibits two different domains with AF and FM order, respectively. The magnetic moments in the FM domain behave similar to the one of the film with x=5. The magnetic moments in the AF domains, on the other hand, orient continuously in the field direction providing an additional magnetic contribution to the first order reflections. This additional FM contribution increases with the temperature and is responsible for the observed intensity increase of the first order reflection with the temperature at a certain magnetic field (see Fig. 5.29).

5.5.3. Discussion and Model (Film Thickness)

The neutron diffraction measurements of the $Fe_{50}Pt_{40}Rh_{10}$ films with thicknesses from 100 nm to 500 nm show similar results for the half, first and second order reflections along the [001]- and [100]-direction as for the previously discussed 200 nm thick film. Therefore also the magnetic configurations will resemble the one determined for the 200 nm thick $Fe_{50}Pt_{40}Rh_{10}$ film (see Fig. 5.49). As already discussed in the section 5.4.3 the only differences are higher transition temperatures and thus the nucleation of the FM domain takes place at higher temperatures and a smaller temperature range for the AF-FM transition. The shift of the temperature behavior can be attributed to slight differences in the Rh concentrations of both sample series.

The decay of the integrated intensities of the half order reflections indicate a slower decrease for the thinner films as is expected for a second order transition. The slower decay is also reflected in the higher values of the critical exponents for the thinner films. The result is in good agreement with the investigations by Yuasa who found a first order AF-FM transition in the bulk $Fe_{50}Pt_{40}Rh_{10}$ system [17]. The transition temperature of about T=150 K determined for the bulk system is also in good agreement with the nucleation temperature of the FM domains observed for the 200 nm thick film while the 100 nm, 300 nm and 500 nm thick films have a nucleation temperature of about T=250 K. Considering the magnetic phase diagram of the bulk system and the higher nucleation temperature of the FM domains it indicates a Rh concentration of about 11% instead of

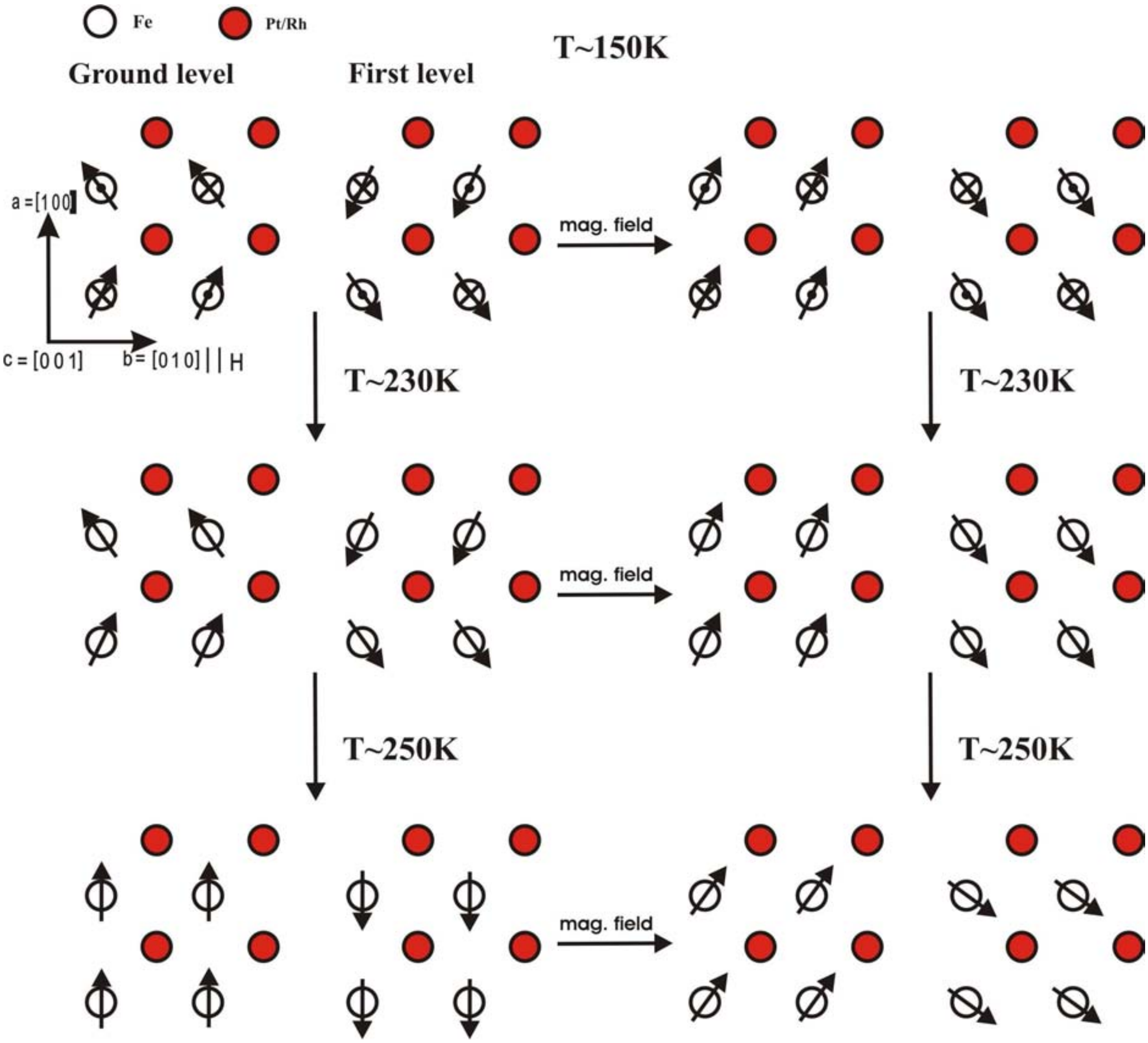

Figure 5.58.: Temperature dependence of the magnetic configuration of the $Fe_{50}Pt_{40}Rh_{10}$ film in the AF domains when a magnetic field is applied parallel to the b-axis.

10%.

The polarization analysis of the 500 nm thick $Fe_{50}Pt_{40}Rh_{10}$ film with an external applied magnetic field indicate similar to the 200 nm thick film a reorientation of the magnetic moments in field direction. The intensity splitting of the NSF channels of the first and second order reflections as well as the intensity difference between the SF and the NSF channel of the $(00\frac{1}{2})$ reflection showed that in the FM and the AF domains a reorientation of the magnetic moments in field direction takes place. In the latter case the applied magnetic field leads to a symmetry breaking. The effect of the magnetic field is more significant on the perpendicular domains than for the parallel domains due to the smaller angle of the magnetic moments to the applied field.

As already discussed before a reduction of the magnetic ordering temperature with decreasing thickness as it is observed in several FM and AF systems [101, 102] due to finite size effects can not be observed for the $Fe_{50}Pt_{40}Rh_{10}$ films with thicknesses down to 100 nm. Even $Fe_{50}Pt_{50-x}Rh_x$ films with thicknesses of about 6 nm studied recently with macroscopic techniques, e.g. vibrating sample magnetometer and super conducting interference device, by Hasegawe at al. [103] showed similar magnetic ordering temperatures as observed in this work.

It should be noted that the thickness of 6 nm is beyond the feasibility of neutron diffraction experiments at today's neutron facilities. The limit of the thickness for the $Fe_{50}Pt_{50-x}Rh_x$ films can be determined from the signal to noise ratio of the raw data of the (100) reflections at about T=330 K. This ratio decreases from 3.6 for the 500 nm thick film to 2.9 for the 300 nm film down to 1.4 for the 100 nm thickness. This indicates a film thickness of about 50 nm as the limit for neutron diffraction experiments on these samples at today's instruments and neutron facilities.

5.5.4. Theoretical Discussion

As mentioned in the introduction the magnetic moments of the Fe atoms in FeRh systems with equiatomic composition are oriented in the in-plane direction without any considerable crystallographic anisotropy. In FePt compounds, however, the magnetic moments are oriented dominantly in the out-of-plane direction. Obviously the magnetic anisotropy depends strongly on the composition and in particular on the elements which are used in the alloy with the Fe compound. The question arising here is what kind of anisotropy is responsible for the observed transitions and thus leads to the magnetic configurations in the $Fe_{50}Pt_{50-x}Rh_x$ alloys which were observed in this work.

The transition from a dominant AF order along the in-plane to the out-of-plane direction or to a dominant FM order in the in-plane direction with decreasing Rh concentration will be described in the following by a phenomenological model. The isotropic Heisenberg exchange model is often used to describe a magnetic structure in a system [104, 105] but it does not take into account different anisotropies. Therefore the isotropic Heisenberg model is not sufficient to describe the magnetic configurations in the tetragonal elongated $Fe_{50}Pt_{50-x}Rh_x$ films with their different spin orientations, e.g. in-plane or out-of-plane, depending on the Rh concentration. Instead a bilinear anisotropic Hamiltonian with a direction-dependent exchange constant plus an one-ion anisotropy term is used for the description which can be written as:

$$\widehat{H} = \widehat{H}^{ex} + \widehat{H}^{an}. \tag{5.60}$$

Here, $\widehat{H}^{ex}$ is a two-ion term and $\widehat{H}^{an}$ an one-ion interaction which describe the anisotropic exchange between the spins and their orientation along the different symmetry directions of the system, respectively. It should be noted that $\widehat{H}^{ex}$ uses a bi-linear anisotropic Hamiltonian with a direction dependent exchange term. For simplification the following assumptions are made: Only the Fe atoms carry a magnetic moment and only the nearest neighbors are taken into account. The exchange between the atoms can be described by the exchange parameter J^i_e:

$$J^i_e = \begin{bmatrix} J^z_{e_x} & J^x_{e_x} & J^y_{e_x} \\ J^z_{e_y} & J^x_{e_y} & J^y_{e_y} \\ J^z_{e_z} & J^x_{e_z} & J^y_{e_z} \end{bmatrix} . \tag{5.61}$$

The absolute values of the matrix elements will be assumed to be in the simplified model identical in all three symmetry directions x, y and z. The different directions are linked to the symmetry axis of the crystal by: x=a, y=b and z=c. Changes and extensions to overcome the simplified model if necessary will be discussed later. In the here assumed model FM and AF order of neighboring spins can be expressed by $-J^i_e$ and $+J^i_e$, respectively. With $|J| = |J^i_e|$ the matrix can be now written as:

$$J = |J| \begin{bmatrix} \pm 1 & \pm 1 & \pm 1 \\ \pm 1 & \pm 1 & \pm 1 \\ \pm 1 & \pm 1 & \pm 1 \end{bmatrix} \tag{5.62}$$

with the appropriate and independent choice of the sign of any of the components.
The two-ion term can be written as [106, 107, 108]:

$$\widehat{H}^{ex} = \sum_{j,i,e} J^i_e S^i_j S^i_{j+e} \tag{5.63}$$

with j denoting the radius-vector of any Fe ion position, $i = x, y, z$ and e are the unit vectors of the Cartesian system. Taking into account the three directions of the crystal it can be written: $\widehat{H}^{ex} = \widehat{H}^{ex}_x + \widehat{H}^{ex}_y + \widehat{H}^{ex}_z$. Here, every term describes the exchange between ions spatially arranged in the corresponding direction:

$$\widehat{H}^{ex}_x = \pm J \sum_j S^z_j S^z_{j+e_x} \pm J \sum_j S^x_j S^x_{j+e_x} \pm J \sum_j S^y_j S^y_{j+e_x} \tag{5.64}$$

$$\widehat{H}^{ex}_y = \pm J \sum_j S^z_j S^z_{j+e_y} \pm J \sum_j S^x_j S^x_{j+e_y} \pm J \sum_j S^y_j S^y_{j+e_y} \tag{5.65}$$

$$\widehat{H}^{ex}_z = \pm J \sum_j S^z_j S^z_{j+e_z} \pm J \sum_j S^x_j S^x_{j+e_z} \pm J \sum_j S^y_j S^y_{j+e_z} . \tag{5.66}$$

The moments can be now expressed in terms of spherical system coordinates, i.e. $S_j = S(\sin\theta_j \cos\phi_j, \sin\theta_j \sin\phi_j, \cos\theta_j)$. The spherical angles shown in Fig. 5.59 are connected with the previously introduced angles α and β by the relations $\alpha = \phi$ and $\beta = \frac{\pi}{2} - \theta$. In the next step the minimum of the energy has to be determined by minimizing the three terms of the exchange Hamiltonian. For some cases several minima can be achieved which give the proper magnetic order between the nearest neighbors. By the use of the one-ion anisotropy $\widehat{H}^{an}$ the orientation of the magnetic moments along the symmetry directions can be described and it can here be used to distinguish between the different minima of the exchange Hamiltonian $\widehat{H}^{ex}$. The one-ion anisotropy term $\widehat{H}^{an}$ can be expressed as

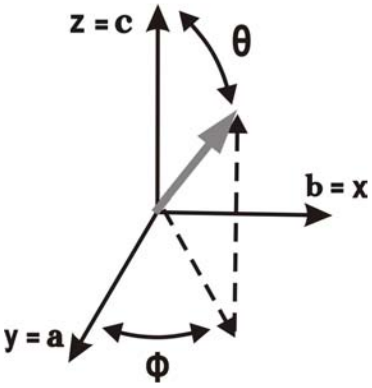

Figure 5.59.: Spherical angles of the magnetic moment (gray arrow) to the y- and z-axis.

[107, 108]:

$$\widehat{H}^{an} = \sum_j -K_1 S_j^{z2} - \frac{1}{S^2}(4K_2 S_j^{x2} S_j^{y2} + K_3(S_j^{z2} S_j^{y2} + S_j^{z2} S_j^{x2})). \tag{5.67}$$

The first term in this equation is the magnetic anisotropy energy (MAE) with $K_1 > 0$ denoting the easy axis anisotropy constant and describes the orientation of the spins in the z-direction. The second term describes the fourfold anisotropy of the tetragonal case. Here, the constants K_2 and K_3 describe the orientation of the spins in the in-plane direction (x-y-plane) and the relation to the z-direction, respectively.

If the proposed magnetic configurations for the different $Fe_{50}Pt_{50-x}Rh_x$ films and temperatures are compared four principle structures can be identified. The FM and AF ordered magnetic structure of the $Fe_{50}Pt_{45}Rh_5$ and $Fe_{50}Pt_{32.5}Rh_{17.5}$ films in Fig. 5.42 and Fig. 5.45, respectively, and the AF configuration at low (T<150 K) and high temperature (T>276 K) for the $Fe_{50}Pt_{25}Rh_{25}$ film, respectively (see Fig. 5.52). The theoretical description of the magnetic configuration will start with the simple FM order of the $Fe_{50}Pt_{45}Rh_5$ film.

As mentioned before the sign + and - denote the neighboring spins being antiparallel or parallel. Subsequently, the FM order of the $Fe_{50}Pt_{45}Rh_5$ film is described by the two-ion term as follows:

$$\widehat{H}_x^{ex} = -J\sum_j S_j^z S_{j+e_x}^z - J\sum_j S_j^x S_{j+e_x}^x - J\sum_j S_i^y S_{j+e_x}^y \tag{5.68}$$

$$\widehat{H}_y^{ex} = -J\sum_j S_j^z S_{j+e_y}^z - J\sum_j S_j^x S_{j+e_y}^x - J\sum_j S_i^y S_{j+e_y}^y \tag{5.69}$$

$$\widehat{H}_z^{ex} = -J\sum_j S_j^z S_{j+e_z}^z - J\sum_j S_j^x S_{j+e_z}^x - J\sum_j S_i^y S_{j+e_z}^y . \tag{5.70}$$

In the case of the out-of-plane FM order of the film with x=5 the orientation of the spins can be simply described by: $\widehat{H}^{an} = \sum_j -K_1 S_j^{z2}$, with $K_1 > 0$ and consequently the minimum is achieved when $\theta_1 = \theta_2 = \theta_3 = \theta_4 = 0$. It should be noted that the indices 1 to 4 denote the Fe atoms and the corresponding spins as it is shown in the magnetic unit cell in Fig. 5.60.

Considering the individual exchange parameters for the different directions the AF

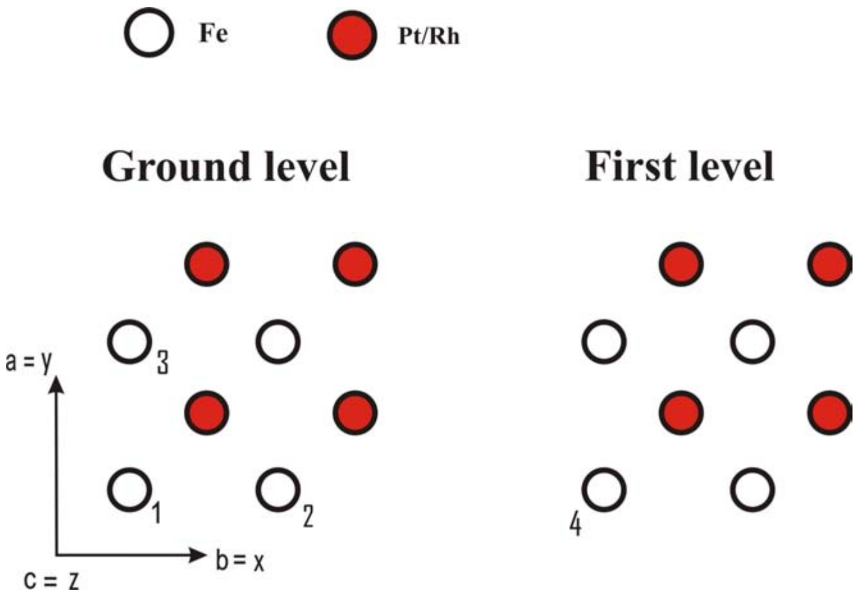

Figure 5.60.: Indices of the atoms and the corresponding magnetic moments used in the phenomenological model.

configuration of the $\mathrm{Fe}_{50}\mathrm{Pt}_{32.5}\mathrm{Rh}_{17.5}$ film is described by the following expressions of $\widehat{H}^{ex}$:

$$\widehat{H}^{ex}_x = J\sum_j S^z_j S^z_{j+e_x} - J\sum_j S^x_j S^x_{j+e_x} - J\sum_j S^y_j S^y_{j+e_x} \quad (5.71)$$

$$\widehat{H}^{ex}_y = J\sum_j S^z_j S^z_{j+e_y} + J\sum_j S^x_j S^x_{j+e_y} - J\sum_j S^y_j S^y_{j+e_y} \quad (5.72)$$

$$\widehat{H}^{ex}_z = J\sum_j S^z_j S^z_{j+e_z} - J\sum_j S^x_j S^x_{j+e_z} + J\sum_j S^y_j S^y_{j+e_z}. \quad (5.73)$$

Since this structure is more complicated than the previously discussed FM structure several solutions or minima, respectively, are possible. If $\widehat{H}^{ex}_x$ is minimized two equivalent minima can be achieved:

1. $|\theta_1 - \theta_2| = \pi$, i.e. the spins of the atom 1 and 2 are perpendicular to the x-y-plane and antiparallel to each other.
2. the spins are in canted positions to the x-y-plane and are mirrored to each other, i.e. $\theta_1 + \theta_2 = \pi$, $\phi_1 = \phi_2$. It should be noted that the exact values of the angles are undefined.

For $\widehat{H}^{ex}_y$ two equivalent minima can be found:

1. spin 1 and 3 are parallel to the z-axis and antiparallel to each other.
2. the spins of the atom 1 and 3 are canted to the x-y-plane and their projections along the in-plane direction are non-parallel, i.e. $\theta_1 + \theta_3 = \pi$, $\phi_1 + \phi_3 = \pi$. The exact values of the angles are again not defined.

For the component $\widehat{H}^{ex}_z$ even three equivalent minima are possible:

1. spin 1 and 4 are parallel to the z-axis and antiparallel to each other.

2. both spins 1 and 4 are canted to the x-y-plane and their projections in the in-plane direction are non-parallel, i.e. $\theta_1 + \theta_4 = \pi$, $\phi_1 + \phi_4 = 2\pi$. The values of the angels are again undefined.

3. the spins of the atoms 1 and 4 are canted to the x-y-plane and their projections in the in-plane direction is parallel, i.e. $\theta_1 + \theta_4 = \pi$, $\phi_1 + \phi_4 = 0$.

The one-ion anisotropy term is now important to distinguish between these possible solutions and to define the angles. The proposed magnetic structure can be described by the following relations of the different anisotropy constants: $0 < K_2 < K_3$ and $\left|\frac{K_1-K_2}{K_3-K_2}\right| < 1$. In such a case the minimum of expression 5.67 can be achieved when the in-plane components of the magnetic moments are aligned close to the diagonals of the bct structure, and are canted to the x-y-plane in such a way that $\cos 2\theta = \frac{K_1-K_2}{K_3-K_2}$. This is equivalent to the second solutions of the three components $\widehat{H}_x^{ex}$, $\widehat{H}_y^{ex}$ and $\widehat{H}_z^{ex}$. The spins of the nearest neighbors of spin 1 are mirrored to it if $\cos 2\theta_1 = \cos 2(\pi - \theta_i)$.

The AF order of the $Fe_{50}Pt_{25}Rh_{25}$ film in the out-of-plane direction at low temperature (T<150 K) is again a simple structure which can be described by the following two-ion term:

$$\begin{aligned}
\widehat{H}_x^{ex} &= +J\sum_j S_j^z S_{j+e_x}^z + J\sum_j S_j^x S_{j+e_x}^x + J\sum_j S_i^y S_{j+e_x}^y && (5.74)\\
\widehat{H}_y^{ex} &= +J\sum_j S_j^z S_{j+e_y}^z + J\sum_j S_j^x S_{j+e_y}^x + J\sum_j S_i^y S_{j+e_y}^y && (5.75)\\
\widehat{H}_z^{ex} &= +J\sum_j S_j^z S_{j+e_z}^z + J\sum_j S_j^x S_{j+e_z}^x + J\sum_j S_i^y S_{j+e_z}^y . && (5.76)
\end{aligned}$$

Similar to the film with x=5 only one minimum is derived and the out-of-plane orientation of the spins can again be described by the simple one-ion term: $\widehat{H}^{an} = \sum_j -K_1 S_j^{z2}$, with $K_1 > 0$. In contrast to the calculations for the $Fe_{50}Pt_{45}Rh_5$ film the minimum is achieved here when $\theta_1 = 0$ and $\theta_2 = \theta_3 = \theta_4 = \pi$, i.e. the spins are aligned perpendicular to the x-y-plane with antiparallel orientation to each other.
For a temperature T>250 K a more complicated structure can be observed (see fig.5.52). Here the two ion term is given by:

$$\begin{aligned}
H_x^{ex} &= -J\sum_j S_j^z S_{j+e_x}^z - J\sum_j S_j^x S_{j+e_x}^x - J\sum_j S_i^y S_{j+e_x}^y && (5.77)\\
H_y^{ex} &= +J\sum_j S_j^z S_{j+e_y}^z + J\sum_j S_j^x S_{j+e_y}^x - J\sum_j S_i^y S_{j+e_y}^y && (5.78)\\
H_z^{ex} &= -J\sum_j S_j^z S_{j+e_z}^z - J\sum_j S_j^x S_{j+e_z}^x + J\sum_j S_i^y S_{j+e_z}^y . && (5.79)
\end{aligned}$$

For $\widehat{H}_x^{ex}$ two minima can be found:

1. $\theta_1 = \theta_2 = 0$, i.e. spin 1 and 2 are parallel to the z-direction and parallel to each other.

2. the spins of atom 1 and 2 are in canted position to the x-y-plane, i.e. $\theta_1 = \theta_2$ and $\phi_1 = \phi_2$. The values of both angles are undefined.

For $\widehat{H}_y^{ex}$ also two minima have to be distinguished:

1. $\theta_1 = \theta_3 = \pi$, i.e. the spins of atom 1 and 3 are perpendicular to the x-y-plane and antiparallel to each other.

2. the spins 1 and 3 are canted to the x-y-plane and their projections in the in-plane direction are non-parallel, i.e. $\theta_1 + \theta_3 = \pi$ and $\phi_1 + \phi_3 = \pi$. The angles are again undefined.

For the component $\widehat{H}_z^{ex}$ three equivalent minima are possible:

1. spin 1 and 4 are perpendicular to the x-y-plane and parallel to each other.

2. the spins of atom 1 and 4 are canted to the x-y-plane and their projections in the in-plane direction are non-parallel, i.e. $\theta_1 = \theta_4$ and $\phi_1 + \phi_4 = 2\pi$. It should be noted that the values of the angles are not defined.

3. the spins 1 and 4 are canted to the x-y-plane and their projections in the in-plane direction are parallel to each other, i.e. $\theta_1 = \theta_4$ and $\phi_1 + \phi_4 = 0$.

The one ion term needs to be used again to distinguish between these solutions. The different orientations of the spins can be described by the following relations of the anisotropy constants: $0 < K_2 < K_3$ and $\left|\frac{K_1 - K_2}{K_3 - K_2}\right| < 1$. As described for the film with x=17.5 the minimum is reached when the x-y components of the spins align close to the diagonals of the bct structure and are canted in such a way that $\cos 2\theta = \frac{K_1 - K_2}{K_3 - K_2}$ which is equivalent to the second solutions of the three components of the two-ion term $\widehat{H}^{ex}$ in x-, y- and z-direction. The nearest neighbors, however, are not mirrored to each other.

For the previous calculations a simplified model was used. It was assumed that the in-plane angles ϕ have values of about 45° due to the in-plane symmetry. The neutron diffraction measurements, on the other hand, showed different results for the angles. For some films even a temperature dependence was found. To include these differences in the phenomenological model the expression of the one-ion anisotropy term in 5.67 has to be modified [108]:

$$\widehat{H}^{an} = \sum_j -K_1 S_j^{z2} - \frac{1}{S^2}\left[4K_2 S_j^{x2} S_j^{y2} + K_3 (S_j^{z2} S_j^{x2} + S_j^{z2} S_j^{y2})\right] + 16\Delta S_j^{y4} S_j^{x4}. \tag{5.80}$$

The additional term $16\Delta S_j^{y4} S_j^{x4}$ describes an eightfold anisotropy in the films and is necessary to include the different in-plane angles ($\phi \neq 45°$) as well as the perpendicular and parallel domains in the phenomenological model. In the next step again the minima of the energy have to be determined by minimizing the one-ion anisotropy term $\widehat{H}^{an}$. Therefore the term is minimized for both angles which lead to the following arguments for ϕ:

$$\sin^2 2\phi = \frac{2K_2 K_3^2}{\Delta (K_3 - K_1)^2} \tag{5.81}$$

and for θ:

$$\cos 2\theta = \frac{K_1}{K_3} \tag{5.82}$$

For $\left|\frac{K_1}{K_3}\right| < 1$ and $0 < \frac{2K_2K_3^2}{\Delta(K_3-K_1)^2} < 1$ with $K_3 > 0$, $K_2 > 0$ and $\Delta > 0$ the angles describe an AF congiguration with out-of-plane components of the spins, e.g. the AF configuration of the $Fe_{50}Pt_{32.5}Rh_{17.5}$ film.
For $\left|\frac{K_1}{K_3}\right| > 1$ two cases have to be distinguished: $\frac{K_1}{K_3} \leq -1$ and $\frac{K_1}{K_3} \to 1$.
For $\frac{K_1}{K_3} \leq -1$ it is $\theta = \frac{\pi}{2}$ and the spins are oriented in-plane as it can be seen for the $Fe_{50}Pt_{40}Rh_{10}$ film in the AF domains above T=230 K. Considering the result for θ and minimizing $\widehat{H}^{an}$ relative to ϕ leads to three solutions:

1. a canted in-plane state of the spins with $\sin^2 2\phi = \frac{K_2}{2\Delta}$ is given when $0 < \frac{K_2}{2\Delta} < 1$.
2. a 45° orientation of the spins in-plane is given when $\frac{K_2}{2\Delta} > 1$, this includes the previous model where $\Delta \to 0$.
3. the spins are directed along the x- or y-axis when $\frac{K_2}{2\Delta} = 0$

For $\frac{K_1}{K_3} \to 1$ and $\cos 2\theta \to 1$, i.e. $\theta \to 0$ or $\theta \to \pi$ an out-of-plane orientation of the spins is realized as it was observed for the $Fe_{50}Pt_{45}Rh_5$ film.

In summary of the phenomenological model for the magnetic configurations of the $Fe_{50}Pt_{50-x}Rh_x$ films one can conclude that the films with low Rh concentration which are FM ordered in the in-plane direction have an anisotropy ratio $\frac{K_1}{K_3} > 1$ and $K_1 > 0$. With increasing Rh concentration this ratio decreases and changes to $\frac{K_1}{K_3} < 1$ at about x=10. At this point an AF order in the out-of-plane direction becomes dominant. In the $Fe_{50}Pt_{40}Rh_{10}$ film the change from $\frac{K_1}{K_3} > 1$ to $\frac{K_1}{K_3} < 1$ can also be observed with increasing temperature. An abnormal behavior from the decreasing $\frac{K_1}{K_3}$-ratio can be observed in the film with x=25 at low temperature, where the ratio is also $\frac{K_1}{K_3} > 1$. The reason for this behavior is not known at the present stage. Besides the decreasing $\frac{K_1}{K_3}$-ratio with the Rh concentration a similar behavior can be observed for the K_2 anisotropy constant with temperature but only in the AF domains of the films with x=10 and x=25 which show a temperature driven magnetic transition. At low temperature the magnetic moments are canted to the x- and y-axes ($\phi \neq 0$ and $\phi \neq \frac{\pi}{2}$) and have an anisotropy constant of $K_2 > 0$. With increasing temperature the anisotropy constant decreases and changes to $K_2 < 0$. At this state the magnetic moments orient along one of the symmetry axes x or y. To the best of the knowledge of the author, similar results as they are presented here for the phenomenological model of the $Fe_{50}Pt_{50-x}Rh_x$ films have not been published for other samples yet.
It should be noted that the $Fe_{50}Pt_{50-x}Rh_x$ alloys are itinerant-electron magnets. Therefore the exchange parameter J_e^i can not be determined simply from the Néel or Curie temperature, respectively, by the use of the equation $T_{N,C} = \frac{2S(S+1)}{3k_B} J(\vec{Q})$ which is often applied for systems with localized spins [109, 110, 111]. The determination of the exchange parameter in an itinerant system is in general much more complicated. Two different approaches to determine the exchange parameter in a Heisenberg model are for example the so-called real-space approach [112, 113, 114] and the frozen-magnon approach [114]. In the latter case the spin-wave energy can be calculated by employing the generalized Bloch theorem [114]. The exchange parameter J_e^i can then be determined by a Fourier transformation of the energy. In the real-space approach the exchange parameter can be calculated directly by employing the change of the energy associated with a constrained rotation of the spin-polarization axes at different sites [112, 113, 114]. The determination

of the exchange parameter is beyond the scope of this work and would require additional measurements with methods as, for example, inelastic neutron scattering. The expected signals in such measurements are comparatively weak. The intensity of the small amount of scatterers of the $Fe_{50}Pt_{50-x}Rh_x$ films in this work would be too low to be measured. For future work inelastic measurements are planned on thicker samples to increase the amount of scatterers.

For the magnetic configuration under the application of a magnetic field two cases have to be distinguished: a FM and an AF order. In the case of a FM order the influence of the magnetic field can be easily described by the use of a simple Heisenberg exchange Hamiltonian and a perpendicular external field which are in competition with the easy axis anisotropy. The out-of-plane angle θ can then be determined by minimizing the one-ion anisotropy term $\widehat{H}^{an}$. It should be noted that an additional Zeeman term has to be taken into account which considers the external magnetic field:

$$\widehat{H}^{an+Ze} = -K_1 S^2 \cos^2\theta - H\,|S|\sin\theta, \tag{5.83}$$

where H denotes the external magnetic field. The minimum of $\widehat{H}^{an+Ze}$ is given when:

$$\sin\theta = \frac{H}{2K_1 S}. \tag{5.84}$$

The saturation field can then be determined by: $H_{sat} = 2K_1 S$. It should be noted that the magnetic fields applied in this work were not sufficient to saturate the samples. The anisotropy constant K_1 could therefore not be determined. For future work neutron diffraction experiments with higher magnetic field and additional super quantum inteference device measurements are planned.

In the case of an AF order the situation is much more complicated. Here, the external magnetic field is in competition with the anisotropic exchange field as well as with the one-ion anisotropy described by formula 5.67. Furthermore as discussed in the previous section the reorientation of the magnetic moments is most likely a continuous process and therefore the model of a spin-flop transition can not be used. Besides these difficulties it was also shown by the neutron diffraction measurements that only the AF domains in the film with x=10 are influenced by the field while the AF order of the other films is not affected. This is an indication that also an influence of the FM domains on the AF order needs to be considered in a theoretical model. For the theoretical description of the behavior the simplified model presented here is not sufficient and needs to be modified and extended. This extension should be based on a more general expression for the Hamiltonian. First of all, the model should take into account that the in-plane and out-of-plane exchange parameters J_e^i are not only different in sign but also in their absolute values, i.e. the Fe-Fe interaction in the Fe-planes should be stronger than those perpendicular to it, mediated by the Pt/Rh atoms. Furthermore, the model should give information about the orientation of domains and domain walls and whether the orientations or propagations, respectively, are connected to the symmetry axes [115], [116]. Moreover it is also important to explain the magnetic field behaviors of the magnetic moments in the AF domains of the film with x=10.

The model presented here takes only Fe magnetic moments into account which is in good agreement with previous ab-initio results for FePt alloys. There it was shown that Pt-Pt interactions can be neglected and Fe-Pt interactions lead only to renormalization of parameters in the Hamiltonian for Fe [117], [118]. The additional Rh atoms make it necessary to prove if these assumptions are still valid for the ternary $\mathrm{Fe}_{50}\mathrm{Pt}_{50-x}\mathrm{Rh}_x$ alloys. Previous theories use power laws to explain the temperature dependence of the magnetic configuration [119]. For the verification a temperature dependence of the anisotropy constants should be included in an extended model.

For future work also the long-range interactions should be included into the model, since it is known from FePt and FeRh ab-initio calculations that they play a significant role. For the work presented here, however, the limitation to short-range interactions were sufficient to explain the experimental results.

6. Conclusions and Outlook

Previous investigations on the magnetic properties of bulk $Fe_{50}Pt_{50-x}Rh_x$ alloys by Yuasa with macroscopic measurements showed that the magnetic phases and the transition temperatures in the alloy can be tuned by the Rh concentration. For technological application, in particular for HDDs, thin films are preferred to reduce device sizes. Therefore the investigations presented in this work focus on 200 nm thick $Fe_{50}Pt_{50-x}Rh_x$ films whose nuclear and magnetic properties have been investigated mainly by polarized and unpolarized neutron diffraction. By the use of neutrons a probe was chosen which are able to analyze the structural and magnetic properties on an atomic level. In contrast to other neutron scattering methods such as neutron reflectivity or small angle neutron scattering the neutron diffraction measurements provide information about the magnetic and the nuclear crystalline structures of the different $Fe_{50}Pt_{50-x}Rh_x$ films. Moreover, it allows to study AF order. The measurements were performed at instruments at the world leading neutron sources. The neutron diffraction experiments carried out at these sources are even suited to study the nuclear and magnetic structures of thin films (thicknesses down to 100 nm) with very low amount of material. In contrast to the macroscopic measurements the results of the neutron diffraction investigations can be used in combination with qualitative and quantitative structure factor calculations to develop a detailed model of the magnetic configuration of the $Fe_{50}Pt_{50-x}Rh_x$ alloys.

The dependence on the composition has been analyzed considering four 200 nm thick $Fe_{50}Pt_{50-x}Rh_x$ films with the concentrations x=5, 10, 17.5 and 25. In a second step the changes of the magnetic configurations and properties under an external magnetic field have been studied. In a last step the influence of the film thickness was investigated by studying three $Fe_{50}Pt_{40}Rh_{10}$ films with film thicknesses of 100 nm, 300 nm and 500 nm. Besides neutron diffraction, X-ray diffraction and MOKE measurements were carried out for the structural and magnetic analysis of the films.

The measurements presented in this work reveal for the 200 nm thick $Fe_{50}Pt_{50-x}Rh_x$ alloys with low Rh concentration a FM order while the films with higher Rh concentration are AF ordered. More precisely, the film with x=5 and x=17.5 are in a pure, single FM and AF state, respectively, before they become PM. In the film with x=10 a transition from an AF order at low temperature to a FM order at high temperature can be observed. The film with x=25 shows also a temperature driven magnetic transition but here these are transitions between different AF configurations. The different magnetic orders and transitions observed with the variation of the Rh concentrations are similar to the results proposed for the bulk $Fe_{50}Pt_{50-x}Rh_x$ system. However, the Néel and Curie temperatures, respectively, of the 200 nm thick films are about T=100 K lower as they were proposed for the bulk system.

The models of the magnetic configuration developed from the neutron diffraction results in combination with the structure factor calculations demonstrate that the 200 nm thick $Fe_{50}Pt_{50-x}Rh_x$ film with low Rh concentration (x=5) has a FM order in the in-plane direction with the magnetic moments aligned in the out-of-plane direction along the c-axis. The film with x=17.5, on the other hand, has a dominant AF order in the out-of-plane direction with the magnetic moments aligned dominantly in the in-plane direction and a small component directed out-of-plane. Both films are in a single magnetic state until they become PM and their magnetic configurations do not change with temperature only a decrease of the strength of the magnetic order can be observed. The film with x=10 possesses at low temperature an AF structure similar to the one proposed for the film with x=17.5 which changes for higher temperature to the FM configuration proposed for the film with x=5. In the AF ordered film with x=25 the dominant orientation of the magnetic moments changes with increasing temperature from the out-of-plane to the in-plane and back to the out-of-plane direction. The origin of the temperature driven magnetic transitions are in both cases a nucleation and growth of domains with FM in-plane order and AF out-of-plane order, respectively. Besides the magnetic transitions again a decrease of the strength of the magnetic order was observed with increasing temperature as expected.

The AF ordered films with x=17.5 and x=25 remain stable for magnetic fields up to 10 T and 3.5 T, respectively. The films with x=5 and x=10, on the other hand, are influenced by a magnetic field if it is applied in the in-plane direction. In both films the magnetic moments turn in the direction of the applied field leading to a resulting magnetic moment in the out-of-plane direction. For the $Fe_{50}Pt_{40}Rh_{10}$ film the reorientation of the magnetic moments in field direction leads to a reduction of the AF-FM transition temperature.

The thickness dependent measurements of the $Fe_{50}Pt_{40}Rh_{10}$ film showed that neither the principal magnetic properties nor the magnetic configuration is influenced by the film thickness in a range from 100 nm to 500 nm. The only effect observed with the film thickness was a more rapid decay of the integrated intensities of the half order reflections indicating a faster AF-FM transition in the thicker films.

The magnetic configurations proposed for the different $Fe_{50}Pt_{50-x}Rh_x$ films can be described theoretically by a phenomenological model taking two terms into account. The first term is a bilinear anisotropic Hamiltonian with direction dependent exchange constants. This term describes the orientation of neighboring magnetic moments to each other. The second term includes the easy axis anisotropy as well as the fourfold tetragonal anisotropy and describes the orientation of the magnetic moments along the three symmetry axes of the crystal. The phenomenological model indicates that the magnetic configuration of the $Fe_{50}Pt_{50-x}Rh_x$ alloys with low Rh concentration ($x \leq 10$) is dominantly determined by the easy axis anisotropy while for high Rh concentration ($x > 10$) the influence of the fourfold anisotropy is more prominent.

In summary it has been shown that neutron diffraction measurements in combination with structure factor calculations are ideally suited to determine the magnetic structure of thin $Fe_{50}Pt_{50-x}Rh_x$ films in great detail. Based on this data it was possible to develop for the first time a detailed model of the magnetic configurations of $Fe_{50}Pt_{50-x}Rh_x$ alloys with thicknesses down to 100 nm.

The detailed knowledge of the magnetic configurations of the $Fe_{50}Pt_{50-x}Rh_x$ alloys can be used to fabricate multilayers with appropriate magnetic properties and configuration. For example, multilayers with FM and AF ordered $Fe_{50}Pt_{50-x}Rh_x$ alloys can be grown to study exchange bias effects or exchange spring effects. The advantage of the different $Fe_{50}Pt_{50-x}Rh_x$ films compared to FeRh/FePt layers is the good lattice match which reduces lattice strains between the different materials. Besides the physical interest the thin films and multilayers are also promising candidates for technological applications.

The addition of Rh to the FePt alloys reduces the Curie temperature which reduces thermal stresses and the magnetic write field which makes the film attractive for HAMR media. The composition range about x=10 with its AF-FM transition is interesting for applications as soft underlayer. Here, the FM phase would help by the reversion of the magnetization of the recording media during the writing process while the AF order stabilizes the system during the data storage. Furthermore a combined recording system can be grown, consisting of a FM ordered $Fe_{50}Pt_{50-x}Rh_x$ alloy with $x<10$ used as recording media with reduced Curie temperature and a film with $x\approx 10$ used as soft underlayer for the further reduction of the write field.

For technological applications a further reduction of the film thickness below 100 nm is preferable to reduce the size of the devices and the production costs. First measurements on 6 nm thin $Fe_{50}Pt_{50-x}Rh_x$ films with macroscopic techniques, e.g. vibrating sample magnetometer and superconducting quantum interference device, by Hasegawe et al. showed similar magnetic properties as proposed for the 200 nm films in this work [103]. To analyze the magnetic structure of such small films with neutrons a higher flux is essential. Since today's continuous neutron facilities reached almost their flux maxima new developments are necessary. One possible solution to study very small amount of material with high enough flux are spallation sources like the SNS or in the near future the ESS.

Bibliography

[1] D. L. Smith. *Thin-film deposition: Principles and practice.* MacGraw-Hill, 1995.

[2] H. S. Nalwa, editor. *Handbook of thin film materials.* Academic Press, 2002.

[3] S.N. Piramanayagam. Perpendicular recording media for hard disk drives. *J. Appl. Phys.*, 102(011301), 2007.

[4] D. A. Thompson and J. S. Best. The future of magnetic data storage technology. *IBM J. Res. Develop.*, 44(3).

[5] D. Weller, A. Moser, L. Folks, M. E. Best, W. Lee, M. F. Toney, M. Schwickert, J.-U. Thiele, and M. F. Doerner. High K_u materials approach to 100 Gbits/in^2. *IEEE Trans. Magn.*, 36(1).

[6] T. Klemmer, D. Hoydick, H. Okumura, B. Zhang, and W. A. Soffa. Magnetic hardening and coercivity mechansims in $L1_0$ ordered FePd ferromagnets. *Scripta Metallurgica et Materialia*, 33(10/11).

[7] Y. Kanai, R. Matsubara, H. Watanabe, H. Muraoka, and Y. Nakamura. Recording Field Analysis of Narrow-Track SPT Head With Side Shields,Tapered Main Pole, and Tapered Return Path for 1 Tbit/in^2. *IEEE Trans. Magn.*, 39(4).

[8] K. Matsumoto, A. Inomata, and S. ya Hasegawa. Thermally Assisted Magnetic Recording. *FUJITSU Sci. Tech. J.*, (42):158–167, 2006.

[9] J. Zhao, B. Cui, Z. Zhang, B. Ma, and Q. Y. Jin. Ultrafast heating effect on transient magnetic properties of $L1_0$-FePt thin films with perpendicular anisotropy. *Thin Solid Films*, 518:2830–2833, 2010.

[10] J. U. Thiele, K. R. Coffey, M. F. Toney, J. A. Hedstrom, and A. J. Kellock. Temperature dependent magnetic properties of highly chemically ordered $Fe_{55-x}Ni_xPt_{45}$ $L1_0$ films. *J. Appl. Phys.*, 91(10), 2002.

[11] S. Khizroev and D. Litvinov. Perpendicular magnetic recording: Writing process. *J. Appl. Phys.*, 95(9), 2004.

[12] J.-U. Thiele, S. Maat, L. Robertson, and E. E. Fullerton. Magnetic and structural properties of FePt-FeRh exchange spring films for thermally assisted magnetic recording media. *IEEE Trans. Magn.*, 40(4):2537, 2004.

[13] S. Inoue, H. Y. Y. Ko, and T. Suzuki. Magnetic properties of single crystalline FeRh alloy thin films. *IEEE Trans. Magn.*, 44:2875–2878, 2009.

[14] E. M. Hofer and P. Cucka. Magnetic properties of Rh-rich FeRh alloy. *J. Phys. Chem. Solids.*, 27:1552–1555, 1966.

[15] J. S. Kouvel and C. C. Hartelius. Anomalous magnetic moments and tansformations in the ordered alloy FeRh. *J. App. Phys.*, 33(3), 1962.

[16] K.Yu. Guslienko, O. Chubykalo-Fesenko, O. Mryasov, R. Chantrell, and D. Weller. Magnetization reversal via perpendicular exchange spring in FePt/FeRh bilayer films. *Phys. Rev. B*, 70(104405), 2004.

[17] S. Yuasa, H. Miyajima, and Y. Otani. Magneto-volume and tetragonal elongation effects on magnetic phase transitions of body-centered tetragonal $\mathrm{FeRh}_{1-x}\mathrm{Pt}_x$. *J. Phys. Soc. Jpn.*, 63(8):3129–3144, 1994.

[18] S. Yuasa, T. Akiyama, H. Miyajima, and Y. Otani. Change in the resistivity of bcc and bct FeRh alloys at first-order magnetic phase transitions. *J. Phys. Soc. Jpn.*, 64(10):3978–3985, 1995.

[19] P.A. Algarabel, M.R. Ibarra, C. Marquina, S. Yuasa, H. Miyajima, and Y. Otani. Magnetostriction and thermal expansion measurements on $\mathrm{FeRh}_{1-x}\mathrm{Pt}_x$ alloys. *J. App. Phys.*, 79(8):4659, 1996.

[20] M. R. Fitzsimmons, S. D. Bader, J. A. Borchers, G. P. Felcher, J. K. Furdyna, A. Hoffmann, J. B. Kortright, I. K. Schuller, T. C. Schulthess, S. K. Sinha, M. F. Toney, D. Weller, and S. Wolf. Neutron scattering studies of nanomagnetism and artificially structured materials. *J. Magn. Magn. Mater.*, 271:103–146, 2004.

[21] T. Suzuki, T. Kiya, N. Honda, and K. Ouchi. High density recording on ultra-thin FePt perpendicular composite media. *IEEE Trans. Magn.*, 36:2417–2419, 2000.

[22] Y. K. Takahashi, K. Hono, T. Shima, and K. Takanashi. Microstructure and magnetic properties of FePt thin films epitaxially grown on MgO (001) substrates. *J. Magn. Magn. Mater.*, 267:248–255, 2003.

[23] N.H. Luong, D.M. Hong, N. Chau, N.D. Linh, M. Kurisu, D.T.K. Anh, and G. Nakamoto. High-coercivity FePt sputtered films. *J. Magn. Magn. Mater.*, 290-291:559–561, 2005.

[24] B. Rellinghaus, S. Stappert, M. Acet, and E. F. Wassermann. Magnetic properties of FePt nanoparticles. *J. Magn. Magn. Mater.*, 266:142–1554, 2003.

[25] R. A. Ristau, K. Barmak, L. H. Lewis, K. R. Coffey, and J. K. Howard. On the realtionship of high coercivity and $\mathrm{L1}_0$ ordered phase in CoPt and FePt thin films. *J. Appl. Phys.*, 86(4527), 1999.

[26] P. T. L. Minh, N. P. Thuy, N. D. Van, and N. T. N. Chan. Structure and magnetic properties of thin FePt alloy films. *J. Magn. Magn. Mater.*, 239:335–337, 2002.

[27] S. C. Chen, P. C. Kuo, C. L. Shen, G. P. Lin, K. T. Huang, S. L. Ou, and W. H. Hong. Effect of capped layer on microstructure and magnetic properties of FePt films. *Materials and Design*, 31:1742–1745, 2010.

[28] W. K. Shen, J. H. Judy, and J.-P. Wang. In situ epitaxial growth of ordered FePt (001) films with ultra small and uniform grain size using a RuAl underlayer. *J. Appl. Phys.*, 97(10H301), 2005.

[29] Y. F. Ding, J. S. Chen, and E. Liu. Structural and magnetic properties of nanostructured FePt/MgO granular films. *Thin Solid Films*, 474:141–145, 2005.

[30] S. Maat, G. Zeltzer, E. E. Fullerton, G. J. Mankey, M. L. Crow, and J. L. Robertson. Antiferromagnetic structure of $FePt_3$ films studied by neutron scattering. *Phys. Rev. B*, 63(134426), 2001.

[31] K. Sumiyama and G. M. Graham. Magneto-volume effect in ordered Pt_3Fe alloy. *Solid State Comm.*, 19:241–243, 1976.

[32] S. Maat, A. J. Kellock, D. Weller ans J. E. E. Baglin, and E. E. Fullerton. Ferromagnetism of $FePt_3$ films induced by ion-beam irradiation. *J. Magn. Magn. Mater.*, 265:1–6, 2003.

[33] Y. Tsunada, D. Tsuchiya, and Y. Higashiyama. Crossover of spin correlations in $Pt_{100-x}Fe_x$ ($16 \leq x \leq 25$) alloys. *J. Phys. Soc. Jpn.*, 72(3):713–717, 2003.

[34] G. E. Bacon and J. Crangle. Chemical and magnetic order in platinum-rich Pt+Fe alloys. *Proc. R. Soc.*, A272(387), 1963.

[35] I. V. Solovyev, P. H. Dederichs, and I. Mertig. Origin of orbital magnetization and magnetocrystalline anisotropy in TX ordered alloys (where T=Fe,Co and X=Pd,Pt). *Phys Rev. B*, 52(18), 1995.

[36] Julia Vladimirovna Lyubina. *Nanocrystalline Fe-Pt alloys: phase transformations, structure and magnetism.* PhD thesis, Technische Universität Dresden, 2006.

[37] http://cst www.nrl.navy.mil/lattice/struk/index.html.

[38] K.-W. Lin, J.-Y. Guo, C. Y. Liu, H. Ouyang, J. van Lierop, N. N. Phuoc, and T. Suzuki. Exchange coupling in FePt-$FePt_3$ nanocomposite films. *Phys. Stat. sol.*, (204):3991–3994, 2007.

[39] T. Saerbeck, F. Klose, D. Lott, G. J. Mankey, Z. Lu, P. R. LeClair, W. Schmidt, A. P. J. Stampfl, S. Danilkin, M. Yethiraj, and A. Schreyer. Artificially modulated chemical order in thin films: A different approach to create ferro/antiferromagnetic interfaces. *Phys Rev. B*, 82(134409), 2010.

[40] K. Barmak, J. Kim, L. H. Lewis, K. R. Coffey, M. F. Toney, A. J. Kellock, and J.-U. Thiele. On the relationship of magnetocrystalline anisotropy and stoichiometry in epitaxial $L1_0$ CoPt (001) and FePt (001) thin films. *J. App. Phys.*, 98(033904), 2005.

[41] C. Paduani. Magnetic properties of Fe-Rh alloys. *J. App. Phys.*, 90(12), 2001.

[42] G. Shirane, C. W. Chen, P. A. Flinn, and R. Nathans. Hyperfine fields and magnetic moments in the Fe-Rh system. *J. App. Phys.*, 34:1044, 1963.

[43] S. Maat, J.-U. Thiele, and E. E. Fullerton. Temperature and field hysteresis of the antiferroamgnetic-to-ferromagnetic phase transition in epitaxial FeRh films. *Phys. Rev. B*, 72(214432), 2005.

[44] Y. Ohtani and I. Hatakeyama. Features of broad magnetic transition in FeRh thin film. *J. Magn. Magn. Mater.*, 131:339–344, 1994.

[45] I. Radu, C. Stamm, N. Pontius, T. Kachel, P. Ramm, J.-U. Thiele, H. A. Dürr, and C. H. Back. Laser-induced generation and quenching of magnetization on FeRh studied with time-resolved x-ray magnetic circular dichroism. *Phys. Rev. B*, 81(104415), 2010.

[46] E. Kren, L. Pal, and P. Szabo. Neutron diffraction investigation of the antiferromagnetic-ferromagnetic transformation in the FeRh alloy. *Phys. Lett.*, 9(4):297, 1964.

[47] F. Garcia-Sanchez, O. Chubykalo-Fesenko, O. N. Mryasov, R. W. Chantrell, and K. Yu. Guslienko. Multiscale versus micromagnetic calculations of the switching field reduction in FePt/FeRh bilayers with perpendicular exchange spring. *J. App. Phys.*, 87(10J101), 2005.

[48] J.-U. Thiele, S. Maat, and E. E. Fullerton. FeRh/FePt exchange spring films for thermally assisted magnetic recording media. *App. Phys. Lett.*, 82(17):2859, 2003.

[49] D. Suess, T. Schrefl, S. Fähler, M. Kirschner, G. Hrkac, F. Dorfbauer, and J. Fidler. Exchange spring media for perpendicular recording. *App. Phys. Lett.*, 87(012504), 2005.

[50] R. V. P. Montsouka, J. Arabski, A. Derory, J. Faerber, G. Schmerber, and V. Pierron-Bohnes. Structural and magnetic study of thin films based on anisotropic ternary alloys $FeNiPt_2$. *Mater. Sci. and Eng. B*, 126:236–239, 2006.

[51] W. Y. Zhang, H. Shima, F. Takano, H. Akinaga, X. Z. Yu, T. Hara, W. Z. Zhang, K. Kimoto, Y. Matsui, and S. Nimori. Enhancement in ordering of $Fe_{50}Pt_{50}$ film caused by Cr and Cu additives. *J. Appl. Phys*, 106(033907), 2009.

[52] D. C. Berry and K. Barmak. Effect of alloy composition on the thremodynamic and kinetic parameters of the A1 to $L1_0$ transformation in FePt, FeNiPt, and FeCuPt films. *J. Appl. Phys.*, 102(024912), 2007.

[53] M. L. Yan, Y. F. Xu, X. Z. Li, and D. J. Sellmyer. Highly (001)-oriented Ni-doped $L1_0$ FePt films and their magnetic properties. *J. Appl. Phys.*, 97(10H309), 2005.

[54] N. V. Baranov and E. A. Barabanova. Electrical resistivity and magnetic phase transitions in modified FeRh compounds. *J. Alloys Compd.*, 219:139–148, 1995.

[55] N. V. Baranov, P.E. Markin, S.V. Zemlyanski, H. Michor, and G. Hilscher. Giant magnetoresistance in antiferromagnetically ordered FeRh and Mn_2Sb based alloys. *J. Magn. Magn. Mater.*, 157/158:401–402, 1996.

[56] P. Kushwaha, A. Lakhani, R. Rawat, and P. Chaddah. Low-temperature study of field-induced antiferromagnetic-ferromagnetic transition in Pd-doped Fe-Rh. *Phys. Rev. B*, 80(174413), 2009.

[57] P. H. Walter. Exchange inversion in ternary modifications of iron rhodium. *J. App. Phys.*, 35(3 (Part2)), 1964.

[58] K. Takizawa, T. Ono, and H. Miyajima. Magnetic phase transitions for body-centered tetragonal $FeRh_{1-x}Pt_x$ system. *J. Magn. Magn. Mater.*, 226-230:572–573, 2001.

[59] S. Yuasa and H. Miyajima. Magnetic properties and phase transition in bct $FeRh_{1-x}Pt_x$ alloys. *NIM B*, 76:71–73, 1993.

[60] W. Lu, N. T. Nam, and T. Suzuki. First-order magnetic phase transition in FeRh-Pt thin films. *J. Appl. Phys*, 105(07A904), 2009.

[61] W. Lu, N. T. Nam, and T. Suzuki. Magnetic properties and phase transition kinetics of $Fe_{50}(Rh_{1-x}Pt_x)_{50}$. *IEEE Trans. Magn.*, 45:4011–4014, 2009.

[62] W. Lu, B. Yan, and T. Suzuki. Magnetic phase transition and magneto-optical properties in epitaxial $FeRh_{0.95}Pt_{0.05}$ (001) single-crystal thin films. *Scripta Materialia*, 64:851–854, 2009.

[63] D. Richter. *Scattering Techniques: Neutron Diffraction, in: Magnetism goes nano.* FZ Jülich GmbH, 2005.

[64] A. D. Krawitz. *Introduction to diffraction in materials science and engineering.* John Wiley & sons, INC., 2001.

[65] J. M. Cowley. *Diffraction physics (Sec. Rev. Ed.).* North Holland Personal Library, 1986.

[66] L. H. Schwartz and J. B. Cohen. *Diffraction from materials.* Academic Press, Inc., 1977.

[67] W. Nolting. *Grundkurs: Theoretische Physik Quantenmechanik Teil 2: Methoden und Anwendungen.* Verlag Zimmermann-Neufang, 1994.

[68] A. Schreyer. *Spin polarized neutron reflectometry and x-ray scattering on exchange coupled superlattices.* PhD thesis, Ruhr-Universität Bochum, 1994.

[69] T. Brückel. *Scattering Techniques II: Magnetic X-Ray Scattering, in: Magnetism goes nano.* FZ Jülich GmbH, 2005.

[70] A. Schreyer. *Physical Properties of Photons and Neutrons, in: Neutrons and Synchrotron Radiation in Engineering Materials Science.* Wiley-VCH, 2008.

[71] G. Shirane, S. M. Shapiro, and J. M. Tranquada. *Neutron Scattering with a Triple-Axis Spectrometer Basic Techniques.* Cambridge University Press, 2002.

[72] J. Bienlein and R. Wiesendanger. *Einführung in die Struktur der Materie.* B. G. Teubner, 2003.

[73] B. E. Warren. *X-Ray Diffraction.* Dover Publications, 1990.

[74] R. Siebrecht. *Untersuchung magnetischer $Fe_{1-x}Cr_x$/Cr-Übergitter mit dem Neutronenreflektometer ADAM.* PhD thesis, Ruhr-Universität Bochum, 2000.

[75] W. Treimer. *Imaging, in: Neutrons and Synchrotron Radiation in Engineering Materials Science.* Wiley-VCH, 2008.

[76] Prakash Mani. *Probing spin ordering in Fe-Pt based antiferromagnetic films using neutron diffraction.* PhD thesis, The University of Alabama, 2006.

[77] http://www.umms.sav.sk/index.php?ID=415.

[78] R. Allmann and A. Kern. *Röntgenpulverdiffraktometrie*. Springer, 2003.

[79] http://institut2a.physik.rwth-aachen.de/de/lehre/praktikum/Anleitungen/FK05 MOKE.pdf.

[80] H. Stillrich. *Magnetische Nanostrukturen basierend auf Co/Pt-Multilagen, hergestellt mittels selbstorganisierter Masken aus Blockpolymer-Micellen*. PhD thesis, Universität Hamburg, 2007.

[81] R. Böttger, H. Friedrich, and H. Janßen. *The PTB thermal neutron reference field at GeNF*. Neutronenphysik PTB-N-47, 2004.

[82] V. Wagner, H. Friedrich, and P. Wille. Higher-order suppression by a mechanical velocity selector. *Physica B*, (213&214):963–965, 1995.

[83] http://www.ill.eu/instruments-support/sample environment/equipment/.

[84] G. Cicognani. *The Yello Book 2005 Guide to Neutron Research Facilities*. Institut Laue-Langevin, 2005.

[85] P. J. Brown. *Magnetic Form Factors, in: Neutron Data Booklet*. Old City Publishing, 2003.

[86] A. B. Shick, V. Drchal, J. Kudrnovsky, and P. Weinberger. Electronic structure and mangetic properties of random alloys: Fully relativistic spin polarized linear muffin-tin-orbital method. *Phys Rev. B*, 54(3), 1996.

[87] J. U. Thiele, L. Folks, M. F. Toney, and D. K. Weller. Perpendicular magnetic anisotropy and mangetic domain structure in sputtered epitaxial FePt (001) $L1_0$ films. *J. Appl. Phys.*, 84(5686), 1998.

[88] T. Takasugi, M. Takazawa, and O. Izumi. Atomistic defect structures of Co_3Ti containing boron, carbon and beryllium. *J. Mater. Sci.*, 25:4226, 1990.

[89] B. D. Cullity and S. R. Stock. *Elements of X-ray Diffraction*. Prentice Hall, Pearson Education International, 2001.

[90] C. Suryanarayana and M. Grant Norton. *X-ray Diffraction A Pratical Approach*. Plenum Press, New York and London, 1998.

[91] A. Singh and A. H. King. Tables of coincidence orientations for ordered tetragonal $L1_0$ alloys for a range of axial ratios. *Acta Cryst.*, B49:266–272, 1993.

[92] C. L. Zha, R. K. Dumas, Y. Y. Fang, V. Bonanni, J. Nogués, and J. Akerman. Continuously graded anisotropy in single $(Fe_{53}Pt_{47})_{100-x}Cu_x$ films. *Appl. Phys. Lett.*, 97(182504), 2010.

[93] Y. M. Hu, J. C. A. Huang, S. Y. Huang, and T. W. Wu. Kerr effect of ordered and disordered $Fe_{1-x}Pt_x$(001) alloy films. *IEEE Trans. Magn.*, 37(4).

[94] O. Hellwig, G. P. Denbeaux, J. B. Kortright, and E. E. Fullerton. X-ray studies of aligned magnetic stripe domains in perpendicular multilayers. *Physica B*, 336:136, 2003.

[95] J. R. Barnes, S. J. O'Shea, M. E. Welland, J.-Y. Kim, E. Evetts, and R. E. Somekh. Magnetic force microscopy of Co-Pd multilayers with perpendicular anisotropy. *J. Appl. Phys.*, 76(2974), 1994.

[96] G. A. Baker. Application of the Pade approximant method to the investigation of some magnetic properties of the sing model. *Phys. Rev.*, 124(3), 1961.

[97] J. W. Essam and M. E. Fisher. Pade approximant studies of the lattice gas and Ising ferromagnet below the critical point. *J. Chem. Phys.*, 38(802), 1963.

[98] G. K. Wertheim, H. J. Guggenheim, and D. N. E. Buchanan. Sublattice magnetization in FeF_3 near the critical point. *Phys. Rev.*, 169(2), 1968.

[99] Z. Lu, R. V. Chepulskii, and W. H. Butler. First-principles study of magnetic properties of $L1_0$-ordered MnPt and FeRh alloys. *Phys. Rev. B*, 81(094437), 2010.

[100] H. Yamada, H. Shimizu, K. Yamamoto, and K. Uebayashi. Structure and magnetism of 3d and 4d transition-metal alloys TT' (T=Mn, Fe and T'=Rh, Pd) with CuAu-I type ordered structure. *J. Alloys Compd.*, 415:31–37, 2006.

[101] E. Weschke, H. Ott, C. Schüßler-Langeheine, D. V. Vyalikh, G. Kaindl, V. Leiner, M. Ay, T. Schmitte, H. Zabel, and P. J. Jensen. Finite-size effect on magnetic ordering temperatures in long-period antiferromagnets: Holmium thin films. *Phys. Rev. Lett.*, 93(15), 2004.

[102] E. L. Lee, P. E. Bolduc, and C. E. Violet. Magnetic ordering and critical thickness of ultrathin iron films. *Phys. Rev. Lett.*, 13(800), 1964.

[103] T. Hasegawa, J. Miyahara, T. Narisawa, S. Ishio, H. Yamane, Y. Kondo, J. Ariake, S. Mitani, Y. Sakuraba, and K. Takanashi. Study of ferro-antiferromagnetic transition in [001]-oriented $L1_0$ $FePt_{1-x}Rh_x$ film. *J. Appl. Phys.*, 106(103928), 2009.

[104] A. Bringer. *Heisenberg Model - Magnetic Interactions, in: Magnetism goes nano.* FZ Jülich GmbH, 2005.

[105] S. Blundell. *Magnetism in Condensed Matter.* Oxford University Press, 2004.

[106] E. L. Nagaev. Anomalous magnetic structure and phase transitions in non-Heisenberg magnetic materials. *Sov. Phys. Usp.*, 25(1), 1982.

[107] M. Getzlaff. *Fundamentals of Magnetism.* Springer, 2008.

[108] R. Skomski. *Simple Models of Magnetism.* Oxford Graduates Texts, 2008.

[109] G. Bihlmayer. *Non-Collinear Magnetism: Exchange Parameter and T_C, in: Computational Nanoscience: Do it Yourself!* John von Neumann Institute for Computing, 2006.

[110] G. Bihlmayer. *Density- functional Theory of Magnetism, in: Handbook of Magnetism and Advanced Magnetic Materials 1.* Wiley, 2007.

[111] I. S. Lyubutin, P. G. Naumov, and B. V. Mill. Magnetic transition and spin rotation in a new multiferroic $Ba_3TaFe_3Si_2O_{14}$ observed by the Mössbauer spectroscopy. *Europhys. Lett.*, 90(67005), 2010.

[112] A. I. Liechtenstein, M. I. Katsnelson, V. P. Antropov, and V. A. Gubanov. Local spin density approach to the theory of exchange interactions in ferromagnetic metals and alloys. *J. Magn. Magn. Mater.*, 67:65–74, year=1987,.

[113] S. Polesya, S. Mankovsky, O. Sipr, W. Meindl, C. Strunk, and H. Ebert. Finite-temperature magnetism of Fe_xPd_{1-x} and Co_xPt_{1-x} alloys. *Phys Rev. B*, 82(214409), 2010.

[114] M. Pajda, J.Kudrnovsky, I. Turek, V. Drchal, and P. Bruno. Ab initio calculations of exchange interactions, spin-wave stiffness constants, and Curie temperatures of Fe, Co, and Ni. *Phys Rev. B*, 82(214409), 2010.

[115] D. Hinzke, U. Nowak, O. N. Mryasov, and R. W. Chantrell. Orientation and temperature dependence of domain wall properties in FePt. *Appl. Phys. Lett.*, 90(082507), 2007.

[116] D. Hinzke, N. Kazantseva, U. Nowak, O. N. Mryasov, P. Asselin, and R. W. Chantrell. Domain wall properties of FePt: From Bloch to linear walls. *Phys Rev. B*, 77(094407), 2008.

[117] N. Kazantseva, D. Hinzke, U. Nowak, R. W. Chantrell, U. Atxitia, and O. Chubykalo-Fesenko. Towards multiscale modeling of magnetic materials: Simulations of FePt. *Phys Rev. B*, 77(184428), 2008.

[118] O. N. Mryasov, U. Nowak, K. Y. Guslienko, and R. W. Chantrell. Temperature-dependent magnetic properties of FePt: Effective spin Hamiltonian model. *Europhys. Lett.*, 69(5):805–811, 2005.

[119] R. Skomski, O. N. Mryasov, J. Zhou, and D. J. Sellmyer. Finite-temperature anisotropy of magnetic alloy. *J. Appl. Phys.*, 99(08E916), 2006.

A. Debye-Waller factor

In section 5.4.3 it was mentioned that the integrated intensities of the second order reflections (002) and (200) of the $Fe_{50}Pt_{40}Rh_{10}$ films with different thicknesses show a nonmagnetic temperature behavior. The observed decay of the integrated intensities is exemplarily shown for the 500 nm thick $Fe_{50}Pt_{40}Rh_{10}$ film in Fig. A.1. The origin of the decay are thermal fluctuations. A magnetic origin can be excluded since the polarization analysis of the second order reflection (002) showed no splitting of the NSF channels or a SF signal which should be observable if a magnetic contribution to the peak intensity exists. Systematic errors due to failures during the measurements can be also excluded since these failures should also be observed in the integrated intensities of the other reflections, in particular in the first order reflections. The decay of the integrated intensity can be explained by thermal lattice vibrations which increase with the temperature and can be expressed by the so-called Debye-Waller factor (DW). The DW-factor f_{DW} depends on the temperature and on the Q-position in the reciprocal space [64]:

$$f_{DW} = e^{-2B\frac{\sin^2\theta}{\lambda^2}} = e^{-2B\frac{Q^2}{8\pi^2}}. \tag{A.1}$$

The factor B can be written as $B = 8/3\pi < u^2 >$, with $< u^2 >$ the mean square oscillation. The mean square oscillation $< u^2 >$ is defined by:

$$< u^2 >= \frac{3k_BT}{M\omega^2} = \frac{3k_BT}{C}, \tag{A.2}$$

where k_B denotes the Boltzmann constant, M the atomic mass and ω the oscillation frequency. By the use of these definitions the above equation A.1 can be written as:

$$f_{DW} = e^{-\frac{Q^2k_BT}{C}}. \tag{A.3}$$

The influence of the lattice vibrations on the integrated intensity is plotted in Fig. A.2 together with the Q-dependence. The Q-dependence is the reason why the second order reflections are more affected by the thermal vibration than the first order or half order peaks (see Fig. A.2). It should be noted that for the correction the constant C was determined from the data of the second order reflection (002) since no magnetic contributions are expected to its intensity. The Debye-Waller corrections are exemplarily shown in Fig. A.1 for the 500 nm film.

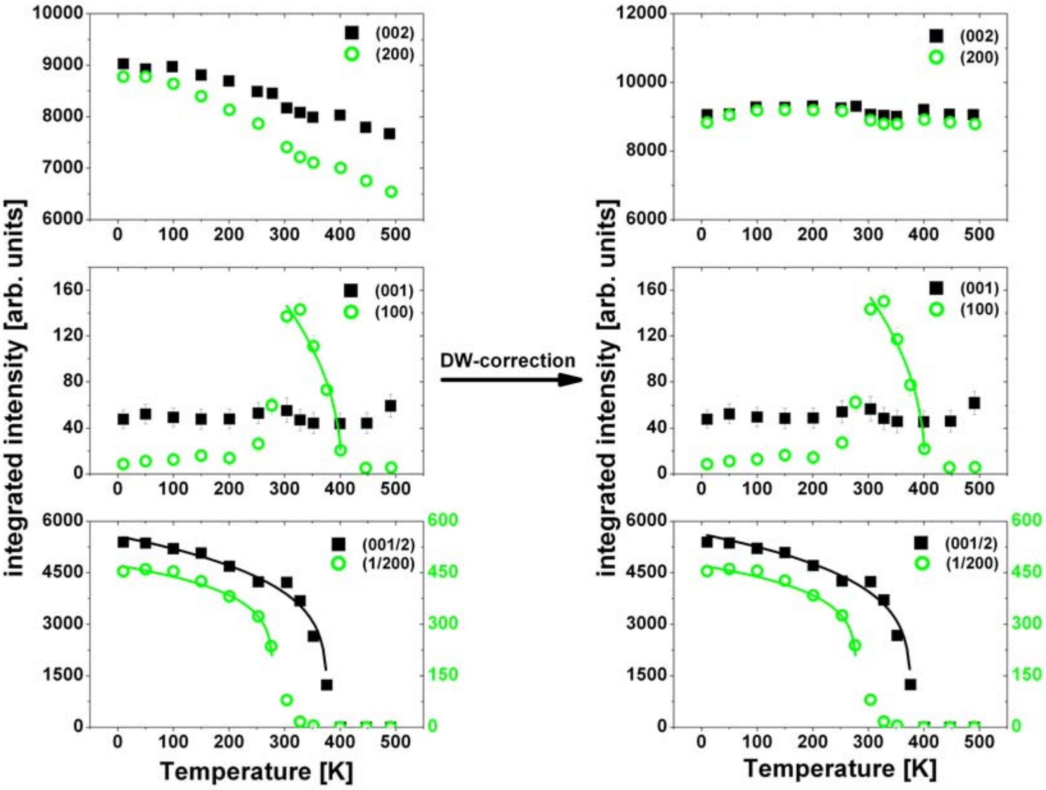

Figure A.1.: Temperature dependence of the integrated peak intensities for the 500 nm $Fe_{50}Pt_{40}Rh_{10}$ film at the half, first and second order reflections along the [001]- (solid symbols) and the [100]-direction (open symbols). The lines are fits to the power law 5.19. The left graphs show the measurements without the Debye-Waller correction.

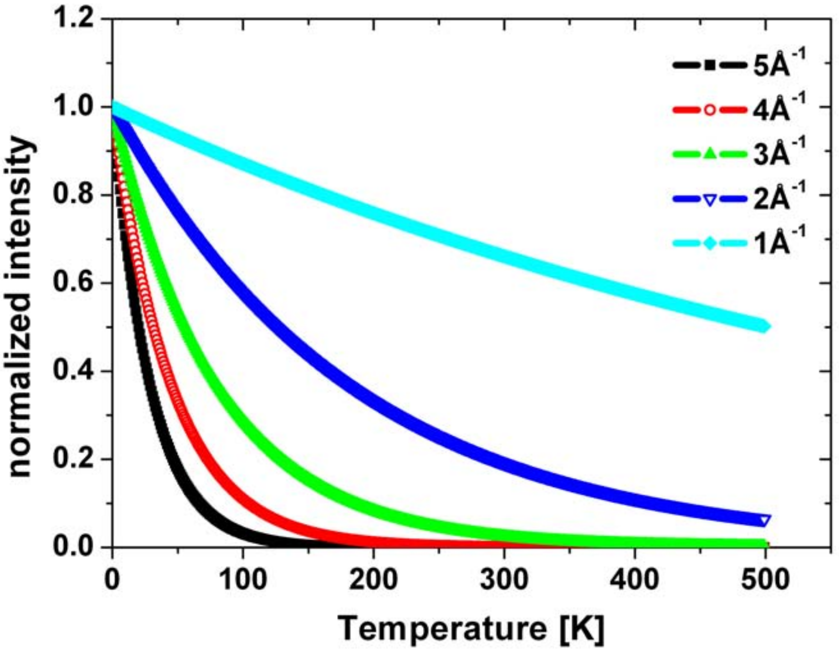

Figure A.2.: Normalized temperature dependence of the Debye-Waller factor for different Q-values. The constant C was set to 1.

Acknowledgements

First I would like to thank my supervisor Prof. Dr. Andreas Schreyer for the opportunity to work in a very interesting research field at the Helmholtz-Zentrum Geesthacht. I also would like to thank him for the support during this work.

Dieter Lott I would like to thank for the support and help during the whole time of this work, for spending a lot of time for discussions and for the corrections of my writings and editorial advices.

I am also deeply grateful to Gary Mankey and his co-workers for spending a lot of time to prepare $Fe_{50}Pt_{50-x}Rh_x$ samples of excellent quality. Without these samples this work would not have been possible.

Another very helpful collaboration was with Elena Tartakovskaya. Her past and ongoing work to develop a theoretical model of the proposed magnetic spin configurations was a great help.

Thanks go also to Frank Klose and Annemieke Mulders for the discussions about the theoretical model.

The instrument responsibles of IN12 and D23, Karin Schmalzl and Wolfgang Schmidt I would like to thank for their support during my neutron diffraction measurements at the ILL.

My gratitude to Simon Heße for the help with the MOKE measurements.

I also would like to thank Prof. Dr. H. P. Oepen for being the second reviewer of my thesis.

Special thanks go to my colleagues from Helmholtz-Zentrum Geesthacht for a wonderful working atmosphere, their support during this thesis and the ongoing work and in particular for the delicious cakes.

I also would like to thank my former colleagues Alexander Grünwald and Wolfgang Kreuzpaintner for their help and the discussions.

Finally I would like to thank my family and friends for their support.